

# Secondary structure mimetic polymer and peptide conjugates – synthesis and structural investigations

## Dissertation

zur Erlangung des Doktorgrades der Naturwissenschaften  
(Dr. rer. nat.)

der

Naturwissenschaftlichen Fakultät II  
Chemie, Physik und Mathematik

der Martin-Luther-Universität  
Halle-Wittenberg

vorgelegt von

Frau Stefanie Deike  
geb. am 23.07.1990 in Braunschweig

Gutachter

1. Prof. Dr. Wolfgang H. Binder
2. Prof. Dr. Pol Besenius

Verteidigung: 19.11.2019

## Danksagung

An dieser Stelle möchte ich mich bei allen bedanken, die zum Gelingen dieser Arbeit beigetragen haben.

Mein erster Dank geht an Prof. Dr. Wolfgang Binder für die Bereitstellung des interessanten Themas, die stets gewährte Unterstützung und die vielen eingeräumten Möglichkeiten, meine Forschungsergebnisse im In- und Ausland präsentieren zu können.

Der gesamten Arbeitsgruppe Binder möchte ich für das angenehme Arbeitsklima und die sehr gute Zusammenarbeit danken. Anke Hassi danke ich für die Unterstützung in administrativen Angelegenheiten sowie Susanne Tanner und Julia Großert für die Durchführung von Messungen und die Bereitstellung von Chemikalien.

Ein besonderer Dank geht an meine Kollegen aus dem Labor 3.23 und dem Büro 4.06, sowie an Diana und Zhanna. Danke für euren Humor, der in schwierigen Situationen oft Wunder gewirkt hat, eure Unterstützung im Laboralltag und die vielen hilfreichen Diskussionen. Dr. Diana Döhler danke ich auch für die kritische Durchsicht meiner Arbeit.

Herrn Dr. Ströhl und seinem Team danke ich für die Anfertigung der zahlreichen NMR-Spektren sowie Prof. Jörg Kressler und Prof. Dariush Hinderberger für die Bereitstellung des Langmuir Troges und Dr. Christian Fuchs sowie Dr. André Hädicke für die Einweisung am Gerät.

Der Core Unit Peptid-Technologie in Leipzig, insbesondere Dr. Sven Rothemund danke ich für die gute Zusammenarbeit und die Herstellung der Peptide. Für die Toxizitätstests danke ich Anne Funtan und Prof. Reinhard Paschke.

Prof. Jochen Balbach danke ich für die Messerlaubnis am Microplate Reader, sowie am CD- und UV-Spektrophotometer und Bruno Voigt für die Einweisung in die Geräte, die Hilfestellung bei auftretenden Fragen sowie für die Anfertigung der TEM Messungen.

Zu guter Letzt geht ein besonderer Dank an meine Familie und meine Freunde, die immer ein offenes Ohr für mich hatten und mich während der ganzen Jahre unterstützt haben.

## Abstract

$\beta$ -Turns fulfill a variety of different functions in natural proteins. Besides their structural role, inducing the backfolding of adjacent chains, their exposure to the environment results in specific molecular interactions. Therefore, mimicking of these structures is of great interest, performed in this work to deduce the influence of turn mimetics on the structural behavior of polymers and proteins.

In the first part of this work,  $\beta$ -turn mimetics were used as structural elements to transfer chirality into polymers. Helical polyisocyanates were precisely synthesized and afterwards linked to  $\beta$ -turn mimetics. The structure and purity of the synthesized conjugates were revealed by NMR spectroscopy, mass spectrometry and chromatography (HPLC, GPC). Furthermore, polyisocyanate copolymers bearing functional side chains for further modifications were synthesized, as well as block-copolymers with poly(ethylene glycol) to obtain a comparison between this amphiphilic copolymer and the amphiphilic conjugate bearing a rigid  $\beta$ -turn mimetic. Chirality investigations revealed an induction effect from the chiral turn mimetic *via* a linked triazole moiety onto the polymer chain. Elongation of the linker and increase of flexibility resulted in a lower chirality induction effect. Furthermore, solvent dependency of the chirality was observed for both,  $\beta$ -turn mimetic polymers and copolymers with PEG, confirming changes in the helical parameters of polyisocyanates in different solvents.

In the second part of this work, the influence of  $\beta$ -turn mimetics on the aggregation of an amyloid peptide ( $A\beta_{40}$ ) was investigated. Turns of different size, rigidity and hydrophobicity were synthesized and incorporated into amyloid  $\beta$  peptide *via* solid phase peptide synthesis (SPPS). Purity of the peptide-conjugates was assessed by HPLC and MALDI-TOF-MS. Aggregation assays revealed a strong influence of position and turn structure on the fibril formation of the amyloid peptides. Both, a hydrophobic aromatic triazole turn mimetic and a flexible linker unit resulted in enhanced fibrillation, whereas a small rigid linker led to reduced fibrillation. Interestingly, peptides containing a rigid bicyclic  $\beta$ -turn mimetic completely lacked the ability to fibrillate under physiological conditions (pH 7.4, 37 °C) and furthermore provided a strong inhibiting effect on the fibrillation of  $A\beta_{40}$  when used as an additive. Replacement of the amino acids glycine and serine at positions 25–26 provided the strongest inhibition effect, indicating the importance of the small glycine, requiring only small space, for the ability of  $A\beta$  to form  $\beta$ -sheet aggregates.

## Kurzzusammenfassung

$\beta$ -Schleifen ( $\beta$ -Turns) erfüllen in natürlichen Proteinen eine Vielzahl von Funktionen. Neben ihrer strukturellen Aufgabe, benachbarte Ketten auf sich selbst zurückzufalten und dadurch eine eng gepackte Struktur zu erzeugen, erfüllen sie durch ihre Exposition an der Oberfläche von Proteinen zahlreiche Funktionen durch molekulare Wechselwirkungen. Daher sind diese Strukturen ein interessantes Ziel für Mimetika, welche im Rahmen dieser Arbeit untersucht wurden und insbesondere deren struktureller Einfluss auf Polymere sowie Peptide.

Im ersten Teil dieser Arbeit wurden mimetische  $\beta$ -Turns als Strukturelement in Polymere eingebaut, um auf diese Chiralität zu übertragen. Dazu wurden helikale Polyisocyanate mit exakt definierter Struktur synthetisiert und anschließend mit dem  $\beta$ -Turn verknüpft. Die Struktur und Reinheit der hergestellten Konjugate wurde durch NMR-Spektroskopie, Massenspektrometrie sowie chromatographische Methoden (GPC, HPLC) gezeigt. Zusätzlich wurden Polymere in der Seitenkette modifiziert und Blockcopolymere mit Poly(ethylene glycol) hergestellt, um einen Vergleich herzustellen zwischen diesem amphiphilen Copolymer und dem amphiphilen Konjugat, welches einen rigiden Turn enthält. Chiralitätsuntersuchungen zeigten einen Induktionseffekt vom chiralen Turn über eine Triazolgruppe auf die Polymerkette auf, wohingegen eine Verlängerung des Verbindungsglieds einen geringeren Induktionseffekts zur Folge hatte. Außerdem wurde sowohl für die  $\beta$ -Turn Konjugate als auch für die Blockcopolymere eine Lösungsmittelabhängigkeit beobachtet und somit bestätigt, dass die helikalen Parameter der Polyisocyanate vom Lösungsmittel abhängig sind.

Im zweiten Teil dieser Arbeit sollte der Einfluss von mimetischen  $\beta$ -Turns auf die Aggregation eines amyloiden Peptids ( $A\beta_{40}$ ) untersucht werden. Dazu wurden Turns verschiedener Größe, Rigidität und Hydrophobizität hergestellt und durch Festphasenpeptidsynthese (SPPS) in  $A\beta_{40}$  eingebaut. Die Reinheit der Peptid-Konjugate wurde durch HPLC und MALDI-TOF-MS bestätigt. Aggregationsuntersuchungen zeigten einen starken Einfluss von Position und Struktur der Turn Mimetika auf die Ausbildung von Fibrillen. Sowohl ein hydrophober, aromatischer Turn, als auch ein flexibles Verbindungsmolekül resultierten in einer beschleunigten Fibrillierung, wohingegen ein kleines starres Verbindungsmolekül einen verzögernden Effekt ausübte. Interessanterweise wiesen die Peptide, die einen rigiden bizyklischen Turn enthielten, keine Aggregation unter physiologischen Bedingungen (pH 7.4, 37 °C) auf und hatten außerdem einen starken Einfluss auf die Aggregation von  $A\beta_{40}$  wenn sie als Additiv zugesetzt wurden. Der Austausch der Aminosäuren Glycin und Serin an den Positionen 25–26 hatte die größte hemmende Wirkung und zeigt somit, dass die kleine Aminosäure Glycin durch ihren geringen Platzanspruch wichtig ist für die Fähigkeit von  $A\beta$  zu fibrillieren.



## Table of contents

1	Introduction .....	1
1.1	Natural and synthetic macromolecules.....	1
1.2	Protein folding.....	2
1.2.1	Structure of proteins .....	2
1.2.2	$\beta$ -Turns and turn mimetics.....	4
1.2.3	Theory of protein folding .....	6
1.2.4	Influence of hairpin and turn structures in the folding process.....	7
1.3	Misfolded proteins .....	9
1.3.1	Structure of $A\beta$ and fibrillation in vitro .....	9
1.3.2	Structure of amyloid fibrils from ssNMR .....	11
1.3.3	Modifications of $A\beta$ .....	14
1.4	Polymer folding .....	16
1.4.1	Helical polymers .....	16
1.4.2	Foldamers.....	17
1.4.3	Single-chain nanoparticles (SCNPs).....	19
2	Aim and concept.....	23
2.1	Scope of the thesis .....	23
2.2	Concept of the thesis.....	24
3	Results and discussion .....	26
3.1	Synthesis of $\beta$ -turn mimetics.....	26
3.1.1	Synthesis of $\beta$ -turn dipeptide for “click” coupling.....	26
3.1.2	Synthesis of Fmoc-protected $\beta$ -turn mimetics for SPPS .....	27
3.1.3	Synthesis of hydrophobic Fmoc-protected $\beta$ -turn mimetic for SPPS .....	29
3.2	Synthesis of alkyne-functionalized helical PHICs.....	30
3.3	Synthesis of $\beta$ -turn mimetic polymer conjugates.....	38
3.4	Synthesis of PHIC-PEG block-copolymers .....	42
3.5	Chirality induction effects in $\beta$ -turn mimetic polymer conjugates and block-copolymers containing PHIC.....	45
3.5.1	Circular dichroism studies of chiral PHICs .....	46
3.5.2	Circular dichroism studies of $\beta$ -turn mimetic conjugates.....	47
3.5.3	Circular dichroism studies of PEG copolymers .....	51
3.6	Behavior at the air / water interface.....	53
3.7	Synthesis of $\beta$ -turn mimetic peptide conjugates .....	58
3.8	Structural investigations of $\beta$ -turn mimetic peptide conjugates .....	61
3.8.1	Aggregation studies of peptide conjugates in comparison with $A\beta_{40}$ .....	61
3.8.2	Aggregation studies of mixtures of $A\beta_{40}$ with peptide conjugates.....	62
3.8.3	Aggregation studies of mixtures of $A\beta_{40}$ with short $A\beta_{16-35}$ peptide conjugates ...	65
3.8.4	Circular dichroism studies of peptide conjugates (20–24) .....	67
3.8.5	TEM measurements.....	70

3.8.6	Cytotoxicity assay .....	72
4	Experimental part .....	73
4.1	Materials and methods.....	73
4.2	Synthesis of $\beta$ -turn mimetics.....	77
4.2.1	Synthesis of 7,5-bicyclic $\beta$ -turn mimetic (1) and (2) .....	77
4.2.2	Synthesis of $\beta$ -turn mimetic (1b) for SPPS.....	78
4.2.3	Synthesis of 6,5-bicyclic $\beta$ -turn mimetic dipeptide (3) for SPPS.....	79
4.2.4	Synthesis of a triazole containing aromatic turn mimetic (TAA, 4) .....	80
4.3	Synthesis of functional monomers.....	83
4.4	Synthesis of polyisocyanates.....	84
4.4.1	Synthesis of poly( <i>n</i> -hexyl isocyanate)s .....	84
4.4.2	Homo- and copolymerization of 2-chloroethyl isocyanate (CIC) and HIC.....	86
4.4.3	Copolymerization of functional isocyanates and HIC .....	89
4.4.4	“Click”-reaction of side chain functional polyisocyanate .....	92
4.5	Synthesis of $\beta$ -turn mimetic PHIC conjugates .....	93
4.6	Synthesis of TEG- / PEG-PHIC copolymers .....	94
4.6.1	Synthesis of azide-functional TEG / PEG.....	94
4.6.2	Synthesis of PEG-PHIC copolymers.....	96
4.7	Synthesis of rhodamine-labeled PHIC .....	98
4.7.1	Synthesis of azide-functionalized rhodamine .....	98
4.7.2	“Click” reaction of rhodamine-azide with PHIC .....	100
4.8	Synthesis of $\beta$ -turn mimetic peptide conjugates .....	101
5	Summary.....	103
6	Appendix .....	108
7	References.....	126

## Abbreviations

ABA	aminobenzoic acid
ACN	acetonitrile
AFM	atomic force microscopy
AlkIC	4-isocyanato-1-butyne
ATR	attenuated total reflectance
ATRP	atom transfer radical polymerization
AVA	4-aminovaleric acid
AzIC	1-azido-5-isocyanatopentane
BTD	beta turn dipeptide
calc	calculated
CD	circular dichroism
CIC	2-chloroethyl isocyanate
Cp	cyclopentadienyl
CuAAC	copper(I)-catalyzed azide/alkyne cycloaddition
$\bar{D}$	PDI, polydispersity index
Da	dalton
DCE	1,2-dichloroethane
DCM	dichloromethane
DIC	<i>N,N</i> -diisopropylcarbodiimide
DIPEA	<i>N,N</i> -diisopropylethylamine
Dithranol	1,8-Dihydroxy-9,10-dihydroanthracen-9-one
DMF	<i>N,N</i> -dimethylformamide
DMSO	<i>N,N</i> -dimethylsulfoxide
DPPA	diphenyl phosphoryl azide
DPFC	1,2-dipalmitoyl- <i>sn</i> -glycero-3-phosphocholine
EA	ethyl acetate
ESI	electrospray ionization
EO	ethylene oxide
equiv.	equivalent
FBS	fetal bovine serum
Fmoc-OSu	Fmoc- <i>N</i> -hydroxysuccinimide ester
GPC	gel permeation chromatography
HCCA	$\alpha$ -cyano-4-hydroxycinnamic acid
HIC	<i>n</i> -hexyl isocyanate
IAA	<i>trans</i> -3-indoleacrylic acid

IR		infrared
	b	broad
	w	weak
	m	middle
	s	strong
LAC		liquid adsorption chromatography
LC		liquid condensed
LCCC		liquid chromatography under critical conditions
LE		liquid expanded
MALDI		matrix-assisted-laser-desorption-ionization
MeOH		methanol
$M_L$		molar mass per unit contour length
$M_n$		number average molar mass
MS		mass spectrometry
$M_w$		weight average molar mass
$m/z$		mass-to-charge ratio
NMP		nitroxide mediated polymerization
NMR		nuclear magnetic resonance spectroscopy
	s	singlet
	bs	broad signal
	d	doublet
	dd	doublet of doublets
	t	triplet
	td	triplet of doublets
	q	quartet
	quint	quintet
	m	multiplet
Oxyma		ethyl cyanohydroxyiminoacetate
PCIC		poly(2-chloroethyl isocyanate)
PDI		polydispersity index ( $PDI = M_w/M_n$ )
PEG		poly(ethylene glycol)
PHIC		poly( <i>n</i> -hexyl isocyanate)
PyBOP		(benzotriazol-1-yloxy)tripyrrolidinophosphonium hexafluorophosphate
RAFT		reversible addition-fragmentation chain-transfer
RI		refractive index
ROMP		ring-opening metathesis polymerization
rpm		revolutions per minute

r.u.	repeating unit
SPPS	solid phase peptide synthesis
$t_{1/2}$	half time of aggregation
TAA	triazole aromatic amino acid
TBTA	tris[(1-benzyl-1 <i>H</i> -1,2,3-triazol-4-yl)methyl]amine
TEG	triethylene glycol
TEM	transmission electron microscopy
TFA	trifluoroacetic acid
th	theoretical
THF	tetrahydrofuran
ThT	thioflavin T
TLC	thin-layer chromatography
TOF	time of flight
UV	ultraviolet
WT	wild type

**Parts of this dissertation have been published in:**

Deike, S.; Binder, W. H., Induction of Chirality in  $\beta$ -Turn Mimetic Polymer Conjugates via Postpolymerization “Click” Coupling. *Macromolecules* **2017**, *50*, 2637–2644.

Deike, S., Malke, M., Lechner, B.-D., Binder, W. H., Constraining Polymers into  $\beta$ -Turns: Miscibility and Phase Segregation Effects in Lipid Monolayers. *Polymers* **2017**, *9*, 369.

Parts of chapters 3.3, 3.5 and 3.6 were adapted with permission from the American Chemical Society (Copyright 2017) and from MDPI (Copyright 2017).

# 1 Introduction

## 1.1 Natural and synthetic macromolecules

How would human life be without macromolecules? – It wouldn't exist.

DNA, RNA and proteins, the three essential building blocks of life, are biological macromolecules and provide genetic information and functionality such as catalysis of biochemical reactions and molecular recognition. Furthermore another class of biological macromolecules, namely carbohydrates are of major importance for energy storage, protection of the body against the environment and other biochemical processes. But today, not only biomacromolecules but also synthetic ones have become irreplaceable in our everyday life. From simple products such as packaging materials to high-tech products for e.g. medical applications, polymers are having a huge impact on human life. The question now arises, what features do these macromolecules of different origin share and where do differences occur?

Biomacromolecules are built from a small number of monomeric units, in the case of DNA these are adenine, cytosine, guanine and thymine, while proteins are composed of a library of 20 amino acids with different functional side chains. Sequence defined biopolymers result from the stepwise addition of monomers, proceeding from a defined amino/N-terminus to a carboxyl/C-terminus for proteins and from the 5' end to the 3' end in case of nucleic acids (see Figure 1).

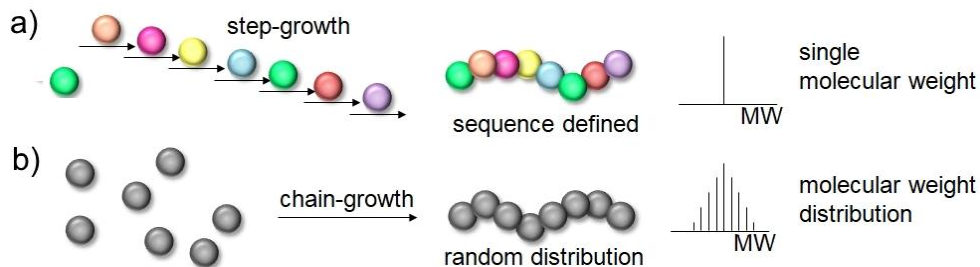


**Figure 1.** Differences occurring between sequence defined biological macromolecules and random synthetic ones.

The synthesis of synthetic polymers is mostly achieved through “living” polymerization techniques, resulting in a random distribution of monomeric units along the polymer chain. These chain growth methods provide polymers with precise functionality at the chain ends and in the side chain, while they still lack exact sequence control and a single molecular weight.

These differences on a molecular level also affect the assembly and structure formation of biological and synthetic macromolecules. Thus, further similarities and differences regarding structures of higher order and folding behavior of both proteins and polymers will be discussed in the following chapters.

## 1.2 Protein folding

### 1.2.1 Structure of proteins

The structure of proteins can be divided into four hierarchical structure levels (see Figure 2a).<sup>[1]</sup> The primary structure describes the amino acid sequence, composed from a repertoire of 20 proteinogenic amino acids, linked via amide bonds, which possess a partial double-bond character as illustrated in Figure 2b. For this reason, these bonds are restricted in rotation with a barrier of about 65-90 kJ/mol and thus all atoms in between  $C_\alpha$  and  $C_{\alpha+1}$  are in plane. The two adjacent  $C_\alpha$  atoms can be arranged either *trans* or *cis* to each other. However, the *cis*-configuration is unfavorable due to the steric hindrance between the residues attached as shown in Figure 2c.

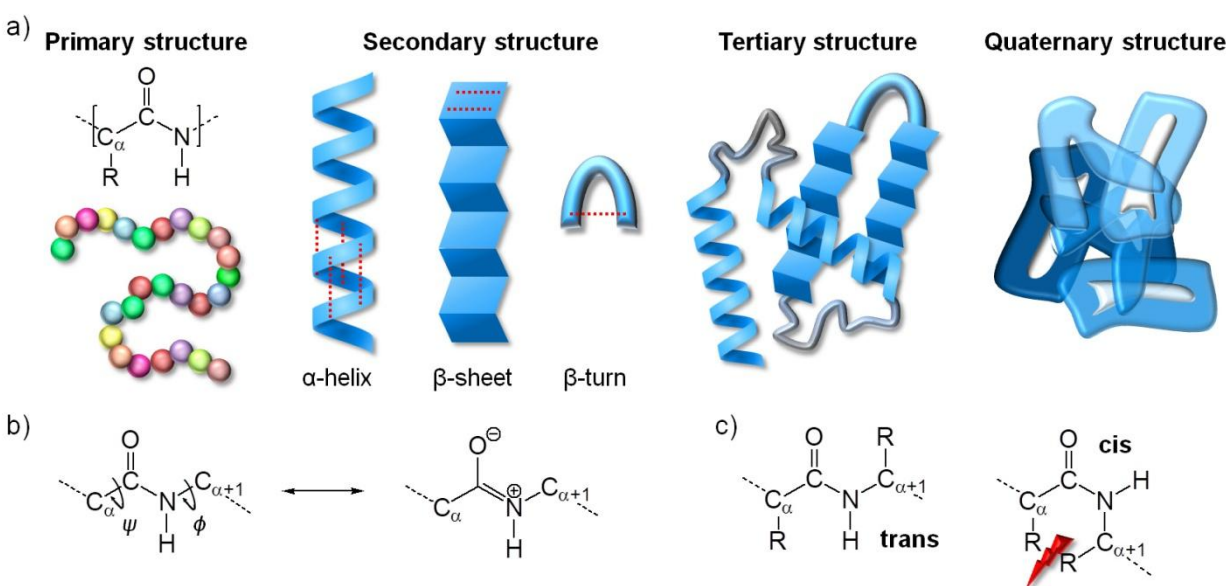


**Figure 2.** a) Four hierarchical structure levels found in proteins; b) structure of the amide bond and indication of dihedral angles  $\phi$  and  $\psi$ ; c) *trans*- and *cis*-conformers.

Besides other rare examples, proline is the most prominent amino acid exhibiting the *cis*-configuration, as the cyclic structure results in increased sterical hindrance in the *trans*-configuration and thus a weaker enthalpic difference between the two structures. In contrast to the amide bond, the single bonds attached to the  $C_\alpha$  atom can rotate, described by the two dihedral angles  $\psi$  and  $\phi$ . In 1963 Ramachandran discovered that a great number of conformations and dihedral angles are forbidden due to sterical hindrance, which is illustrated by the Ramachandran plot<sup>[2]</sup> (see Figure 3) showing allowed (colored) and forbidden (white) combinations of  $\psi$  and  $\phi$ . Proposed as a model in 1951,<sup>[3]</sup>  $\alpha$ -helices and  $\beta$ -sheets emerged as the two major secondary structure elements, which can be also assigned in the Ramachandran plot in the allowed regions. These two structures have the ability to include all carbonyl groups and amine protons in hydrogen bonding, resulting in a high stability for these secondary structures. While  $\alpha$ -helices are stabilized by intramolecular hydrogen bonds between a carbonyl group and



the amine proton which are four amino acids apart ( $i+4 \rightarrow i$ ),  $\beta$ -sheets establish intermolecular hydrogen bonds between adjacent sheets, which can be arranged parallel or antiparallel.

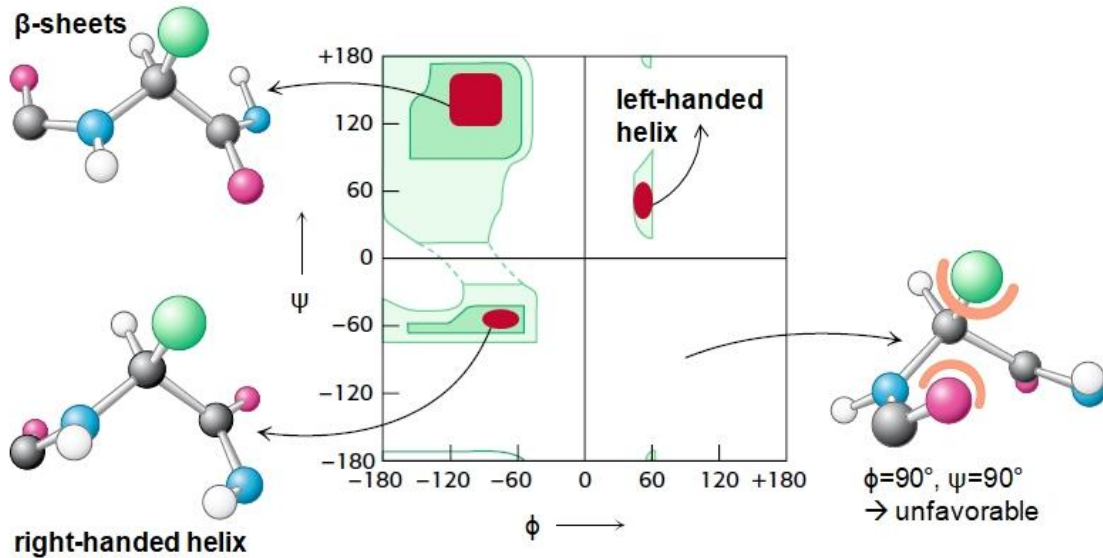


**Figure 3.** Ramachandran plot showing allowed and forbidden combinations of dihedral angles. Figure adapted by permission from Springer Nature: Biochemie by Jeremy M. Berg, John L. Tymoczko, Lubert Stryer<sup>[1]</sup> (Copyright 2013).

Besides these two major secondary structures, others such as the  $\pi$ -helix<sup>[4-5]</sup>, occurring in about 10-15 % of all investigated proteins, the  $3_{10}$ -helix,<sup>[6]</sup> or the  $\alpha$ -sheet<sup>[7-9]</sup> have been characterized. The third major secondary structure element, the reverse turn, enables backfolding of the polypeptide chain by linking two strands of  $\beta$ -sheet or  $\alpha$ -helix, therefore providing the ability to form a globular structure.<sup>[10]</sup> As shown in Figure 2, the tertiary structure describes the structural arrangement of single polypeptide chain in such three-dimensional structures, containing a variety of secondary structure elements. Organization of two or more of such tertiary folded subunits and thus the relationship between different polypeptide chains is described by the quaternary structure of a protein. One example of a protein with a quaternary structure as its active form is hemoglobin, a metalloprotein responsible for the oxygen transport in mammals, consisting of four polypeptide subunits thus forming a so-called tetramer.<sup>[11]</sup> In contrast, the related oxygen-binding protein myoglobin consists of only one polypeptide chain and thus lacks a quaternary structure.<sup>[12]</sup>

In the following chapters, general folding principles, the role of  $\beta$ -turns during protein folding as well as misfolding of proteins will be discussed.

### 1.2.2 $\beta$ -Turns and turn mimetics

Reverse turns can be defined according to the number of amino acids present and are named  $\gamma$ -,  $\beta$ - and  $\alpha$ -turns consisting of three, four or five residues respectively.<sup>[13]</sup> The  $\beta$ -turn was first described by Venkatachalam<sup>[14]</sup> and a general structure is given in Figure 4. While the definition of Venkatachalam relied on the formation of a hydrogen bond involving the backbone CO(i) and NH(i+3), nowadays also “open turns” lacking this hydrogen bond are classified as  $\beta$ -turns, if the distance between C $^{\alpha}$ (i) and C $^{\alpha}$ (i+3) is less than 7 Å and if the backbone torsion angles deviate less than 30° from those of standard  $\beta$ -turns.<sup>[10, 15]</sup> Ten different types of  $\beta$ -turns were classified according to their backbone torsional angles upon which type I and type II are the most prominent ones, representing together about two thirds of all natural occurring  $\beta$ -turns in proteins.<sup>[16-17]</sup> The turn itself is frequently pointing towards the surface of the protein and hence possesses not only a structural function but furthermore participates in protein-protein interactions, molecular recognition or ligand binding.<sup>[18-19]</sup> Owing to the exposure to the hydrophilic environments, polar amino acids possess high turn propensities from which proline, glycine, asparagine and aspartic acid are the most dominating ones.<sup>[10, 20]</sup>

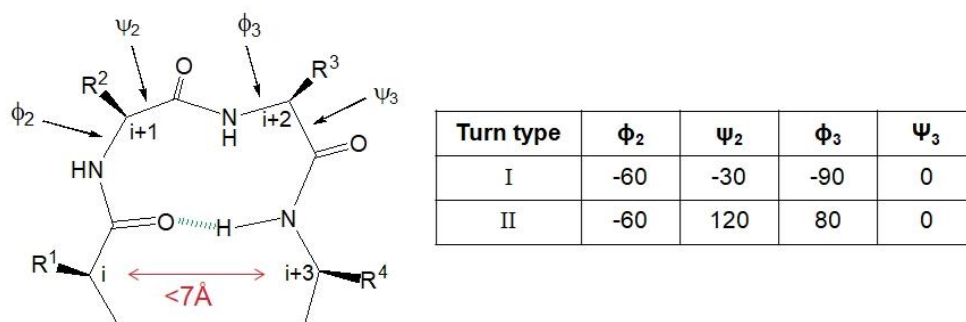


**Figure 4.** General representation of a type II  $\beta$ -turn and dihedral angles for type I and type II  $\beta$ -turn.<sup>[1]</sup>

Due to their bifunctionality of structure and function and the resulting importance of  $\beta$ -turns in peptides and proteins, mimetics of these structures have gained a huge interest and application of modified peptides in drug delivery can be one goal. Using natural peptides in drug delivery displays several disadvantages, as they can easily undergo enzymatic proteolysis, possess a low oral bioavailability and poor membrane permeability.<sup>[21-22]</sup> Consequently it is aimed to replace natural  $\beta$ -turns by mimetic structures to increase the stability, specificity and affinity compared to their natural analogue.

Turn mimetics can be divided into two groups according to their backbone nature into peptidic mimetics and structural mimetics (see Figure 5). Systematic investigations of peptidic mimetics revealed that heterochirality is one major factor for the stabilization of  $\beta$ -turns, which is related to the side chain orientation in  $\beta$ -turns.<sup>[23-24]</sup> In several  $\beta$ -turns (type I, I', II, II') the i+1 and i+2 residues adopt an equatorial and axial orientation respectively, which is best achieved by using a combination of D- and L-amino acid at these positions.<sup>[23]</sup> Besides using D-amino acids,<sup>[25-26]</sup> especially D-proline, also achiral amino acids such as 2-aminoisobutyric acid (Aib)<sup>[27-28]</sup> or

other heterochiral non-natural amino acids such as the dinipectic acid,<sup>[29]</sup> proved to effectively induce  $\beta$ -turns. Proline, which lacks the free NH proton, is one of the amino acids favoring turn formation most. Therefore, using *N*-methylated amino acids, acting as pseudo-prolines, appeared as another possibility to sterically restrict the protein backbone by shifting the equilibrium between *trans*- and *cis*-conformer towards the otherwise unfavorable *cis*-conformation.<sup>[30-32]</sup> Furthermore, *N*-alkylation or a combination with heterochirality results in an increased ability to induce turn conformation.<sup>[33-34]</sup>

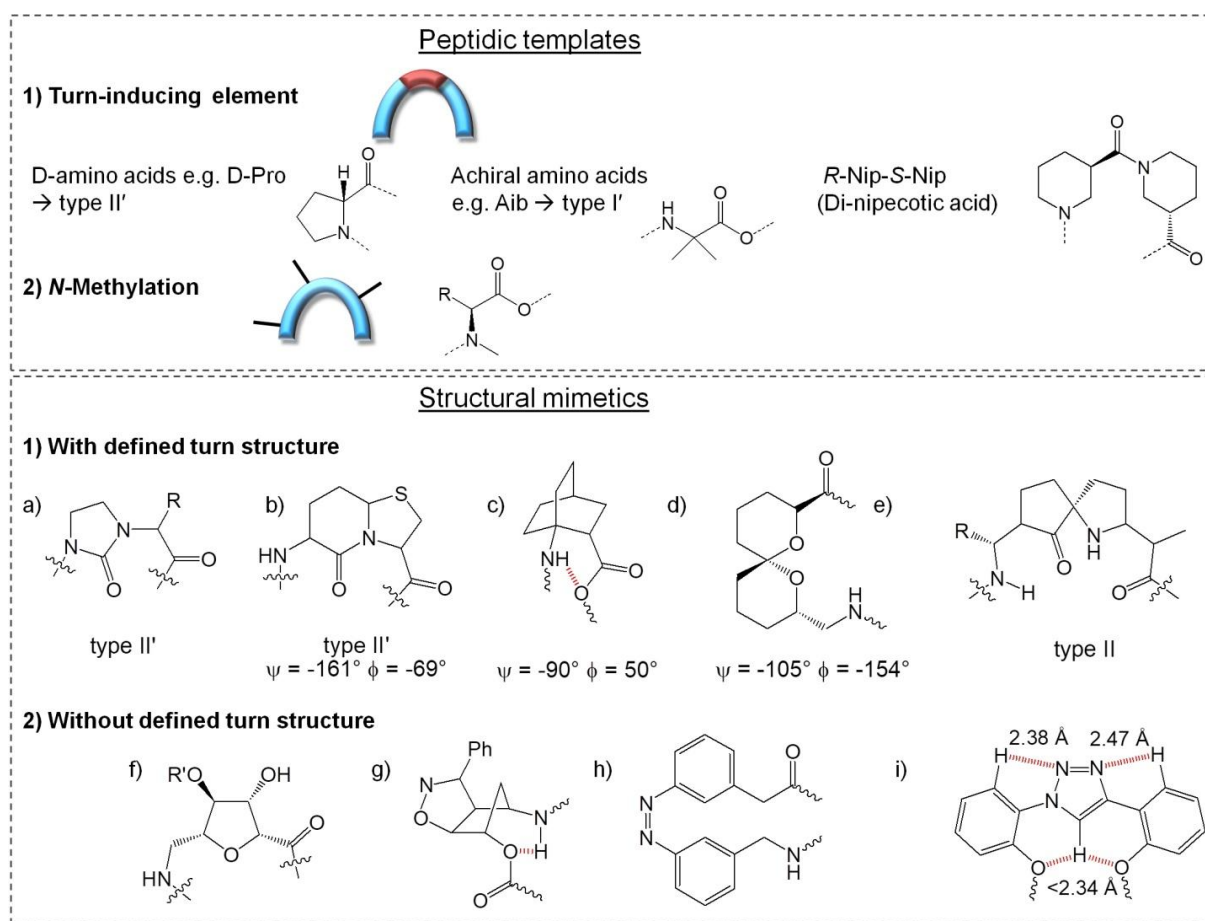


**Figure 5.** Examples of peptidic templates and structural  $\beta$ -turn mimetics.<sup>[35-40]</sup>

The first non-peptidic  $\beta$ -turn mimetic was a lactam developed by Freidinger (see Figure 5a),<sup>[41]</sup> which resulted in higher biological activity than for the original peptide. The Freidinger lactam as well as several other  $\beta$ -turn mimetics are designed to replace only the *i*+1 and *i*+2 positions of the  $\beta$ -turn in a polypeptide chain instead of all four amino acids. Further peptide mimetic  $\beta$ -turns were obtained by introducing a cyclic moiety, which restricts the rotation and leads to a defined conformation such as the bicyclic peptides developed by Nagai (Fig. 5b)<sup>[42-43]</sup> showing a type II' turn structure. Furthermore structural  $\beta$ -turn mimetics which were restricted in rotation by bridging such as in (*S*)-aminobicyclo-[2.2.2]octane-2-carboxylic acid (Fig. 5c),<sup>[36]</sup> 6,6-spiroketal (Fig. 5d)<sup>[37]</sup> and in cyclopenta[*d*]isoxazoline (Fig. 5g)<sup>[35]</sup>. Moreover, aromatic turn mimetics such as a photoswitchable azo dye (Fig. 5h)<sup>[39-40]</sup>, which provides further function due

to the possibility of switching between the *cis*- and *trans*-isomers by UV-light. Several examples have been described based on a triazole moiety as restricting element derived from the copper(I) catalyzed azide/alkyne cycloaddition (CuAAC).<sup>[38, 44-45]</sup> The triazole ring mimics the *trans*-amide bond and can contribute to hydrogen bonding, stabilizing the turn structure in an almost planar structure as illustrated in Figure 5i.<sup>[38]</sup> While some of the structural mimetics can be assigned to a specific type of  $\beta$ -turn, this is not valid for other templates, which deviate much more from the natural  $\beta$ -turns.

### 1.2.3 Theory of protein folding

Folding of proteins has raised huge interest during the past decades, as it is important to understand the mechanisms, to be able to design peptides with enhanced stability, bioactivity and molecular recognition. It is well established, that the native state of a protein is in most cases the one with the lowest free energy and thus the thermodynamically most stable one, which was first postulated by Anfinsen in 1973 and is known as the “thermodynamic hypothesis”.<sup>[46-47]</sup> Folding occurs as interplay between different interactions present in proteins such as hydrophobic interactions, van-der-Waals interactions, hydrogen bonds and electrostatic interactions. Furthermore, some proteins are stabilized by covalent bonds, especially disulfide bridges connecting two cysteine residues.<sup>[48]</sup>

Based on these different interactions contributing to the folding of proteins, three main models have been proposed in the following decades to describe the folding behavior of proteins. In the framework model,<sup>[49-51]</sup> formation of intramolecular hydrogen bonded secondary structures (mainly  $\alpha$ -helical or turn structures) occurs first, which then enables the formation of tertiary structures through hydrophobic interactions. In contrast to this, the hydrophobic-collapse model<sup>[52-53]</sup> assumes that formation of a hydrophobic cluster is the starting point of protein folding, followed by the rearrangement and formation of secondary structures. Formation of the hydrophobic core is driven by the hydrophobic residues which avoid contact with the surrounding water.<sup>[54]</sup> Later, the nucleation-condensation mechanism was proposed,<sup>[55-56]</sup> combining the previous models and hence characterized by a parallel formation of secondary structures stabilized by hydrophobic tertiary interactions resulting in the formation of a nucleus, which can induce the rapid condensation of the whole protein.<sup>[53]</sup>

Despite these classical chemical dynamics, which consider folding as a chemical reaction pathway, a thermodynamic description of protein folding was established in the 90s.<sup>[57]</sup> In contrast to the classical mechanisms, in which a single pathway with defined intermediates is assumed, the so-called “new view” describes folding through multiple pathways and intermediates.<sup>[58-61]</sup> The free energy landscape theory illustrated by a funnel-like structure (see Figure 6) describes on- and off-pathway folding of proteins leading to the native state or misfolded conformations.<sup>[62]</sup>

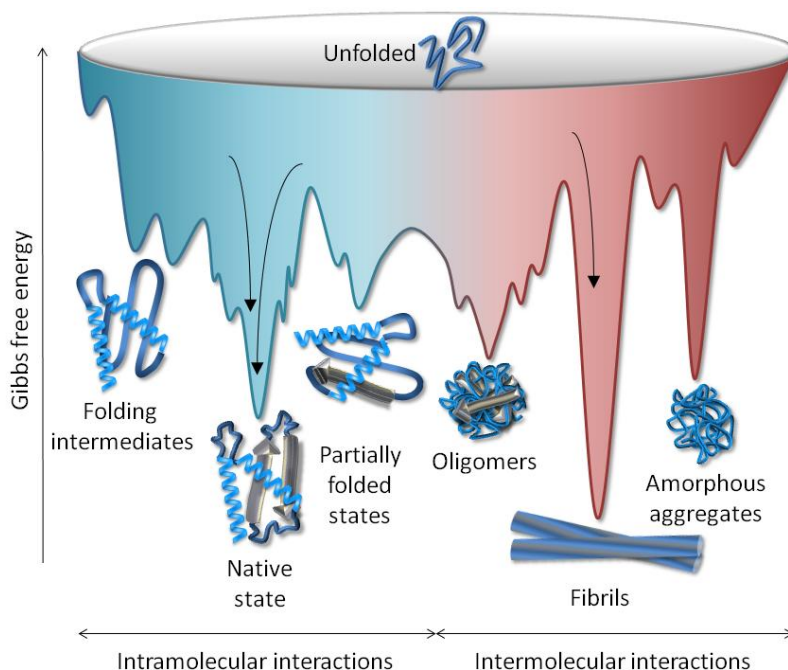


**Figure 6.** Protein energy landscape describing the folding and misfolding of proteins (Figure adapted from reference<sup>[63]</sup> with permission from John Wiley and Sons) (Copyright 2005).

While on-pathway folding is characterized by intramolecular hydrophobic interactions which stabilize the hydrophobic core of the peptide, off-pathway folding occurs through intermolecular hydrophobic interactions, which lead to the formation of aggregates.<sup>[63]</sup> Despite their lack of native structure, off-pathway proteins can still form highly ordered structures, namely amyloid fibrils,<sup>[64]</sup> which will be discussed later.

#### 1.2.4 Influence of hairpin and turn structures in the folding process

Folding of a whole protein is often difficult to study, due to a variety of different secondary structure elements and interactions present and therefore model systems are used to deduce the influence of different structural groups on the folding behavior. One important model system is the  $\beta$ -hairpin structure, since folding frequently starts with the formation thereof.<sup>[65]</sup> The stability of a folded  $\beta$ -hairpin structure depends on several factors, such as the  $\beta$ -turn structure itself and its turn propensity, hydrophobic side chain interactions, also described as the hydrophobic cluster and hydrogen bonds between the antiparallel  $\beta$ -sheets.<sup>[65]</sup>

The first studies describing in detail an underlying mechanism of  $\beta$ -hairpin formation were conducted in 1997 by Muñoz *et al.*<sup>[66]</sup> They described two probable mechanisms, favoring the “zipper”-mechanism which initiates the folding from the  $\beta$ -turn, while the second mechanism starting from the hydrophobic cluster is not excluded. As illustrated in Figure 7, the “zipper”-mechanism starts by formation of the reverse turn and propagates outwards by formation of hydrophobic side chain interactions and hydrogen bonds. The “hydrophobic collapse”-

mechanism was later described by Karplus *et al.*<sup>[67]</sup> who investigated the same 16-residue peptide as Munoz using Monte Carlo simulations. Starting from a central hydrophobic cluster, hydrophobic interactions and hydrogen bonds propagate in both directions to form the hairpin without the necessity of a preformed turn.

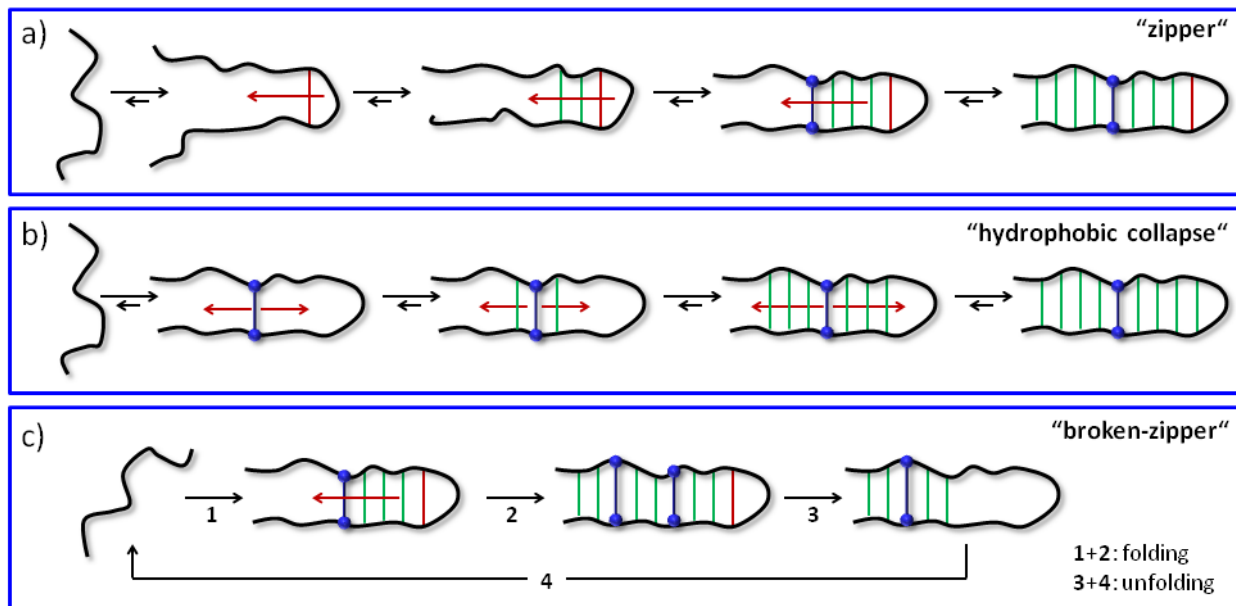


**Figure 7.** Proposed mechanisms for the formation of hairpin structures. (Adapted with permission from ref<sup>[68]</sup>, Copyright (2006), American Chemical Society and from ref<sup>[65]</sup>, Copyright (2010), with permission from Elsevier).

Further investigations revealed a disagreement between experimental and theoretical studies.<sup>[68]</sup> On the one hand, experimental studies favored the "zipper"-mechanism, where the turn-formation is the rate-limiting step.<sup>[69-72]</sup> For instance, thermal stability and kinetic experiments, using CD and time-resolved IR, suggested that hydrophobic side chain interactions do not stabilize the folding transition state, but only decrease the unfolding rate and thus stabilize the final hairpin.<sup>[69]</sup> On the other hand, theoretical studies supported the "hydrophobic collapse"-mechanism<sup>[73]</sup> and proposed a passive role of the reverse turn, acting as a simple connector of the strands, which might facilitate the hairpin formation but does not act as an active promoter.<sup>[74-75]</sup>

Based on the previous studies and on their own work, Scheraga *et al.*<sup>[65]</sup> proposed a mechanism similar to the "zipper"-mechanism with slight differences. Hairpin formation according to this "broken-zipper"-mechanism (see Figure 7) is initiated by the turn, which facilitates the formation of hydrophobic side chain interactions by reducing the distance between the two  $\beta$ -sheets close to the turn structure. Similar to the "zipper"-mechanism, the formation of these first hydrophobic contacts facilitates the growth of the hydrophobic cluster outwards. In contrast to the "zipper"-mechanism, hydrogen bonds are excluded as a main force for the hairpin formation. Furthermore, the unfolding process is not the reverse of the folding process, as stated for the other mechanisms, but proceeds in an inverse manner, meaning that



hydrophobic interactions between residues which were formed first during folding (and thus are close to the turn region) also break first, while those formed as last are also the most stable ones. Marcelino *et al.*<sup>[10]</sup> proposed two distinct pathways that can be described as followed. In the first, the turn acts as an active promoter of the folding due to the conformational restrictions, which then leads to the formation of adjacent secondary structures such as  $\beta$ -sheets or higher structures such as a  $\beta$ -hairpin. In the second pathway, turns are only passively enabling the folding and long-range interactions *e.g.* between adjacent  $\beta$ -sheets are the driving force for the folding. The turn is thus only required to enable the folded conformation. Several factors, such as the intrinsic tendency for turn formation, sequence conservation and the presence of other functional regions will decide if the turn is an active promoter or a passive “enabler”. Thus, in this work one major aspect is to investigate the influence of the  $\beta$ -turn structure on the folding behavior of polymers and peptides.

### 1.3 Misfolded proteins

As briefly mentioned in chapter 1.2.3, proteins can also exhibit misfolding behavior. Up to know, about 25 diseases originating from misfolded proteins have been revealed, the most prominent ones being neurodegenerative diseases such as Alzheimer’s, Parkinson’s and Huntington’s disease.<sup>[76-78]</sup> The common feature of these diseases is the formation of insoluble amyloid fibrils or plaques from soluble proteins. Although there is no evident similarity in the primary protein sequence of different amyloid fibrils, they all share the same cross- $\beta$  structure, which was revealed by the same X-ray diffraction patterns with a main reflection at 4.7–4.8 Å.<sup>[79-80]</sup> This distance arises from the length of hydrogen bonds in between parallel stacked  $\beta$ -sheets, which align perpendicular to the fibril axis. The structure and fibrillation propensities of amyloid peptides related to Alzheimer’s disease (AD) will be discussed below in more detail.

#### 1.3.1 Structure of A $\beta$ and fibrillation in vitro

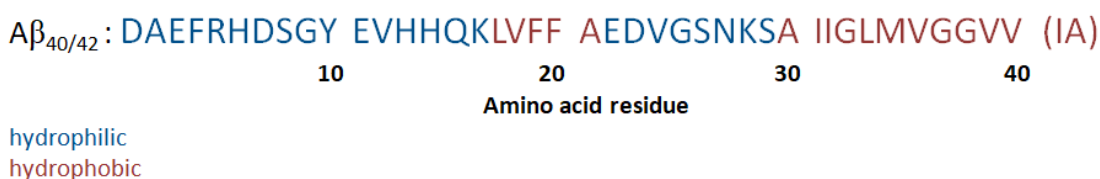


**Figure 8.** Primary sequence of A $\beta_{40/42}$  and marked hydrophilic and hydrophobic regions.

Amyloid beta (A $\beta$ ) peptides are formed by enzymatic cleavage from the amyloid precursor protein (APP) and are composed of 39 to 42 amino acids. Alois Alzheimer was the first to discover these senile plaques in the brains of AD patients, which were later structurally characterized. The primary structure of A $\beta$  peptides can be divided into four different regions

of different hydrophilicity (see Figure 8). Two regions, namely the N-terminal tail up to residue K16, and the central region around E22–G29 are hydrophilic, while two hydrophobic regions are present in the central part L17–A21) and at the C-terminus (A30–V40/A42).<sup>[81]</sup>

A $\beta$  is natively unfolded and belongs to the class of intrinsically disordered proteins (IDPs), lacking an overall structure in solution. Aggregation of soluble monomeric A $\beta$  *in vitro* leads to the formation of amyloid fibrils as schematically shown in Figure 9 and the underlying mechanism is described as a nucleation-dependent self-assembly<sup>[82-83]</sup>, which can be divided into three different regions.

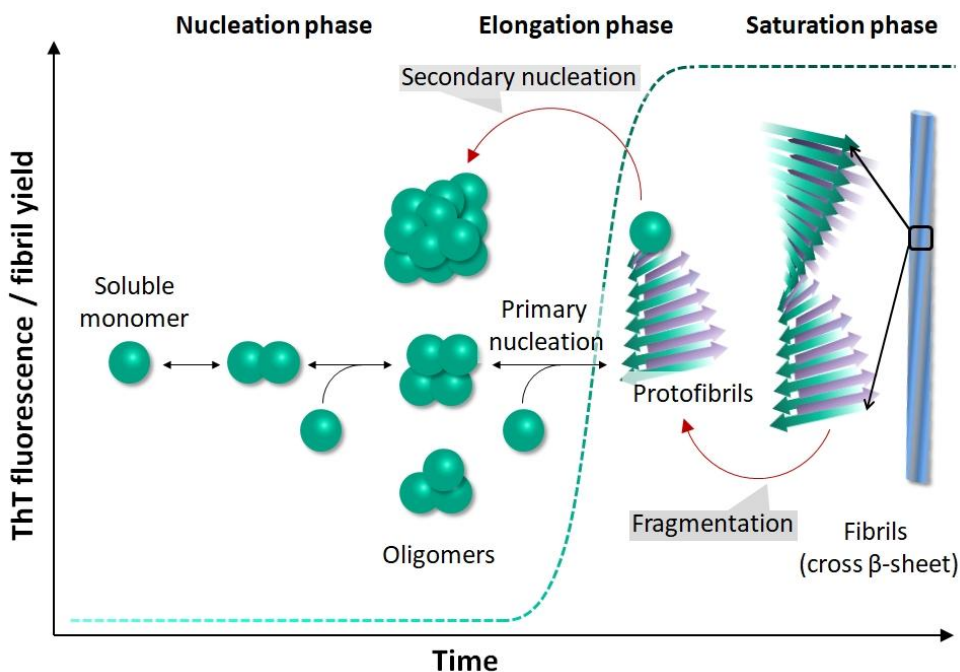


**Figure 9.** Thioflavin T (ThT) fluorescence curve of A $\beta$  fibrillation and therein occurring processes (Adapted from ref<sup>[78]</sup> with permission from Springer Nature, Copyright (2018)).

The first plateau region known as “lag phase” or “nucleation phase” is characterized by a low amount of mature fibrils and a low fluorescence response, while the second plateau region, the “saturation phase” is described by a high amount of fibrils and thus high fluorescence intensity. The “growth phase” or “elongation phase” preceding the saturation phase, is characterized by an exponential increase which results in the overall sigmoidal curvature as shown in Figure 9.<sup>[78, 84]</sup>

The kinetics of fibril formation can be measured using the fluorescent dye thioflavin T (ThT). This dye does not bind monomeric and oligomeric species but only fibrillar aggregates and hence the fluorescence increases with increasing fibril yield. The term monomer herein describes a single peptide chain, while oligomers are small aggregates of varying size, which are heterogeneous in structure, stability and stoichiometry.<sup>[85]</sup> Importantly, all three different phases cannot be assigned to a single event, but are composed of several microscopic processes,



which are ongoing and can be present at all time.<sup>[84]</sup> Four main processes have been described in detail (see Figure 9).<sup>[86-87]</sup> Primary nucleation, which describes the formation of fibrils/primary nuclei from soluble monomers, is simply depending on the monomer concentration and hence labeled as primary pathway. Elongation and secondary nucleation depend on both monomer and fibril concentration. Elongation describes the formation of bigger aggregates by monomer addition to a preexisting aggregate, while secondary nucleation is defined as the formation of new fibrils from monomers, catalyzed at the surface of existing fibrils. Fragmentation of mature fibrils into smaller protofibrils occurs in agitated samples and depends only on the fibril concentration. All three secondary pathways, which depend on the fibril concentration, lead to an acceleration of fibril formation and hence induce exponential fibril growth.<sup>[86]</sup>

During the lag phase, monomers start to assemble into oligomers of varying size, which are difficult to isolate due to their instability, and thus determination of their structure is very challenging. Interestingly, oligomers are only present in a very low amount (< 2 %) over the whole time range.<sup>[88]</sup> Formation of primary nuclei from oligomers is starting, when a critical nucleus size is attained, which is characterized as the state with the highest free energy and hence the most unstable one.<sup>[78]</sup> Investigations of A $\beta$ <sub>42</sub> revealed, that the first primary nucleus is formed at the very beginning of the lag phase (< 10 $\mu$ s) and that several hundreds of millions of primary nuclei are formed during lag phase.<sup>[84]</sup> Due to a much higher reaction rate for elongation than for primary nucleation, fibril formation occurs only shortly after appearance of the first primary nuclei. Subsequently, these fibrils display the catalytic surface for secondary nucleation, reaching the highest activity when monomer and fibrils are present equally, as they both contribute to the reaction rate, occurring at the half time  $t_{1/2}$  of the aggregation in the center of the “growth phase”.<sup>[84]</sup>

### 1.3.2 Structure of amyloid fibrils from ssNMR

Apart from using fluorescent dyes to obtain the kinetics of fibrillation, atomic force microscopy (AFM) and solid state NMR (ssNMR) are among the techniques which are used most to unravel the structure of amyloid fibrils. In this work, fibrillation of A $\beta$ <sub>40</sub> and the influence of additives on the fibrillation were investigated. Therefore, the structural features of A $\beta$ <sub>40</sub> will be discussed here in more detail. Based on ssNMR investigations, Petkova *et al.* proposed the first high resolution structures of A $\beta$ <sub>40</sub> fibrils.<sup>[89-90]</sup> Homogeneous fibrils were obtained in two different ways, once under gentle agitation and once under quiescent conditions, yielding two different types with a similar subunit structure. Both fibril structures contain hydrophobic  $\beta$ -strand regions in the central part (Y10–E22) and at the C-terminus (A30–V39), linked *via* a hydrophilic bend (D23–G29) and possess an unstructured N-terminus. These structural features lead to the formation of a U-shaped conformation, which consists of in-register parallel  $\beta$ -sheets, stabilized by intermolecular hydrogen bonds. Several of these

$\beta$ -sheets align perpendicular to the fibril axis to form the characteristic cross- $\beta$  unit. The different fibril morphology based upon the preparation method is related to the overall symmetry of the protofilaments, which are the basic structural units of fibrils. Protofilaments of fibrils formed under gentle agitation contain two cross- $\beta$  units, which show a two-fold rotational symmetry and form striated ribbons (see Figure 10a).<sup>[89-90]</sup>

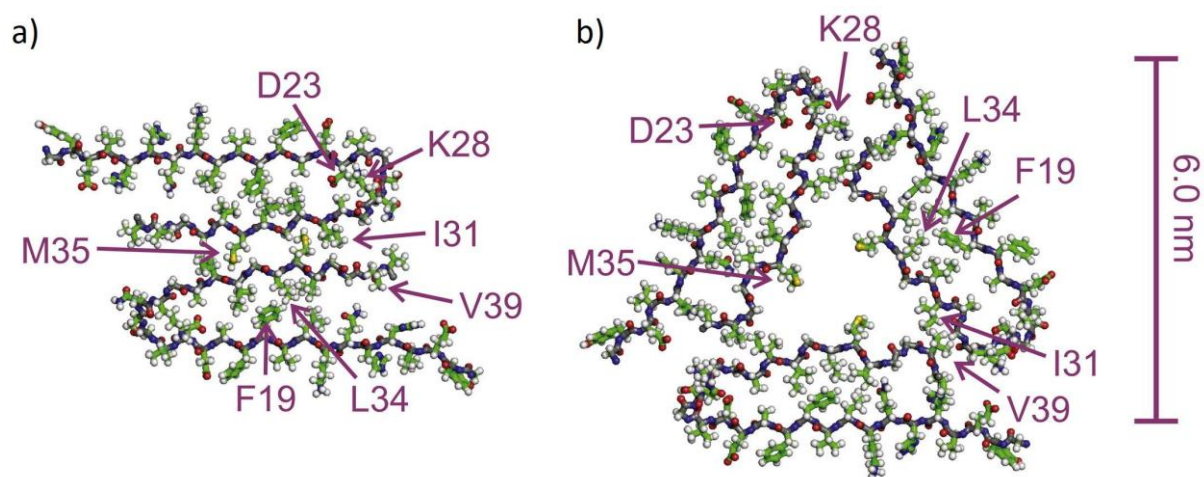


**Figure 10.** Structure of A $\beta$ <sub>40</sub> *in vitro* fibrils determined by ssNMR. a) Two-fold symmetric fibrils<sup>[89-91]</sup> and b) three-fold symmetric fibrils<sup>[92]</sup> (Reprinted from ref<sup>[93]</sup>, Copyright (2013), with permission from Elsevier).

Magnetic dipole-dipole couplings suggested the formation of an intermolecular salt bridge connecting the residues D23 and K28, which is absent in fibrils generated under quiescent conditions.<sup>[92, 94]</sup> Instead, residues D23 and K28 are pointing outwards in the second type of fibrils and are thus unable to interact. Furthermore, a twisted morphology and a three-fold rotational symmetry are observed for these fibrils (see Figure 10b).

These investigations clearly show that A $\beta$ <sub>40</sub>, similar to various other amyloids, exhibits polymorphism. Thus, a variety of external factors such as pH, agitation and presence of metal ions but also intrinsic factors such as point mutations can influence the structure of A $\beta$  fibrils. Upon investigation of A $\beta$ <sub>40</sub> fibrils obtained from brain tissue of two Alzheimer's patients, polymorphism was also discovered *in vivo*.<sup>[93]</sup> The study revealed a single predominant fibril structure in both brain tissues, which were clearly distinct from one another according to ssNMR and transmission electron microscopy (TEM) measurements. Detailed structural analysis was performed for one fibril structure, revealing a three-fold symmetric structure (see Figure 11). In contrast to previous *in vitro* studies (see Figure 10b), which showed an unstructured N-terminus, the entire A $\beta$  sequence of these *in vivo* fibrils appears structurally ordered. Furthermore, the salt bridge between D23 and K28 was present, as opposed to the *in vitro* model.

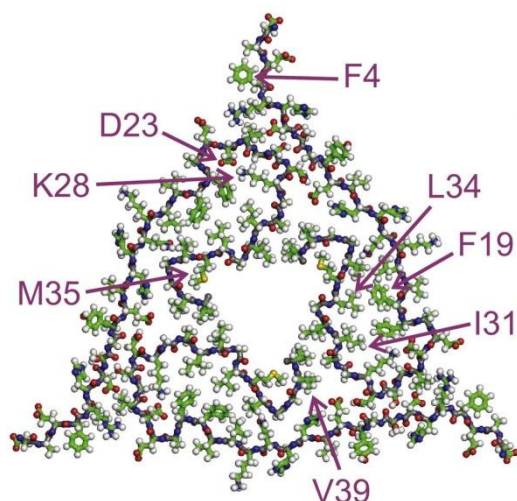


**Figure 11.** Structure of A $\beta$ <sub>40</sub> *in vivo* fibrils determined by ssNMR (Figure reprinted and adapted from reference<sup>[93]</sup>).

Further investigations demonstrated that the second polymorph was the prevalent structure found in most brain tissues of deceased AD patients.<sup>[95-96]</sup> In contrast to the polymorph depicted in Figure 11, only about 50 % of this second structure is ordered, making it more difficult to propose a structural model, which has thus up to now not been achieved.

As previously discussed, hairpin formation can influence the folding of proteins. Thus, also the role of the loop/bend in A $\beta$  fibrillation is under investigation and emphasis is laid on elucidating monomeric and oligomeric structures. Teplow and co-workers<sup>[97]</sup> studied a protease-resistant segment of A $\beta$ <sub>40/42</sub>, which comprises the residues A21–A30 and contains a  $\beta$ -turn within V24–K28. They proposed that intramolecular nucleation of A $\beta$  monomers and formation of a folding nucleus is the first step during the A $\beta$  folding process. Structure determination of A $\beta$  monomers is difficult due to its transient nature and thus Hoyer *et al.*<sup>[98]</sup> investigated A $\beta$  which was bound to an engineered protein, inhibiting the aggregation. NMR studies were used to obtain the solution structure of A $\beta$  monomer, which revealed similarities to the fibrillar structure, possessing antiparallel  $\beta$ -strands with a loop region at residues 24–29, stabilized by intramolecular interactions instead of intermolecular ones found in A $\beta$  fibrils. Teplow and co-workers revealed that residues G25 and S26, which are part of the four residue turn of G25–K28, are important for the organization of A $\beta$ <sub>42</sub> monomers and could thus be a target for therapeutic strategies.<sup>[99]</sup> Investigations of membrane-bound oligomers of A $\beta$ <sub>40</sub> revealed a  $\beta$ -turn between residues D23 and K28,<sup>[100]</sup> which is different to the  $\beta$ -hairpin found in mature A $\beta$ <sub>40</sub> fibrils. Although these engineered A $\beta$  structures provide insights into the structure of transient monomers and oligomers, deviations from the actual structure of A $\beta$  without stabilization cannot be excluded. Regarding the final fibril structure, ssNMR investigations performed by Bertini and co-workers indicated local disorder and turn formation around G25 and S26, which possess a significantly reduced tendency to form a  $\beta$ -sheet structure.<sup>[91]</sup>

### 1.3.3 Modifications of A $\beta$

Natural point mutations occurring mainly at positions 21 to 23 and originating from mutations in the APP gene, are related to familial AD characterized in most cases by an early onset of the disease (< 65 y). However, less than 5 % of all AD cases are related to familial AD.<sup>[101-102]</sup> The main point mutations and some of the most intriguing differences to wild type A $\beta_{40/42}$  are summarized in Table 1.

“Dutch” (E22Q) and “Italian” (E22K) mutations of A $\beta_{42}$  showed faster aggregation *in vitro* than A $\beta_{42}$ , while the “Flemish” (A21G) mutation did not fibrillate at all under the same conditions.<sup>[103]</sup> This decreased fibril formation results in an increased formation of toxic intermediates, which is supposed to be the reason for the strong reduction of the age of onset occurring for this point mutation.<sup>[104]</sup> Investigations of A $\beta_{40}$ <sup>[105]</sup> and A $\beta_{42}$  mutations<sup>[106]</sup> revealed the fastest aggregation for the “Arctic” (E22G) mutation, followed by “Iowa” (D23N) and “Dutch”. “Iowa” mutant D23N is an unusual exception regarding its structure. While all other mutations and the wild type A $\beta$  form parallel  $\beta$ -strands, D23N is able to form antiparallel ones, stabilized by a salt-bridge between residues K16-E22.<sup>[107]</sup>

Furthermore also the turn region, comprising residues D23 to K28, has been subjected to modifications. By introducing a lactam bridge between D23 and K28 a pre-organization of the turn region was achieved. This modification resulted in a 1000-fold enhanced fibrillation compared to A $\beta_{40}$ . Furthermore, acceleration of A $\beta_{40}$  aggregation occurred upon seeding with lactam-fibrils. Hence, this pre-organization in a bend structure facilitates  $\beta$ -sheet formation and thus fibril formation.

**Table 1.** Overview about important point mutations of A $\beta_{40/42}$ .

Name	Substitution	Comparison with WT	Lit.
“Flemish”	A21G	Lower aggregation rate; increased formation of toxic intermediates $\rightarrow$ early-onset AD (age 40-50) <sup>[104]</sup>	[108-110]
“Osaka”	E22 $\Delta$	Highly ordered structure; striking differences compared to WT; more stable fibrils; higher toxicity	[111-113]
“Italian”	E22K	Increased A $\beta_{40}$ production; related to hemorrhagic stroke	[114-115]
“Arctic”	E22G	Accelerated protofibril and fibril formation; increased ratio of fibrillar vs nonfibrillar structures; reduced stability at residues 15-25	[116-119]
“Dutch”	E22Q	Higher oligomerization and aggregation rate; $\beta$ -structure in solution	[114-115, 120]
“Iowa”	D23N	Both antiparallel and parallel fibrils	[107, 121-124]

In 2012, Hu and co-workers<sup>[125]</sup> modified turn positions D23–S26 or G25–K28 of A $\beta$ <sub>40</sub> by introducing  $\beta$ -turn forming amino acid sequences and investigated their aggregation behavior. The mutation A $\beta$ <sub>25PPGK28</sub> showed no fibrillation, while A $\beta$ <sub>25YNGK28</sub> resulted in an enhanced formation of oligomeric structures, however no further conversion into mature fibrils was observed. Nevertheless, upon addition of these mutant peptides to A $\beta$ <sub>40</sub>, no inhibitory effects occurred and the oligomeric mutant strongly enhanced the fibrillation. Different findings resulted from replacing two amino acids in the region of V24–N27 by <sup>D</sup>Pro-Gly as a turn-nucleating motif, which led to an enhanced fibrillation.<sup>[126]</sup> Both examples reveal that the turn region has a strong impact on aggregation, while the influence of a mutation on aggregation can still not be predicted and thus further investigations need to be carried out.

Besides exchanging different amino acids against each other, some rare reports have been interested in the incorporation of synthetic molecules. Nilsson and co-workers explored a photoswitchable azobenzene turn-mimetic, replacing positions G25–N27 or S26–N27 of A $\beta$ <sub>42</sub> (see Figure 12a).<sup>[127]</sup> In contrast to expectations, the *trans*-isomer exhibited aggregation into fibrillar structures with cytotoxicity similar to A $\beta$ <sub>42</sub>, while the *cis*-isomer assembled into amorphous aggregates with a very low toxicity. The formed fibrils of the *trans*-isomer resembled fibrils of A $\beta$ <sub>42</sub> and thus they concluded that the  $\beta$ -turn is not necessarily involved during fibril formation. Even though the *cis*-isomer lacked fibrillation, mixed systems and the inhibition effect of this turn-mimetic peptide on aggregation of pure A $\beta$  peptide was not investigated. Kiso and co-workers<sup>[128]</sup> reported about A $\beta$  sequences containing a dibenzofuranyl-based turn mimetic in between four amino acids (see Figure 12b). The turn mimic replaced three amino acids in the range of S26–I32 of the peptide sequence and aggregation assays of mixtures with A $\beta$ <sub>42</sub> were monitored by ThT fluorescence.

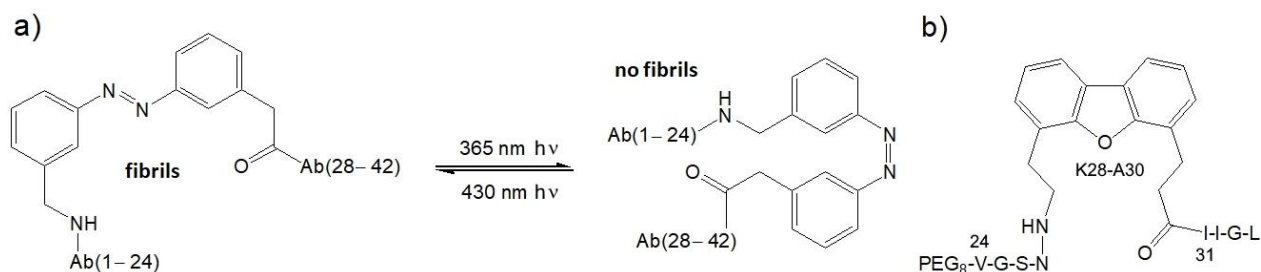


**Figure 12.** A $\beta$  mimetics containing synthetic turns. a) Full length A $\beta$ <sub>42</sub> containing a switchable azobenzene turn mimetic<sup>[127]</sup>; b) Dibenzofurane-based turn mimic in a truncated A $\beta$  sequence.<sup>[128]</sup>

Only one peptide, in which positions K28–A30 were replaced, showed some inhibition effects on the fibrillation of A $\beta$ <sub>42</sub>. While the fluorescence intensity was reduced by a factor of two, the half time of fibrillation did not significantly decrease, even though a ten-fold excess of the peptide in regard to A $\beta$ <sub>42</sub> was used. As visible from the examples given, reports on turn modification and the resulting effect on A $\beta$  fibrillation are scarce and this work is aimed to contribute to this topic.

## 1.4 Polymer folding

As previously discussed, proteins possess a defined primary structure, forming perfectly ordered secondary, tertiary and quaternary structures to fulfill certain functions. Polymer chemistry has always been inspired by nature and thus also the precise synthesis of functional macromolecular structures has gained huge interest. In the following, three different strategies to obtain polymers with defined secondary and tertiary folded structure will be discussed.

### 1.4.1 Helical polymers

The most prevalent secondary structure in proteins is the  $\alpha$ -helix and similarly helical structures are also found in a variety of different polymers (see Figure 13).<sup>[129-130]</sup> In contrast to  $\alpha$ -helical structures of proteins, most of these polymers lack intramolecular stabilization by e.g. hydrogen bonds, unless specifically introduced in the side chains and are thus only stabilized by electronic and steric factors depending on the different polymer backbones and side chains.

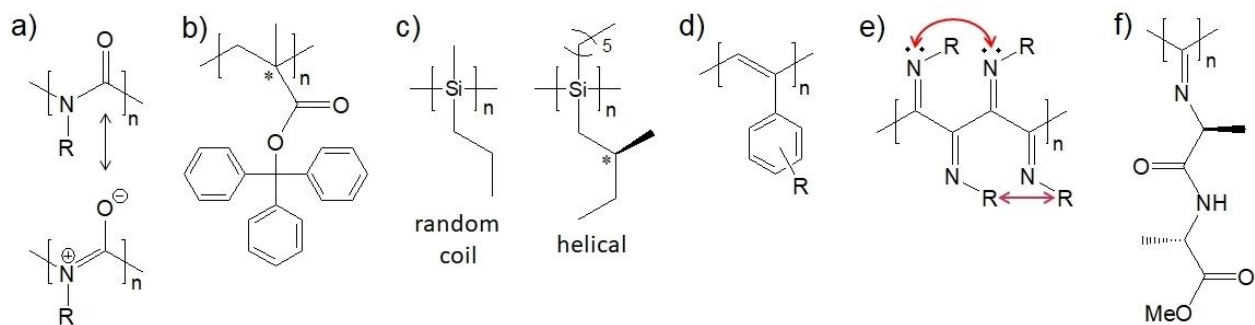


**Figure 13.** Overview about different helical polymers; a) polyisocyanate, b) poly(triphenylmethyl methacrylate), c) polysilane, d) polyacetylene, e) polyisocyanide, f) poly(isocyanopeptide).

*Polyisocyanates*<sup>[131-132]</sup>, which were investigated in this work, consist of a substituted amide backbone, with a partial double bond character similar to proteins and thus a tendency to adopt a planar conformation. However, no freely rotating carbon centers are located in between the amide bonds, leading to an increased stiffness of the polymer backbone. Steric hindrance between the side chains and the carbonyl groups prevents a coplanar conformation and twisting of the backbone to release this strain results in the formation of a stiff helical structure. *Polymethacrylates* exhibit a helical structure only when a stereoregular isotactic structure is obtained during polymerization. In order to retain the helical structure after polymerization, bulky substituents such as a triphenylmethyl group are necessary.<sup>[133]</sup> The bulkiness of the side chains then results in a kinetic stabilization of the helix, which is vanishing upon removal of the sterically demanding group. *Polysilanes*, possessing a  $\sigma$ -conjugated backbone, exhibit a  $7_3$ -helical structure, which means that seven repeating units form three helical turns.<sup>[134]</sup> The helix stability depends on the two side chains as illustrated in Figure 13. Small substituents result in a random coil structure, while increasing the length and branching of the side chains results in increase of the persistence length. *Polyacetylenes* consist of conjugated double bonds



and can be synthesized using different metal catalysts such as titanium-, rhodium- or iron-catalysts. Induction of a one-handed helical structure in polyacetylenes is achieved by introducing chiral side chains or by stereoselective polymerization resulting in *cis-transoidal* polymers.<sup>[129]</sup> As aliphatic polyacetylenes exhibit a more flexible structure with a small persistence length ( $\approx 10$  nm) most research focuses on poly(phenyl acetylene)s (PPAs), bearing one or various substituents at the phenyl group which is directly attached to the polymer backbone.<sup>[135]</sup> *Polyisocyanides* exhibit a  $4_1$ -helical structure, as two factors prevent the formation of a planar conformation.<sup>[136]</sup> Electronic repulsions between the free electron pairs of neighboring nitrogen atoms are a major factor in polyisocyanides with a very small substituent (i.e.  $(\text{H}-\text{N}=\text{C}\langle)_n$ ), while steric repulsion between side chains is a limiting factor for bulky side chains (i.e.  $((\text{CH}_3)_3\text{C}-\text{N}=\text{C}\langle)_n$ ).<sup>[136]</sup> Regarding intermediate sized side chains, both aspects contribute to the formation of a helical structure. *Polyisocyanopeptides* are a special subclass, in which side chain functionalities introduced by using *e.g.* amino acids, results in further stabilization of the helical structure by hydrogen bond interactions. These examples clearly show that helical polymers are not folded in terms of intramolecular interactions as in peptides / proteins but in contrast due to intrinsic factors depending on the chemical structure.

### 1.4.2 Foldamers

Foldamers represent another class of synthetic helical molecules, which show some differences in comparison to the helical polymers described previously. While the latter are only stabilized by constraints in the backbone of the polymer chain and steric demands of the side chains, the former are mainly of oligomeric structure and are stabilized by non-covalent interactions similarly to natural secondary structures.<sup>[137-138]</sup> Foldamers can be divided according to their structural origin into peptidomimetic<sup>[139]</sup> (see Figure 14) and abiotic foldamers.

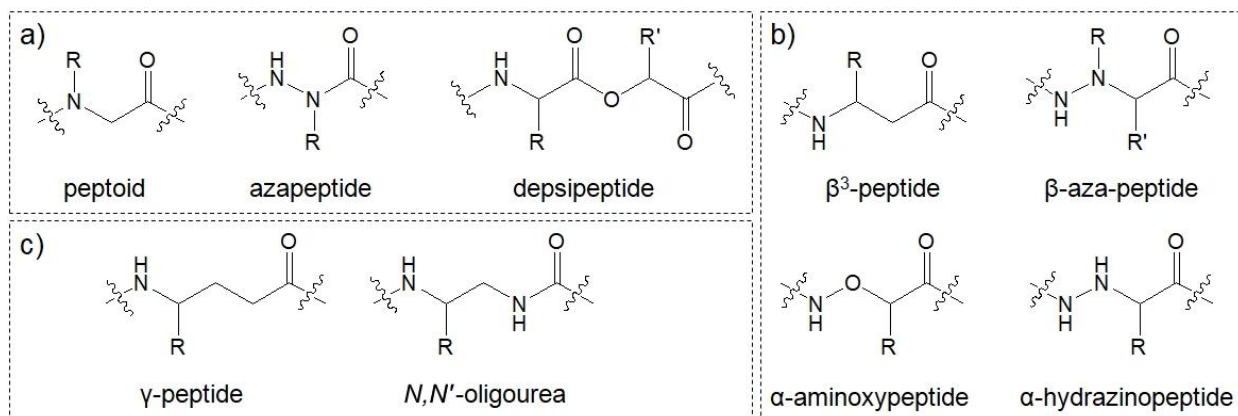


**Figure 14.** Overview about peptidomimetic foldamers. a)  $\alpha$ -peptides, b)  $\beta$ -peptides, c)  $\gamma$ -peptides.<sup>[139]</sup>

The former comprise *e.g.*  $\alpha$ -peptide foldamers, named peptoids, containing a side chain residue attached to the nitrogen instead of the  $\text{C}_\alpha$  atom, thus lacking the ability to form hydrogen bonds. Nevertheless, these molecules are able to form stable helical structures. Increasing the

distance between the amide bonds by one carbon atom generates  $\beta$ -peptides, forming a helical structure with higher stability compared to  $\alpha$ -peptides.<sup>[140]</sup> Due to their additional advantage of higher resistance towards proteolysis, numerous investigations of  $\beta$ -peptides have been performed and also analogues, such as  $\alpha$ -aminoxypeptides and  $\alpha$ -hydrazinopeptides have been developed.<sup>[139]</sup> Further increasing the spacer length between the amine and the carboxylic acid leads to  $\gamma$ -peptides, with the  $N,N'$ -oligourea being one analogue.<sup>[141]</sup>

Abiotic foldamers frequently contain aromatic units, and some general examples are shown in Figure 15. While the main driving force for folding of these molecules are  $\pi$ - $\pi$ -interactions, especially for simple aromatic structures such as *o*-phenylenes and aza-heterocycles, further interactions can also contribute.

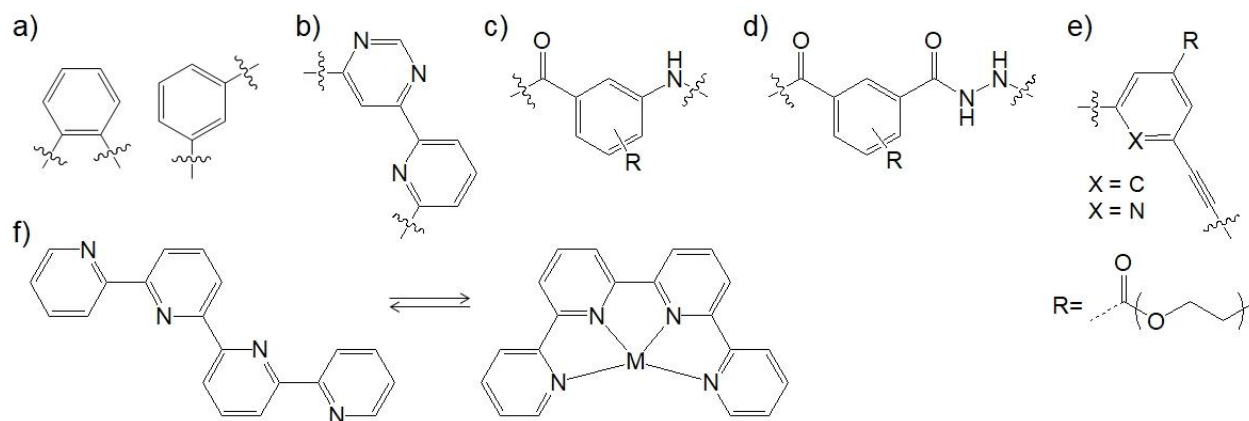


**Figure 15.** Overview about abiotic aromatic foldamers. a) *o*/*m*-phenylene, b) aza-heterocycle, c) oligoamide, d) oligohydrazide, e) *m*-phenylene ethynylene (X = C), *m*-ethynylpyridine (X = N), f) oligopyridine as an example of a helicate.<sup>[137]</sup>

Folding of oligoamides and oligohydrazides is additionally supported by hydrogen bonding interactions, while solvophobic interactions can initiate the folding of *e.g.* oligo(*m*-phenylene ethynylene)s. Upon introduction of polar side chains, the latter show a transition from random coil structure in a good solvent to helical structure in a bad solvent. While in a good solvent both the backbone and the side chains are solvated, changing the polarity of the solvent results in a collapse of the chain and formation of stabilizing aromatic interactions.<sup>[142]</sup> So called helicates fold upon coordination to metals, such as shown for an oligopyridine in Figure 15f.

While a vast number of foldamers mimicking helical structures were found as described above, the number of reports of  $\beta$ -sheet foldamers is only scarce. Owing to the presence of intermolecular interactions instead of intramolecular ones,  $\beta$ -sheets tend to aggregate, hindering their successful synthesis. Thus, most reported  $\beta$ -sheets are only monomeric or dimeric to achieve solubility. Besides examples employing hydrogen bonding as stabilizing interactions<sup>[143-144]</sup> recent investigations are based on  $\pi$ - $\pi$ -stacking of linear aromatic systems. Aromatic oligoamides could be tuned into three- and five-stranded artificial sheets by using two restricting elements. Aggregation in these oligoamides was inhibited by choosing



chloroform as a solvent, which weakens the  $\pi$ - $\pi$ -stacking and additionally a turn element for pre-organization was introduced, leading to the successful synthesis of  $\beta$ -sheet foldamers.<sup>[145]</sup> Another successful strategy towards artificial  $\beta$ -sheets was applied by implementing orthogonal groups and a flexible linker unit.

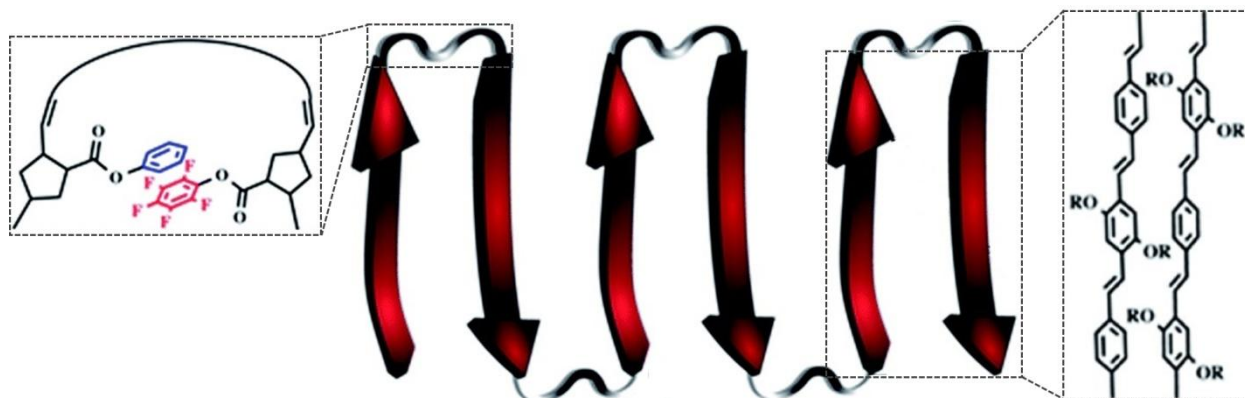


**Figure 16.** Artificial  $\beta$ -sheet featuring  $\pi$ - $\pi$ -stacking and perfluorophenyl-phenyl interactions (Figure reprinted and adapted from reference<sup>[146]</sup>)

As depicted in Figure 16, artificial hairpins were obtained featuring co-polymers of poly(*p*-phenylenevinylene) (PPV) and of flexible poly(norbornene) (PNB) by employing ring-opening metathesis polymerization (ROMP) polymerization. While the PPV blocks act as strands, stabilized by  $\pi$ - $\pi$ -stacking, the PNB coils are employed as linker units, featuring perfluorophenyl-phenyl interactions. By using this orthogonal strategy, five-stranded artificial hairpins were obtained.<sup>[146]</sup>

### 1.4.3 Single-chain nanoparticles (SCNPs)

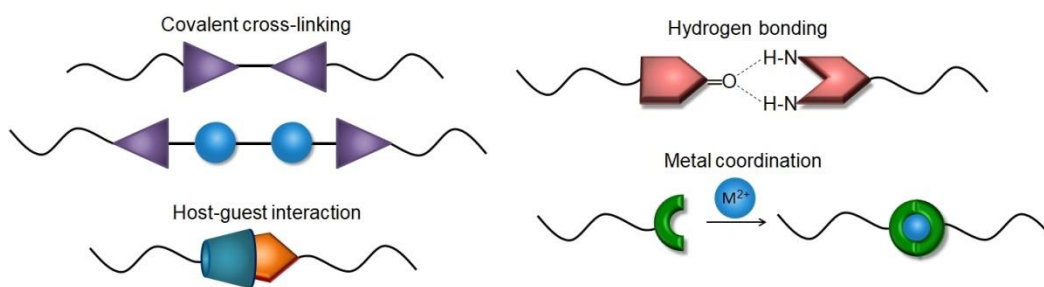


**Figure 17.** Covalent and non-covalent cross-linking strategies in SCNPs.

SCNPs are obtained by covalent cross-linking or intramolecular self-assembly of a single polymer chain (see Figure 17; Table 2). Covalent cross-linking strategies include cycloaddition reactions,<sup>[147]</sup> disulfide formation, thiol-ene/-yne reaction or dynamic covalent cross-linking,<sup>[148]</sup> while supramolecular self-assembly strategies include hydrogen bonding, metal-ligand complexation and host-guest interactions.<sup>[149-150]</sup> Examples for hydrogen bonding motifs are the urea group,<sup>[151]</sup> cyanuric acid and Hamilton wedge interactions<sup>[152]</sup> and the

dimerization of 2-ureidopyrimidinone.<sup>[153]</sup> Another versatile approach to obtain SCNPs using supramolecular interactions is based on host-guest chemistry.<sup>[154-156]</sup> A common host-guest system is based on the interactions of adamantane and  $\beta$ -cyclodextrine ( $\beta$ -CD).<sup>[157]</sup>

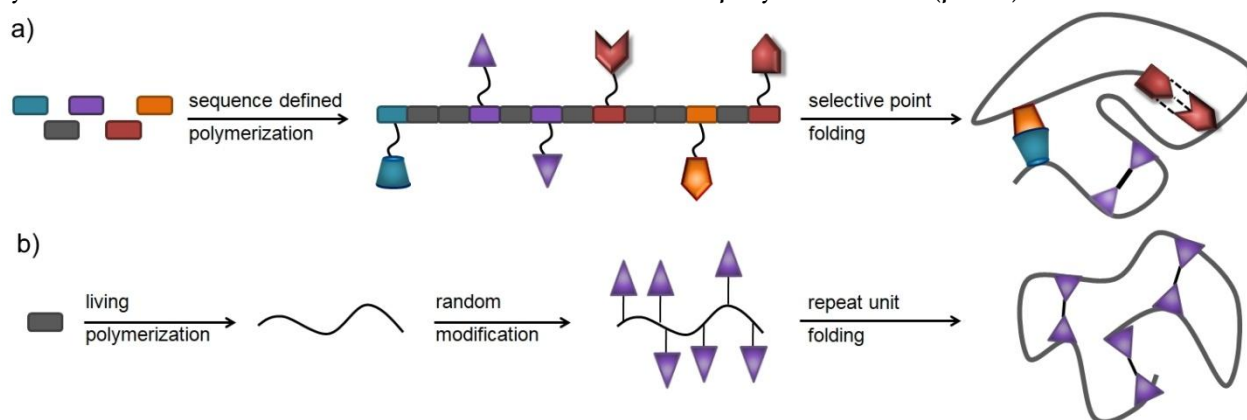


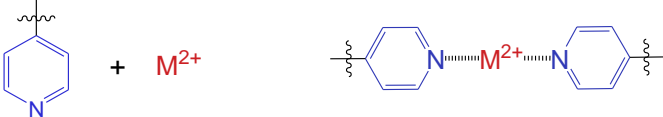
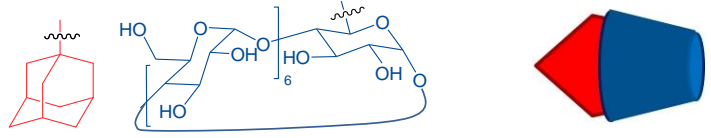
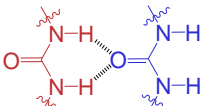
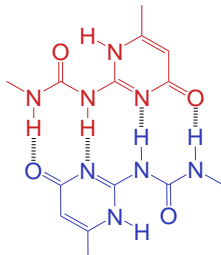
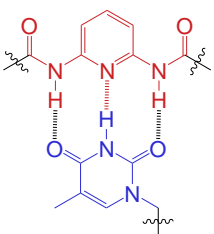
**Figure 18.** a) Selective point folding and b) repeat unit folding of SCNPs.

Two major synthetic strategies can be described to obtain SCNPs, selective point folding and repeat unit folding (see Figure 18).<sup>[150]</sup> In order to obtain defined three-dimensional structures *via* selective point folding, precise synthesis and implementing of different folding elements with orthogonal folding abilities into the polymer chains has to be achieved.<sup>[158]</sup> This strategy is synthetically much more demanding than the second approach, which uses well established polymerization techniques such as ATRP, NMP or RAFT, together with postpolymerization modifications. However, this second approach results in less ordered SCNPs, as the intramolecular cross-links are formed in a statistical process.

**Table 2.** Overview about cross-linking strategies for SCNPs.

Before cross-linking	Cross-linked structure	Reaction type	Ref.
<i>Covalent strategies</i>			
$R-SH + HS-R'$ $R-S-S-R' + R''-SH$	$R-S-S-R'$ $R-S-S-R'' + R'-S$	Disulfide-formation / -exchange	[159-160]
		Thiol-ene / -yne	[161-163]
		Urethane formation	[164]
		Azide-alkyne “click” reaction	[165-167]

**Continuation of Table 2.** Overview about cross-linking strategies for SCNPs.

Non-covalent strategies			
		Metal coordination	[168-169]
		Host-guest	[157]
Hydrogen bonding – Cross-linked structure			
a)	b)	c)	
			Hydrogen bonding
			a) Urea
			b) Dimerization of UPy (2-ureido-4[1H]-pyrimidinone)
			c) Thymine – diaminopyridine

As the techniques to precisely collapse single polymer chains into well-defined particles have improved over the years, further aims such as providing catalytic function or mimicking of biological functions were envisioned. Recently, one example comparable to metalloenzymes based on metal-coordination was reported.<sup>[172]</sup> Therefore, copolymers of modified norbornene monomers were synthesized *via* ROMP. After postpolymerization modifications, folding into SCNPs was achieved in water at high dilution by incorporation of  $\text{Cu}^{2+}$ , resulting in the formation of intermolecular cross-linking by metal-ligand interactions. Further investigations were conducted to evaluate the use of this Cu-SCNP as catalyst for the copper(I)-catalyzed azide/alkyne “click” reaction (CuAAC). Therefore, sodium ascorbate was added to generate  $\text{Cu}^{\text{I}}$  *in situ* and the reaction between different aromatic terminal alkynes and aliphatic azides was investigated in water at 50 °C. In most studied examples, using Cu concentrations below 20  $\mu\text{M}$  resulted in conversion of 90 % or more, which is a sufficiently low amount for a biocompatible “click” reaction.

Besides the targeting of chemical reactions in the development of SCNPs,<sup>[173]</sup> further use as drug carriers, for *in vivo* imaging or as enzyme and protein mimics are envisioned.<sup>[174]</sup> The main advantage of SCNPs for drug delivery is their small size, which is in the range of 1-30 nm and which has a major impact on biodistribution. Recently, two examples of protein-mimicking SCNPs, both containing iron as metal were reported.<sup>[175-176]</sup> A four-arm macroinitiator based on the structure of porphyrin was used for the copolymerization of MMA with an anthracene functionalized analogue, to generate a central core in which  $\text{Fe}^{\text{II}}$  was inserted and subsequently

oxidized by air. Single-chain folding was achieved *via* photodimerization of the anthracene units generating SCNPs as protein mimics of the heme complex.

Relying on only one type of cross-linking may be disadvantageous when structure and functionality should be incorporated. Therefore, it is of interest to implement orthogonal cross-linking moieties into the same polymer chain. Figure 19 shows one example in which supramolecular self-assembly was combined with photoinduced formation of covalent bonds to obtain defined SCNPs mimicking the folding of proteins.<sup>[147]</sup> Therefore, polymethacrylate backbones modified with benzene-1,3,5-tricarboxamide (BTA) and 4-methylcoumarin were synthesized *via* RAFT polymerization. BTAs self-assemble into threefold-symmetric helical stacks (see Figure 19c) *via* hydrogen bonding, while 4-methylcoumarin dimerizes upon irradiation forming a covalent bond (see Figure 19b).

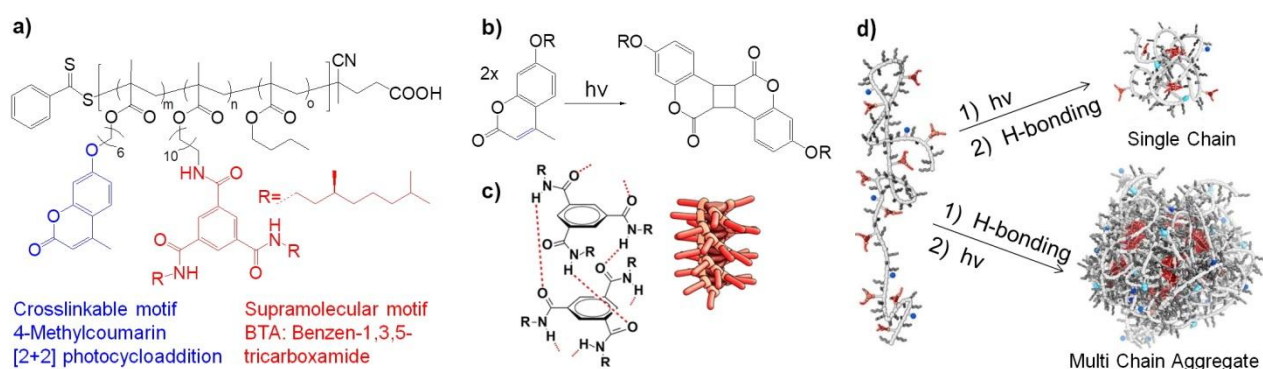


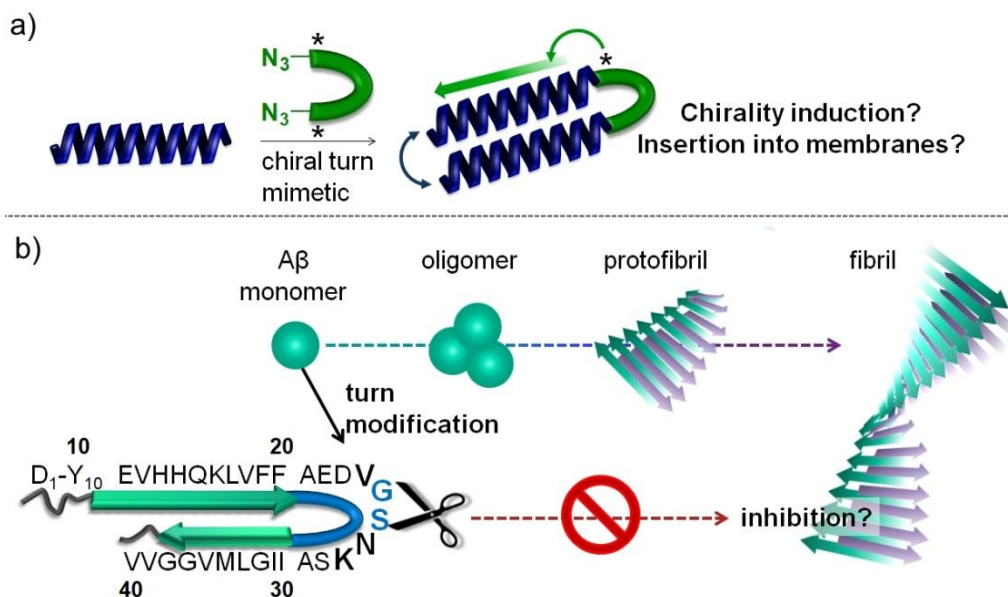
**Figure 19.** a) Chemical structure of the random copolymers. b) Photoinduced 4-methylcoumarin dimerization. c) Helical self-assembly of chiral BTAs *via* threefold hydrogen bonding. d) Schematic representation of the two pathways applied to fold and cross-link the polymers. (Figures adapted with permission from references<sup>[147, 177]</sup>. Copyright (2017, 2018) American Chemical Society).

Differences in folding behavior of these copolymers depending on irradiation and solvent were investigated, revealing two different aggregation pathways. In the first pathway (see Figure 19d) the polymers were dissolved in THF, which prevents the formation of hydrogen bonds. Hence, the solution contains individual polymer chains and upon irradiation with UV-A light, dimerization and formation of intramolecular cross-links occurs. Exposing these particles to 1,2-dichloroethane (DCE) afterwards results in the rebuilding of hydrogen bonds between the supramolecular BTA groups and formation of single chain particles occurs. In contrast to this, when using DCE as a solvent for the photodimerization, aggregates of several polymer chains are preformed due to the presence of hydrogen bonds. Thus, upon irradiation, cross-linking occurs not only intra- but also intermolecular and hence multi chain aggregates are formed.

## 2 Aim and concept

### 2.1 Scope of the thesis

Aim of this work was to investigate the influence of  $\beta$ -turn mimetics on the structure formation of polymers regarding their helicity and their behavior at the air / water interface as well as on peptides in view of their aggregation behavior in comparison to unmodified peptide.



**Scheme 1.** Structural influence of  $\beta$ -turn mimetics on polymers and peptides. a) Chirality induction effects and insertion into model membranes of helical polymer conjugates. b) Schematic representation of the aggregation of amyloid  $\beta$  peptide and the ability of inhibition by turn modification.

In the first part helical alkyne-functionalized polymers possessing the ability to exhibit chirality had to be synthesized and linked with azide-functional  $\beta$ -turn mimetics. Subsequently, chirality of the helical polymers should be investigated in regard to several factors such as the molecular weight as well as the influence of linkage with  $\beta$ -turn mimetics or hydrophilic polyethylene glycol and the use of different solvents. In order to gain further insight into the structure formation, the behavior of such amphiphilic conjugates should be investigated at the air / water interface.

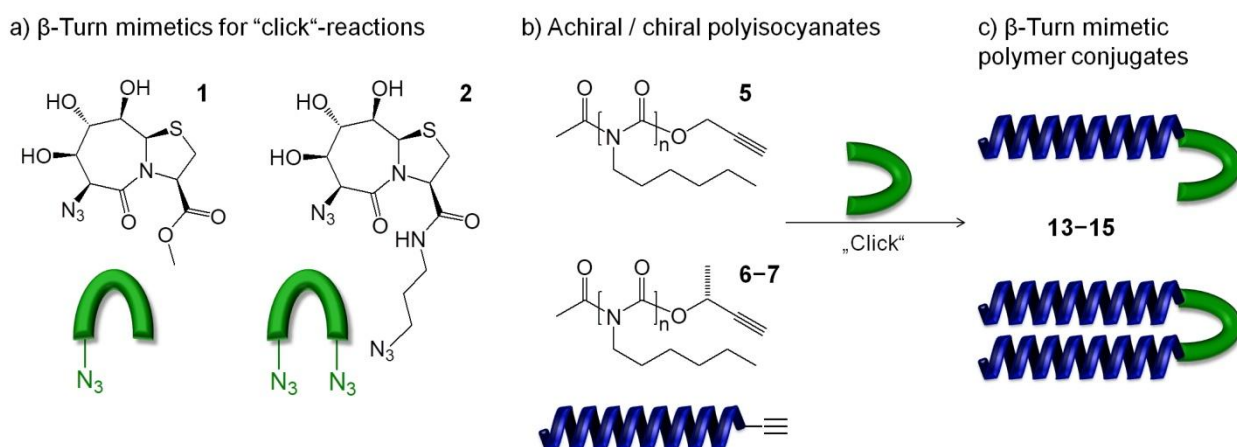
In the second part, amyloid  $\beta$  peptides modified with different  $\beta$ -turn mimetics should be prepared, to investigate the influence of turn variation on the aggregation behavior of amyloidogenic peptides.  $\beta$ -Turn mimetics of different size, rigidity and hydrophobicity had to be introduced into amyloid peptides by solid phase peptide synthesis to subsequently perform aggregation investigations of these peptide conjugates using different methods such as ThT assays, CD spectroscopy and TEM imaging.



## 2.2 Concept of the thesis

In order to obtain  $\beta$ -turn mimetic polymer and peptide conjugates for further investigations, several requirements had to be fulfilled. The turn mimetic should provide chirality when linked to the polymer chains, as well as similarity to natural occurring  $\beta$ -turns. Thus, bicyclic dipeptides (BTD) **1** and **2** bearing a rigid system of linked 5- and 7-membered rings were selected (see Scheme 2a). For the linkage of polymers and  $\beta$ -turn mimetics, the copper(I)-catalyzed azide/alkyne “click” reaction (CuAAC) was chosen, as it tolerates numerous functional groups, proceeds under mild conditions and results in only one regioisomer. Therefore, one or two azide functionalities were required at the  $\beta$ -turn mimetic structure.

The polymers should be suitable for the investigation of chirality transfer and should necessarily be synthesized by a living polymerization (PDI < 1.2), so that a defined molecular weight and complete end group modification can be achieved. Therefore, dynamic helical polyisocyanate was chosen, which can be synthesized *via* titanium-catalyzed coordination polymerization, resulting in well defined polymers with a low polydispersity and a functional end group for further modification. A straightforward synthesis towards alkyne functional poly(*n*-hexyl isocyanate) (PHIC) resulted in achiral and chiral PHICs (**5–7**) of different molecular weights (3700–12500 g/mol), possessing narrow molecular weight distributions and complete end group functionalization (see Scheme 2b).

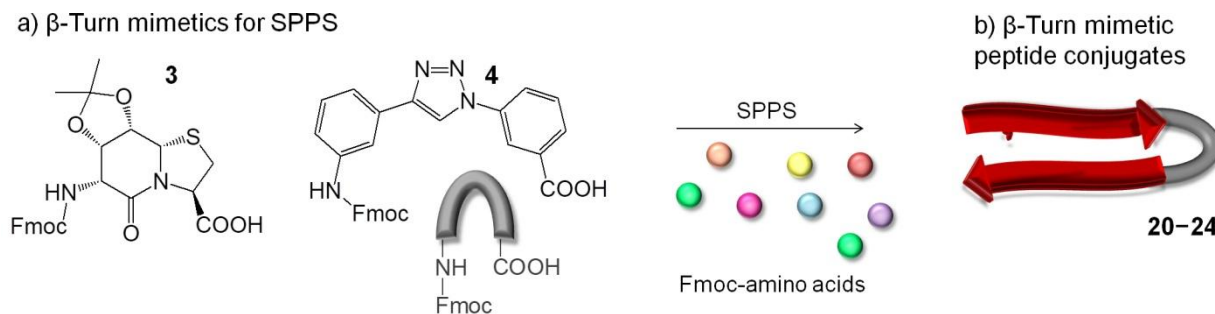


**Scheme 2.** Synthetic concept of polymer conjugates. a) One- and two-arm  $\beta$ -turn mimetics **1** and **2** for “click”-reactions bearing azide-functional groups. b) Helical polyisocyanates **5–7** synthesized by titanium-catalyzed polymerization with defined alkyne end group and the possibility to implement chirality by the end groups. c)  $\beta$ -turn mimetic polymer conjugates **13–15** obtained *via* “click” reaction of azide-functional  $\beta$ -turn mimetics and alkyne functional polyisocyanates.

Postpolymerization modification *via* CuAAC “click” reaction of helical alkyne-functional polymers and azide-functional  $\beta$ -turn mimetics then resulted in  $\beta$ -turn mimetic polymer conjugates **13–15**, while the reaction with polyethylene glycol resulted in the amphiphilic block-copolymers **16–17**. The polymers (**5–7**) as well as the conjugates (**13–15**) and copolymers (**16–17**) possess different helicity according to their chiral center at the chain end. Thus,

helicity of the pure polymers as well as chirality induction effects in the  $\beta$ -turn mimetic polymer conjugates should be investigated using circular dichroism (CD) spectroscopy. Furthermore, the behavior of these conjugates/copolymers at the air / water-interface should be studied as well as their interactions with lipid model membranes, and thus Langmuir-film measurements coupled with epifluorescence microscopy were performed.

In the second part,  $\beta$ -turn mimetics which are suitable for Fmoc solid phase peptide synthesis (SPPS), and thus necessitate a carboxylic acid and an Fmoc-protected amine group, should be synthesized to achieve the introduction into peptides. Therefore, rigid BTD **3** was chosen, possessing structural similarities to turn mimetics **1** and **2** and the hydrophobic  $\beta$ -turn mimetic **4**, consisting of an aromatic system with a triazole ring, was selected as a comparison (see Scheme 3a).  $\beta$ -Turn mimetic peptide conjugates **20-24** synthesized by SPPS should be investigated in regard to their aggregation behavior. Therefore, thioflavin T fluorescence assays (ThT assay) were performed, providing information about the speed of aggregation from monomeric peptide into fibrillar structures. Further insight into the structure formation should be obtained by CD measurements, which can indicate changes in the secondary structure, as well as by transmission electron microscopy (TEM) to gain insight into the fibrillar structures.



**Scheme 3.** Synthetic concept of peptide conjugates. a)  $\beta$ -turn mimetics **3** and **4** for Fmoc solid phase peptide synthesis (SPPS) bearing Fmoc-protected amine and carboxylic acid functionalities. b)  $\beta$ -turn mimetic peptide conjugates **20-24** obtained by SPPS.

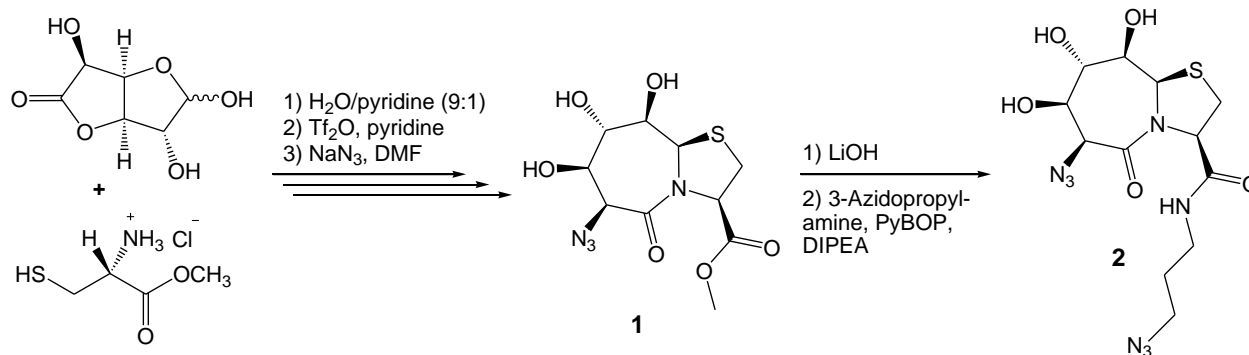
## 3 Results and discussion

### 3.1 Synthesis of $\beta$ -turn mimetics

Based on the knowledge about  $\beta$ -turns and their mimetic structures described in the introduction, different turn mimetics have been chosen in this work. For the postpolymerization modification of polyisocyanates, the azide/alkyne-“click” reaction has been chosen and therefore the turn mimetic requires an azide functionality as it is planned to introduce the alkyne moiety at the polymer chain end. The turn mimetics for SPPS necessitate a carboxylic acid and an amine group for further modification. Therefore, in addition to a bicyclic dipeptide, a more hydrophobic and aromatic triazole amino acid (TAA)<sup>[44]</sup> was synthesized *via* “click”-chemistry. This reaction leads to the formation of a triazole ring, which acts as a *trans*-amide mimetic but possesses a higher proteolytic stability than the amide bond and tolerates the conditions used in peptide synthesis.<sup>[178-180]</sup>

#### 3.1.1 Synthesis of $\beta$ -turn dipeptide for “click” coupling

An overview of the synthetic pathway towards bicyclic dipeptides (**1** and **2**) is shown in Scheme 4. Previous X-ray analysis of **1** revealed the rigidity of the structure with a distance of only 0.7 nm<sup>[181]</sup> between the two reactive sites, which is in good correlation with the distance of natural occurring  $\beta$ -turn structures.<sup>[15, 20]</sup>



**Scheme 4.** Synthetic pathway towards  $\beta$ -turn mimetic **1** and **2** for “click” coupling.

The synthesis of **1** was performed in several steps according to Geyer.<sup>[182-184]</sup> In the first step, a condensation of D-glucurono-3,6-lactone and L-cysteine methylester hydrochloride resulted in the formation of the bicyclic scaffold, which was further modified by selective transformation of one hydroxyl group into the triflate and afterwards into the azide group. The structure of **1** was confirmed by ESI-TOF-MS and <sup>1</sup>H-NMR spectroscopy (see Appendix, Figure A1) and it was subsequently used for the linkage of one polymer chain to obtain mono-functional polymers. Hydrolysis of the methyl ester and amidation using 3-azido propylamine, yielded bi-functional BTD **2**. The final structure was confirmed by ESI-TOF-MS (see Appendix, Figure A2) and <sup>1</sup>H-NMR spectroscopy (see Figure 20). In the negative mode, the main peak occurring in the ESI-spectrum can be attributed to the chlorine adduct of the product, while another peak at a mass-



to-charge ratio of 385.114 can be assigned to the deprotonated structure of the final product. The peak at 312.930 is resulting from a structure in which both azide functional groups were reduced to the amine, which presumably occurred during the measurement. The  $^1\text{H-NMR}$  spectrum further confirms the structure, as the signal at 1.60 ppm corresponds to the central ethylene protons of the 3-azidopropyl group, while the signals at 3.15 ppm and 3.27 ppm originate from the two adjacent ethylene groups. All other signals can also be assigned and the integrals are matching to the number of protons.

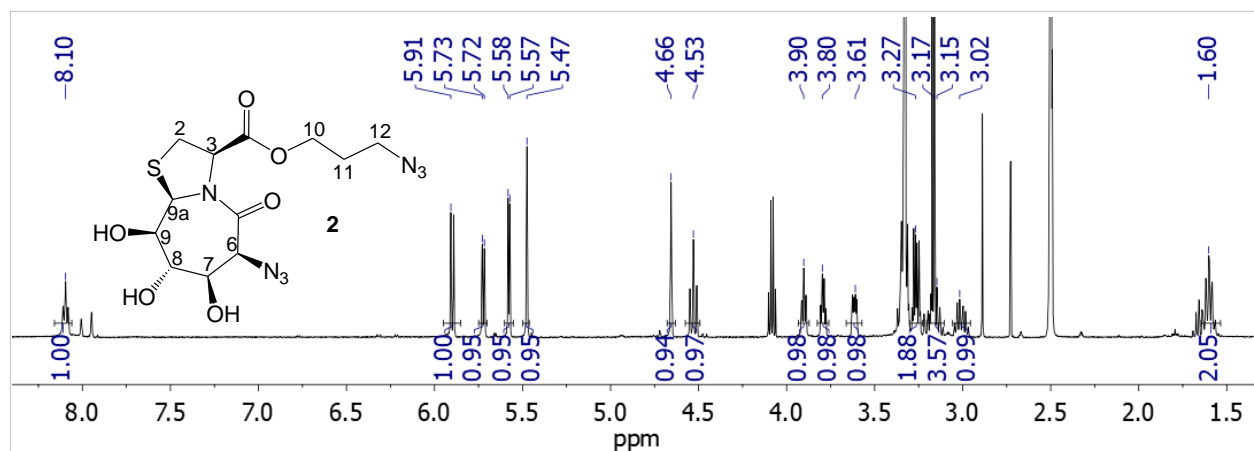
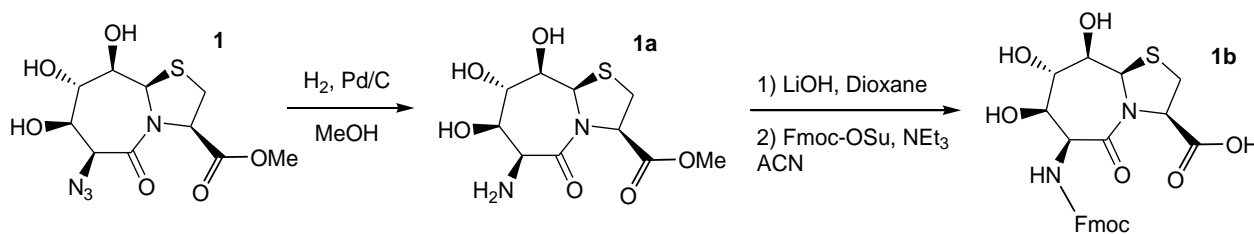


**Figure 20.**  $^1\text{H-NMR}$  spectrum of **BTD 2**.

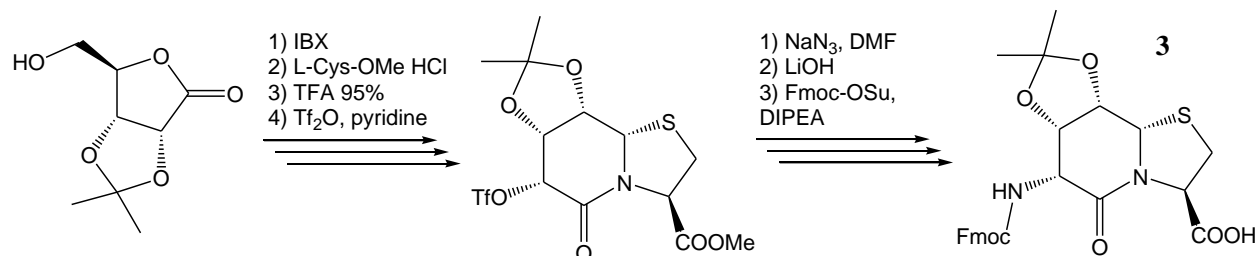
### 3.1.2 Synthesis of Fmoc-protected $\beta$ -turn mimetics for SPPS

Starting from **BTD 1** a  $\beta$ -turn mimetic suitable for Fmoc solid phase peptide synthesis (SPPS) should be synthesized. Therefore, hydrogenation of the azide, deprotection of the ester and protection of the amine by attachment of an Fmoc group was performed according to Scheme 5. Hydrogenation was achieved using palladium on activated charcoal, hydrolysis of the ester was performed as previously described for the synthesis of **2** and Fmoc protection was achieved using the corresponding *N*-hydroxysuccinimide ester and triethylamine as a base. Even though the synthesis was successful (see Appendix, Figure A3), further investigations revealed the unsuitableness of this turn mimetic in SPPS.



**Scheme 5.** Synthesis of Fmoc-protected  $\beta$ -turn mimetic **1b** for SPPS.

While the structure could be successfully introduced into a peptide chain, purification by HPLC was not possible afterwards due to very small elution differences between the functionalized and the non-functionalized peptide. Therefore, another turn reported by Geyer *et al.*<sup>[185]</sup> was chosen, exhibiting a similar structure but possessing protected hydroxyl groups as illustrated in Scheme 6.



**Scheme 6.** Synthetic route towards Fmoc-protected  $\beta$ -turn mimetic **3** suitable for SPPS.

Formation of the bicyclic scaffold is achieved in the first step and is followed by isomerization and modification of one hydroxyl group into triflate, then azide and finally amine group. Hydrolysis of the methyl ester and Fmoc-protection of the amine group resulted in the final product which can be used for SPPS. This product was investigated by NMR spectroscopy and ESI-TOF-MS. Figure 21 shows the <sup>1</sup>H-NMR spectrum of **3**, wherein the aromatic signals in the range of 7.80 ppm to 7.29 ppm confirm the presence of the Fmoc-protecting group, which is necessary for SPPS. Furthermore, the isopropylidene acetal protecting groups are still visible at 1.33 ppm.

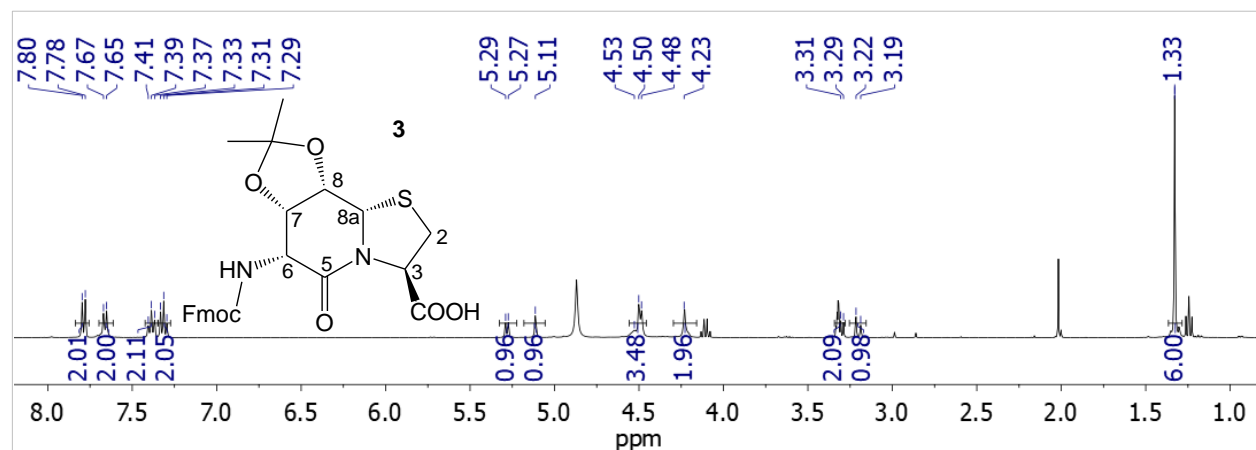
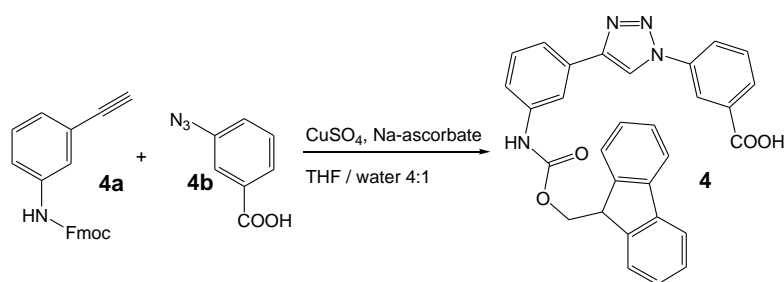


**Figure 21.** <sup>1</sup>H-NMR spectrum of Fmoc-protected BTD **3**.

The ESI-TOF-MS spectrum (see Appendix, Figure A4) additionally confirms the structure, as the calculated values for the lithium, sodium and potassium adducts deviate less than five ppm from the measured values.

### 3.1.3 Synthesis of hydrophobic Fmoc-protected $\beta$ -turn mimetic for SPPS

As comparison to the hydrophilic  $\beta$ -turn mimetic dipeptides, a hydrophobic turn has been chosen for the incorporation into A $\beta$  via SPPS. It has previously been reported, that this aromatic turn mimetic, shown in Scheme 7, exhibited chirality and a hairpin shape in the solid state and in solution.<sup>[44]</sup> The triazole ring, linking two aromatic moieties, provides rigidity, mimics the *trans*-amide bond<sup>[178, 180]</sup> and should thus be suitable as a molecular scaffold. The synthesis of **4** was performed in three steps and was adapted from literature procedures.<sup>[186-187]</sup> Fmoc-protection of 3-ethynyl aniline yielded precursor **4a** and treatment of 3-aminobenzoic acid with sodium nitrite generated **4b**, which were then linked by the copper(I)-catalyzed azide/alkyne “click”-reaction (CuAAC) using copper(II)sulfate and sodium ascorbate as reducing agent.



**Scheme 7.** Synthetic route towards hydrophobic Fmoc-protected  $\beta$ -turn mimetic **4**.

In the ESI-TOF-MS of **4** (see Appendix, Figure A7), the peak with the highest intensity can be assigned to the sodium adduct of **4** and all other structures can be also assigned to adducts with different ions, proving the successful synthesis of the product. The formation of the triazole ring in product **4** can be confirmed in the <sup>1</sup>H-NMR spectrum by the appearance of a signal at 9.41 ppm, while the aromatic signals can be found from 8.50 to 7.36 ppm. The methylene and methine group of the Fmoc-protecting group are also visible at 4.49 and 4.34 ppm, respectively.

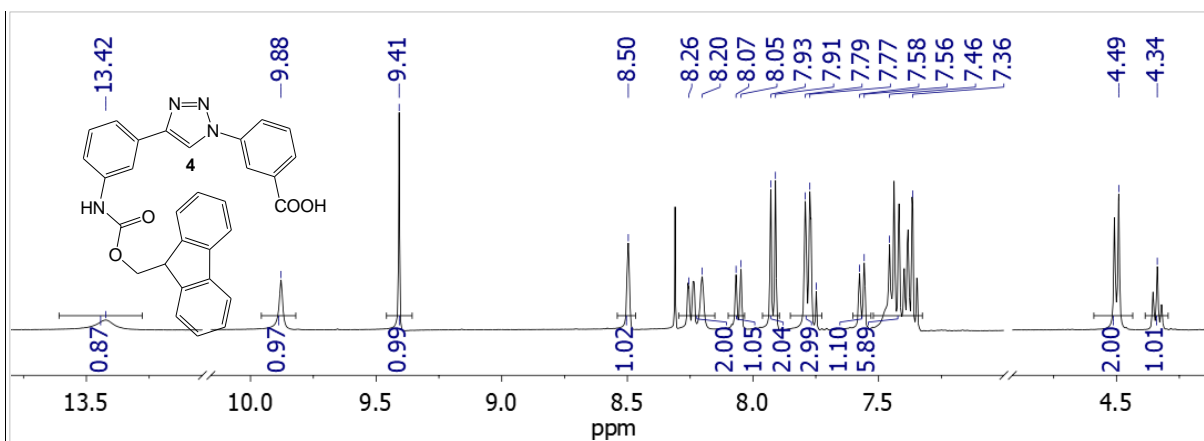
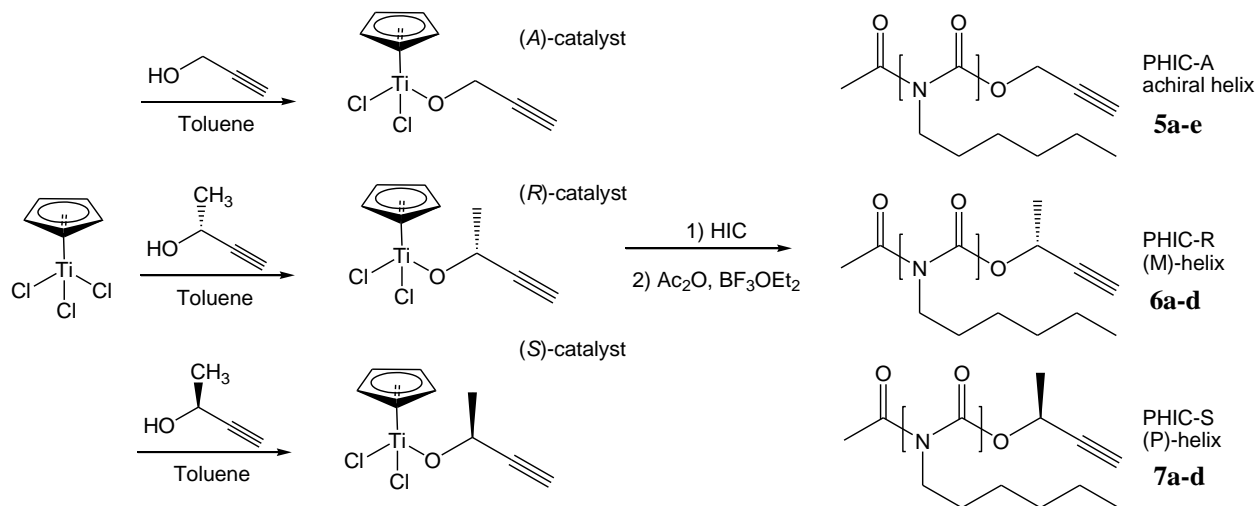


**Figure 22.** <sup>1</sup>H-NMR spectrum of Fmoc-protected  $\beta$ -turn mimetic **4**.

## 3.2 Synthesis of alkyne-functionalized helical PHICs

For the preparation of telechelic polymers with complete end group functionalization, a living polymerization is necessary and both, the anionic polymerization and the titanium-catalyzed coordination polymerization of isocyanates fulfill the criteria. In this work, the second type has been chosen, as it opens the opportunity to introduce an alkyne end group, which can be used in subsequent azide/alkyne “click”-reaction for postpolymerization modification. Novak and coworkers showed, that the use of a modified organotitanium(IV) catalyst leads to a living polymerization with a linear increase in molecular weight and a low polydispersity index ( $D < 1.20$ ).<sup>[188-189]</sup> Using an alkyne-modified titanium catalyst leads to the formation of an alkyne moiety at the initiating site of the polymer,<sup>[190]</sup> while quenching with acetic anhydride and boron trifluoride ethyletherate introduces a terminal acetyl group, which protects the polymer chain from depolymerization.<sup>[191-192]</sup> Scheme 8 shows the general procedure of the polymerizations.



**Scheme 8.** Synthesis pathway of achiral and chiral alkyne-functional PHICs.

Besides the use of achiral propargyl alcohol, two chiral alkynes with inverse chirality were used to synthesize chiral polyisocyanates and to later on investigate chirality induction effects implemented through this chiral initiating group. The polymerization is conducted in bulk and thus does not proceed until full conversion, as the viscosity of the reaction mixture strongly increases with increasing molecular weight. Therefore, the theoretical molecular weight ( $M_{n(th)}$ ) calculated for 100% conversion and the experimental values ( $M_{n(GPC)}$  and  $M_{n(NMR)}$ ) do not match perfectly. Furthermore, the titanium-catalyst is generated *in-situ* and is not further purified. Thus, the amount of active catalytic centers cannot be determined. As a result, the experimental molecular weights are about two to three times higher than the theoretical ones. A summary of the experimental results of achiral and chiral PHICs is given in Table 3.

**Table 3.** Results of polymerizations of *n*-hexyl isocyanate.

Polymer	Chirality	$M_{n(\text{th})}$ [g mol <sup>-1</sup> ]	$M_{n(\text{GPC})}^a$ [g mol <sup>-1</sup> ]	PDI <sup>a</sup>	$M_{n(\text{NMR})}^b$ [g mol <sup>-1</sup> ]	Yield [%]
<b>5a</b>	/	640	4,800	1.19	4,600	24
<b>5b<sup>c</sup></b>	/	950	2,200	1.22	3,400	19
<b>5c</b>	/	2,600	4,000	1.09	4,600	59
<b>5d</b>	/	2,000	5,300	1.08	5,000	75
<b>5e</b>	/	4,000	10,200	1.20	10,800	66
<b>6a</b>	( <i>R</i> )	670	4,400	1.09	3,400	27
<b>6b</b>	( <i>R</i> )	2,000	4,700	1.13	5,400	83
<b>6c</b>	( <i>R</i> )	2,600	6,500	1.13	5,900	81
<b>6d</b>	( <i>R</i> )	3,900	12,500	1.84	12,000	75
<b>7a</b>	( <i>S</i> )	730	3,700	1.12	3,700	40
<b>7b</b>	( <i>S</i> )	2,000	5,300	1.18	5,400	85
<b>7c</b>	( <i>S</i> )	3,900	5,700	1.12	5,000	72
<b>7d</b>	( <i>S</i> )	2,600	6,500	1.15	6,200	77

<sup>a</sup> determined *via* GPC in THF using polystyrene standards. <sup>b</sup> determined *via* <sup>1</sup>H-NMR: integration of resonances of initiator at 4.78 ppm (achiral) and 5.44 ppm (chiral) and of polymer resonances (CH<sub>2</sub>; CH<sub>3</sub>) at 0.88 to 1.62 ppm and at 3.69 ppm. <sup>c</sup> Polymer synthesized during master thesis.<sup>[193]</sup>

Purification of the synthesized polymer was achieved by repeated precipitation in methanol and the analysis of the purified polymers was conducted using gel permeation chromatography (GPC), <sup>1</sup>H-NMR spectroscopy and ESI-TOF-MS. Figure 23 shows the <sup>1</sup>H-NMR spectrum of achiral PHIC (**5c**,  $M_{n(\text{NMR})} = 4.6$  kDa) as an example. Besides the main signals resulting from the protons of the repeating unit around 0.88–1.62 ppm and 3.69 ppm, smaller signals arise from the protons of the initiator and end group. The alkyne and methylene protons appear at 2.53 and 2.28 ppm, respectively, while the methyl end group occurs at 4.78 ppm.

ESI-TOF-MS spectra were recorded to further confirm the presence of the end groups, which are necessary for postpolymerization modifications. Figure 24 shows the mass spectrum of achiral PHIC **5c**, exhibiting two series. Both, a low molecular weight double charged series and a high molecular weight single charged series could be assigned to the desired polymer, as revealed by the simulated spectra.

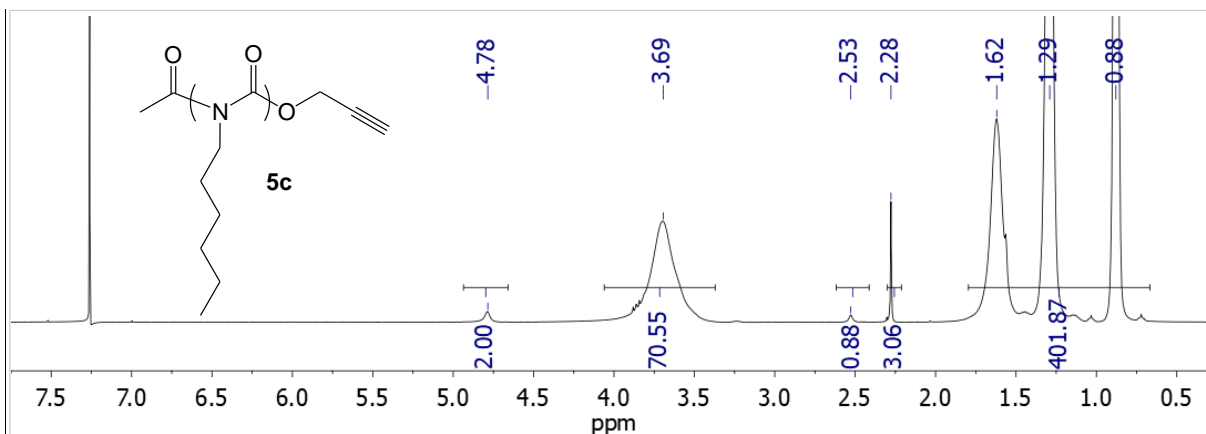


Figure 23.  $^1\text{H-NMR}$  spectrum of achiral PHIC **5c**.

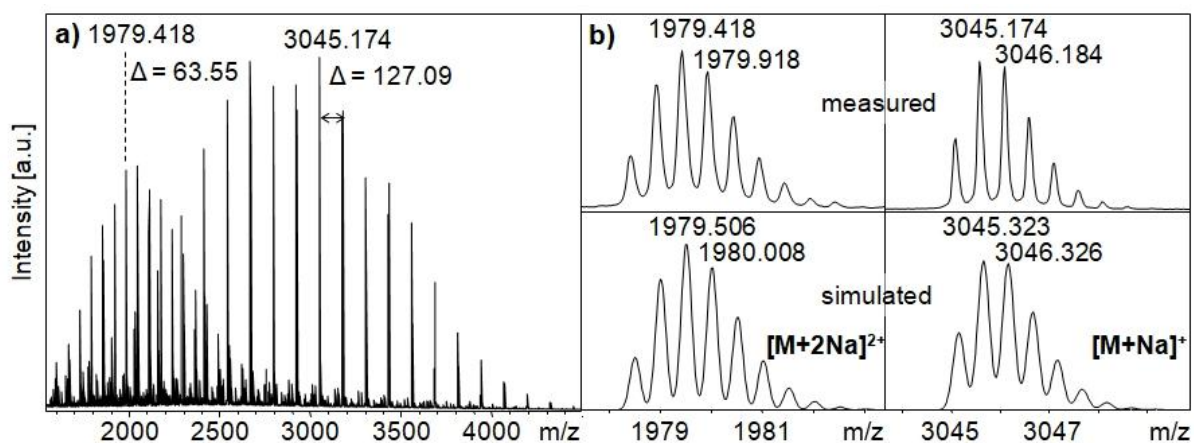
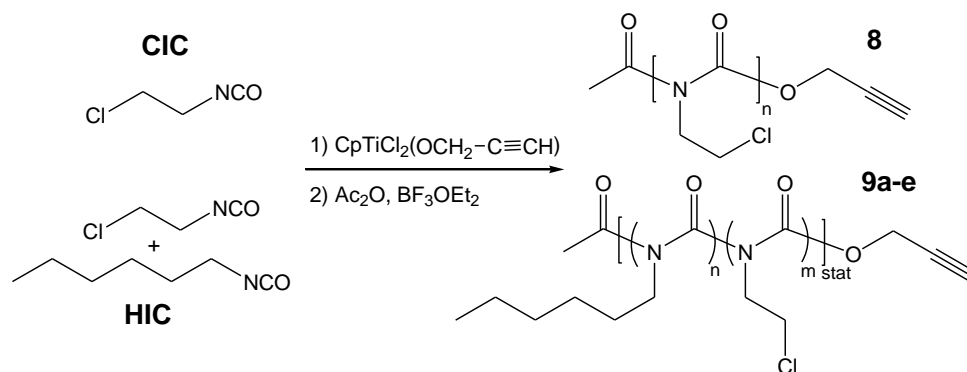


Figure 24. ESI-TOF-MS of achiral PHIC **5c**; a) full spectrum, b) measured and simulated series.

Besides the polymerization of *n*-hexyl isocyanate (HIC), also the homo- and copolymerization using 2-chloroethyl isocyanate (CIC) was investigated, yielding polymers **8** and **9a-e** (see Scheme 9), to obtain the possibility for further side chain modifications of the polymers. Similarly to the polymerization of HIC, the achiral titanium-alkoxide catalyst was used and quenching was achieved using acetic anhydride and boron trifluoride.



Scheme 9. Homo- and copolymerization of 2-chloroethyl isocyanate (CIC) and *n*-hexyl isocyanate (HIC).

The homopolymer of CIC **8** showed a bimodal distribution in GPC and furthermore exhibited only low solubility in all common organic solvents (< 0.7 mg/mL), resulting in difficulties for the analysis and further reactions. In contrast to this, the copolymers were well defined with a low polydispersity and were well soluble in common organic solvents. Therefore, further investigations were carried out and the copolymerization parameters were determined, by conducting several polymerizations with different monomer ratios of HIC to CIC and stopping the reaction at a low conversion. The obtained samples were analyzed by GPC and <sup>1</sup>H-NMR spectroscopy, to obtain the molecular weight and the ratio of the two monomers in the polymer chain. The results are summarized in Table 4.

**Table 4.** Results of homo- and copolymerizations of 2-chloroethyl isocyanate (CIC) and *n*-hexyl isocyanate (HIC).

Polymer	Theoretical ratio HIC/CIC	$M_{n(th)}$ [g mol <sup>-1</sup> ]	$M_{n(GPC)}^a$ [g mol <sup>-1</sup> ]	PDI <sup>a</sup>	$M_{n(NMR)}^b$ [g mol <sup>-1</sup> ]	Experimental ratio HIC/CIC <sup>c</sup>	Yield [%]
<b>8</b>	100:0	2,000	5,400 + 1,250	1.09 1.22	2,600	/	72
<b>9a</b>	10:1	2,500	5,200	1.09	6,400	22:1	56
<b>9b</b>	1:1	2,500	5,100	1.09	4,750	52:48	69
<b>9c</b>	80:20	10,000	3,900	1.13	5,800	87:13	4
<b>9d</b>	65:35	14,000	3,700	1.16	11,000	77:23	5
<b>9e</b>	50:50	10,000	4,200	1.10	6,300	67:33	3
<b>9f</b>	35:65	10,000	3,300	1.22	5,600	45:55	4
<b>9g</b>	20:80	10,000	2,800	1.23	4,400	74:26	8

<sup>a</sup> determined via GPC in THF using polystyrene standards. <sup>b</sup> determined via <sup>1</sup>H-NMR: integration of the resonances of the initiator protons at 4.80 ppm and of polymer resonances (CH<sub>2</sub>; CH<sub>3</sub>) at 0.88 to 1.64 ppm and at 3.68 to 4.10 ppm. <sup>c</sup> determined via <sup>1</sup>H-NMR: Integration of the resonances of HIC at 0.88 to 1.64 ppm and of CIC at 4.10 ppm.

Figure 25 shows the <sup>1</sup>H-NMR spectrum of **9b** and the <sup>13</sup>C-NMR spectrum is shown in the Appendix (Figure A9). Additionally to the previously described signals of HIC, signals at 3.76 and 4.10 ppm result from the methylene protons of CIC. Interestingly, the signal corresponding to the acetyl end group, resulting from the quenching with acetic anhydride, is slightly shifted downfield to 2.34 ppm, when the attached polymer unit is CIC instead of HIC. By comparing the integral values, it appears that 75 % of the end groups are attached to a CIC unit, even though the ratio of HIC and CIC is about 1:1, indicating that HIC polymerizes faster than CIC does. In order to further confirm this assumption, copolymerization parameters were determined. Therefore, polymerizations **9c–9g** were stopped at a very low conversion. By calculating the amount of monomer incorporated in these polymers by <sup>1</sup>H-NMR spectroscopy and comparison with the feed ratio, Fineman-Ross and Kelen-Tüdös parameters can be

determined and the corresponding plots (see Figure 56–57, Experimental part) can be generated. The following copolymerization parameters are obtained by linear fitting:

Fineman-Ross:  $r_{CIC} = 0.80$ ;  $r_{HIC} = 2.04$

Kelen-Tüdös:  $r_{CIC} = 0.67$ ;  $r_{HIC} = 1.81$

In conclusion, a gradient copolymer is obtained when copolymerizing HIC and CIC by titanium-catalyzed polymerization. HIC is preferentially introduced at the beginning of the polymerization, due to the higher propagation rate, whereas CIC is mostly incorporated at the chain end.

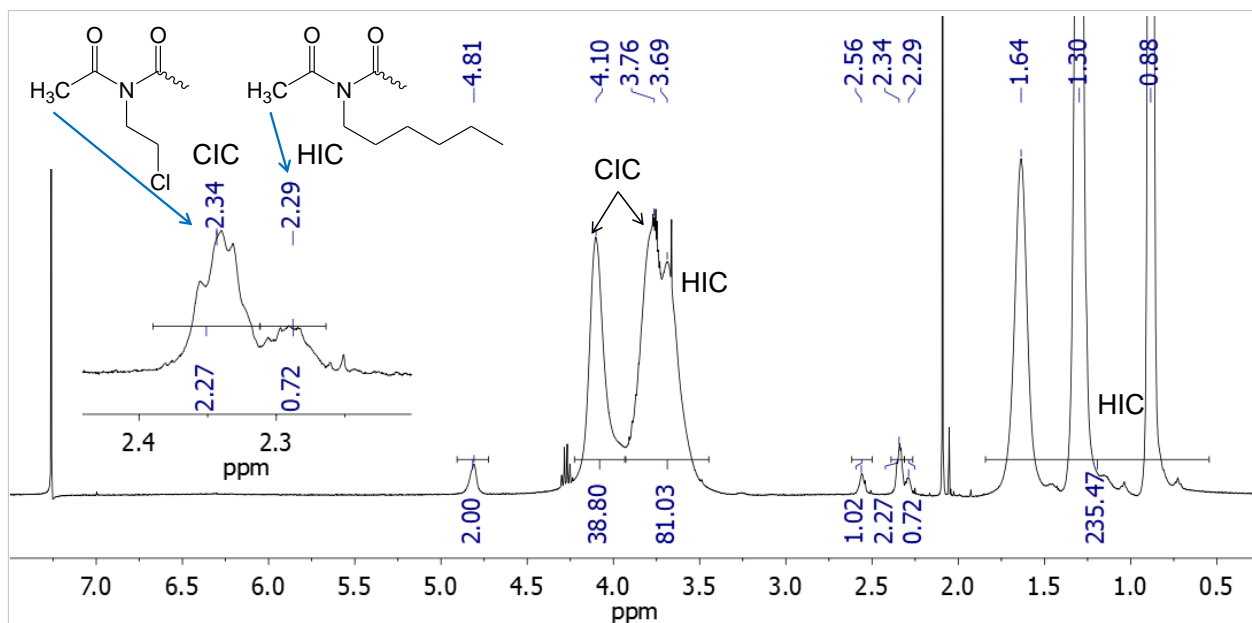
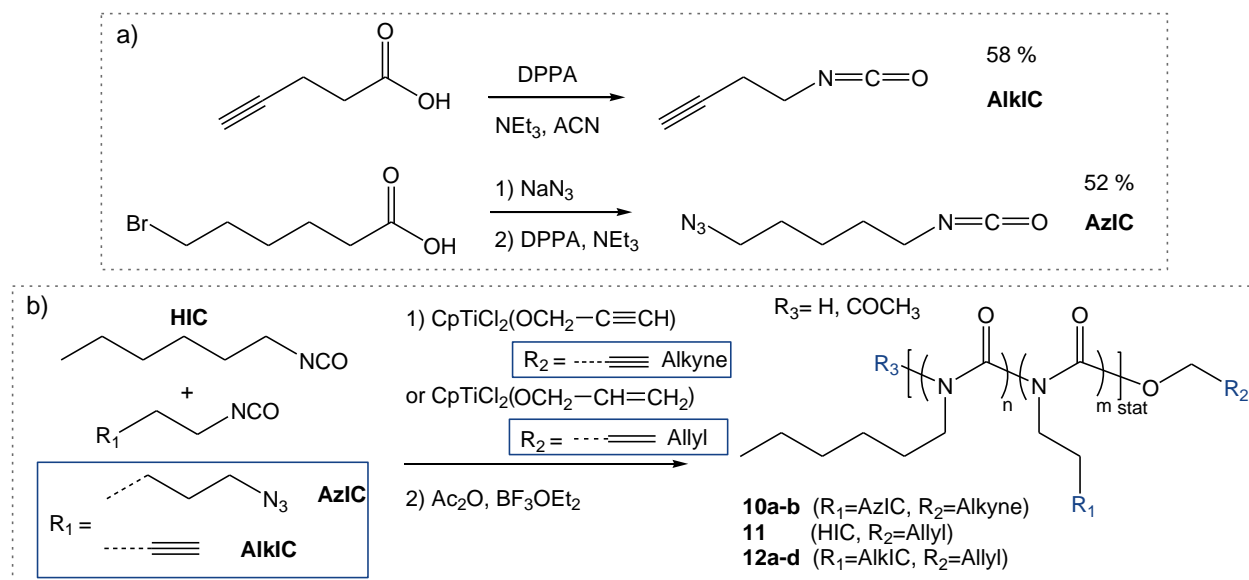


**Figure 25.**  $^1\text{H-NMR}$  spectrum of PHIC-PCIC copolymer **9b**.

Besides using the chloroethyl isocyanate as comonomer, azide- and alkyne-modified isocyanates were synthesized as shown in Scheme 10a to introduce further side chain functionalities into polyisocyanate copolymers. The synthesis of functional isocyanates was performed starting from the acid, by using diphenylphosphoryl azide (DPPA) yielding the acyl azide, which then undergoes Curtius rearrangement to result in the isocyanate monomer (see Appendix, Figure A10–A12 for NMR- and IR-spectra). For the polymerization of azide-functional isocyanates, the previously described achiral alkyne-functional titanium-catalyst was employed (see Scheme 10b). Using this catalyst would result in the same functionality in the side chain and the end group upon copolymerization with the alkyne monomer, and thus an allyl titanium catalyst was used instead, to obtain orthogonal functional groups for postpolymerization modifications. The successful use of the allyl catalyst was investigated beforehand in a homopolymerization of HIC (see Table 5, Entry **11**) and confirmed by GPC,  $^1\text{H-NMR}$  and MALDI-TOF-MS (see Appendix, Figure A13–A14). The results of copolymerizations with azide- and alkyne-functional monomers are summarized in Table 5.





**Scheme 10.** a) Synthetic pathways of alkyne- and azide-functional isocyanate monomers. b) Copolymerization of HIC with functional isocyanates AlkIC and AziC.

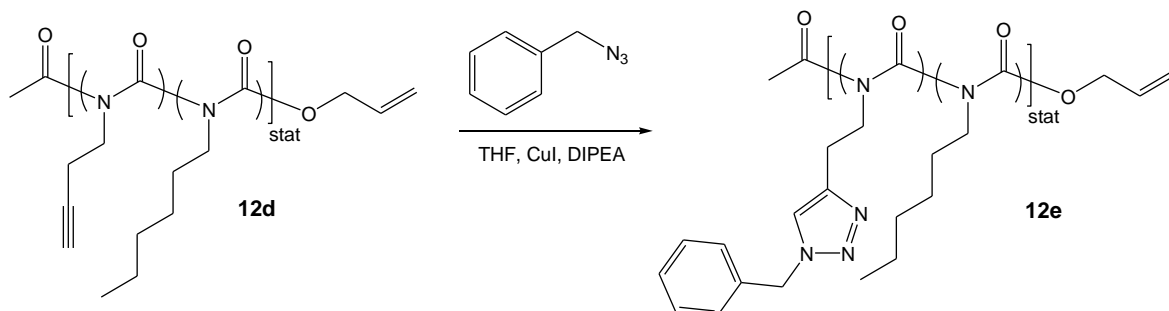
**Table 5.** Results of copolymerization of *n*-hexyl isocyanate and functional isocyanates.

Entry	Comonomer R <sub>1</sub>	End group R <sub>2</sub>	R <sub>th</sub> <sup>a</sup> HIC/Co	M <sub>n(GPC)</sub> <sup>b</sup> [g mol <sup>-1</sup> ]	PDI <sup>b</sup>	M <sub>n(NMR)</sub> <sup>c</sup> [g mol <sup>-1</sup> ]	R <sub>exp</sub> <sup>d</sup> HIC/Co	Yield [mg]
<b>10a</b>	AziC	Alkyne	10:1	4,700	1.11	7,100	16:1	6
<b>10b</b>	AziC	Alkyne	1:1	/	/	/	/	/
<b>11</b>	/	Allyl	1:0	4,500	1.07	5,300	/	170
<b>12a</b>	AlkIC	Allyl	4:1	4,100	1.10	6,500	12:1	13
<b>12b</b>	AlkIC	Allyl	1:4	/	/	/	/	/
<b>12c</b>	AlkIC	Allyl	1:1	/	/	/	/	/
<b>12d</b>	AlkIC	Allyl	4:1	4,900	1.08	6,300	24:1	135

<sup>a</sup> R<sub>th</sub>: theoretical feed ratio of HIC / comonomer. <sup>b</sup> determined *via* GPC in THF using polystyrene standards. <sup>c</sup> determined *via* <sup>1</sup>H-NMR: integration of resonances of initiator at 4.68 ppm and of polymer resonances (CH<sub>2</sub>; CH<sub>3</sub>) at 0.88 to 1.62 ppm and at 3.69 ppm. <sup>d</sup> R<sub>exp</sub>: experimental ratio of HIC / comonomer determined <sup>1</sup>H-NMR: integration of HIC resonances at 0.88 to 1.62 ppm and of comonomer at 2.58 ppm. The theoretical molecular weight of all samples was 2,500 g/mol.

Similar to the previous polymerizations, all obtained polymers show a low polydispersity. By comparing the theoretical and experimental ratios of HIC and the comonomers determined by integration of <sup>1</sup>H-NMR spectra (see Figure 26 (top) and Figure A15) it can be seen, that the latter is embedded into the polymer in a much lower amount, indicating a low reactivity of these azide- and alkyne-functionalized monomers. However, using a higher amount of comonomer resulted in the failure of the polymerization (entry **10b**, **12b**, **12c**), probably due to

a destruction of the catalyst, as a color change to dark brown was observed upon addition of the comonomer. As the ESI-TOF-MS spectrum of **12d** confirmed the presence of alkyne side chains (see Appendix, Figure A16), the possibility for further functionalization by “click” chemistry was investigated using **12d** and benzyl azide as a test system (see Scheme 11).



**Scheme 11.** “Click” reaction of PHIC-PALKIC copolymer **12d** and benzyl azide.

The successful linkage was confirmed by <sup>1</sup>H-NMR spectroscopy upon comparison with the spectrum of **12d** (see Figure 26). While the protons of the allyl end group are still present at 5.94, 5.35 and 4.68 ppm respectively, the signals of the alkyne side chain at 1.93 and 2.58 ppm disappear and new signals for the triazole ring appear at 7.44 and 3.09 ppm respectively.

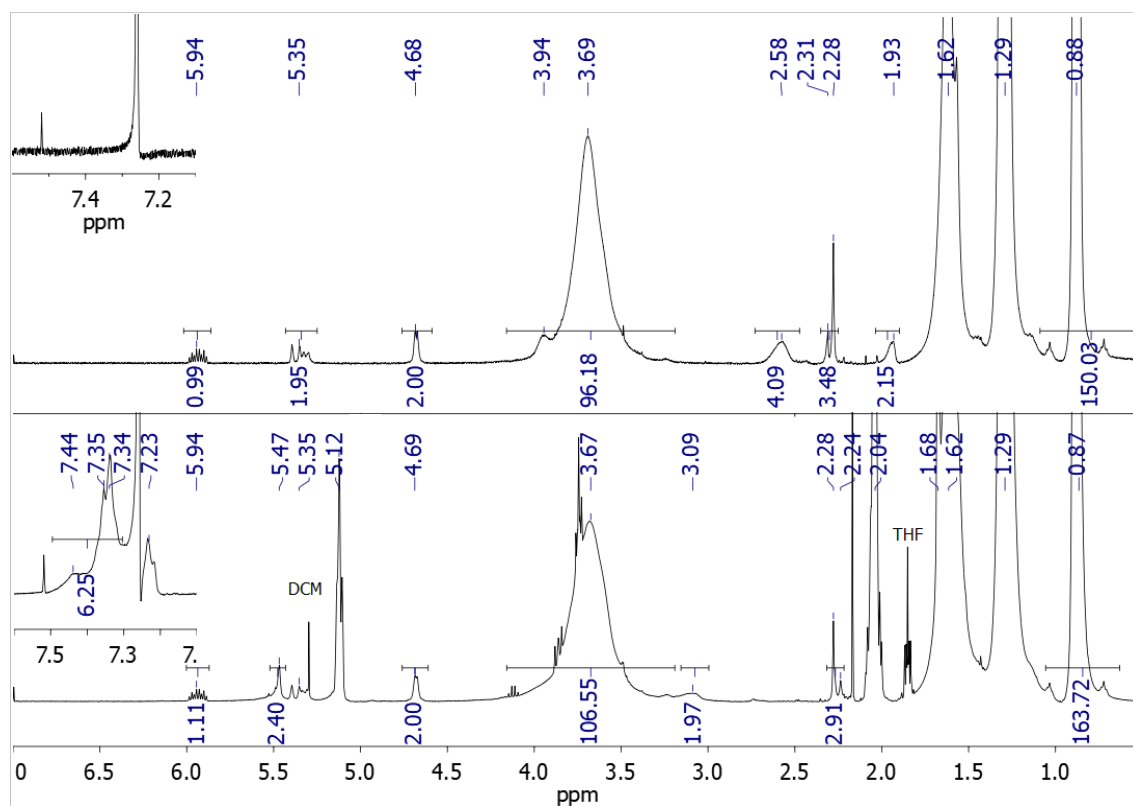


**Figure 26.** <sup>1</sup>H-NMR spectrum of PHIC-PALKIC copolymer **12d** (top) and “click” product **12e** with benzyl azide (bottom).

Furthermore, aromatic protons of the benzyl group appear around 7.25–7.35 ppm and the methyl group next to the benzyl group appears at 5.47 ppm. According to the integral values, only one benzyl group is attached to one polymer chain, even though the signals for two alkyne groups of the precursor polymer disappear. Moreover, additional signals at 2.04 and 5.12 ppm are present, which could not be assigned, indicating some impurities.

However, ESI-TOF-MS measurement confirmed the successful “click” reaction (see Figure 27). One series of unfunctionalized PHIC appears with a maximum at  $m/z = 2792.972$ , resulting from polymer chains lacking any alkyne functionality. Several series appearing at a lower  $m/z$  ratio are double charged and can be assigned to structures bearing either no side chain functionality ( $m/z = 1853.313$ ) or the synthesized “click” product with one ( $m/z = 1903.187$ ), two ( $m/z = 1890.302$ ) or three ( $m/z = 1876.357$ ) functional groups per chain, while the peaks for alkyne-functional precursor polymer **12d** were not observed. Thus, side chain modification *via* “click” chemistry was successful, but limitations for further use occurred, especially due to the low amount of alkyne side chains incorporated into the polymer and the low yields of the copolymerization.

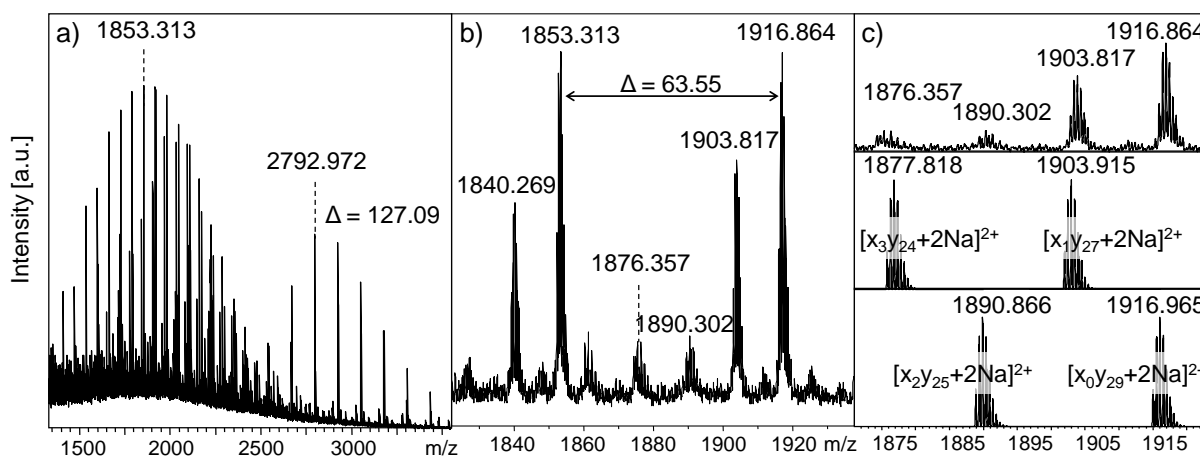
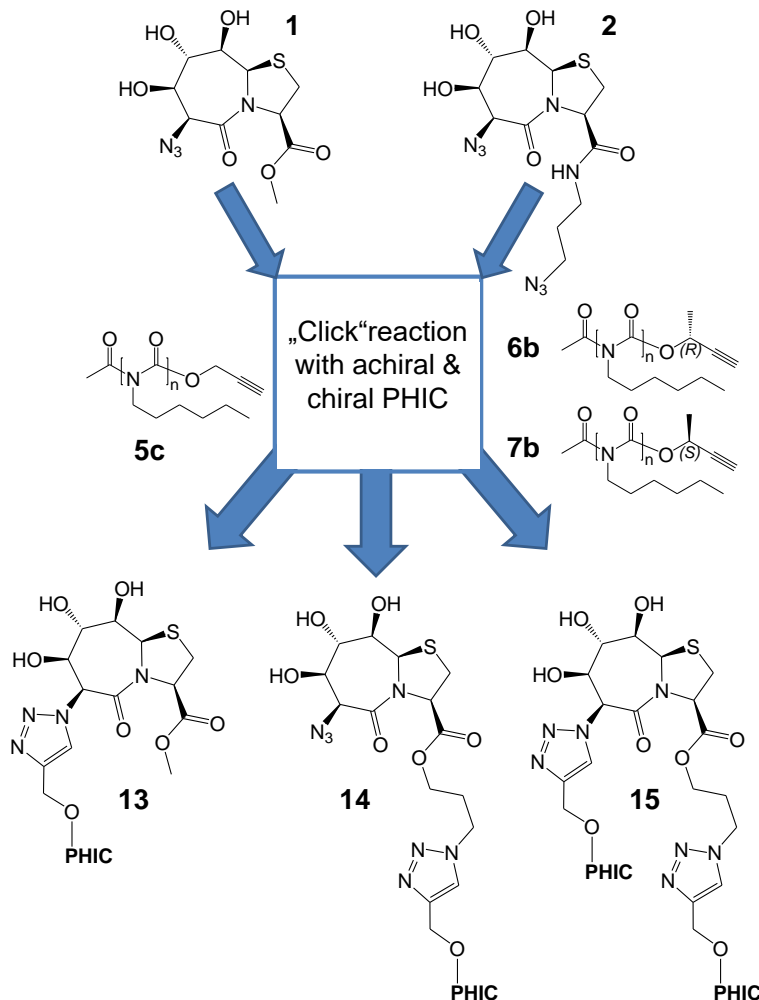


**Figure 27.** ESI-TOF-MS spectrum of **12e**; a) full spectrum, b) insight, c) measured (top) and simulated series (middle, bottom).

### 3.3 Synthesis of $\beta$ -turn mimetic polymer conjugates<sup>[194]</sup>



**Scheme 12.** Synthetic pathway for the synthesis of  $\beta$ -turn mimetic PHIC conjugates *via* „click“-reaction.

In order to obtain  $\beta$ -turn mimetic polymer conjugates which can be further investigated concerning their chirality and insertion behavior into membranes, the previously synthesized and purified polymers and  $\beta$ -turn mimetics had to be linked. The copper(I)-catalyzed azide/alkyne cycloaddition reaction is a valuable method for the linkage of polymers,<sup>[195-197]</sup> but also of small organic molecules<sup>[198]</sup> and peptides<sup>[199-201]</sup> and was thus employed in this work. Alkyne-functional PHICs were connected to  $\beta$ -turn mimetic structures bearing either one or two azide groups as illustrated in Scheme 12, resulting in one- or two-arm conjugates.

Due to the sterical hindrance resulting from the additional methyl group in the chiral PHICs (**6b**, **7b**), the linkage of these polymers to the  $\beta$ -turn mimetic structures proved to be challenging. Especially the attachment of a second polymer strand was difficult, due to the small distance between the two reactive azide groups of **2**. However, it was possible to obtain the one- and two-arm polymer conjugates, as summarized in Table 6.

**Table 6.** Overview about synthesized  $\beta$ -turn mimetic PHIC conjugates.

PHIC conjugate	Precursor polymer <sup>a</sup>	Cotton effect <sup>b</sup>	$M_{n, GPC}$ <sup>c</sup> [g mol <sup>-1</sup> ]	PDI <sup>c</sup>	$M_{n, NMR}$ <sup>d</sup> [g mol <sup>-1</sup> ]	Yield [%]
<b>13-A</b>	<b>5c</b>	+	4,500	1.07	4,800	46
<b>14-A</b>	<b>5c</b>	+	4,400	1.14	5,800	3
<b>15-A</b>	<b>5c</b>	+	7,900	1.14	9,900	2
<b>13-R</b>	<b>6b</b>	+	4,600	1.15	6,400	13
<b>14-R</b>	<b>6b</b>	-	5,100	1.19	/ <sup>e</sup>	5
<b>15-R</b>	<b>6b</b>	-	7,700	1.17	/ <sup>e</sup>	3
<b>13-S</b>	<b>7b</b>	+	5,500	1.16	7,300	15
<b>14-S</b>	<b>7b</b>	+	5,500	1.18	/ <sup>e</sup>	4
<b>15-S</b>	<b>7b</b>	+	9,600	1.16	/ <sup>e</sup>	3

<sup>a</sup> see Table 3 <sup>b</sup> determined in THF. <sup>c</sup> determined *via* GPC in THF using polystyrene standards. <sup>d</sup> determined *via* <sup>1</sup>H-NMR: Integration of resonances of initiator at 4.68 ppm and of polymer resonances (CH<sub>2</sub>; CH<sub>3</sub>) at 0.88 to 1.62 ppm and at 3.69 ppm.

<sup>e</sup> Due to the low amount of the product, it was not possible to calculate the molecular weight from the NMR spectrum.

Since the conjugates (**13–15**) should be further investigated with respect to their chirality as well as their behavior at the air / water-interface and their interaction with model membranes, it was critical to proof the purity of the conjugates and thus chromatographic, spectroscopic and spectrometric measurements were performed. Two different chromatographic methods, gel permeation chromatography (GPC, Figure 28a) and high-performance liquid chromatography (HPLC, Figure 28b, 28c) were employed. Due to the livingness of the polymerization, all conjugates show narrow molecular weight distributions and thus a low polydispersity ( $\mathcal{D} = 1.07–1.19$ ). While the one-arm conjugates exhibit only a small shift towards higher molecular weight, due to the additional molecular weight of attached BTD **2**, the two-arm conjugate **15-A** (blue triangle) exhibits a strong shift towards lower retention times, indicating the successful attachment of the second PHIC chain onto the same  $\beta$ -turn structure and thus a doubling of the molecular weight. GPC calibration was performed using PS standards and hence, deviations from the actual molecular weight may arise from the more rigid PHIC structure and from the compact structure of two closely linked polymer chains. In contrast to GPC analysis, which depends solely on size differences, HPLC analysis is based on polarity differences and is thus suitable to illustrate the difference between hydrophobic PHIC and  $\beta$ -turn mimetic conjugates containing the hydrophilic BTD. Alkyne-functional PHICs of different molecular weights ( $M_{n, GPC} = 2.2–12.0$  kDa) were investigated in order to obtain the LCCC conditions, meaning that the method is independent of the molecular weight and hence only sensitive towards different end group functionality. Generally, three different types of elution can be described in HPLC measurements. In the GPC mode, elution is mainly based on

an entropic effect and results in elution according to the molecular weight. As shown in Figure 28b, this principle occurs when using THF as elution solvent for PHICs. In contrast, the adsorption mode (LAC) results in an elution according to the molecular weight in an inverse manner, which was found for PHICs when adding 35 % of the non-solvent methanol to the elution solvent THF. In between these two modes, the LCCC conditions were found at 30.5 % of methanol at 30 °C on a reversed phase column. Subsequently, this method was applied as end group sensitive method for the  $\beta$ -turn mimetic polymer conjugates and the results are shown in Figure 28c. As anticipated, all three conjugates and the pure PHIC elute at different retention times ( $R_t = 7.00$  (achiral PHIC **5c**); 6.34 (**13-A**); 6.20 (**14-A**); 6.00 min (**15-A**)). The significant lowering of the retention time for the conjugates in comparison to pure PHIC indicates the higher hydrophilicity and proves the successful linkage of PHIC and BTD, as well as the complete removal of non-functionalized PHIC. The chiral conjugates showed similar elution profiles and retention times (see Appendix, Figure A17).

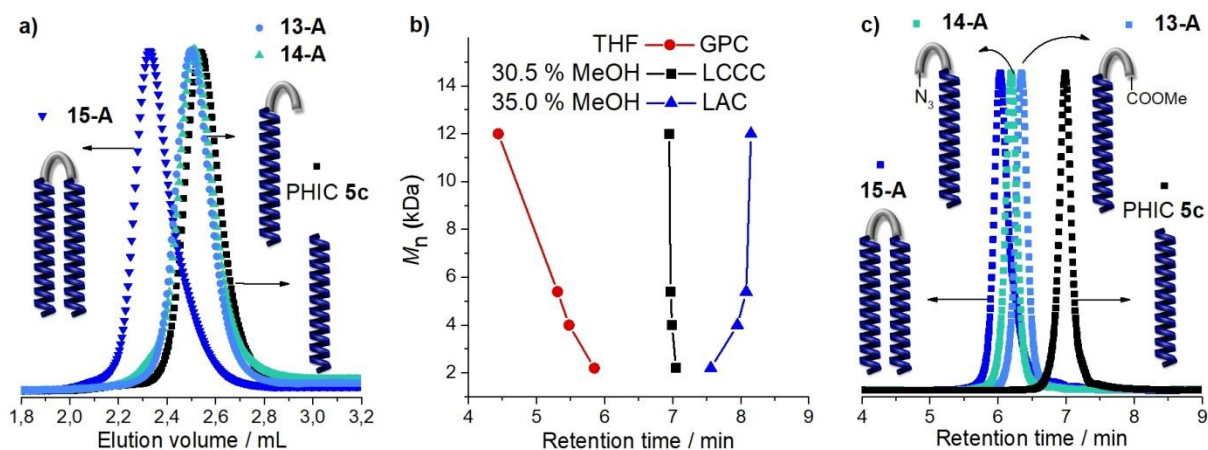


**Figure 28.** a) GPC, b) different conditions of HPLC, c) HPLC curves of achiral PHIC and PHIC-conjugates.

Further proof of the successful linkage was obtained using  $^1\text{H-NMR}$  spectroscopy, as shown for mono-functional conjugate **13-A** (see Figure 29). The acetylenic proton of PHIC at 2.53 ppm disappeared, due to the formation of a triazole ring during CuAAC, which results in the appearance of a new singlet at 8.25 ppm. Furthermore, the proton of the methine group directly linked to the triazole is shifted to 6.18 ppm and all other signals of the  $\beta$ -turn mimetic structure could be assigned by comparison with the spectra of the starting materials and previously obtained data.<sup>[202]</sup> Integration of the signals corresponding to the polymer backbone (1.8–0.8 ppm) in comparison to the integrals of the end group result in a calculated molecular weight of 4.8 kDa, which matches closely to the molecular weight determined by GPC (4.9 kDa). NMR analysis of the chiral one-arm conjugates **13-R** and **13-S** resulted in similar spectra (see Appendix, Figure A18). NMR spectroscopy of the one-arm BTD-PHIC conjugates (**14-A**, **14-R**, **14-S**) and of the two-arm BTD-PHIC conjugates (**15-A**, **15-R**, **15-S**) was challenging, due to low yields and the high molecular weight.

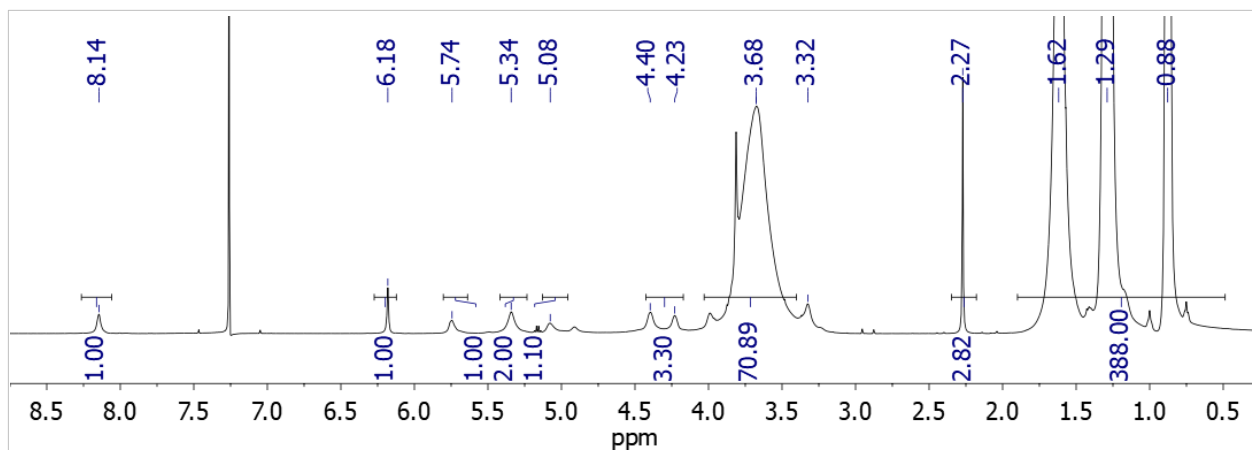


Figure 29.  $^1\text{H-NMR}$  spectrum of **13-A**.

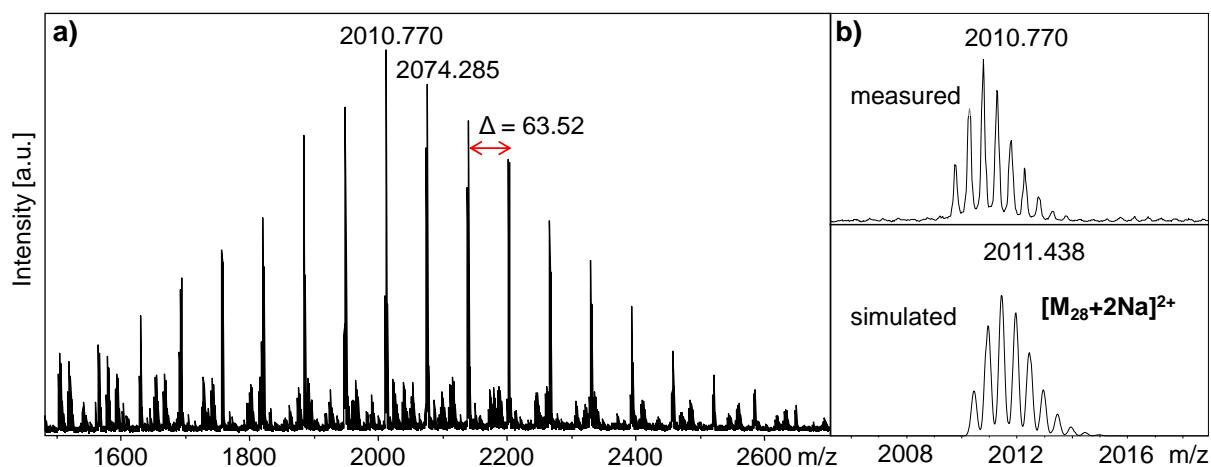
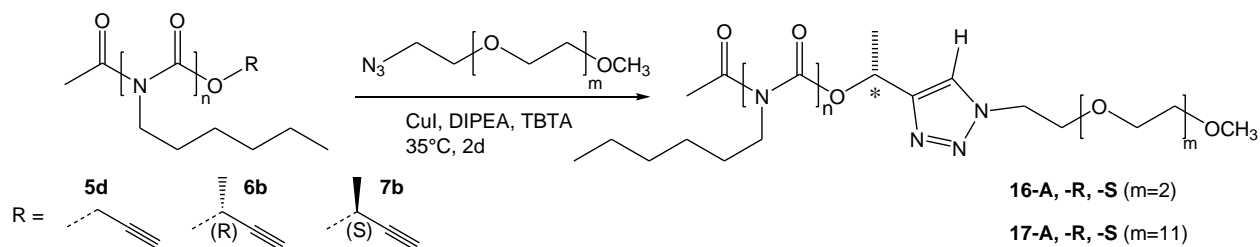


Figure 30. ESI-TOF-MS of achiral **13-A**; a) full spectrum, b) measured and simulated pattern.

ESI-TOF-MS was performed in order to further confirm the end group functionality of the  $\beta$ -turn mimetic PHIC conjugates. Figure 30 shows the ESI-TOF-MS spectrum of **13-A** displaying one PHIC series, with a maximum at a mass-to-charge ratio of 2010.770 and a mass difference of 63.5, which matches with the double charged sodium adduct of **13-A**. Thus the molecular weight ranges from 3.0 to 5.2 kDa with a maximum around 4.0 kDa, which is slightly lower but still comparable to the results obtained from GPC (4.5 kDa) and  $^1\text{H-NMR}$  (4.8 kDa) investigations. In contrast to the precursor polymer **5c**, no single charged series was observed and the molecular weight increased only by 60 Da. However, no peaks from residual PHIC were observed, confirming the structure and purity of the product. ESI-TOF-MS and MALDI-TOF-MS measurements of the two-arm conjugates were not successful, due to the limitations of these methods for high molecular weights, which was previously already observed for other PHICs.<sup>[203]</sup>

### 3.4 Synthesis of PHIC-PEG block-copolymers

As a comparison to the  $\beta$ -turn mimetic PHIC conjugates, copolymers with polyethylene glycol (PEG) as hydrophilic block were synthesized, to investigate the difference in chirality and in the behavior at the air / water-interface between a pure hydrophilic moiety and the  $\beta$ -turn mimetic structure linked to PHIC. The synthesis of diblock-copolymers containing hydrophobic PHIC and hydrophilic ethylene glycol units was achieved by the use of the CuAAC reaction similar to the synthesis of BTD-conjugates as shown in Scheme 13 and summarized in Table 7.



**Scheme 13.** Synthesis of PHIC-PEG copolymers *via* CuAAC.

Two different ethylene glycol chain lengths have been chosen, triethylene glycol (TEG) acting as a very short block, comparable to the short hydrophilic BTD and one longer PEG chain of about  $550 \text{ g mol}^{-1}$  and thus of about 12 repeating units. Azide-functionalization of TEG and PEG was achieved according to literature<sup>[204-205]</sup> and was confirmed by NMR- and IR-spectroscopy (see Appendix, Figure A19-20). As it was already observed for the PHIC-BTD conjugation, also the conjugation with PEG was challenging for the chiral PHICs, resulting in low yields. The purity of the copolymers was investigated with chromatographic, spectroscopic and spectrometric methods. The GPC results revealed a small increase in molecular weight, while the polydispersities proved to be still very low ( $\mathcal{D} < 1.12$ ).

**Table 7.** Overview about synthesized TEG / PEG-copolymers *via* “click” reaction.

TEG- / PEG-copolymers	Precursor polymer <sup>a</sup>	Cotton effect <sup>b</sup>	$M_{n, \text{GPC}}^c$ [g mol <sup>-1</sup> ]	PDI <sup>c</sup>	$M_{n, \text{NMR}}^d$ [g mol <sup>-1</sup> ]	Isolated yield [%]
<b>16-A</b>	<b>5d</b>	/	5,500	1.07	5,300	27
<b>17-A</b>	<b>5d</b>	/	5,050	1.08	5,100	45
<b>16-R</b>	<b>6b</b>	-	5,400	1.11	5,500	2
<b>17-R</b>	<b>6b</b>	-	6,200	1.11	6,000	3
<b>16-S</b>	<b>7b</b>	+	5,400	1.10	5,900	2
<b>17-S</b>	<b>7b</b>	+	5,600	1.09	6,200	2

<sup>a</sup> see Table 3. <sup>b</sup> determined in THF. <sup>c</sup> determined *via* GPC in THF using polystyrene standards. <sup>d</sup> determined *via* <sup>1</sup>H-NMR: integration of resonances of the O-CH<sub>2</sub> (achiral) and O-CH (chiral) group of the PHIC chain at 5.32 and 6.05 ppm respectively and of polymer resonances (CH<sub>2</sub>; CH<sub>3</sub>) at 0.88 to 1.62 ppm.



HPLC measurements were performed using the same conditions as previously described for the  $\beta$ -turn mimetic PHIC conjugates to demonstrate the successful linkage of TEG / PEG to PHIC, resulting in an increased hydrophilicity and thus in a shift in HPLC. As anticipated, the attachment of a short hydrophilic TEG chain results in a small shift ( $R_t \approx 6.14$  min) compared to pure PHIC ( $R_t \approx 6.47$  min), while the attachment of the longer PEG chain induces a stronger shift towards lower retention times ( $R_t \approx 5.88$  min) (see Figure 31a).

Further confirmation was obtained by  $^1\text{H-NMR}$  spectroscopy (see Figure 31b). The disappearance of the acetylenic proton at 2.53 ppm and the appearance of the triazole proton at 7.82 ppm indicate the successful formation of the triazole ring. Furthermore, the methylene group connecting the polymer chain and the triazole ring is shifted from 4.78 ppm to 5.32 ppm and the methylene group connecting the triazole ring and the ethylene glycol chain appears at 4.55 ppm. In the chiral copolymers, a shift of the methine signal from 5.44 ppm to 6.05 ppm as well as the appearance of signals at 7.73 ppm and 4.54 ppm can be observed (see Appendix, Figure A21–A22).

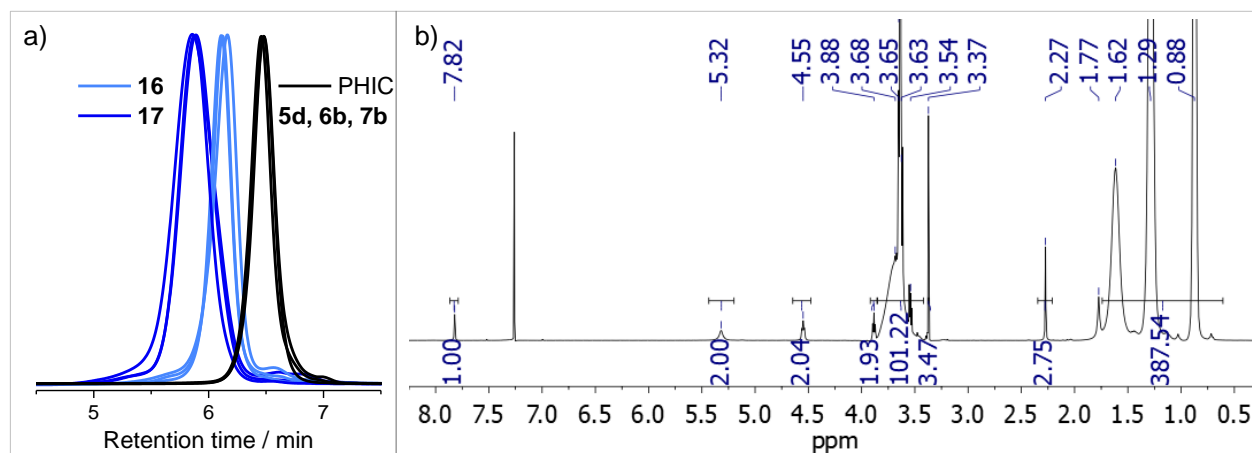


**Figure 31.** a) HPLC traces of PHIC precursor polymers, TEG copolymers 16-A, -R, -S and PEG copolymers 17-A, -R, -S. b)  $^1\text{H-NMR}$  spectrum of achiral PEG copolymer 17-A.

Additionally, ESI-TOF-MS was carried out, to obtain more detailed information about the structure of the synthesized copolymers and the mass spectrum of achiral PEG copolymer 17-A is shown in Figure 32. In the low molecular weight range ( $m/z = 1200$ – $2000$ ), structures with a triple, positive charge can be observed and the difference of around 42 matches to the triply charged repeating unit of PHIC (127.18 g/mol), while the smaller peaks in between, with a distance of around 15, correspond to the triply charged repeating unit of PEG (44.05 g/mol). In the higher molecular weight region ( $m/z = 2000$ – $2600$ ) the series are doubly charged. Structures with different repeating units of *n*-hexyl isocyanate (HIC) and ethylene oxide (EO) could be assigned, as shown in the simulated spectra in comparison to the measured spectrum, which consists of the triply charged sodium adducts of the products. The number of EO units varies from seven to fourteen and the series with the highest intensities contain nine to eleven EO units. The overall molecular weight ranges from 3.6 to 6.0 kDa with a maximum at 4.8 kDa,

which matches with the molecular weight obtained from GPC (5.0 kDa) and  $^1\text{H-NMR}$  investigations (5.1 kDa).

Further investigations of these copolymers were carried out regarding their chirality and insertion behavior into model membranes.

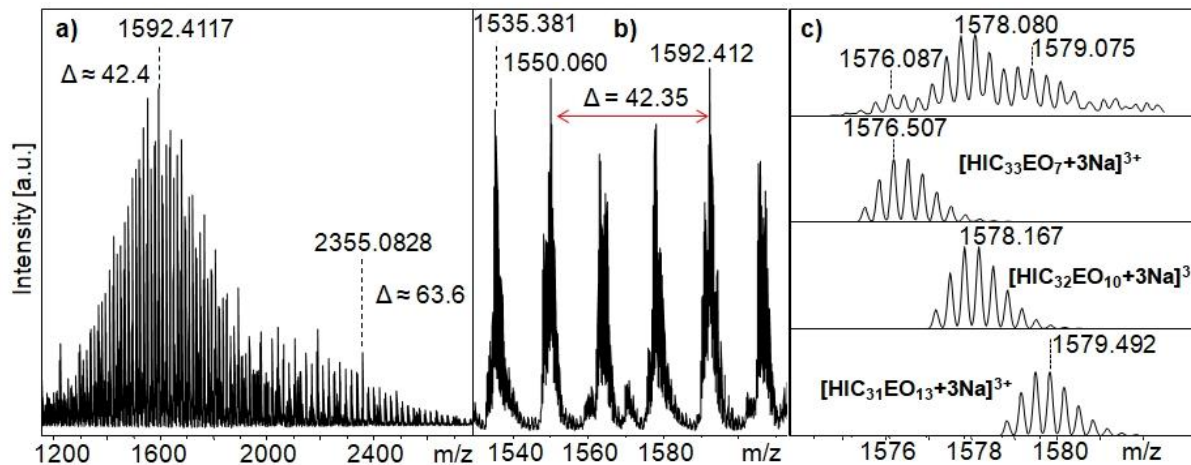


**Figure 32.** ESI-TOF-MS of achiral PEG copolymer 17-A; a) full spectrum, b) expansion, c) measured (top) and simulated (below) spectra.

### 3.5 Chirality induction effects in $\beta$ -turn mimetic polymer conjugates and block-copolymers containing PHIC

After the successful synthesis and characterization of  $\beta$ -turn mimetic polymer conjugates and of amphiphilic diblock-copolymers, investigations of chirality induction effects should be performed.

Chirality<sup>[206]</sup> is an important feature in natural structures such as amino acids, DNA and carbohydrates and is a major factor for the function of these molecules. It describes an object or molecule which cannot be superimposed with its mirror image.<sup>[207-208]</sup> Different types of chirality can be distinguished, the most common one being point chirality, in which an asymmetric carbon center possesses four different substituents. Besides stereogenic centers, also chirality-axes which can be found *e.g.* in allenes and chirality-planes as *e.g.* in *trans*-cycloocten can result in chirality.<sup>[208-209]</sup> Another type of chirality, frequently occurring in biological macromolecules as well as in synthetic ones, is the helicity. Helical molecules are described according to their handedness as right- or left-handed helices. In synthetic macromolecules, it was revealed that a variety of polymers, such as polyisocyanides, polyacetylenes and polysilanes, can exhibit chirality due to the formation of a helical structure.<sup>[210]</sup> Polyisocyanates, which are discussed in this work, possess an amide backbone with partial double-bond character and should thus favor a *trans*-planar structure. Nevertheless, they are helical, as steric interactions between the alkyl side groups and the carbonyl group, result in a slight out-of-plane rotation to release the strain.<sup>[131, 211-212]</sup> In contrast to polypeptides, the helix is not stabilized by intramolecular hydrogen bonds, and both left- and right-handed helices are formed equally when using achiral monomers. X-ray studies<sup>[211]</sup> and quantum mechanical calculations<sup>[213]</sup> revealed a  $8_3$ -helix for poly(*n*-butyl isocyanate), as eight monomers are forming three turns. The contour length of polyisocyanates is about 2 Å per monomer and the diameter of the rodlike PHIC helix was found to be around 1.6 nm.<sup>[214-215]</sup>

Using achiral monomers results in a mixture of left- and right-handed helices and abolishes an overall visible chirality. Preference of one helical sense can be induced into polyisocyanates by introducing chiral side chains,<sup>[216-217]</sup> chiral initiators<sup>[218-219]</sup> and chiral end groups<sup>[190, 220]</sup> or by providing host-guest interactions with chiral molecules<sup>[221]</sup> and interactions with chiral solvents.<sup>[222]</sup> Principles like “majority rules”<sup>[223]</sup> and the sergeant-and-soldiers principle<sup>[224]</sup> have been established and describe underlying phenomena. The sergeant-and-soldiers principle can also be applied to the synthesized polymers described in this work. Due to the chiral end group, introduced through initiation, chirality is transferred onto the polymer chain and the formation of a one-handed helix is observed. Below a critical number of repeating units, an increase in chirality is observed, due to the increased amount of repeating units with the same helical sense. Above this critical number, helix inversion can occur and thus the overall observed chirality is reduced with further increasing molecular weight. In the scope of this thesis, the influence of a  $\beta$ -turn mimetic structure on the helicity of polyisocyanates was

investigated. Furthermore, comparison with hydrophilic block-copolymers as well as studies in different solvents were conducted.

Chirality and the helical sense in polyisocyanates can be detected *via* circular dichroism (CD) spectroscopy, resulting in spectra of ellipticity  $\theta$  in dependence of the wavelength  $\lambda$ . For a better comparison of different molecular weights, molar ellipticity values are calculated from the measured values of ellipticity by applying equation 1.

$$[\theta] \cdot 10^{-3} = \frac{\theta \cdot M}{c \cdot d \cdot 10} \text{ mdeg} \cdot \text{cm}^2 \cdot \text{dmol}^{-1}$$

$\theta$ : Ellipticity [mdeg]

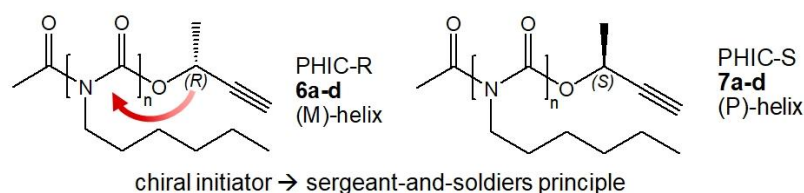
$M$ : Molar mass of polymer [g/mol]

$c$ : Concentration of solution [mg/mL]

$d$ : Path length [cm]

**Equation 1.** Calculation of molar ellipticity values.

### 3.5.1 Circular dichroism studies of chiral PHICs



**Scheme 14.** Chiral PHICs investigated *via* CD spectroscopy showing a preferred helical sense due to the chiral initiator.

CD measurements of the chiral PHICs **6** and **7** were performed in three different solvents, THF, *n*-hexane and DCM (see Figure 33). In all solvents, PHICs bearing the (*S*)-end group showed a positive Cotton effect at around 255 nm, corresponding to the  $n \rightarrow \pi^*$  transition of the amide backbone, and are thus present as preferably right-handed helices ((*P*)-helix, clockwise), while the inverse can be observed for (*R*)-PHICs (left-handed helix, (*M*)-helix, anti clockwise). The assignment of left- and right-handed helices in CD spectroscopy has previously been performed with empirical field force and by a molecular orbital study.<sup>[213, 225]</sup> The maximum CD intensity observed in *n*-hexane (~6 mdeg) is in agreement with reported literature of an anionic polymerization with a chiral initiator.<sup>[226]</sup> Similar to literature, an increase in ellipticity was observed with increasing molecular weight and the maximum is reached at 5–6 kDa.<sup>[220, 227]</sup> Thus, one chiral end group can induce chirality into a polyisocyanate chain with up to around 45 repeating units, which is known as the sergeant-and-soldiers principle.<sup>[228-229]</sup> Above this number of repeating units, helix reversals can occur and thus the overall helicity decreases, which can be seen for the PHIC with a high molecular weight (12.5 kDa).

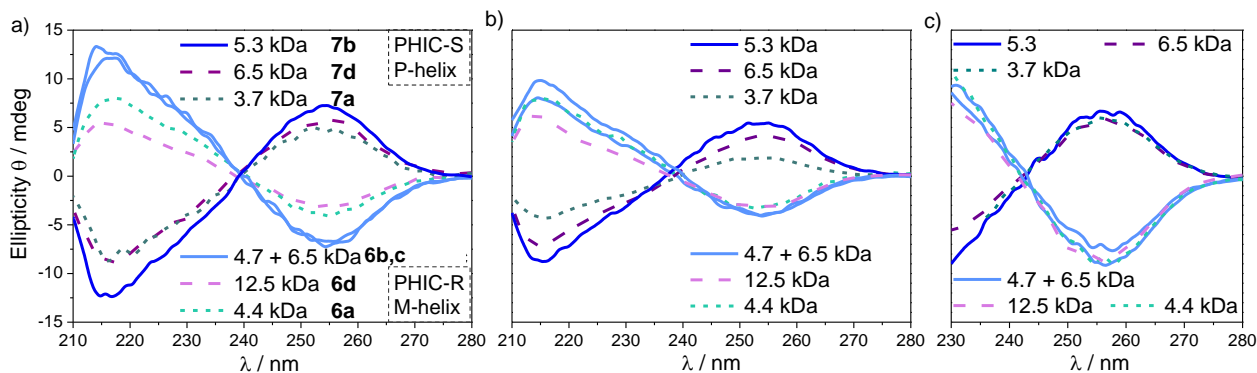
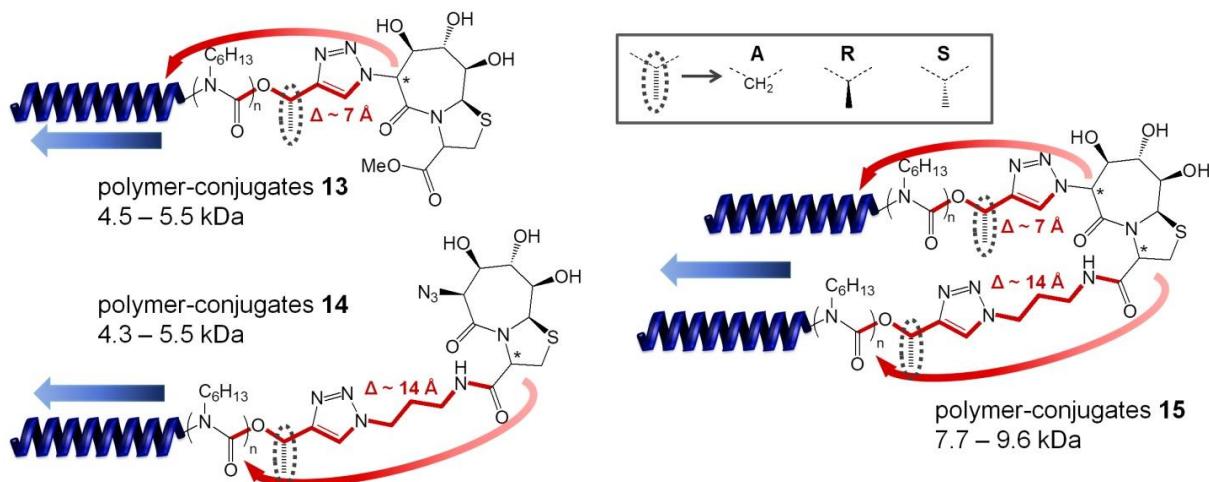


**Figure 33.** CD spectra of chiral PHICs **6** and **7** (see Table 3) of different molecular weights in a) THF, b) *n*-hexane (0.25 mg/mL) and c) DCM (0.5 mg/mL).

Interestingly, no clear difference between the spectra of different molecular weights was observable in DCM. A comparison of the chain dimensions of polyisocyanate in different solvents revealed a lower chain-stiffness in DCM compared to *n*-hexane and THF and thus a lower persistence length.<sup>[230]</sup> Slight differences in these three different solvents have also been observed for other chiral polyisocyanates containing a chiral end group<sup>[203]</sup>, however the influence of molecular weight has not been investigated.

### 3.5.2 Circular dichroism studies of $\beta$ -turn mimetic conjugates



**Scheme 15.** Representation of the achiral and chiral  $\beta$ -turn mimetic PHIC conjugates **13-15** investigated *via* CD spectroscopy and the distances between chiral  $\beta$ -turn mimetic and polymer backbone.

Investigations of  $\beta$ -turn mimetic polymer conjugates were performed similar to the pure polymers in different solvents. Due to the attachment of the hydrophilic BTM, it was not possible to measure the conjugates with one polymer chain (**13**, **14**) in *n*-hexane, as they were not soluble in this solvent. The conjugates containing two polymer strands (**15**) were however soluble, as the hydrophilic part was much smaller in comparison to the hydrophobic polymer

chains, and these measurements gave similar results than the one in DCM (see Appendix, Figure A23).

First, the achiral polymer conjugates (**13-A**, **14-A**, **15-A**) were investigated, as the effect of a chiral  $\beta$ -turn mimetic should be directly visible in comparison to the achiral PHIC, which showed no CD signal due to an equal mixture of right- and left-handed helices. All conjugates exhibit a clear CD signal in DCM (see Figure 34a), with a maximum or minimum at 258 nm, which is the characteristic signal of the polyisocyanate backbone corresponding to the  $n \rightarrow \pi^*$  transition of the amide backbone. As a comparison, the CD spectrum of the pure BTD **1** was recorded, exhibiting clearly different maxima and minima compared to the polymer-conjugates with much lower molar ellipticity values (see Appendix, Figure A23). Consequently, the signals of the conjugates are only arising from the helicity of the backbone and not from the turn structure itself. The one-arm conjugates **13-A** and **14-A** possess similar molar ellipticity values but with the inverse Cotton effect. Apparently, different sides of the  $\beta$ -turn mimetic induce opposite helical structures in DCM. Such a helicity inversion was previously observed in self-assembled systems and polythiophenes revealing to an odd-even effect.<sup>[231-233]</sup> Upon increasing the distance to the backbone by one atom each, an alternation of the sign of the Cotton effect was observed in CD studies. The herein described  $\beta$ -turn mimetic conjugates also possess one odd (conjugate **13**) and one even (conjugate **14**) linker unit, which could explain this behavior in DCM.

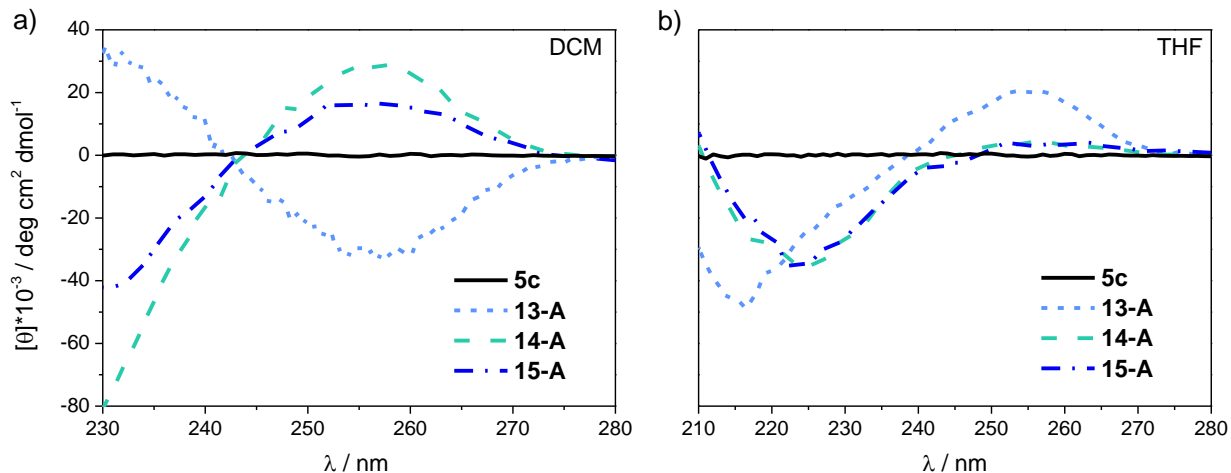


**Figure 34.** CD spectra of achiral  $\beta$ -turn mimetic conjugates in a) DCM and b) THF.

The linkage of two achiral polymer chains onto both sides of the  $\beta$ -turn mimetic structure leads to a positive signal, with slightly lower values than both one-arm conjugates. It might have been expected, that the two-arm conjugate is a simple combination of the spectra of the one-arm conjugates, which is not the case as this would result in a slightly negative signal around 258 nm. Thus, either the induction effect from one side of the turn is stronger than from the other side, or intramolecular interactions between the two polymer strands connected to each other favor the right-handed helix.

The spectra in THF (see Figure 34b) revealed strong differences from those in DCM. Interestingly, the one-arm conjugate **13-A** resulted in a positive signal instead of a negative one in DCM, indicating helical inversion due to the change of solvent. Previous calculations for chiral polyisocyanates showed that only a small energetic difference separates the right- and left-handed helices and thus an inversion can easily occur.<sup>[210, 225]</sup> The other two conjugates **14-A** and **15-A** showed lower molar ellipticity values in THF compared to DCM. While possessing similar polarity, these two solvents differ in their donor character, DCM being a non-donor and THF acting as donor-solvent. Previous investigations of polyacetylenes bearing amide groups in the side chain, revealed an increased tendency for the amide groups to adopt a *cis*-conformation in donor solvents, thus resulting in different helical conformations.<sup>[234]</sup> An increased amount of *cis*-conformation can disturb the helix and thus explain the low Cotton effect in THF for the conjugates in which the chiral center is further away from the polymer backbone.

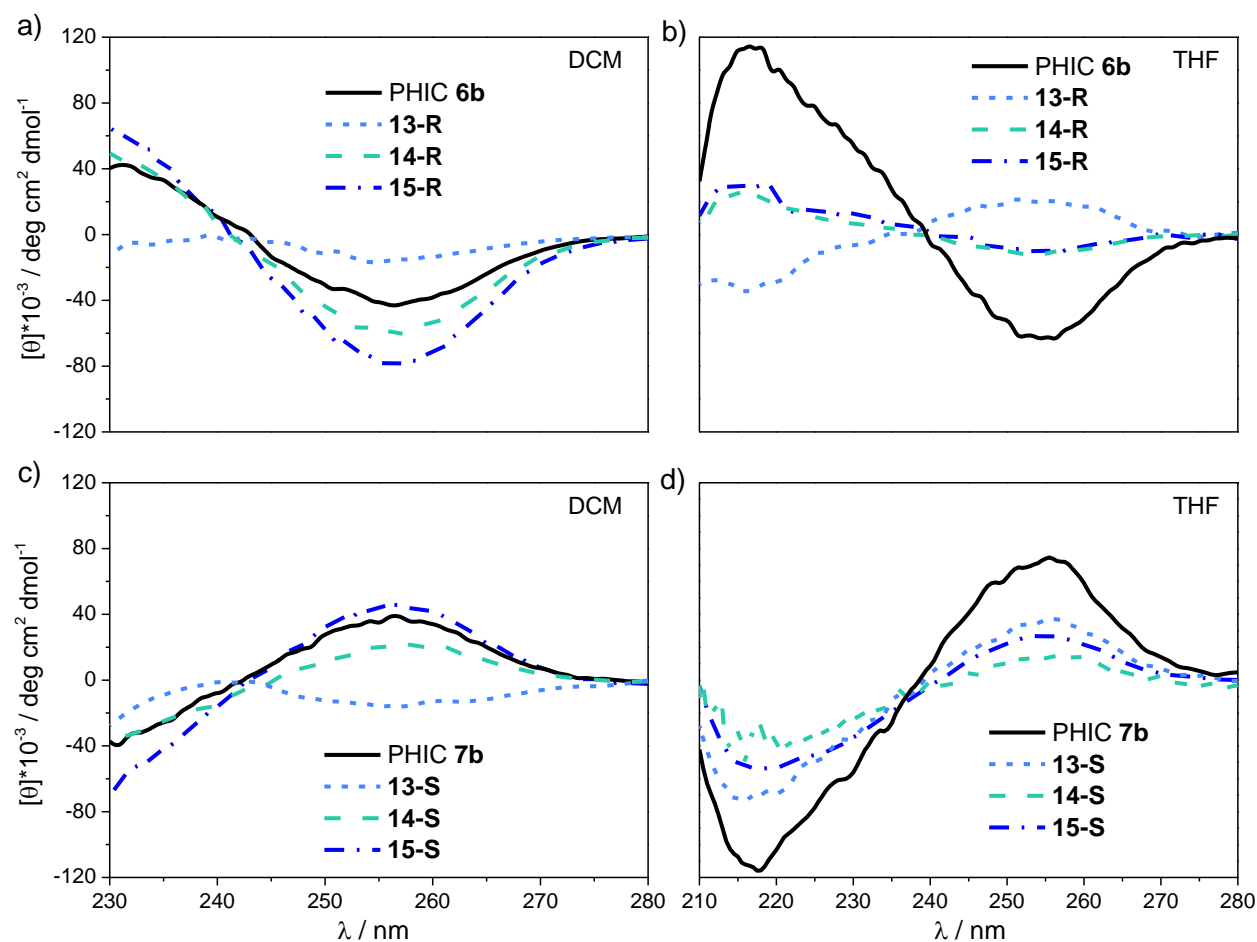


**Figure 35.** CD spectra of  $\beta$ -turn mimetic conjugates **13**, **14**, **15** in comparison to PHIC. (*R*)-conjugates in a) DCM and b) THF. (*S*)-conjugates in c) DCM and d) THF.



Afterwards, the chiral conjugates were investigated, which again exhibited clear differences between the spectra in DCM and THF (see Figure 35). Interestingly, the one-arm conjugates **13-R** and **13-S** both exhibited positive signals in THF, while they possessed the inverse sign in DCM, being the same as in the achiral conjugate. Even though the chiral center of the  $\beta$ -turn mimetic is further apart from the polymer backbone than the chiral center of the initiator, the induction effect from the  $\beta$ -turn mimetic can suppress the chirality that was induced during polymerization. The triazole unit in between the  $\beta$ -turn mimetic and the polymer backbone thus transmits the stereochemical information effectively. Previous investigations of polyacetylenes, another type of dynamic helical polymers,<sup>[130]</sup> revealed the ability to transmit chiral information over distances up to 23 Å when using a rigid linker.<sup>[235]</sup> Similar to the pure polymers, a weak bathochromic shift from 255 nm in *n*-hexane and THF to 258 nm in DCM is observable. The R-conjugates show a slight increase in DCM, while they exhibit a strong decrease in THF and loss of one preferred helical sense for the two-arm conjugate.

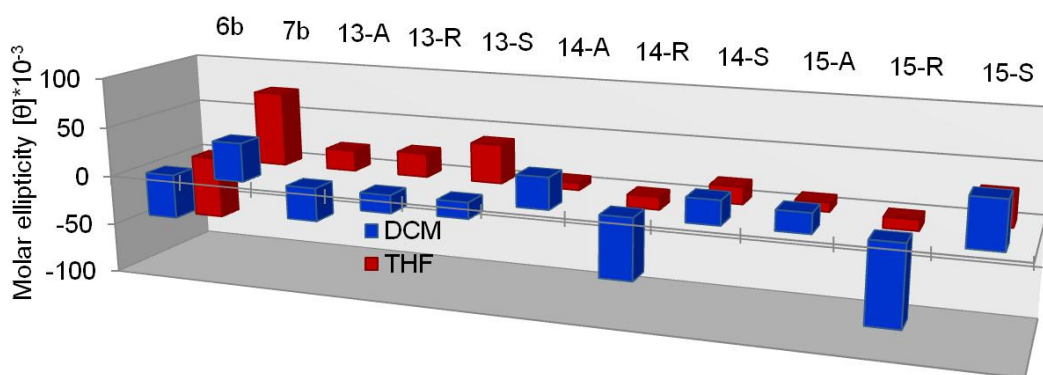
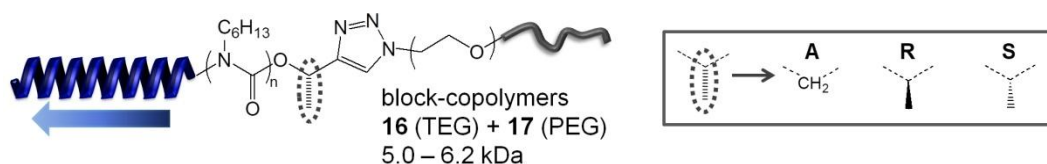


**Figure 36.** Overview about the results of circular dichroism studies obtained for  $\beta$ -turn mimetic conjugates in DCM and THF.

A summary of the results obtained from the circular dichroism studies of  $\beta$ -turn mimetic conjugates is shown in Figure 36. Again the interesting feature of conjugate **13**, with a short rigid linker becomes apparent, inducing the same helical sense in all three conjugates and inverse Cotton effects in THF and DCM. The molar ellipticity values are lower in THF for all conjugates **14**, bearing one linker with a higher distance, due to the previously described effects originating from the donor effect of THF.



### 3.5.3 Circular dichroism studies of PEG copolymers



**Scheme 16.** Representation of the achiral and chiral PHIC-TEG / -PEG block-copolymers **16+17** investigated *via* CD spectroscopy.

Compared to the  $\beta$ -turn mimetic polymer conjugates, linkage of PHIC to TEG or PEG chains does not introduce another chiral center and therefore only diminishing effects are expected upon investigation *via* CD spectroscopy. Similarly to the BTD-conjugates, CD measurements of the copolymers were performed in *n*-hexane, THF and DCM to obtain further information about the influence of solvents. The strongest signals for the TEG-copolymers **16** and PEO-copolymers **17** were obtained in DCM, while only weak signals are visible in THF, which is in agreement with the results from  $\beta$ -turn mimetic polymer conjugates.

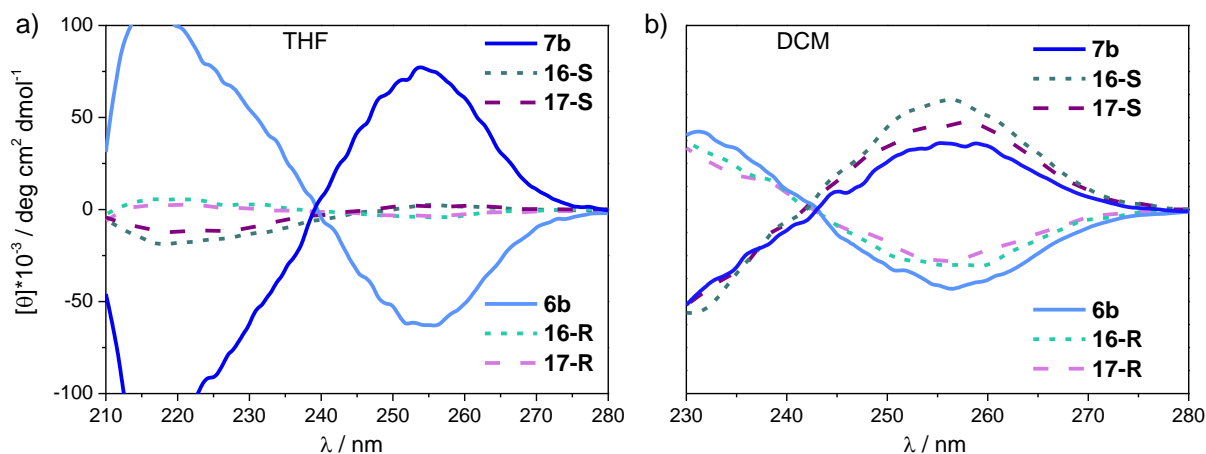
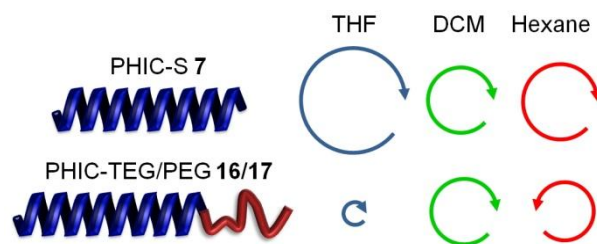


**Figure 37.** Molar ellipticity spectra of PHIC-TEG / -PEG copolymers **16** and **17** in a) THF and b) DCM.

As visible from Figure 37, the molar ellipticity values for right-handed PHICs linked to TEG and PEG slightly increase in DCM, while they decrease for left-handed PHICs. However, in THF the intensities are reduced by about ten times and in *n*-hexane (see Figure 38) about half. The strong effect in THF can again be attributed to the donor-effect as observed for  $\beta$ -turn mimetic conjugates **14** and **15**. The differences between *n*-hexane and DCM can originate from the different polarity. *N*-hexane as non-polar solvent preferentially solubilizes the alkyl side chains, whereas the more polar solvents DCM and THF can also interact with the amide backbone.<sup>[203]</sup> Differences also occur in the solubility of the EO chains, which are insoluble in *n*-hexane but soluble in DCM and THF.

Interestingly, an inversion of the CD signal occurred in *n*-hexane for all TEG- / PEG-copolymers, resulting in a negative signal for (*S*)-conjugates and positive signals for

(*R*)-conjugates (see Figure 38a). Such an inversion upon switching from DCM to *n*-hexane was previously observed in a polycarbodiimide possessing an anthracene side chain.<sup>[236]</sup> There it was attributed to a bond rotation around the anthracene, possessing the lowest energy barrier however a helix inversion due to N-C bond rotation with an estimated energy barrier of 12.5 kcal/mol<sup>[225]</sup> was not excluded.



**Scheme 17.** Overview about the influence of solvent on helicity of polyisocyanate in PHIC-TEG/PEG copolymers 16 and 17.

In order to further investigate this phenomenon, CD spectra of **16-S** were measured in different ratios of DCM and *n*-hexane (see Figure 38b, c). With increasing content of *n*-hexane, the molar ellipticity value decreases compared to pure DCM, until the spectrum appears featureless at a ratio of 9:1 (*n*-hexane / DCM), meaning that right- and left-handed helices are present in the same ratio.

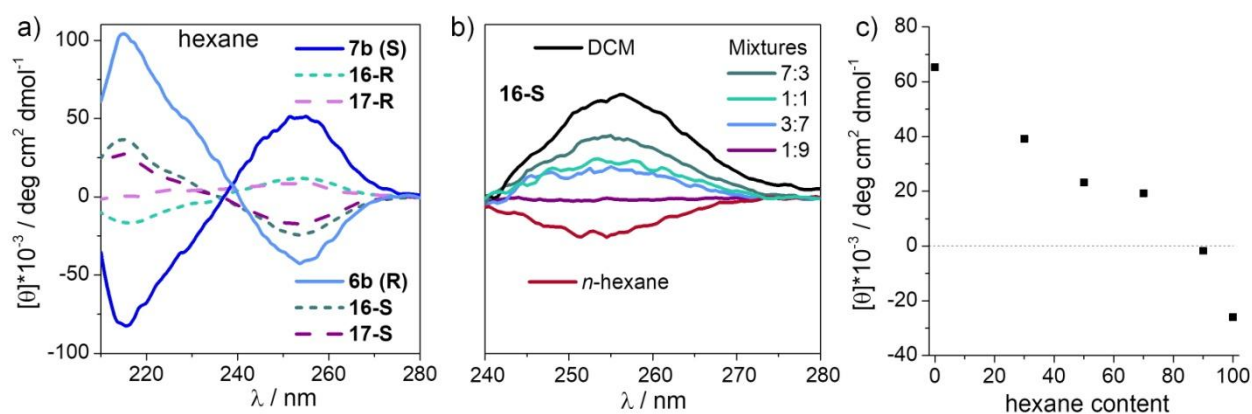


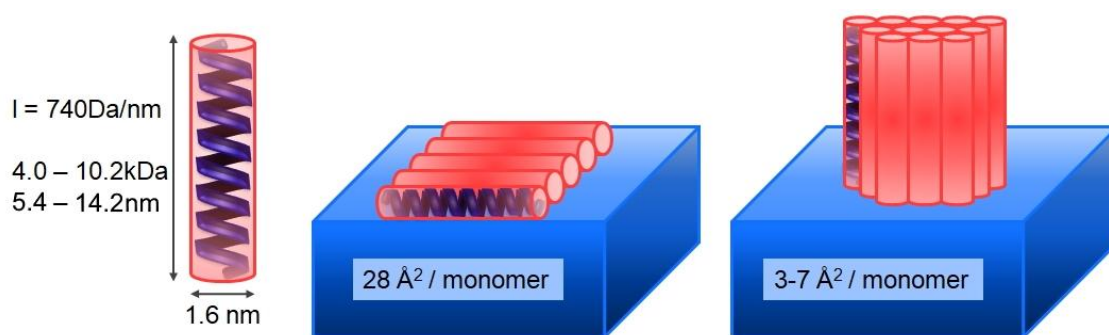
**Figure 38.** CD spectra of a) PHIC-TEG / PEG copolymers 16 and 17 in *n*-hexane and of b) **16-S** in different ratios of DCM and *n*-hexane. c) Change of molar ellipticity of **16-S** with increasing content of *n*-hexane.

Thus, a preference for a right-handed helical sense can be seen, just as in the pure PHIC and the copolymer preferentially solvates in DCM. As it has been previously discussed, solvent polarity has a huge influence on the helicity of PHIC. Additionally, *n*-hexane is a non-solvent for the EO block, which influences the chain dimensions and the structure. Similarly, it was shown that PHIC-PEG block-copolymers with comparable molecular weights and a similar concentration as in this work, formed micelles in toluene which is another non-solvent for the PEG block.<sup>[237]</sup>

### 3.6 Behavior at the air / water interface<sup>[238]</sup>

Helical PHIC homo- and copolymers have previously been investigated at the air / water-interface,<sup>[239-240]</sup> but mostly of a much higher molecular weight than the polymers synthesized in this work and without a preferred helical sense. Furthermore, the previously chosen copolymers were more hydrophobic than PHIC (polystyrene, polyisoprene, poly(2-vinyl acetate)).<sup>[241-242]</sup> Thus, investigation of these PHIC copolymers containing a hydrophilic anchor, either the  $\beta$ -turn mimetic structure or the ethylene glycol chain, is a new approach. Furthermore, the interactions of the conjugates with model membranes, such as 1,2-dipalmitoyl-*sn*-glycero-3-phosphocholine (DPPC) should be investigated. This phospholipid is a good mimic for half of a lipid bilayer at the air / water interface and can thus be used to investigate interactions of the conjugates with membranes. Surface pressure-area ( $\pi$ -A) isotherms of achiral and chiral PHICs of different molecular weights were recorded to reveal the influence of the molecular weight and the chirality on the behavior at the air / water interface.

Scheme 18 shows a structural representation of the PHIC helix, which can be considered a rigid rod in the low molecular weight range investigated in this work.<sup>[240]</sup> The molar mass per unit contour length ( $M_L$ ) and diameter of the cylindrical helix were previously determined in different solvents yielding values around 1.6 nm and 740 Da/nm respectively.<sup>[214, 243]</sup> Consequently, the length of the measured samples in this work ranges from 5.5-14 nm. Assuming that the rigid rod lies on the water surface, an area of 28 Å<sup>2</sup> is occupied by one monomer unit, while this area is reduced to 3-7 Å<sup>2</sup> for an upright helix, depending on the molecular weight.



**Scheme 18.** Structural characteristics of the PHIC helix and possible conformations at the air / water interface.

Figure 39a shows the dependence of the surface pressure from the mean molecular area, while Figure 39b shows the normalized area per repeating unit (r.u.). In Figure 39a, the polymer with the highest molecular weight ( $M_n = 10.0 \text{ kDa}$ ) exhibits a rise in surface pressure (lift-off), at much higher values than the low molecular weight polymers, while the value is the same as for low molecular weight PHIC when compared to the repeating unit (Figure 39b). The lift-off occurs because of intermolecular interactions between PHIC chains, which are forced into a restricted space. By extrapolation of the increase to zero surface pressure, the limiting area  $A_0$

is obtained. Similar to previous investigations,<sup>[240, 244-245]</sup> this value is at  $25\text{--}27 \text{ \AA}^2$  which matches to the area occupied by a helical rod lying flat on the surface ( $28 \text{ \AA}^2$ ).<sup>[239-240]</sup> Thus, the investigated low molecular PHICs show no dependence on the molecular weight, as it occurred for high molecular weight PHICs (12–390 kDa).<sup>[240]</sup> This can be explained as the helix is much stiffer in the low molecular weight range (5–12 kDa) than at higher molecular weight, where it shows a wormlike structure. Furthermore, no significant differences can be observed between achiral and chiral PHIC and thus helix reversals occurring in achiral PHIC do not significantly influence the size of the helical rod. Upon further compression, a pseudo plateau is reached in which the surface pressure remains almost constant around 4–8 mN/m. This was previously attributed to the formation of bilayers or even multilayers.<sup>[239, 246]</sup> Further reduction of the surface area leads to an increase in surface pressure, which was previously described as the liquid condensed state, followed by a second pseudo plateau ( $5\text{--}8 \text{ \AA}^2/\text{r.u.}$ ), which can be attributed to the transition from liquid condensed to condensed state.<sup>[241]</sup> However, the second plateau is independent of the molecular weight, occurring at the same area per repeating unit in all cases. This excludes the possibility for the formation of upright helices on the surface as depicted in Scheme 18, as this would result in different area values.

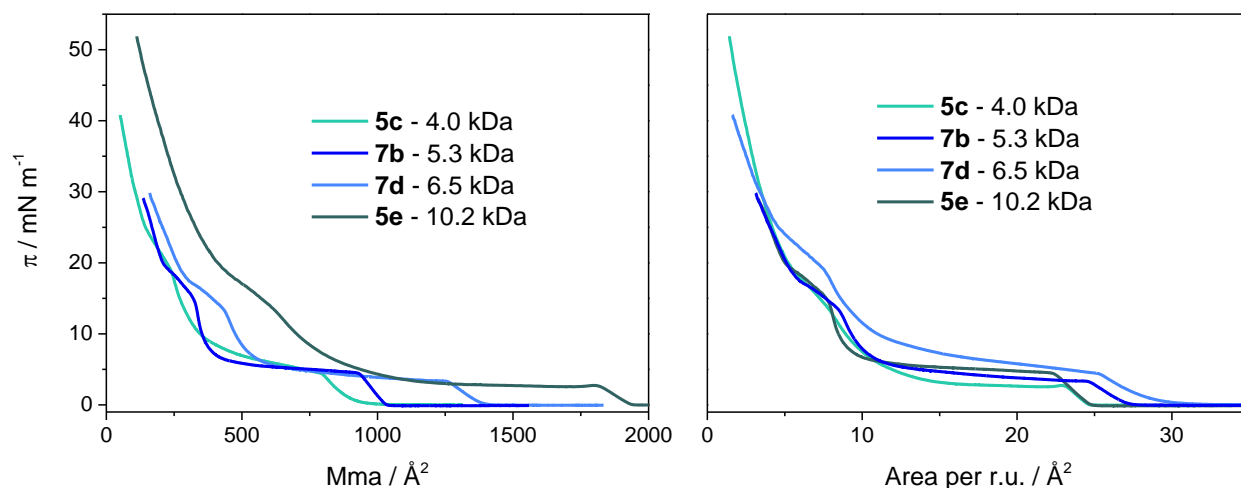


**Figure 39.**  $\pi$ -A-isotherms of PHICs of different molecular weights in regard to a) the mean molecular area b) the area per repeating unit of the polymer chain.

Monolayer compression isotherms were then conducted for the  $\beta$ -turn mimetic conjugates, bearing either one or two arms of PHIC. Due to the attachment of two polymer chains, the bi-functional conjugate shows a rise of surface pressure at much higher value than the mono-functional conjugate (see Appendix, Figure A24). In relation to the repeating unit this difference is vanishing and the limiting area is  $23\text{--}24 \text{ \AA}^2$  for both conjugates, as visible in Figure 40a. This value is lower than for the pure PHIC **5c**, but only a slight difference can be seen in regard to another pure polymer (**5d**). The second pseudo plateau is shifted to higher surface pressures for mono-functional conjugate **13-A** followed by a rapid increase in surface pressure, which is characteristic for the condensed state leading to the collapse at  $75 \text{ \AA}^2$  ( $2.1 \text{ \AA}^2/\text{r.u.}$ ) and

55 mN/m. Instead of a steep increase directly after the second pseudo plateau, bi-functional conjugate **15-A** shows a linear increase before reaching the condensed state. This linear region has been previously observed for PS-PEG copolymers and was attributed to a reorganization in a quasi-brush regime.<sup>[247]</sup> The collapse occurs at the same area per repeating unit ( $2.1 \text{ \AA}^2$ ) and a slightly lower surface pressure (51 mN/m) compared to the mono-functional conjugate.

PHIC-PEG copolymers were synthesized to investigate the influence of the length of the hydrophilic block on the behavior at the air / water interface and as a comparison to the rigid  $\beta$ -turn mimetic conjugates. Both conjugates **16-A** (TEG) and **17-A** (PEG) exhibit a rise in surface pressure at a similar area as the homopolymer, as illustrated in Figure 40b. However, the second rise of the surface pressure occurs at higher surface areas than for the homopolymers. This can be attributed to the complete submersion of the EO chains into the subphase, occurring at around 10 mN/m.<sup>[247-249]</sup>

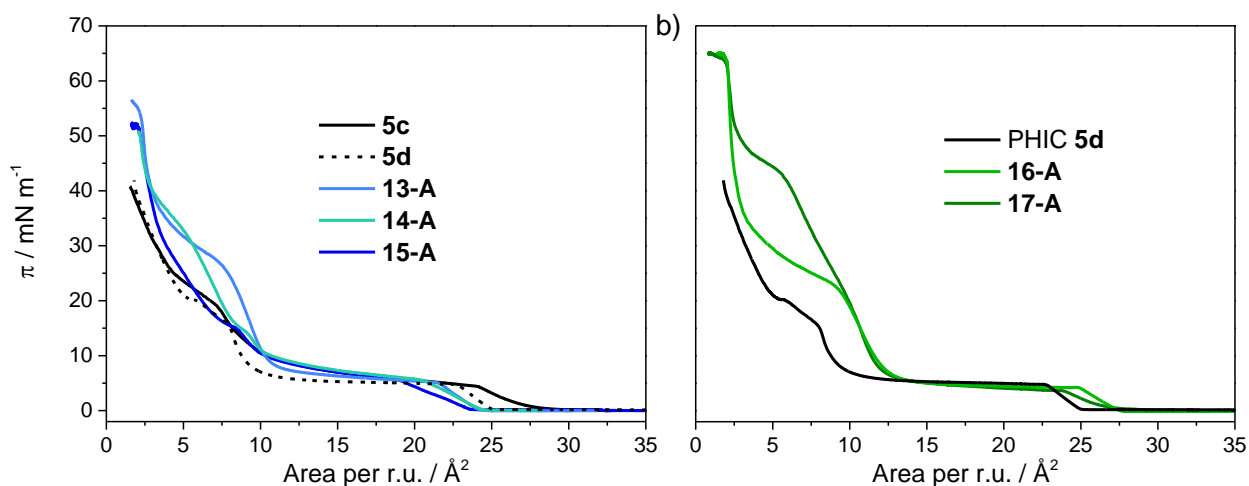


**Figure 40.**  $\pi$ -A-isotherms of a) achiral  $\beta$ -turn mimetic conjugates **13-A**, **14-A**, **15-A** in comparison to precursor polymer **5c** and b) TEG / PEG-copolymers **16** and **17** in comparison to precursor polymer **5d**.

Furthermore, the surface pressure at the second pseudo plateau is higher than the one observed for pure PHIC, indicating a higher stability of the films of these amphiphilic polymers at the surface, resulting from the anchoring due to the hydrophilic moiety. This effect is larger for the PEG conjugate ( $\pi \approx 45 \text{ mN/m}$ ) compared to the TEG conjugate ( $\pi \approx 28 \text{ mN/m}$ ), which matches to the value obtained for mono-functional BTM-conjugate **13-A** ( $\pi \approx 30 \text{ mN/m}$ ), indicating that the length of the hydrophilic chain influences the stability, while no difference occurs between a flexible and a rigid hydrophilic moiety. The collapse of both copolymers occurs at the same surface pressure ( $\pi \approx 65 \text{ mN/m}$ ) and area ( $2.0 \text{ \AA}^2/\text{r.u.}$ ). This is a further indication of the increased stability of the copolymers at the surface in contrast to PHIC.

Further measurements were conducted using mixtures of polymer-conjugates and DPPC. Figure 41 shows the  $\pi$ -A-isotherms of a mixture of DPPC with **13-A** and **17-A** in different ratios. The addition of conjugate **13-A** or copolymer **17-A** leads to a change in the plateau of DPPC corresponding to the phase transition from a liquid expanded to a liquid condensed

phase (LE / LC).<sup>[250]</sup> The plateau is shifted to both higher surface areas and higher surface pressures and is less pronounced than for pure DPPC. Upon further addition of **13-A** or **17-A**, the second pseudo plateau appears, similarly to the pure conjugates. As previously observed, this second pseudo plateau is at higher surface pressures for the PEG copolymer than for the BTD-conjugate.

When calculating the theoretical surface area occupied by the mixed systems, smaller experimental values occur for low amounts of added conjugate (< 20%), while the two values coincide at higher amounts. Thus, some favorable interactions between DPPC and the polymer conjugates may be present when adding a small amount, while at higher amounts phase separation between the two samples occurs.

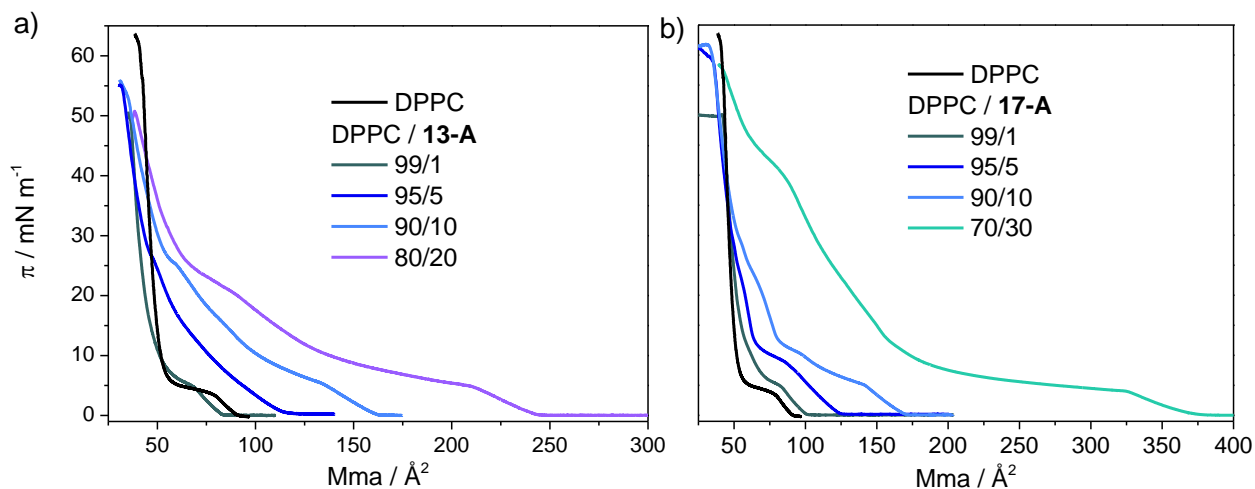
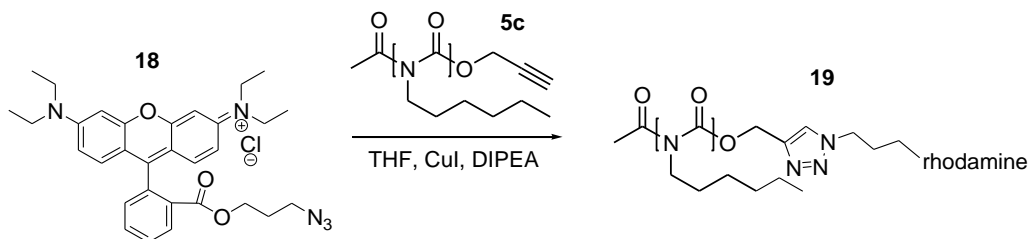


**Figure 41.**  $\pi$ -A-isotherms of mixtures of DPPC with a)  $\beta$ -turn mimetic conjugate **13-A** and b) PHIC-PEG copolymer **17-S**.

Epifluorescence measurements were conducted to obtain further insight in the behavior of the conjugates at the surface. The LE / LC phase transition of DPPC leads to a phase separation and the formation of domains, which can be visualized using a fluorescent dye. Mostly, phospholipid dyes were used in previous research.<sup>[239-240]</sup> However, these dyes possess a very different structure from PHIC and therefore a rhodamine-labeled PHIC (Rh-PHIC) was synthesized for better comparison (see Scheme 19). NMR-spectroscopy and MALDI-TOF-MS (see Appendix, Figure A25-28) proved the successful synthesis and purification of **19**.





**Scheme 19.** Synthesis of rhodamine-labeled PHIC (Rh-PHIC) **19**.

At very low surface pressures, the whole surface occurs bright, indicating a homogenous distribution of the dye around the surface. With increasing surface pressure small dark domains occur, due to the expulsion of the dye. While small spots, which grow in number, are visible for conjugates **13-A** and **15-A**, a more heterogeneous surface is visible for the pure PHIC **5c**, forming domains of different size and appearance. Thus, from a macroscopic view, the hydrophilic turn enhances the ability of PHIC to form a more homogeneous surface.

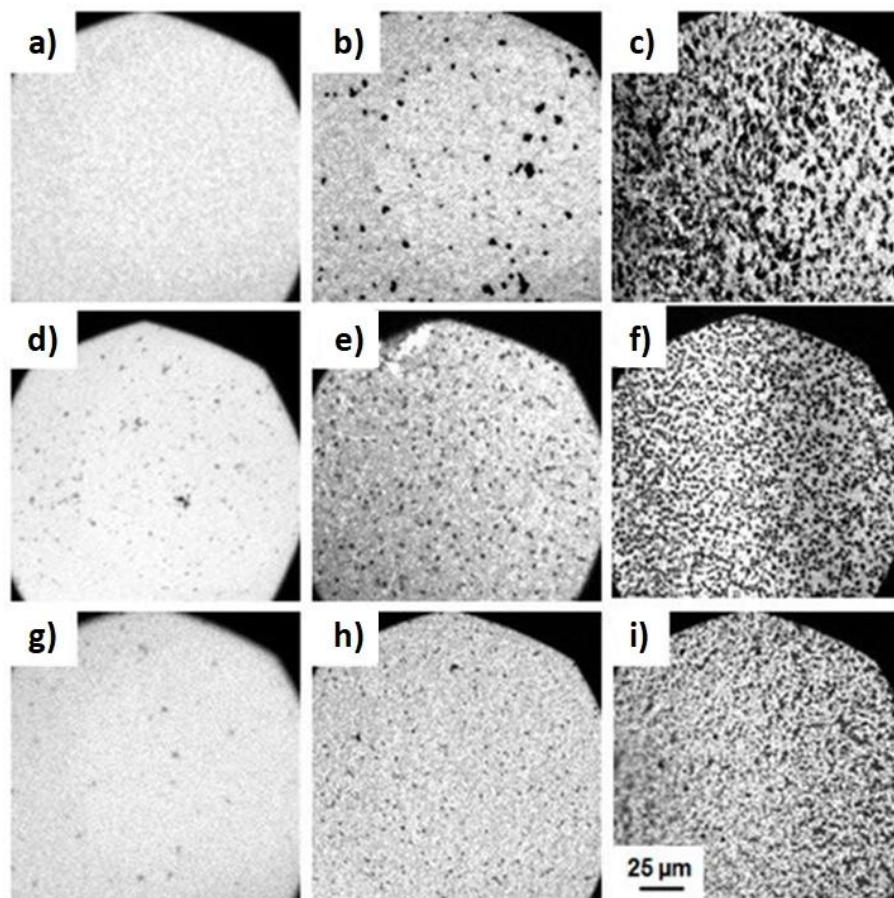
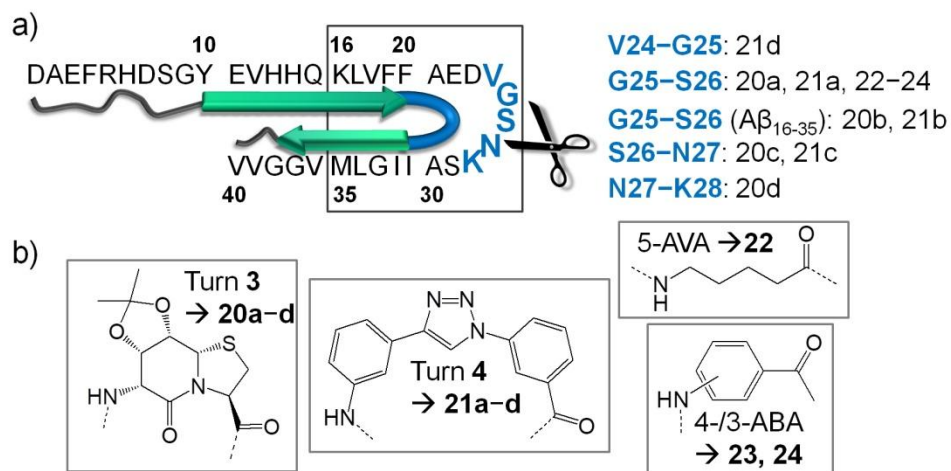


**Figure 42.** Epifluorescence microscopy images of monolayers of PHIC **5c** (a–c), **13-A** (d–f), **15-A** (g–i) at the air / water interface at 20 °C. Rh-PHIC was added for imaging (0.01 mol%). The images were recorded at constant compression of the spread monolayer at the following surface pressures: (a) 4.3, (b) 21.0, (c) 28.4, (d) 5.0, (e) 15.6, (f) 34.4, (g) 0.1, (h) 9.2, (i) 20.0 mN m<sup>-1</sup>. (Reprinted with permission from Ref<sup>[238]</sup>)

### 3.7 Synthesis of $\beta$ -turn mimetic peptide conjugates

In the scope of this thesis,  $\beta$ -turn mimetic peptides should be synthesized and investigated in regard to their ability to inhibit aggregation of  $A\beta_{40}$ , their influence on fibril structure and their toxicity. According to structural investigations using solid-state NMR,<sup>[91]</sup> the bend/loop region in  $A\beta_{40}$  is located around residues V24-A30. Therefore, different positions in this region from Val24-Lys28 were chosen to be replaced with the  $\beta$ -turn mimetics **3** and **4** as well as the linker molecules 5-AVA, and 3-/4-ABA.

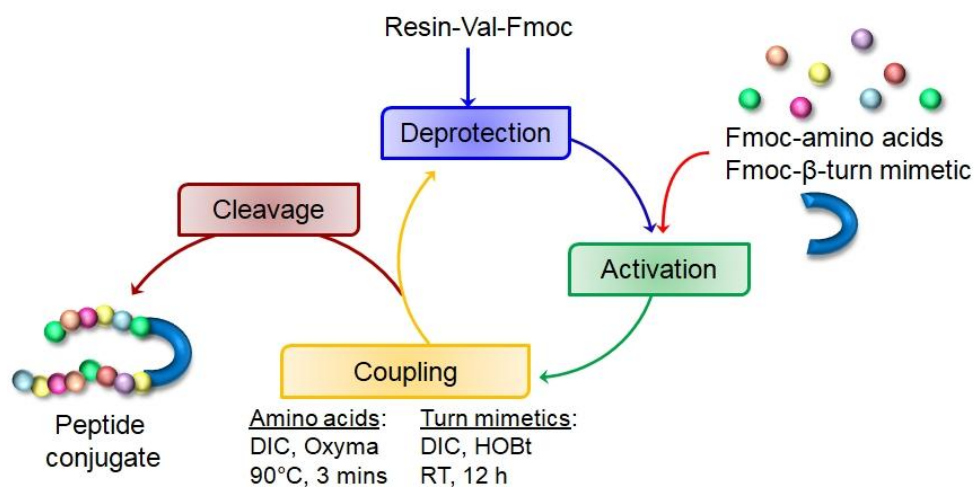
Different turn mimetics have been chosen based on several considerations. Turn mimetic **3**, with a rigid bicyclic structure, showed a good correlation with natural occurring  $\beta$ -turns.<sup>[185]</sup> Thus, this turn mimetic should result in a similar aggregation behavior as  $A\beta_{40}$  if a true  $\beta$ -turn structure is present during aggregation and in the final fibrillar structure of  $A\beta_{40}$ .  $\beta$ -Turn mimetic **4** should not fit as perfectly into the  $A\beta$  fibrils as the turn mimetic **3** and therefore changes along the aggregation are expected. Furthermore, the two small molecules 5-AVA and 4-ABA possess the same number of atoms in between the carbonyl group and the amine compared to turn mimetic **3**, however lacking any heteroatom in between. Thus, 5-AVA should act as a flexible linker which can fit into any conformation occurring during the aggregation process and should therefore be more likely to enhance aggregation, while 4-ABA serves as a rigid linker bearing the ability to provide inhibitory effects. 3-ABA is used as comparison, possessing a reduced distance between the carboxylic acid and the amine group.



**Scheme 20.** a) Representation of the  $A\beta_{40}$  sequence indicating the turn region in blue (V24-K28) and the replaced amino acids and corresponding peptide conjugates **20-24**. The black box indicates the short peptide  $A\beta_{16-35}$ . b) Structures of the turn mimetics **3**, **4**, 5-AVA, 3-/4-ABA in the peptide conjugates **20-24**.



$\beta$ -Turn mimetic peptides were synthesized by solid phase peptide synthesis (SPPS) as illustrated in Scheme 21. As SPPS is started from the carboxyl end (C-terminus) of the peptide, a copolymer resin linked to Fmoc-protected valine was used as solid support. After deprotection of the amine using piperidine in DMF, followed by a washing step using DMF, coupling of the neighboring Fmoc-protected amino acid is performed using *N,N*-diisopropylcarbodiimide (DIC) and oxyma at 90 °C, followed again by washing with DMF. These steps of deprotection, activation and coupling were repeated with single amino acids until the first peptide sequence was finished. Then, coupling with the Fmoc-protected  $\beta$ -turn mimetics was performed using HOBt and DIC and DMF as solvent and gentle stirring at room temperature for twelve hours. This adapted method assured complete modification, which was shown by MALDI-TOF-MS. Further elongation of the peptide was performed again *via* SPPS as described above. After the final step, the peptide is cleaved off from the solid resin using TFA, purified *via* preparative HPLC and analyzed *via* analytical HPLC and MALDI-TOF-MS.



**Scheme 21.** Synthetic pathway of  $\beta$ -turn mimetic peptide-conjugates and of  $A\beta_{1-40}$ .

Different positions of  $A\beta_{40}$  have been chosen to be exchanged with the synthetic  $\beta$ -turn mimetics **3** and **4**, together with other model compounds, namely 3-/4-aminobenzoic acid (ABA) and 5-aminovaleric acid (AVA), as comparison. In due course, the positions G25-S26 exhibited the most promising results and thus further modifications were performed at this position. Additionally smaller peptides were synthesized, containing only fragments of  $A\beta_{16-35}$  from K16 to M35. Thus, both  $\beta$ -sheet regions and the  $\beta$ -turn structure are still present, but the influence of the removed amino acids can be investigated. Furthermore, smaller peptides are useful as future drugs in contrast to a large peptide which only mimics the amyloid peptide. An overview of the synthesized peptide-conjugates is given in Table 8. The HPLC traces (see Appendix, Figure A29–31), revealed a purity higher than 95 % for all conjugates. Confirmation of the structure is obtained by MALDI-TOF-MS, as shown exemplary for entry **20a** in Figure 43 and for all other entries in the Appendix (see Figure A32–35). The major peak, appearing at a mass-to-charge ratio of 4357.400, matches with the simulation of the protonated structure of

the peptide ( $m/z = 4358.091$ ), while the double charged structure can also be assigned at  $m/z = 2179.796$ .

**Table 8.** Overview of synthesized  $\beta$ -turn mimetic peptide conjugates.

Entry	Replaced amino acids	Peptide sequence	Turn structure	$M_{th}$ [g mol <sup>-1</sup> ]	Isolated yield [mg]	Purity <sup>a</sup> [%]
<b>20a</b>	Gly25-Ser26	A $\beta_{40}$	<b>3</b>	4456.06	13.6	98.7
<b>20b</b>	Gly25-Ser26	A $\beta_{16-35}$	<b>3</b>	2235.44	4.4	96.3
<b>20c</b>	Ser26-Asn27	A $\beta_{40}$	<b>3</b>	4399.00	5.7	98.3
<b>20d</b>	Asn27-Lys28	A $\beta_{40}$	<b>3</b>	4357.91	8.0	98.4
<b>21a</b>	Gly25-Ser26	A $\beta_{40}$	<b>4</b>	4448.03	14.8	100
<b>21b</b>	Gly25-Ser26	A $\beta_{16-35}$	<b>4</b>	2227.46	5.0	95.8
<b>21c</b>	Ser26-Asn27	A $\beta_{40}$	<b>4</b>	4391.17	17.6	97.8
<b>21d</b>	Val24-Gly25	A $\beta_{40}$	<b>4</b>	4435.73	14.0	99.7
<b>22</b>	Gly25-Ser26	A $\beta_{40}$	5-AVA	4284.77	5.7	99.8
<b>23</b>	Gly25-Ser26	A $\beta_{40}$	4-ABA	4304.82	6.0	94.7
<b>24</b>	Gly25-Ser26	A $\beta_{40}$	3-ABA	4304.82	13.2	100

<sup>a</sup> Determined by analytical HPLC

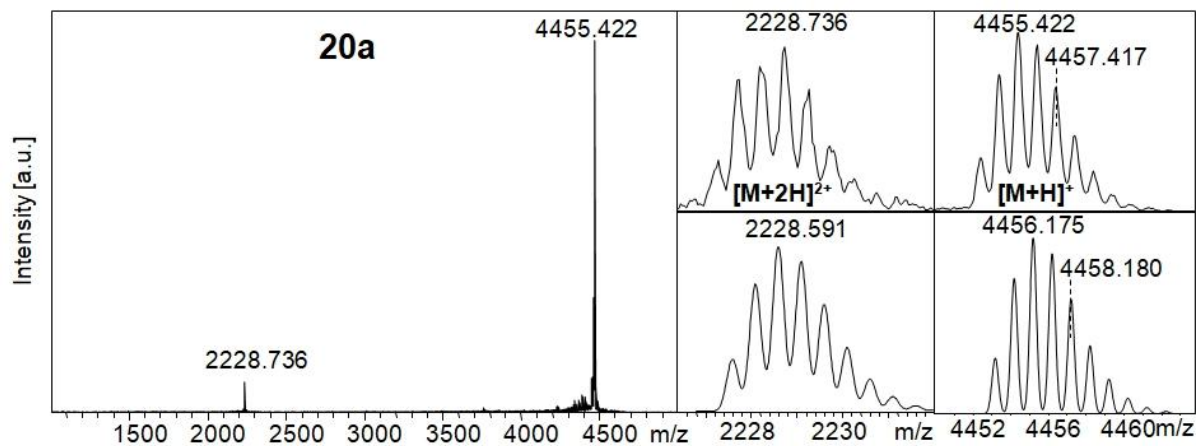


**Figure 43.** MALDI-TOF-MS of peptide-conjugate **20a**.

## 3.8 Structural investigations of $\beta$ -turn mimetic peptide conjugates

### 3.8.1 Aggregation studies of peptide conjugates in comparison with $A\beta_{40}$

Kinetic investigations of the fibril formation of  $A\beta_{40}$  conjugates were performed by thioflavin T assays. ThT is known to bind to fibril structures<sup>[251]</sup> and can thus be used to investigate the aggregation of wild type (WT)  $A\beta_{40}$  and of the peptide conjugates.

The ThT assays of pure  $A\beta$ -conjugates are shown in Figure 44. Three replicates were measured at the same time and the measurement was repeated at least once. For reason of clarity, only one representative curve per conjugate is presented and for those conjugates which exhibited a sigmoidal curve, fitting was performed and the fitted curves are displayed. For conjugates **21a**, **21c** and **24**, no sigmoidal curve was obtained and the curves are shown as measured. Conjugates **20a-d**, containing the bicyclic turn mimetic **3**, exhibit no fluorescence increase in the measured range of 40 hours, and hence the lack of aggregation can be assumed, which was subsequently confirmed by CD and TEM measurements (see chapter 3.8.4, 3.8.5). In contrast to this, TAA-conjugates **21a-d**, bearing the triazole aromatic turn mimetic **4**, exhibit a strong increase in fluorescence intensity after a short time, with differences in curvature and intensity occurring between the different positions. Conjugate **21c** displayed the most rapid aggregation without any lag time visible, whereas around one hour lag time was observed for all other TAA-conjugates.

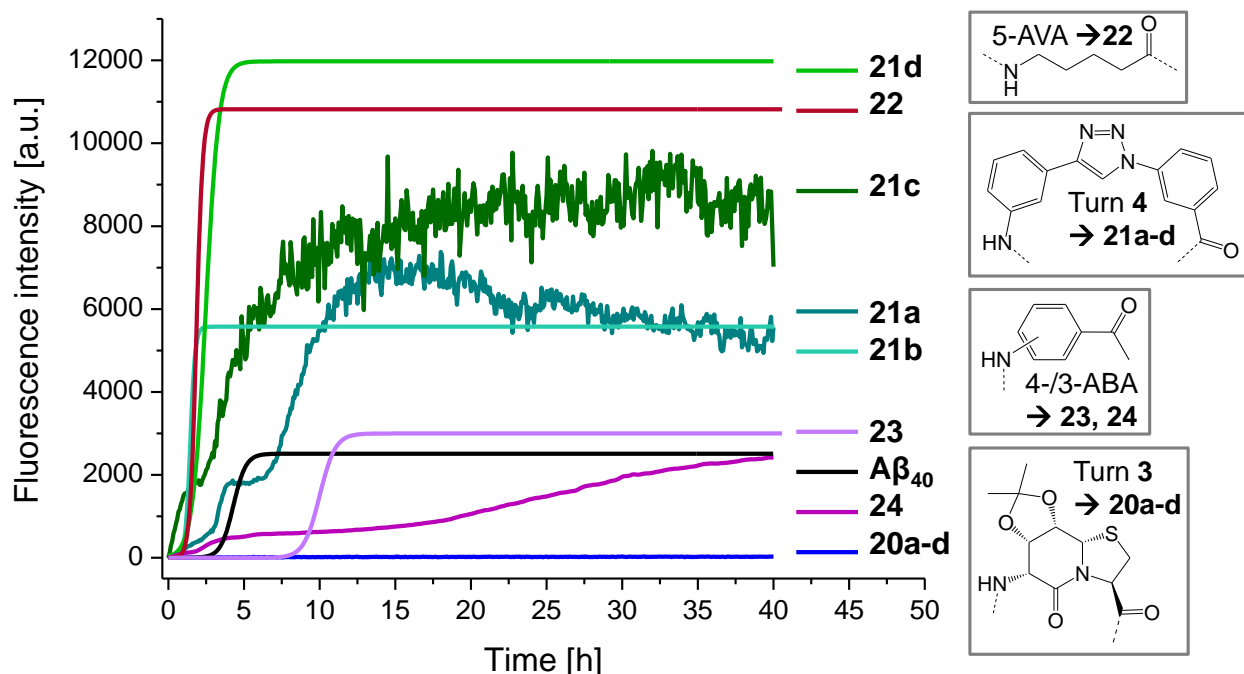


**Figure 44.** Aggregation kinetics for  $\beta$ -turn mimetic peptide conjugates **20–24** and wild type  $A\beta_{40}$ .

Peptides bearing 5-AVA (**22**), 4-ABA (**23**) and 3-ABA (**24**) turn mimetics displayed ambiguous behavior. Similar to conjugates **21d** and **21b**, the more flexible 5-AVA conjugate **22** exhibits a

fast fibrillation, whereas the more rigid ABA structure induces different fibrillation behavior depending on the benzyl-ring substitution. While 4-ABA conjugate **23** exhibits a sigmoidal curve with an increased lag time (~8 hours) compared to  $A\beta_{40}$ , the 3-ABA conjugate **24** displays a nearly constant increase in fluorescence intensity. Hence, it can be concluded that both the molecular structure of the turn mimetic and the position of replacement influence the aggregation kinetics. Further confirmation of the differences in aggregation was obtained by CD measurements, which were performed before and directly after the ThT assays, as well as by TEM images. These results will be discussed in chapter 3.8.4 and 3.8.5.

### 3.8.2 Aggregation studies of mixtures of $A\beta_{40}$ with peptide conjugates

To reveal whether or not these conjugates can also influence the fibrillation of WT  $A\beta_{40}$ , further investigations were carried out. Therefore, measurements of mixtures were performed using 10  $\mu\text{M}$   $A\beta_{40}$  and varying concentrations of the conjugates from 1 to 20  $\mu\text{M}$ . The first comparison will be drawn between two of the BTD-conjugates **20a** and **20d**, which were modified at positions G25-S26 and N27-K28 respectively. The corresponding ThT assays of mixtures are displayed in Figure 45.

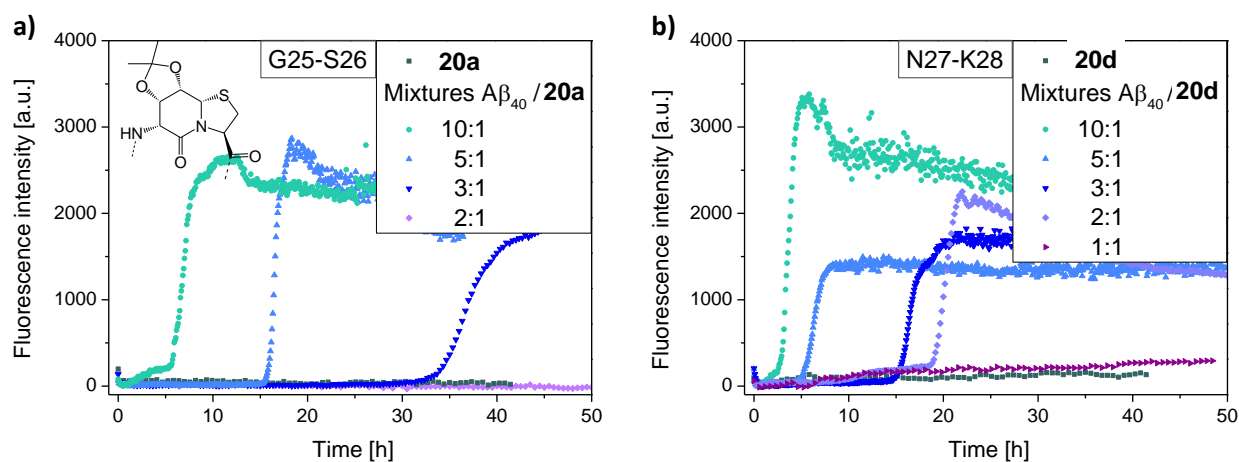


**Figure 45.** Aggregation kinetics for mixtures of  $A\beta_{40}$  with  $\beta$ -turn mimetic peptide conjugates a) **20a**, b) **20d**.

Figure 45b illustrates the influence of additional conjugate **20d** on the kinetic curves. While a concentration of only 1  $\mu\text{M}$  is not sufficient to inhibit fibrillation, increasing the amount of conjugate results in an increased lag time, which reaches more than 50 hours at a concentration of 8  $\mu\text{M}$ . Even a concentration which is less than equimolar is sufficient to increase the lag time by a factor of 10. This influence is even more pronounced using conjugate **20a**, where 0.3 to 0.5 equivalents are sufficient to inhibit fibrillation up to 50 hours, indicating that the turn location has a great effect on the kinetic behavior of  $A\beta_{40}$ . Conjugate **20c**, in which amino acids S26 and N27 were replaced, had a stronger influence on fibrillation than conjugate **20d**, but a lower effect than conjugate **20a**, as shown in the Appendix (Figure A36). In order to verify this effect

of different positions, ThT assays of TAA-conjugates in mixtures with  $A\beta_{40}$  were performed. Figure 46 shows a comparison between conjugate **21a** (replacing positions G25-S26) and **21d** (V24-G25). Conjugate **21d** exhibits a small inhibiting effect and thus an increase in lag time of about five hours in comparison to pure  $A\beta_{40}$  upon addition of 0.2–0.32 equivalents of the conjugate. However, when further increasing the amount of conjugate to 0.5 equivalents, a decrease in lag time and an increase in fluorescence intensity can be observed. Conjugate **21a** behaves similar, but to a different extent. While the addition of only 0.1 equivalents of the conjugate results in an increased lag time of more than 20 hours, further increasing the amount up to 0.32 equivalents has only a smaller impact on the lag time, which then reaches 35 hours. Similarly to conjugate **21d**, a different influence can be observed at a higher concentration of the conjugate. Again, the lag time decreases and furthermore the curvature changes from a sigmoidal curve to a transition with two plateau regions (1:1) in analogy to the pure conjugate **21a**. The behavior of the third TAA-conjugate Conjugate **21c** (S26-N27) is shown in the Appendix (Figure A36), revealing the weakest inhibition effect of all TAA-conjugates.

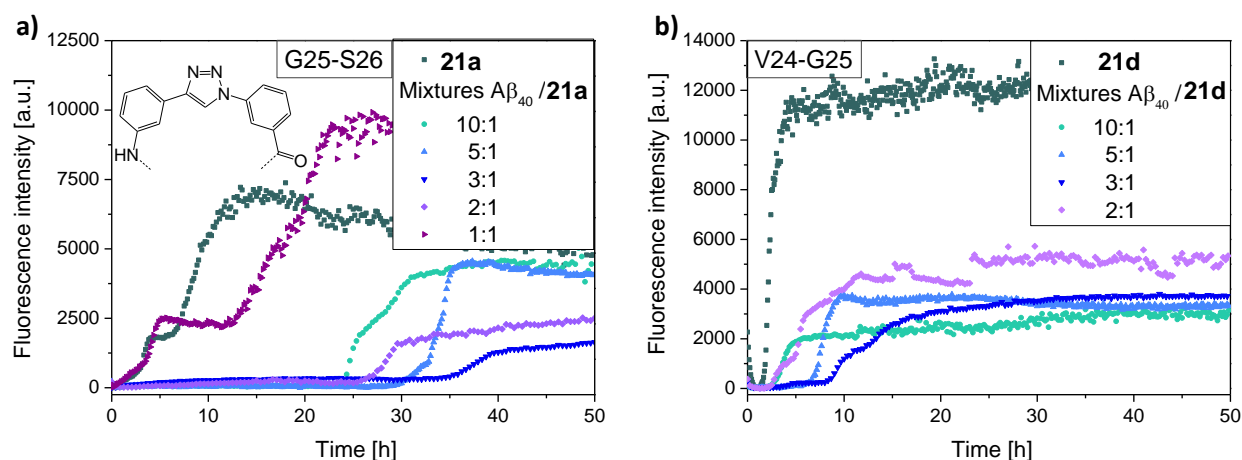


**Figure 46.** Aggregation kinetics for mixtures of  $A\beta_{40}$  with  $\beta$ -turn mimetic peptide conjugates a) **21a**, b) **21d**.

In conclusion, both peptide conjugates containing either of the two  $\beta$ -turn mimetics **3** and **4**, displayed the highest inhibiting effect upon replacing position G25 and S26. Previously, the impact of glycine 25 on the aggregation behavior of  $A\beta_{18-35}$  was investigated.<sup>[252]</sup> Removal of this small amino acid leads to a steric crowding in the turn region and hence an expanding of the hairpin structure. It was found that the deletion mutant formed oligomers with random coil structure instead of  $\beta$ -sheet and fibrils with anti-parallel  $\beta$ -sheet appeared only at high concentrations. This confirms that replacement of G25 can have a considerable effect on the aggregation of  $A\beta$ . Nilsson and co-workers<sup>[127]</sup> synthesized a modified  $A\beta_{42}$ , in which two or three amino acids in the turn region (25–27) were replaced by an azobenzene photoswitch. In contrast to the expectations, it was found that the *cis*-conformers showed no fluorescence increase in ThT analysis and that furthermore the cytotoxicity of these conformers was strongly reduced compared to  $A\beta_{42}$  and the *trans*-conformer. Thus, it was shown, that the turn structure is not necessarily required to form fibrillar and toxic structures. In another

investigation,<sup>[126]</sup> mutations of A $\beta$ <sub>40</sub> at positions 24–27 were synthesized by replacing two amino acids with D-ProGly, an effective  $\beta$ -hairpin inducing segment.<sup>[253]</sup> All three DPG variants showed an enhanced aggregation in ThT assays, confirming that pre-organization *via* turn formation can facilitate the fibril formation.

Consequently, three other A $\beta$  conjugates (**22-24**) with commercially available amino acids were synthesized, replacing amino acids G25-S26, to obtain a broader overview about the influence of rigidity or flexibility on the aggregation behavior.

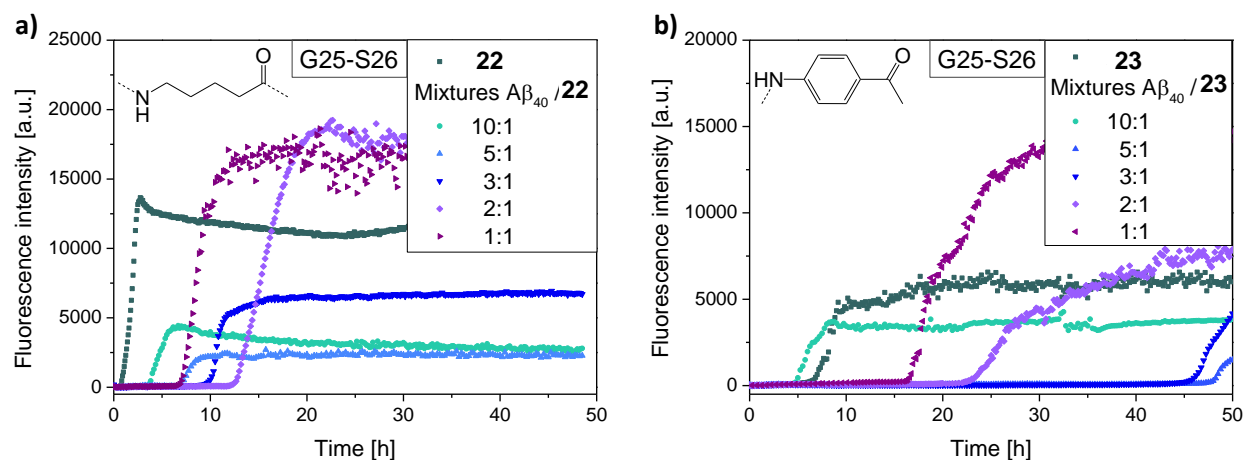


**Figure 47.** Aggregation kinetics of mixtures of A $\beta$ <sub>40</sub> and  $\beta$ -turn mimetic a) **22**, and b) **23**.

Peptide **22** exhibited a very short lag time (< 1 h; see Figure 47a) and thus favors the formation of the amyloid structure. This peptide contains 4-aminovaleric acid (4-AVA) as a flexible linker in the  $\beta$ -turn region, which facilitates the arrangement of the sequence and the formation of  $\beta$ -sheet structure. Upon addition of small amounts of this peptide to A $\beta$ <sub>40</sub> an increase in lag time can be observed, which reaches a maximum of around 12 hours when using 0.5 equivalents of **22**. However, further addition of the peptide results again in an enhanced fibrillation. ThT assays of conjugate **23** (see Figure 47b), bearing a rigid 4-aminobenzoic acid (4-ABA) linker exhibits a different behavior than peptide **22**. The fibrillation behavior of the pure conjugate is comparable to the one of pure A $\beta$ <sub>40</sub> possessing a lag time of around seven hours. Interestingly, addition of 0.33 equivalents of **23** to A $\beta$ <sub>40</sub> leads to an increase in lag time to 45 hours, therefore providing a strong inhibition effect, while a higher amount (0.5–1.0 equiv) again results in a reduced lag time. Thus, this conjugate behaves similar to **21a**, which also contains an aromatic turn mimetic. The last modification was performed with 3-aminobenzoic acid yielding peptide **24**, which only exhibited a weak inhibition effect (see Appendix, Figure A37).



### 3.8.3 Aggregation studies of mixtures of A $\beta$ <sub>40</sub> with short A $\beta$ <sub>16-35</sub> peptide conjugates

Having obtained these promising results, further modifications were performed at positions Gly25-Ser26. While the previously described conjugates consisted of the complete A $\beta$ <sub>40</sub> structure, two short peptides with a sequence of Lys16–Met35 were synthesized, to investigate whether this structure reduction can be performed without losing the positive inhibitory effects. The influence of short sequences of A $\beta$  comprising *e.g.* residues 1–16, 10–20 and 17–40 on A $\beta$ <sub>40</sub> aggregation was studied earlier. Therein it was found that short peptides containing residues 17–20 and 30–35 resulted in an enhanced fibrillation, revealing the importance of these fragments on A $\beta$ <sub>40</sub> aggregation.<sup>[254]</sup> Furthermore, a previous investigation showed that many biophysical properties remain unaffected in the central 18–35 fragment compared to A $\beta$ <sub>40</sub>.<sup>[255]</sup> In this work, the segment was further elongated by two amino acids to include the full K<sub>16</sub>LVFF<sub>20</sub> sequence, which is forming a core  $\beta$ -strand structure and is thus critical for the aggregation of A $\beta$ .<sup>[89]</sup> Nordstedt *et al.* revealed that a short KLVFF peptide can bind to the  $\beta$ -sheet region of A $\beta$ <sub>40</sub> and thus inhibits the aggregation.<sup>[256-257]</sup> Therefore, this sequence has been intensely studied and various modifications have been performed to develop a potent A $\beta$  aggregation inhibitor.<sup>[258-261]</sup> Modeling studies of A $\beta$ <sub>16-35</sub> proposed a bent hairpin-like conformation with Gly-25 and Ser-26 located at the edge of the bent, matching with the synthesized structures in this work.<sup>[262]</sup>

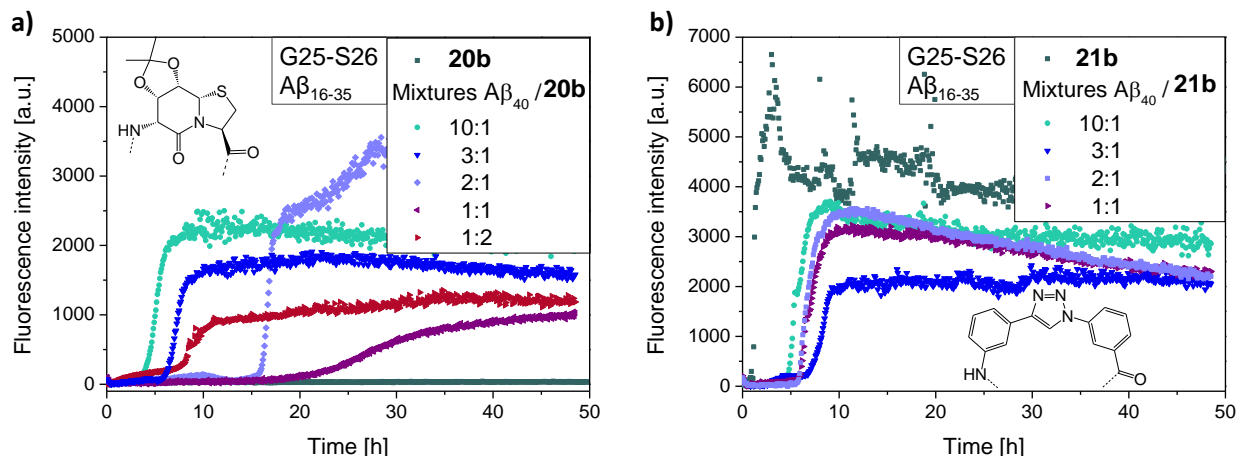


**Figure 48.** Aggregation kinetics of mixtures of A $\beta$ <sub>40</sub> and a) **20b**, b) **21b**.

Figure 48 shows the ThT-curves for the mixtures of A $\beta$ <sub>40</sub> and the short peptide conjugates **20b** and **21b**. The TAA-conjugate **21b** exhibits a strong increase in fluorescence intensity after a very short lag time of about one hour, while the BTD-conjugate **20b** does not show any fluorescence in the course of 50 hours and thus their behavior correlates to their full-length A $\beta$ <sub>40</sub> analogue. Regarding the mixtures with A $\beta$ <sub>40</sub> differences can be observed. The short TAA-conjugate **21b** bearing the triazole aromatic  $\beta$ -turn 4 shows no inhibitory effect, reaching a maximum lag time of only seven hours upon addition of 0.3 equivalents, which is contrary to

its full-length analogue. However, a different effect is observed using conjugate **20b** containing the bicyclic  $\beta$ -turn mimetic **3**. Mixtures containing 0.5–1.0 equivalents of **20b** show an increased lag time, reaching a maximum of 20 hours. As previously observed, this positive effect is reduced upon further increasing the ratio of conjugate to  $A\beta_{40}$  to 2:1. Besides an increased lag time for a 1:1 mixture, reduced fluorescence intensity occurs, indicating the successful inhibition of aggregation. This will be further discussed with additional CD spectra in chapter 3.8.4.

The obtained results are summarized by plotting the aggregation half time ( $t_{1/2}$ ) versus the ratio of  $A\beta_{40}$  to the different conjugates as shown in Figure 49. Aggregation investigations of the pure conjugates clearly prove the influence of turn structure on the aggregation propensity. While conjugates **20a-d** containing the bicyclic turn moiety **3** with a clearly defined turn structure exhibit lack of aggregation over at least 50 hours, implementation of aromatic turn mimetic **4** and of 5-AVA with higher flexibility lead to the inverse effect, increasing the rate of aggregation in conjugates **21a-d** and **22**. In between these two extremes, the rigid aromatic linker 4-ABA results in a retardation of aggregation for conjugate **23**. Furthermore, the influence of substitution position was demonstrated upon investigation of mixed systems, which revealed that replacement of position Gly25-Ser26 in conjugates **20a** and **21a** was most effective within the four different positions studied in this work. Conjugates **21a** and **23** showed the best inhibition properties when used in low amounts (2–3  $\mu\text{M}$ ).

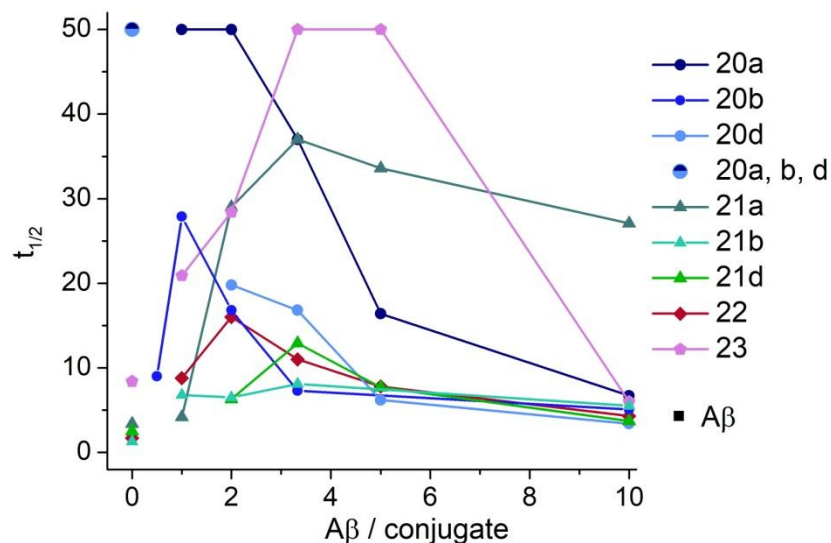


**Figure 49.** Overview about characteristic times  $t_{1/2}$  for the aggregation of  $\beta$ -turn mimetic peptide conjugates and mixtures with  $A\beta_{40}$ .  $A\beta_{40}$  concentration is 10  $\mu\text{M}$  and conjugate concentration varies from 1 to 20  $\mu\text{M}$ .



### 3.8.4 Circular dichroism studies of peptide conjugates (20–24)

CD spectroscopy is a useful tool to investigate the secondary structure of peptides, as distinct maxima and minima appear for random coil,  $\alpha$ -helix and  $\beta$ -sheet structures. Random coil structure is characterized by a local minimum around 195 nm,  $\alpha$ -helix by two local minima around 222 and 208 nm together with a local maximum near 193 nm and  $\beta$ -sheets exhibit a local minimum at 218 nm and a local maximum around 195 nm.<sup>[263-264]</sup> Therefore, solution investigations of the secondary structure of  $A\beta_{40}$  and of the peptide-conjugates were carried out using CD.

First, different conditions for the disaggregation and monomer formation of the peptide conjugates were probed, to find optimized starting conditions for the ThT assays. Disaggregation of the peptides was probed in phosphate buffer (50 mM) at pH 9.1<sup>[265-266]</sup> and in NaOH (10 mM)<sup>[267-269]</sup> at pH 10.5, which were previously described as suitable disaggregation conditions for  $A\beta_{40}$  in preparation for ThT assays. The disaggregated peptide-conjugates should exhibit characteristic random coil spectra, while  $\beta$ -sheet signals should appear upon fibril formation.  $A\beta_{40}$  was effectively disaggregated in phosphate buffer at pH 9.1, indicated by a random coil CD spectrum (see Figure 50a), whereas  $\beta$ -sheet secondary structure appeared for the more hydrophobic TAA-conjugates (**21a–d**), implying that they were not successfully disaggregated. The spectra of BTD- and 4-AVA-conjugates (**20a–d**, **22**) appeared as random coil structure at pH 9.1, but with a slightly reduced signal intensity compared to  $A\beta_{40}$ . Hence, dissolution in 10 mM NaOH was probed as alternative disaggregation procedure and proved to be effective, as revealed by characteristic random coil CD spectra for all conjugates (see Figure 50b).

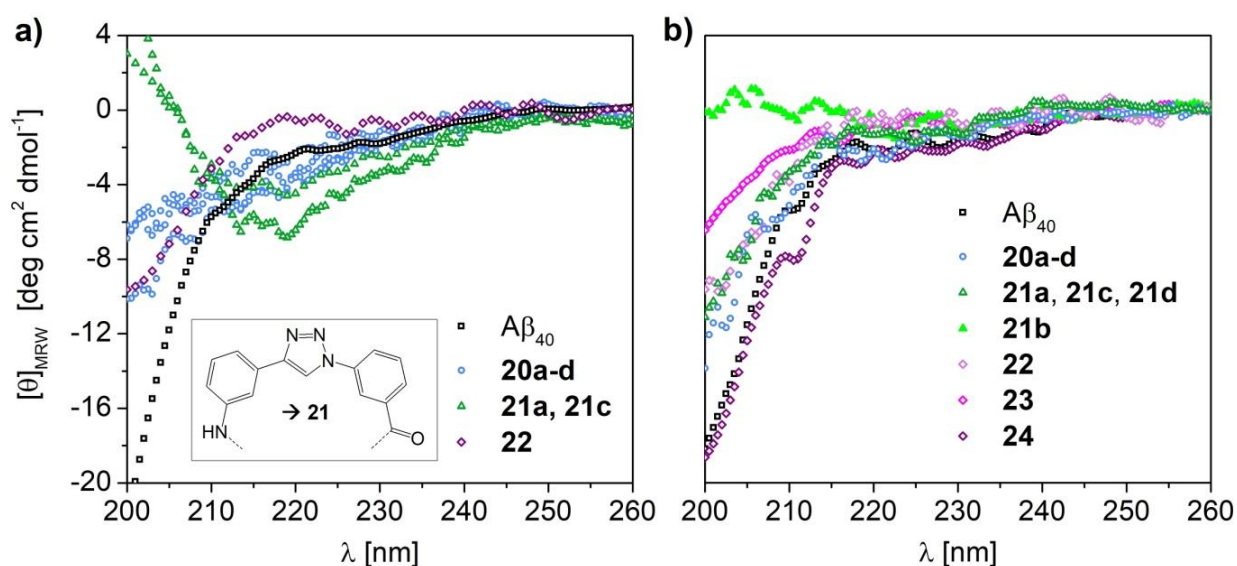


**Figure 50.** CD spectra of WT  $A\beta_{40}$  and of peptide-conjugates **20–24** in a) phosphate buffer (50 mM), b) NaOH (10 mM).

Interestingly, conjugate **21b** with a short peptide chain ( $A\beta_{16-35}$ ) exhibited a spectrum coinciding with the baseline, which might originate from overlapping  $\beta$ -sheet and random coil spectra. Thus, oligomeric structures cannot be excluded in this case, which might explain the fast aggregation observed in the ThT assays of this conjugate. In order to investigate whether different disaggregation protocols result in different fibrillation curves, preliminary ThT assays were carried out using WT  $A\beta_{40}$ . Only slight differences in the characteristics of kinetic curves, such as lag time, were observed between the samples disaggregated at pH 9.1 and pH 10.5 (see Appendix, Figure A38), thus confirming the usability of the pretreatment procedure.

CD spectra after aggregation were measured directly from the samples in the microwell plate used for ThT assays. Figure 51 shows the CD spectra obtained for  $A\beta_{40}$  as well as for different conjugates, clearly indicating  $\beta$ -sheet secondary structure for the former, with a local minimum at 218 nm and a maximum around 200 nm. Since the samples were measured in 50 mM sodium phosphate buffer, it was not possible to measure below 200 nm as the voltage strongly increased. As it was anticipated from the low fluorescence intensity, BTM-conjugates (e.g. **20a**) exhibited the same random coil structure as before fibrillation and no indication of  $\beta$ -sheet secondary structure was observed. This was also found for the small peptide conjugate **20b**.

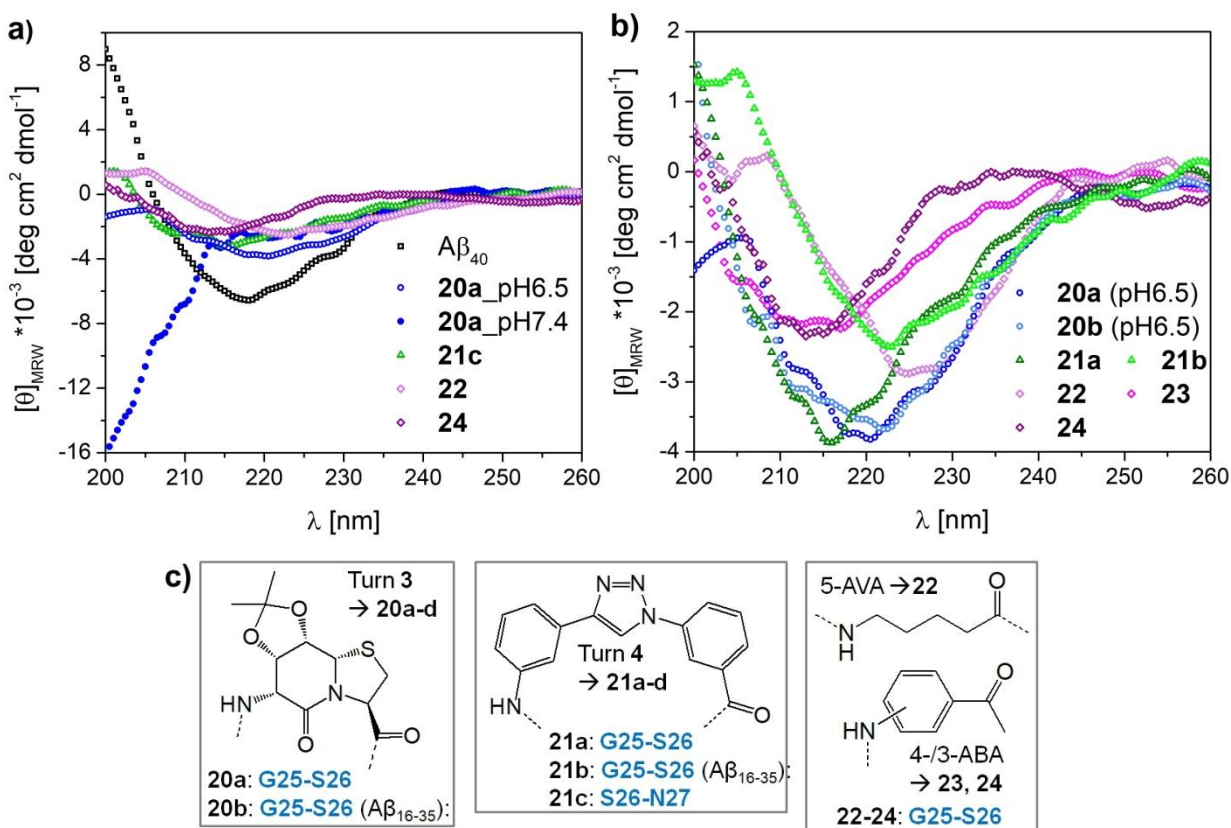


**Figure 51.** a) and b) CD spectra of  $A\beta_{40}$  and of peptide conjugates after fibrillation and c) the corresponding structures of  $\beta$ -turn mimetics and substitution positions.

Nevertheless, it was possible to obtain fibrils of these peptides at lower pH 6.5 and higher salt- (500 mM NaCl) and peptide-concentrations (100  $\mu$ M), which then exhibited a characteristic minimum for  $\beta$ -sheet around 220 nm, with a lower intensity as for the WT. Full-length peptide **20a** and short peptide **20b** modified at the same position then exhibited a similar CD spectrum (Figure 51b). Also in accordance with the ThT assays, CD spectra of TAA-conjugates (e.g. **21c**) indicated  $\beta$ -sheet secondary structure. The minimum is slightly shifted to lower wavelength around 216 nm and the intensity is comparable to the one of BTD-conjugates. Additionally, also the short TAA-mimetic peptide **21b** exhibited a  $\beta$ -sheet secondary, with a slightly shifted minimum to 222 nm. Conjugates **23** and **24** bearing a rigid aminobenzoic acid linker with different substitution positions, exhibited a similar spectrum with a minimum around 214 nm, reaching only a lower value than the one for TAA-conjugates. Incorporation of the most flexible linker 5-aminovaleric acid (**22**) results in a shift of the minimum to higher wavelength around 226 nm. Thus, the rigidity of the linker around the turn positions influences the formed  $\beta$ -sheet secondary structure.

Besides the pure conjugates, further investigations were conducted using mixtures with  $A\beta_{40}$ . Two examples will be discussed below (see Figure 52). Mixtures of 4-ABA conjugate **23** and  $A\beta_{40}$  exhibit  $\beta$ -sheet secondary structure in all ratios, in correlation with the ThT assays which showed aggregation for all mixtures. However, the fluorescence intensity cannot be correlated with the intensity observed in the CD spectra. A slight shift of the minimum from around 218 nm for  $A\beta_{40}$  to 215 nm for the mixtures containing more than 3  $\mu$ M of the conjugate can be observed. This value is identical with the one of pure conjugate **23**, thus possessing a stronger influence on the structure than  $A\beta_{40}$ . The mixtures of short BTD-peptide **20b** show a different behavior. While  $\beta$ -sheet secondary structure is clearly visible at a ratio of 2:1, a structural change occurs at ratio of 1:1 and 1:2, with a shift of the minima to around 205–208 nm, indicating the presence of helical content and hence a change in the fibrillar structure.

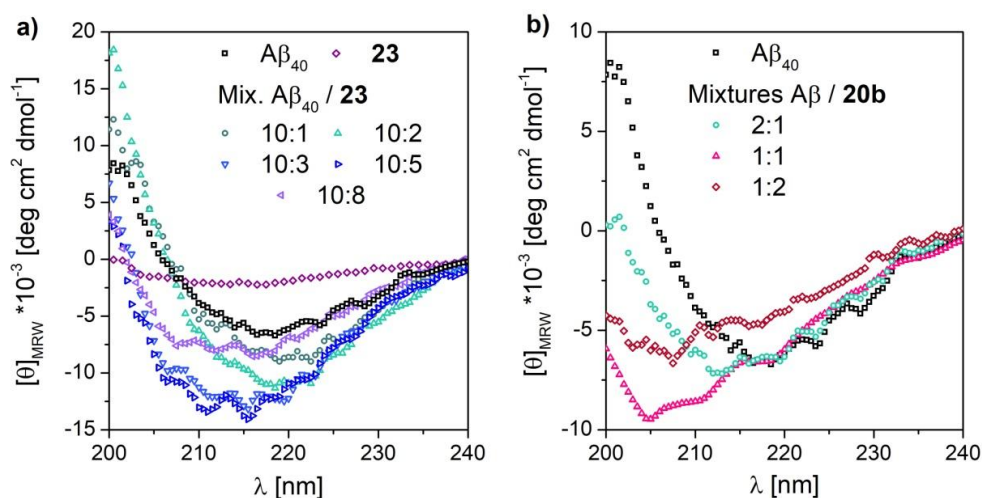


**Figure 52.** CD spectra of a) mixtures of 4-ABA conjugate **23** with  $A\beta_{40}$  and b) mixtures of short BTD-conjugate **20b** with  $A\beta_{40}$  after fibrillation.

### 3.8.5 TEM measurements

With the results of ThT assays and CD measurements, which provided information about aggregation and  $\beta$ -sheet formation, TEM measurements were performed to reveal the fibrillar structure of aggregated peptides. The TEM images of BTD-conjugates **20a** (see Figure 53a), **20c** and **20d** (see Appendix, Figure A39) showed the absence of any fibrillar structure, which supports the findings from ThT assays and CD spectroscopy, proving the lack of aggregation propensity for conjugates bearing the bicyclic BTD-turn mimetic under the used conditions.

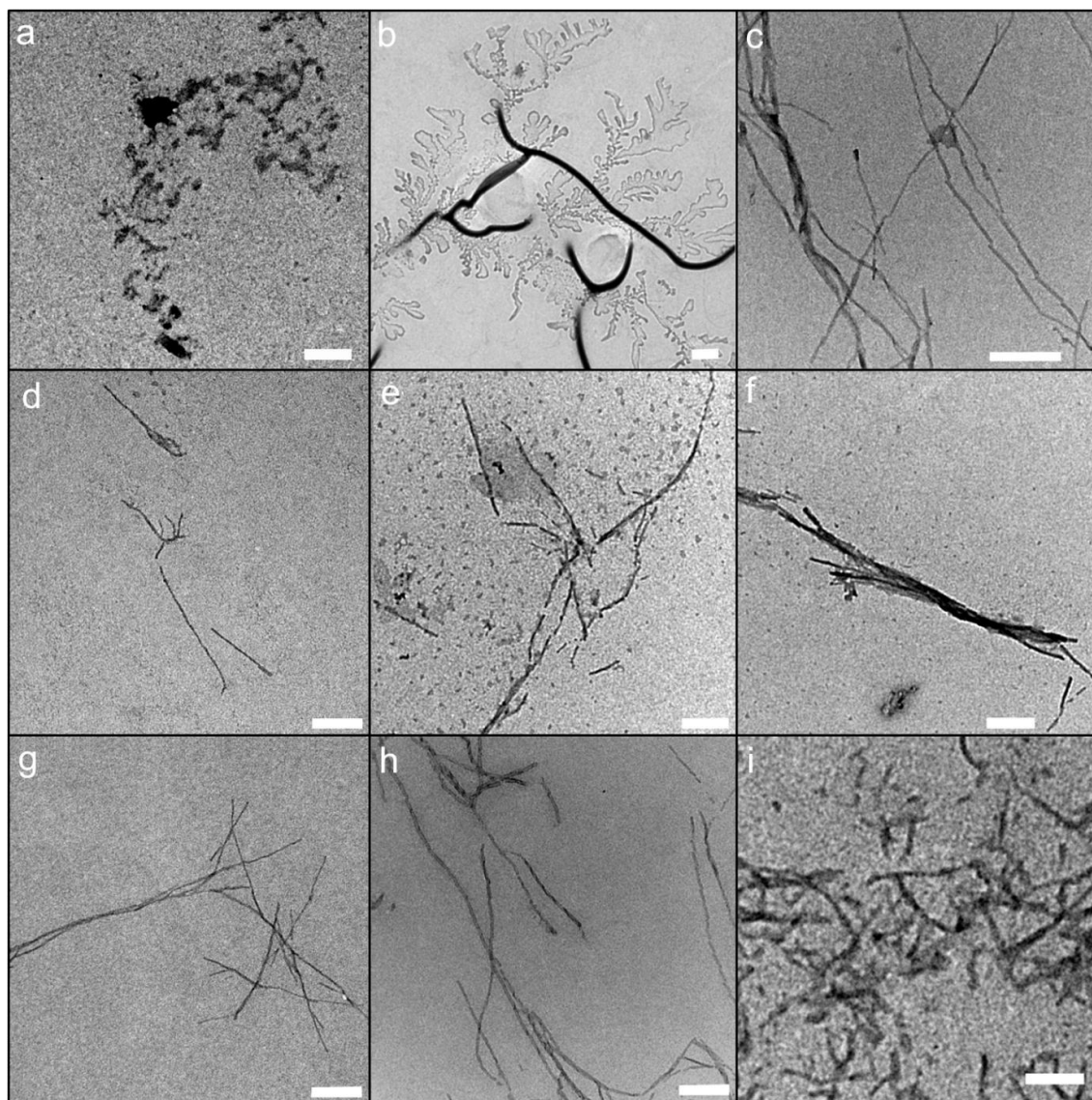


**Figure 53.** TEM images of pure  $\beta$ -turn mimetic conjugates after fibrillation. Scale bars indicate 250 nm (a, c-i) or 500 nm (b). a) **20a** after fibrillation at pH7.4, b) **20a** after fibrillation at pH6.5, c)  $A\beta_{40}/\mathbf{20a}$  10:3, d) **21a**, e), f) **21b**, g) **22**, h) **23**, i) **24**.

When using different fibrillation conditions (pH 6.5, 500 mM NaCl), aggregation and the formation of  $\beta$ -sheet secondary structure was observed as shown by CD for **20a** and the corresponding short peptide **20b**. However, only for **20a** TEM images of fibrillar like structure were obtained, possessing a ten-fold larger diameter compared to all other peptides (Figure 53b, Table 9). Additionally, smaller leaf-like structures can be observed, growing from the large fibrillar core. Conjugates **21a**, **21b**, **22** and **23** show fibrils similar to the ones of  $A\beta_{40}$ , with diameters ranging from 8.0 nm (**21a**) to around 14.5 nm (**21b**, **23**) and lengths of several hundred nanometers up to around 3–5  $\mu$ M ( $A\beta_{40}$ , **22**). In contrast, fibrils formed by conjugate **24** appear very short, with a small diameter.

A comparison between mixtures of  $A\beta_{40}$  with conjugate **20b** in a ratio of 2:1 and 1:1 revealed an influence of additional conjugate on the fibrillar structure as already seen in the ThT assays and CD spectra. Upon addition of 0.5 equivalents of conjugate, the diameter of the resulting fibrils stayed around the same value (11.1 nm ( $A\beta_{40}$ ); 11.4 nm (2:1)), whereas it increased to 14.4 nm at a 1:1 ratio. This indicates that the conjugate is embedded into the fibrils of  $A\beta_{40}$  leading to increase fibril thickness.

**Table 9.** Comparison of fibril diameters of  $A\beta_{40}$ , peptide conjugates and mixtures thereof obtained *via* TEM imaging.

Peptide	Thickness [nm]	Peptide	Thickness [nm]	Peptide	Thickness [nm]
$A\beta_{40}$	11.1 $\pm$ 1.8	<b>20a_pH6.5</b>	107 $\pm$ 25	<b>22</b>	10.8 $\pm$ 1.8
$A\beta_{40}$ / <b>20b</b> 1:1	14.4 $\pm$ 1.5	<b>21a</b>	8.0 $\pm$ 1.0	<b>23</b>	14.7 $\pm$ 1.2
$A\beta_{40}$ / <b>20b</b> 2:1	11.4 $\pm$ 1.5	<b>21b</b>	14.5 $\pm$ 1.7	<b>24</b>	8.8 $\pm$ 0.9

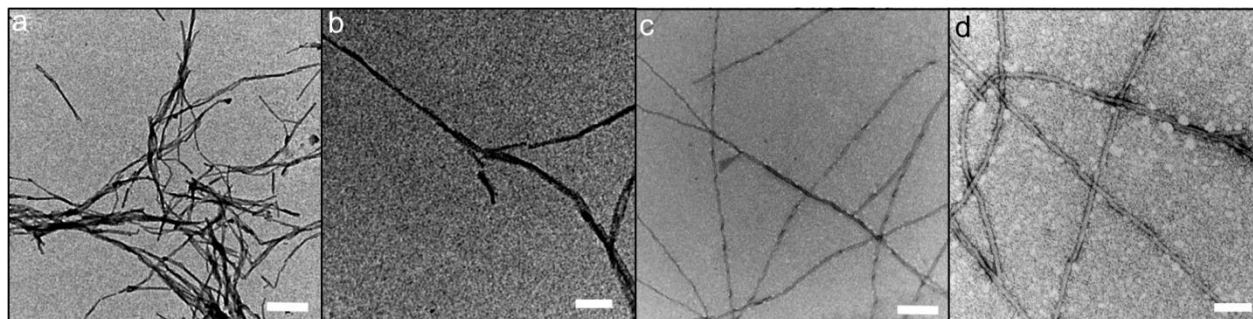


**Figure 54.** TEM images of mixtures of  $A\beta_{40}$  and  $\beta$ -turn mimetic conjugate **20b** after fibrillation. Scale bars indicate 250 nm (a-c) or 100 nm (d). a), b) 2:1  $A\beta_{40}$  / **20b**, c), d) 1:1  $A\beta_{40}$  / **20b**.



### 3.8.6 Cytotoxicity assay

In order to assess whether modification of the turn region has an impact on the toxicity of the peptides, cytotoxicity assays were performed. Therefore, Neuro2a (N2a) cells, a mouse neuroblastoma cell line which is commonly used for amyloid cytotoxicity investigations,<sup>[270-272]</sup> were exposed to the synthesized peptides and  $A\beta_{40}$  in comparison. All samples were applied both in their disaggregated, monomeric state<sup>[273-274]</sup> and as mature fibrils, which were generated beforehand according to previously described methods,<sup>[275-276]</sup> and cell viability was determined after 72 hours using the MTT assay.

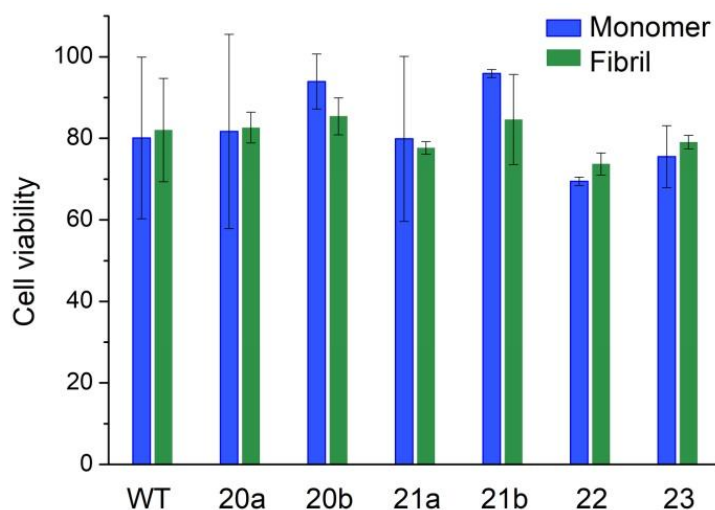


**Figure 55.** Cell viability (N2a cells) in response to treatment with  $A\beta_{40}$  and artificial peptides **20a**, **20b**, **21a**, **21b**, **22**, **23** as monomeric or fibrillar samples (20  $\mu$ M).

As shown in Figure 55, the cell viability of N2a cells after 72 hours exposure to the peptides, revealed no clear difference between monomeric and fibrillar samples on the one hand and the different peptides on the other hand. The highest toxicity was observed for conjugate **22**, containing the flexible linker 5-AVA, while the lowest toxicities are observed for both short peptides bearing only the  $A\beta_{16-35}$  sequence (**20b**, **21b**). Previous investigations showed that short  $A\beta$  peptides exhibit different toxicity depending on their truncation. While  $A\beta_{17-42}$ , derived from the more cytotoxic  $A\beta_{42}$ , resulted in higher cell death than  $A\beta_{40}$ , the segment of  $A\beta_{1-16}$  resulted in low cell death, indicating the importance of the central core for aggregation and toxicity of Amyloid  $\beta$  proteins.<sup>[277]</sup> This was further confirmed by investigations of  $A\beta_{25-35}$ , exhibiting even a slightly higher cell death rate than  $A\beta_{42}$ .<sup>[278]</sup> Regarding all investigated samples, only 10-30 % cell death was detected. This is consistent with similar investigations, showing that  $A\beta_{40}$  and its mutations exhibit only low cytotoxicity when applied as monomeric or fibrillar samples, while a much higher toxicity was observed when oligomeric samples were used.<sup>[270-271]</sup> As the synthesized artificial peptides all show largely different aggregation behavior, finding a defined oligomeric state which is comparable for all conjugates is challenging and is thus an open topic for further investigations.

## 4 Experimental part

### 4.1 Materials and methods

All solvents were purchased in technical grade and were distilled prior to use. Dichloromethane (DCM) and pyridine were predried over KOH and freshly distilled over CaH<sub>2</sub> under nitrogen atmosphere before used. Tetrahydrofuran (THF) was predried over KOH and freshly distilled over sodium and benzophenone under nitrogen atmosphere before use. Toluene was dried over sodium and freshly distilled over sodium and benzophenone under nitrogen atmosphere before used. *N,N*-Dimethylformamide (DMF), methanol (MeOH), acetonitrile (MeCN) and triethylamine were freshly distilled over CaH<sub>2</sub> under nitrogen atmosphere before used.

L-Cysteine methyl ester hydrochloride, sodium azide, palladium on charcoal, sodium nitrite, *N,N*-diisopropylethylamine (DIPEA), magnesium sulfate, *n*-hexyl isocyanate, 2-chloroethyl isocyanate, triethylamine, diphenyl phosphoryl azide (DPPA), sodium (in mineral oil), *p*-toluenesulfonyl chloride, copper(I) iodide (CuI), propargyl alcohol, trifluoroacetic acid (TFA), *N,N*-dicyclohexylcarbodiimide, *N,N*-dimethylaminopyridine (DMAP), calcium hydride and sodium ascorbate were purchased from Sigma Aldrich. Trifluoromethanesulfonic anhydride (Tf<sub>2</sub>O), 3-bromo-1-propanol and benzyl azide were received from Alfa Aesar. 2-Iodoxybenzoic acid (IBX) and Fmoc-*N*-hydroxysuccinimide ester (Fmoc-OSu) were purchased from Fluorochem. Sodium sulfate, Ce(SO<sub>4</sub>)<sub>2</sub>·4H<sub>2</sub>O, (NH<sub>4</sub>)<sub>6</sub>Mo<sub>7</sub>O<sub>24</sub>·4H<sub>2</sub>O and copper(II) sulfate pentahydrate were purchased from VEB, *N,N*-Dimethylformamide (DMF), sodium hydroxide, hydrochloric acid, ammonium chloride and acetic anhydride were received from Gruessing, (*R*)- and (*S*)-3-butyn-2-ol from TCI, D-glucurono-3,6-lactone from Fluka, pyridine from Acros Organics, lithium hydroxide from Lachema and benzophenone from Reachim. All these chemicals were used without further purification unless the following ones. Propargyl alcohol and *n*-hexyl isocyanate were stored over CaH<sub>2</sub> under nitrogen atmosphere and freshly distilled under vacuo before use.

All ***nuclear magnetic resonance*** (NMR) spectra were recorded on a Varian Gemini 400 or 500 spectrometer (400 MHz or 500 MHz) at 27 °C in CDCl<sub>3</sub> (Chemotrade, 99.8 Atom%D), DMSO-*d*<sub>6</sub> (Chemotrade, 99.8 Atom%D) or CD<sub>3</sub>OD (Chemotrade, 99.8 Atom%D). Chemical shifts are given in ppm and referred to the solvent residual signal (CDCl<sub>3</sub>: 7.26 ppm for <sup>1</sup>H and 77.0 ppm for <sup>13</sup>C; DMSO-*d*<sub>6</sub>: 2.50 ppm for <sup>1</sup>H and 39.5 ppm for <sup>13</sup>C; CD<sub>3</sub>OD: 3.31 ppm for <sup>1</sup>H and 49.0 ppm for <sup>13</sup>C). MestReNova 6.0.2-5475 was used for data interpretation.

***Attenuated total reflection infrared spectroscopy*** (ATR-IR) measurements were performed on a Bruker Tensor VERTEX 70 equipped with a Golden Gate Heated Diamond ATR Top-plate. Opus 6.5 was used for analyzing data.

***Gel permeation chromatography*** (GPC) was performed on a Viscotek GPCmax VE 2002 using a column set of CLM3008 and CLM3011 columns in THF at a constant column temperature of 30 °C and a constant flow rate of 1 mL/min. Detection was carried out by refractive index with

a VE 3580 RI detector of Viscotek at 35 °C. For external calibration, poly(styrene) (PS) standards with a molecular weight range from 1050 to 115 000 g/mol were used (purchased from Polymer Standards Service). The investigated samples were dissolved in THF (HPLC grade) at a concentration of 1-4 mg/mL and the results were analyzed using OmniSec 4.5.6 software.

**Matrix-assisted laser desorption/ionisation time-of-flight mass spectrometry** (MALDI-TOF-MS) measurements were carried out on a Bruker Autoflex III system equipped with a smart beam laser (355 nm, 532 nm, 808 nm and 1064 nm  $\pm$  5 nm; 3 ns pulse width; up to 2500 Hz repetition rate) accelerated by a voltage of 20 kV and detected as positive ions in reflectron or linear mode. The data evaluation was performed on flexAnalysis software (version 3.0). Polymeric samples were dissolved in THF at a concentration of 10 mg/mL. Dithranol or IAA was used as matrix and NaTFA was used as salt. Matrix and salt were dissolved in THF at a concentration of 20 mg/mL. The solutions of matrix, sample and salt were mixed in a volume ratio of 5:2:5 and 1  $\mu$ L of the solution mixture was spotted on the MALDI-target plate. Peptidic samples were dissolved in 0.1 % TFA at a concentration of 0.1 mg/mL. HCCA was used as matrix and dissolved in ACN / 0.1 % TFA (1:1) at a concentration of 20 mg/mL. The solutions of matrix and sample were mixed in a volume ratio of 1:1 and 1  $\mu$ L of the solution mixture was spotted on the MALDI-target plate. The instrument was externally calibrated with a PEG monomethyl ether standard ( $M_n = 4200$  g/mol,  $M_w/M_n = 1.05$ ) applying a quadratic calibration method.

**Electrospray ionization time-of-flight mass spectrometry** (ESI-TOF-MS) measurements were performed on a Bruker Daltonics microTOF. Samples were dissolved in HPLC grade solvents (MeOH, THF or mixtures; purchased from Sigma Aldrich) at concentrations of 0.1 mg/mL and measured *via* direct injection with a flow rate of 180  $\mu$ L/h using the positive mode with a capillary voltage of 4.5 kV. The spectra were analyzed with Bruker Data Analysis 4.0.

**Column chromatography** was carried out using Merck silica gel 60 (230–400 mesh). Thin-layer chromatography (TLC) was performed on Merck TLC aluminum sheets (silica gel 60 F<sub>254</sub>). Spots on TLC plates were visualized by UV light (254 or 366 nm) or by oxidizing agent “blue stain” consisting of Ce(SO<sub>4</sub>)<sub>2</sub>·4H<sub>2</sub>O (1 g) and (NH<sub>4</sub>)<sub>6</sub>Mo<sub>7</sub>O<sub>24</sub>·4H<sub>2</sub>O (1 g) dissolved in a mixture of distilled water (90 mL) and concentrated sulphuric acid (6 mL).

**High performance liquid chromatography** (HPLC) of polymers was performed on a LaChrom Elite by Hitachi VWR equipped with a pump (L-2100), an autosampler (L-2200), a degasser, a diode array detector (DAD; L-2455) and a column oven (L-2300) with temperature control. The measurements were carried out on a reversed phase column (RP C-18) Waters Atlantis<sup>®</sup>-T3, 5  $\mu$ m, 100 Å, 4.6  $\times$  250 mm. THF and methanol were applied as the mobile phase system. The critical conditions (LCCC) of alkyne-functional PHICs were found using THF/MeOH = 69.5 : 30.5 (v/v) as mobile phase at a temperature of 30 °C. This method was applied for all measured samples. The concentration of all samples was 1 mg/mL, the flow rate



was 0.4 mL/min and the injected sample volume was 10  $\mu$ L. DAD signals were recorded using EZchrom elite software version 3.3.2 SP2 with an operating wavelength from 190 to 900 nm.

**Monolayer experiments:** The surface pressure  $\pi$  of monolayers of the pure compounds and of different binary mixed systems of PHICs and DPPC at the air / water interface *via* Langmuir film technique were performed using a Langmuir trough system (KSV, Helsinki, Finland) with a maximum available surface of 76 800 mm<sup>2</sup>. The investigated mixtures of PHIC and DPPC were dissolved in chloroform (HPLC grade, Sigma Aldrich) at a concentration of 1 mM. Defined amounts of the prepared solutions were spread on the subphase (ultrapure water; total organic carbon < 5 ppm; conductivity < 0.055  $\mu$ S/cm) using a digital microsyringe (Hamilton). The monolayer was compressed at a barrier speed of 5 mm/min and compressing was started 15 min after spreading to ensure full evaporation of the solvent and a uniform monolayer formation. A constant temperature of 20 °C was applied throughout the entire experiment.

**Epifluorescence microscopy** for the imaging of monolayers at the air / water interface was performed using an “axio Scope A1 Vario” epifluorescence microscope (Carl Zeiss MicroImaging, Jena, Germany) with a Langmuir Teflon trough (maximum area 264 cm<sup>2</sup>, two movable barriers; Riegler & Kirstein GmbH, Berlin, Germany). The trough was mounted on an x-y stage (Marzhauser, Wetzlar, Germany) with x-y-z motion control (Mac5000 system, Ludl Electronic Products, Hawthorne, NY, USA). The air / water surface was imaged by a 100 W mercury lamp, a long-distance objective (LD EC Epiplan-NEOFLUAR 50x) was used and the respective wavelengths were selected with a filter / beam splitter combination. An excitation wavelength of 557 nm and an emission wavelength of 571 nm were used with the appropriate Zeiss filter set (filter set 20, green light). The fluorescence images were taken during compression with a speed of 2  $\text{\AA}^2 \text{ molecule}^{-1} \text{ minute}^{-1}$  and recorded using an EM-CCD camera (ImageEM C9100-13, Hamamasu, Herrsching, Germany). The analysis and data acquisition were done using AxioVision software (Carl Zeiss MicroImaging, Jena, Germany). Monolayer Films of pure or mixed compounds in different molar ratios were prepared with a total spreading concentration of 1 mM in chloroform (HPLC-grade, Carl Roth, Karlsruhe, Germany) and fluorescence-labeled Rh-PHIC (0.01 mol%) was added to the stock solution. A defined volume of the solution was spread on the water surface and the compression was started after 15 min waiting time.

**Circular dichroism** (CD) spectra were recorded on a Jasco J-815 spectropolarimeter using a 2 mm path length cell. Polymeric samples were measured at a concentration of 0.25–0.5 mg/mL in *n*-hexane, THF or DCM. Peptidic samples were measured at concentrations of 10–20  $\mu$ M in phosphate buffer (20–50 mM).

**Aggregation kinetics** (ThT assays) of artificial peptides and mixtures with WT A $\beta$ <sub>40</sub> were investigated by fluorescence intensity measurements using thioflavin T (ThT) as fluorescent dye. Lyophilized peptides were dissolved in 10 mM NaOH at a concentration of 1 mg/mL. The samples were left to stand for 10 minutes and applied to ultrasound for 1 minute for complete

dissolution of the peptides. The solutions were centrifuged at 10,000 rpm for 1 hour at 4 °C, the supernatant was transferred to another tube and the sample was kept on ice in the next steps. The samples were diluted with 50 mM phosphate buffer (pH 7.4, 150 mM NaCl) to obtain final concentrations of 10 μM WT Aβ<sub>40</sub>, 10 μM ThT and different concentrations of peptide conjugate (1–10 μM). For each sample, a total volume of 480 μL was prepared and 3×150 μL were pipetted to a 96-well plate. The plate was sealed with a microplate cover. The fluorescence intensity was monitored at 37 °C using a BMG FLUOStar Omega multi-mode plate reader using fluorescence excitation and emission wavelengths at 440 nm and 482 nm respectively. One measurement cycle of 5 minutes consisted of double-orbital shaking for 240 s and waiting for 60 s. Concentrations of WT Aβ<sub>40</sub> and conjugates **20a**, **20c**, **20d** and **22** were determined by absorbance at 280 nm using a Jasco V-660 absorbance spectrometer and the molar extinction coefficient of Aβ<sub>40</sub>, based on the tyrosine residue Y<sub>10</sub> ( $\epsilon_{280} = 1490 \text{ cm}^{-1} \text{ M}^{-1}$ ). The concentrations of conjugates **20b**, **21a-d**, **23** and **24** were estimated by weight.

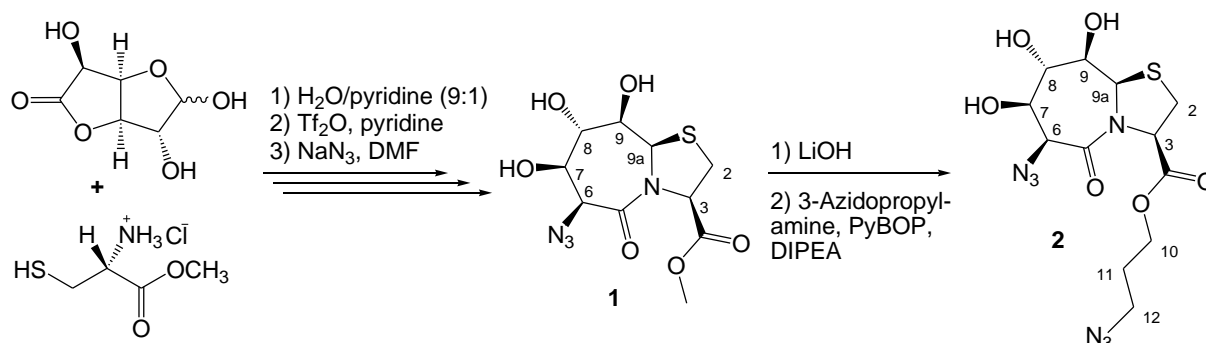
**Transmission electron microscopy (TEM)** images were taken with an electron microscope (EM 900; Zeiss) at 80 kV acceleration voltage. For preparation, 5 μL of the peptide solution (2–5 μM) was dropped on Formvar/Cu grids (mesh 200). After three minutes waiting, the grids were gently cleaned with water for one minute and then negatively stained using uranylacetate (1%, w/v) for one minute.

**Cell viability assay with MTT reduction assay:** N2a cells were cultured in a RPMI medium containing L-Glutamine, FBS (10 %) and 1 % penicillin-streptomycin at 37 °C in 5 % CO<sub>2</sub>. After 2-3 days, the cells were trypsinized for five minutes, then diluted with the medium and plated onto 96-well plates (5000 cells/well). After 24 hours of incubation, monomeric or fibrillar Aβ was added. Fibrillar samples were re-suspended in the medium at a concentration of 100 μM and 30 μL were added to the cells. Monomeric samples were obtained by a previously described protocol.<sup>[279-281]</sup> Briefly, peptide conjugates were dissolved in TFA (1 mg/mL) and sonicated for 10 minutes at room temperature. After evaporation under a stream of nitrogen, HFIP was added, followed by evaporation using nitrogen to yield a peptide film at the wall of the tube. This process was repeated twice. Afterwards, the sample was subjected to high vacuum for 30 minutes and was afterwards kept under dry nitrogen atmosphere. The samples were treated with NaOH (60 mM, 5 μL), PBS (30 μL), HCl (60 mM, 5 μL) and RPMI medium (40 μL) in this order to yield a concentration of 100 μM. 30 μL were added to the cells to reach a final concentration of 20 μM. The measurements were performed as triplicates.

Cell viability was determined after 72 hours using a MTT reduction assay. Therefore MTT was added to each well to a final concentration of 0.5 mg/mL. After 3.5 hours incubation at 37 °C, the medium was removed and the blue crystals were dissolved in DMSO (100 μL/well). The plate was read on a micro plate reader at a wavelength of 570 nm. Cell viability was related to the 100 % control.

## 4.2 Synthesis of $\beta$ -turn mimetics

### 4.2.1 Synthesis of 7,5-bicyclic $\beta$ -turn mimetic (1) and (2)



**Scheme 22.** Synthesis of  $\beta$ -turn mimetics **1** and **2**.

The synthesis of  $\beta$ -turn mimetic **1** was performed in three steps according to literature procedures<sup>[282-283]</sup> as shown in Scheme 22. The synthesis of  $\beta$ -turn mimetic **2** was performed with slight modifications from literature procedures.<sup>[283]</sup> In a one-necked round-bottom flask **1** (200 mg, 0.63 mmol) was dissolved in dioxane (5 mL) and 0.5 M LiOH (1.5 mL, 0.75 mmol, 1.1 equiv.) was added under stirring. The reaction mixture was stirred for 30 minutes, controlled by TLC (THF;  $R_f = 0$ ) and was neutralized by the addition of 1 M HCl. The solvent was removed under vacuum and the intermediate was used without further purification. In a Schlenk-flask with septum, the intermediate and PyBOP (0.4 g, 0.76 mmol, 1.2 equiv.) were dissolved in DMF (5 mL) and the solution was degassed by purging with nitrogen for 15 minutes. 1-Azido-3-propylamine in diethylether (0.5 mL, 20 %) and DIPEA (214  $\mu$ L, 1.3 mmol, 2.0 equiv.) were added *via* Eppendorf pipette and the solution was further degassed for ten minutes. The reaction mixture was stirred at room temperature for 14 hours, the solvent was removed under vacuum and the crude product was purified by silica gel column chromatography (EA;  $R_f = 0.3$ ) to yield 172 mg of a colorless product (0.45 mmol, 71 %).

Structural analysis of **1**:

**<sup>1</sup>H-NMR** (400 MHz, DMSO-*d*<sub>6</sub>):  $\delta$  (ppm) 5.67 (d,  $J_{\text{OH,H}} = 3.6$  Hz, 1H, OH-8), 5.57 (d,  $J_{\text{OH,H}} = 6.3$  Hz, 1H, OH-7), 5.50 (s, 1H, H-9a), 4.78–4.75 (m, 2H, H-3; H-6), 4.43 (d,  $J_{\text{OH,H}} = 10.5$  Hz, 1H, OH-9), 3.86 (m, 1H, H-7), 3.81 (dd,  $J_{\text{H,H}} = 3.2$  Hz, 1H, H-8), 3.35 (s, 1H, H-2).

**<sup>13</sup>C-NMR** (100 MHz, DMSO-*d*<sub>6</sub>):  $\delta$  (ppm) 170.4 (COO), 166.6 (C-5), 76.7 (C-9), 74.9 (C-7), 70.9 (C-8), 64.0 (C-3), 61.4 (C-6), 61.0 (C-9a), 52.3 (OCH<sub>3</sub>), 31.5 (C-2).

**IR** [ $\text{cm}^{-1}$ ]: 3464 (s), 2938 (w), 2919 (w), 2110 (s, azide), 1750 (s), 1649 (s), 1434 (m), 1354 (m), 1311 (m), 1252 (s), 1217 (s), 1172 (s), 1093 (m), 1068 (s), 886 (m).

Structural analysis of **2**:

**<sup>1</sup>H-NMR** (400 MHz, DMSO-*d*<sub>6</sub>):  $\delta$  (ppm) 8.10 (t,  $J = 5.6$  Hz, 1H, NH), 5.90 (d,  $J = 6.5$  Hz, 1H, OH-9), 5.72 (d,  $J = 4.7$  Hz, 1H, OH-7), 5.58 (d,  $J = 3.8$  Hz, 1H, OH-8), 5.47 (s, 1H, H-9a), 4.66 (s,

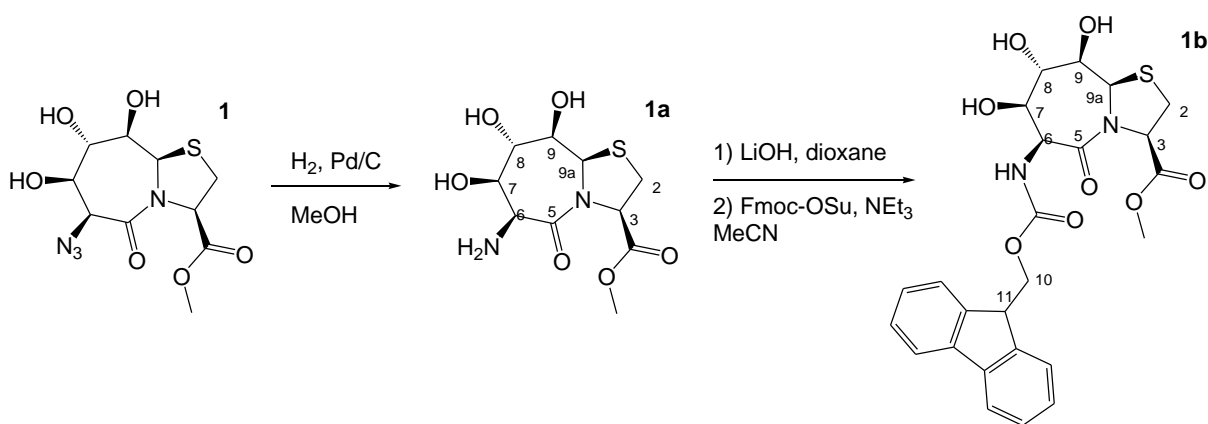
1H, *H*-6), 4.53 (t, *J* = 7.8 Hz, 1H, *H*-3), 3.90 (t, *J* = 4.8 Hz, 1H, *H*-7), 3.79 (q, *J* = 3.8 Hz, 1H, *H*-8), 3.61 (dd, *J* = 6.4, 3.1 Hz, 1H, *H*-9), 3.37–3.31 (m, 1H, *H*-2), 3.26 (dd, *J* = 7.8, 4.4 Hz, 2H, *H*-12), 3.20–3.13 and 3.05–2.97 (m, 2H, *H*-10), 1.64–1.57 (m, 2H, *H*-11).

<sup>13</sup>C-NMR (100 MHz, DMSO-*d*<sub>6</sub>): δ (ppm) 169.6, 167.0 (*C*-5, COO), 76.3 (*C*-9), 75.0 (*C*-7), 72.2 (*C*-8), 66.2 (*C*-3), 61.5, 61.4 (*C*-6, *C*-9a), 48.2 (*C*-12), 35.7 (*C*-10), 32.7 (*C*-2), 28.1 (*C*-11).

ESI-TOF-MS (MeOH) *m/z*: C<sub>12</sub>H<sub>17</sub>N<sub>8</sub>O<sub>5</sub>S<sup>-</sup> [M-H]<sup>-</sup>, calc.: 385.1043, found: 385.1141; C<sub>12</sub>H<sub>18</sub>N<sub>8</sub>O<sub>5</sub>SCl<sup>-</sup> [M+Cl]<sup>-</sup>, calc.: 421.0809, found: 421.0932.

IR [cm<sup>-1</sup>]: 3433 (b), 2926 (w), 2114 (m, azide), 1651 (m), 1384 (s), 1062 (w).

#### 4.2.2 Synthesis of β-turn mimetic (**1b**) for SPPS



Scheme 23. Synthesis of β-turn mimetic **1b** for SPPS.

The synthesis of **1b** was performed with slight modifications from literature procedures<sup>[284-285]</sup> in three steps. 10 wt% Pd on charcoal (10 %, 40 mg) was placed into a 100 mL two-necked round bottom flask equipped with a septum and gas tap. The gas tap was connected to a three way tap, one attached to a vacuum/nitrogen line and one to a balloon. The flask was evacuated and flushed with nitrogen three times. **1** (400 mg, 1.3 mmol, 1.0 equiv.) was added under a counterflow of nitrogen and methanol (60 mL) was added. The flask was evacuated and backfilled with hydrogen three times. Afterwards the reaction mixture was stirred vigorously at room temperature for 16 hours under a hydrogen atmosphere. The reaction mixture was filtered through celite and the solvent was removed under vacuum to yield **1a** as a light yellow solid. (270 mg, 0.92 mmol, 72 %)

<sup>1</sup>H-NMR (400 MHz, DMSO-*d*<sub>6</sub>): δ (ppm) 5.54 + 5.27 (bs, 2H, OH-7, OH-8), 5.45 (s, 1H, *H*-9a), 4.68 (t, *J* = 7.7 Hz, 1H, *H*-3), 4.28 (d, *J* = 11.0 Hz, 1H, OH-9), 4.06 (s, 1H, *H*-6), 3.81 (m, 1H, *H*-8), 3.74 (d, *J* = 4.3 Hz, 1H, *H*-7), 3.63 (s, 3H, OCH<sub>3</sub>), 3.54 (dd, *J* = 10.9 Hz, 1H, *H*-9), 3.29 (m, 2H, *H*-2).

<sup>13</sup>C-NMR (100 MHz, DMSO-*d*<sub>6</sub>): δ (ppm) 171.4 + 170.7, (*C*-5, COO), 77.3 (*C*-9), 76.7 (*C*-7), 71.2 (*C*-8), 64.0 (*C*-3), 60.9 (*C*-9a), 53.3 (*C*-6), 52.1 (OCH<sub>3</sub>), 31.5 (*C*-2).

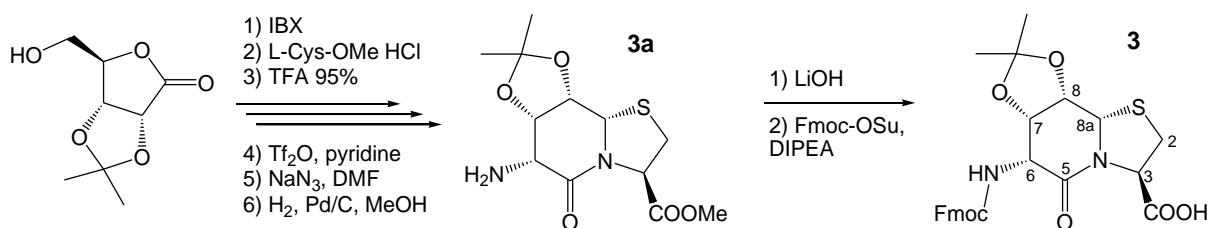
In the second step, **1a** (200 mg, 0.68 mmol) was added to a one-necked round-bottom flask and then dissolved in dioxane (5 mL). LiOH (0.5 M, 1.5 mL, 0.75 mmol, 1.1 equiv.) was added under stirring, the reaction was controlled by TLC (THF;  $R_f = 0$ ) and neutralized after 30 minutes by the addition of 1 M HCl. The solvent was removed under vacuum and the product was used without further purification. The intermediate was dissolved in water (5 mL) cooled with an ice bath, followed by addition of triethylamine (95  $\mu$ L, 0.68 mmol, 1.0 equiv.) and Fmoc-OSu (275 mg, 0.82 mmol, 1.2 equiv.) in acetonitrile (5 mL). The pH was checked every 15 minutes and adjusted to 8–9 with triethylamine until no further drop was visible. The reaction was also monitored by TLC (CHCl<sub>3</sub> / MeOH 5:1;  $R_f = 0.1$ ) showing complete conversion after one hour. The solution was acidified with 1 M HCl and the solvent was removed under vacuum. The product was purified by column chromatography on silica (CHCl<sub>3</sub> / MeOH 20:1,  $R_f = 0.1$ ) and **1b** was obtained as a colorless powder (240 mg, 0.48 mmol, 70 %).

**<sup>1</sup>H-NMR** (400 MHz, DMSO-*d*<sub>6</sub>):  $\delta$  (ppm) 7.89 (d,  $J = 7.5$  Hz, 2H, Fmoc arom.), 7.74 (t,  $J = 6.5$  Hz, 2H, Fmoc arom.), 7.42 (t,  $J = 7.2$  Hz, 2H, Fmoc arom.), 7.33 (t,  $J = 7.4$  Hz, 2H, Fmoc arom.), 7.13 (d,  $J = 8.4$  Hz, 1H, NH), 5.56 (d,  $J = 3.5$  Hz, 1H, OH-7), 5.51 (s, 1H, H-9a), 4.81 (d,  $J = 8.4$  Hz, 1H, H-6), 4.66 (t,  $J = 6.6$  Hz, 1H, H-3), 4.33–4.23 (m, 3H, H-10, H-11), 3.84 (d,  $J = 3.6$  Hz, 1H, H-8), 3.76 (d,  $J = 3.6$  Hz, 1H, H-7), 3.51 (d,  $J = 2.9$  Hz, 1H, H-9), 3.24 (m, 2H, H-2).

**<sup>13</sup>C-NMR** (100 MHz, DMSO-*d*<sub>6</sub>):  $\delta$  (ppm) 167.3, 155.7 (C=O), 127.6, 127.1, 125.3, 120.1 (C-Fmoc arom.), 75.5 (C-9), 75.0 (C-7), 71.6 (C-8), 65.9 (C-10) 65.6 (C-3), 61.1 (C-9a), 54.4 (C-6), 46.6 (C-11), 32.7 (C-2).

**ESI-TOF-MS** (MeOH)  $m/z$ : C<sub>24</sub>H<sub>24</sub>N<sub>2</sub>O<sub>8</sub>SNa<sup>+</sup> [M+Na]<sup>+</sup>, calc.: 523.1146, found: 523.1032; C<sub>24</sub>H<sub>24</sub>N<sub>2</sub>O<sub>8</sub>SK<sup>+</sup> [M+K]<sup>+</sup>, calc.: 539.0885, found: 539.0750; C<sub>24</sub>H<sub>23</sub>N<sub>2</sub>O<sub>8</sub>SLiK<sup>+</sup> [M+Li+K-H]<sup>+</sup>, calc.: 545.0967, found: 545.0919.

#### 4.2.3 Synthesis of 6,5-bicyclic $\beta$ -turn mimetic dipeptide (**3**) for SPSS



**Scheme 24.** Synthesis of 6,5-bicyclic  $\beta$ -turn mimetic dipeptide **3**.

The synthesis of **3** was performed in several steps as shown in Scheme 24 with slight modifications from literature procedures.<sup>[185]</sup> In the last step, **3a** (450 mg, 1.5 mmol, 1.0 equiv.) was dissolved in dioxane (10 mL) together with LiOH (3.6 mL, 20 mg/mL, 1.1 equiv.). After 20 minutes TLC (DCM / MeOH 5:1;  $R_f = 0$ ) showed full conversion, the reaction mixture was neutralized with 1 M HCl and the solvent was removed in vacuo. The residue was dissolved in dioxane / water (6 mL, 4:1) and Fmoc-OSu (675 mg, 2.0 mmol, 1.3 equiv.) in dioxane (2 mL) was

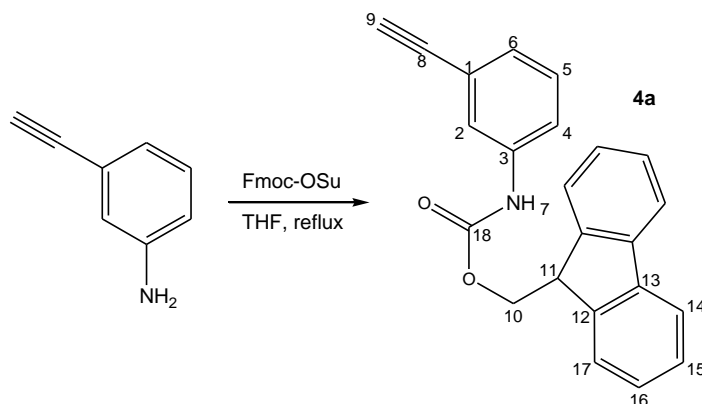
added slowly. The pH was adjusted to 9 with DIPEA. After 3 hours at room temperature TLC (DCM / MeOH 5:1;  $R_f = 0.43$ ) showed complete transformation of the starting material and the solvent was removed under vacuum. The residue was taken up in ethyl acetate (10 mL) and water (5 mL) and the aqueous phase was adjusted to pH 2 with 1 M HCl. The aqueous phase was extracted three times with ethyl acetate and the combined organic phases were dried over  $MgSO_4$ . After filtration and removal of the solvent, silica gel column chromatography was performed (DCM / MeOH 50:1; followed by 20:1) and 330 mg (0.65 mmol, 43 %) of compound **3** were obtained as a colorless powder and used in subsequent polypeptide syntheses.

**$^1H$ -NMR** (400 MHz,  $CD_3OD$ ):  $\delta$  (ppm) 7.79 (d,  $J = 7.5$  Hz, 2H, Fmoc arom.), 7.66 (d,  $J = 7.4$  Hz, 2H, Fmoc arom.), 7.39 (t,  $J = 7.5$  Hz, 2H, Fmoc arom.), 7.31 (t,  $J = 7.4$  Hz, 2H, Fmoc arom.), 5.28 (d,  $J = 6.3$  Hz, 1H,  $H$ -8a), 5.11 (s, 1H,  $H$ -3), 4.53 (m, 1H,  $H$ -8), 4.49 (d,  $J = 6.1$  Hz, 1H,  $H$ -7), 4.24-4.21 (m, 2H,  $H$ -6, Fmoc CH), 3.30 (d,  $J = 6.7$  Hz, 1H,  $H$ -2<sup>proS</sup>), 3.20 (d,  $J = 11.0$  Hz, 1H,  $H$ -2<sup>proR</sup>), 1.33 (s, 3H, isopr.CH<sub>3</sub>).

**$^{13}C$ -NMR** (100 MHz,  $CD_3OD$ ):  $\delta$  (ppm) 173.2, 167.9, 158.1 (C=O), 145.3/145.1 (Fmoc arom), 142.7/142.6 (Fmoc arom), 128.8 (Fmoc arom), 128.2/128.1 (Fmoc arom), 126.1/126.1 (Fmoc arom), 120.9/120.9 (Fmoc arom), 110.5 (isopr. quart.), 77.9 (C-7), 76.8 (C-8), 67.9 (Fmoc-CH<sub>2</sub>), 63.5 (C-8a), 61.6/61.5 (C-3), 56.9 (Fmoc-CH), 48.5 (C-6), 32.5 (C-2), 26.6 (isopr.CH<sub>3</sub>), 24.2 (isopr.CH<sub>3</sub>).

**ESI-TOF-MS** (MeOH)  $m/z$ :  $C_{26}H_{26}N_2O_7SLi^+$   $[M+Li]^+$ , calc.: 517.1616, found: 517.1629;  $C_{26}H_{26}N_2O_7SNa^+$   $[M+Na]^+$ , calc.: 533.1353, found: 533.1328;  $C_{26}H_{26}N_2O_7SK^+$   $[M+K]^+$ , calc.: 549.1092, found: 549.1081.

#### 4.2.4 Synthesis of a triazole containing aromatic turn mimetic (TAA, 4)



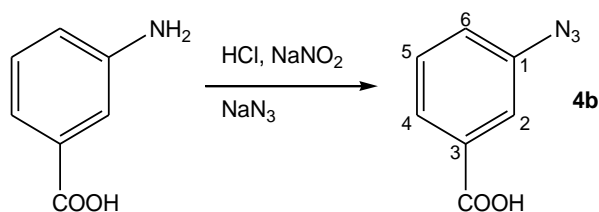
**Scheme 25.** Synthesis of (9H-fluoren-9-yl)methyl (3-ethynylphenyl)carbamate **4a**.

The synthesis of (9H-fluoren-9-yl)methyl (3-ethynylphenyl)carbamate **4a** was performed according to literature.<sup>[186]</sup> 3-Ethynyl aniline (1.0 g, 0.9 mL, 8.6 mmol, 1.0 equiv.) and Fmoc-OSu (3.2 g, 9.4 mmol, 1.1 equiv.) were dissolved in THF (100 mL) and the reaction mixture was heated under reflux overnight. The solvent was removed under vacuum and the crude product

was dissolved in ethylacetate (50 mL) and extracted with water (20 mL). The organic phase was dried over Na<sub>2</sub>SO<sub>4</sub>, filtered, concentrated under vacuum and the residue was purified by flash silica chromatography (Hex / EA 8:1; R<sub>f</sub> = 0.2) to afford the Fmoc-protected product **4a** as a white powder (1.8 g, 5.2 mmol, 60 %).

**<sup>1</sup>H-NMR** (400 MHz, DMSO-d<sub>6</sub>): δ (ppm) 9.80 (bs, 1H, NH), 7.91 (d, *J* = 7.5 Hz, 2H, *H*-14), 7.74 (d, *J* = 7.4 Hz, 2H, *H*-17), 7.60 (bs, 1H, *H*-2), 7.47 (bs, 1H, *H*-4), 7.43 (d, *J* = 7.4 Hz, 2H, *H*-15), 7.35 (td, *J* = 7.4, 1.1 Hz, 2H, *H*-16), 7.27 (t, *J* = 7.9 Hz, 1H, *H*-5), 7.09 (d, *J* = 7.6 Hz, 1H, *H*-6), 4.51 (d, *J* = 6.5 Hz, 2H, *H*-10), 4.31 (t, *J* = 6.5 Hz, 1H, *H*-11), 4.15 (s, 1H, C≡CH).

**<sup>13</sup>C-NMR** (100 MHz, DMSO-d<sub>6</sub>): δ (ppm) 153.3 (C-18), 143.7 (C-12), 140.8 (C-3), 139.3 (C-13), 129.2, 127.7 (C-6, C-14), 127.1 (C-16), 125.7 (C-5), 125.0 (C-15), 122.0 (C-17), 121.0 (C-2), 120.2 (C-4), 118.9 (C-1), 83.4 (C-8), 80.5 (C-9), 65.6 (C-10), 46.6 (C-11).

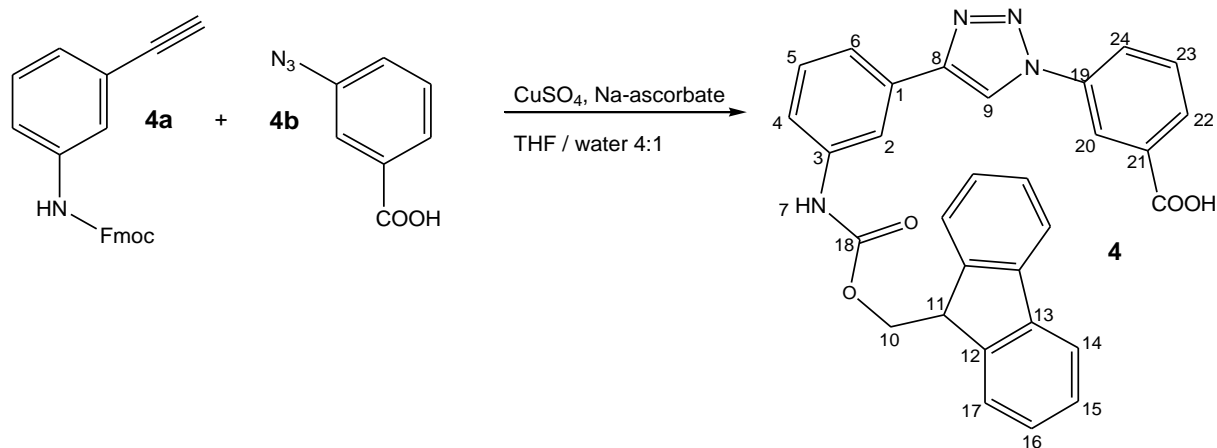


**Scheme 26.** Synthesis of 3-azidobenzoic acid **4b**.

The synthesis of 3-azidobenzoic acid **4b** was performed according to Scheme 26 similar to a literature procedure.<sup>[187]</sup> Sodium nitrite (1.2 g, 17.5 mmol, 1.2 equiv.) in water (10 mL) was added dropwise to a stirred solution of 3-aminobenzoic acid (2.0 g, 14.6 mmol, 1.0 equiv.) in 2 M HCl (140 mL) at 0 °C. The reaction mixture was stirred for 30 minutes at 0 °C and a solution of NaN<sub>3</sub> (1.1 g, 17.5 mmol, 1.2 equiv.) in water (15 mL) was added dropwise, upon which gas evolution and the formation of a foam was visible. The mixture was stirred for further two hours at room temperature. Afterwards, the solution was extracted with ethyl acetate (60 mL), the organic phase was washed with 0.1 M HCl (25 mL), saturated NH<sub>4</sub>Cl (25 mL) and brine (25 mL), was dried over Na<sub>2</sub>SO<sub>4</sub>, filtered and concentrated under vacuum to yield 1.9 g of **4b** as a colorless solid (11.7 mmol, 80 %).

**<sup>1</sup>H-NMR** (400 MHz, DMSO-d<sub>6</sub>): δ (ppm) 13.23 (s, 1H, COOH), 7.75 (dt, *J* = 7.7, 1.2 Hz, 1H, *H*-4), 7.57 (dd, *J* = 3.8, 1.8 Hz, 1H, *H*-2), 7.53 (d, *J* = 7.8 Hz, 1H, *H*-5), 7.37 (ddd, *J* = 8.0, 2.3, 0.9 Hz, 1H, *H*-6).

**<sup>13</sup>C-NMR** (100 MHz, DMSO-d<sub>6</sub>): δ (ppm) 166.4 (COOH), 139.9 (C-1), 132.6 (C-3), 130.3 (C-5), 125.8 (C-4), 123.5 (C-6), 119.4 (C-2).



**Scheme 27.** Synthesis of aromatic  $\beta$ -turn mimetic TAA **4**.

The synthesis of aromatic  $\beta$ -turn mimetic **4** was performed as shown in Scheme 27, similar to literature procedure.<sup>[187]</sup> **4a** (500.0 mg, 1.47 mmol, 1.0 equiv.) and **4b** (240.0 mg, 1.47 mmol, 1.0 equiv.) were added to a Schlenk flask with magnetic stir bar and septum. THF and water (4:1; 20 mL) were added and the solution was degassed by purging with nitrogen for 30 minutes. Copper (II) sulfate pentahydrate (36.7 mg, 0.15 mmol, 0.1 equiv.), sodium ascorbate (146.6 mg, 0.74 mmol, 0.5 equiv.) and triethylamine (0.25 mL, 1.76 mmol, 1.2 equiv.) were added and the solution was further degassed by purging with nitrogen for 15 minutes. The reaction mixture was heated to 50 °C overnight. The solvent was removed under vacuum and the crude product was purified by silica gel column chromatography (CHCl<sub>3</sub> / MeOH 20:1,  $R_f$  = 0.2) to yield **4** as a colorless powder (130 mg, 0.26 mmol, 18 %).

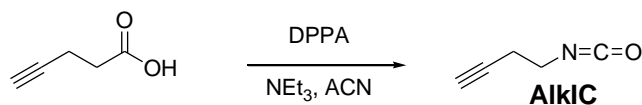
**<sup>1</sup>H-NMR** (400 MHz, DMSO-*d*<sub>6</sub>):  $\delta$  (ppm) 13.42 (s, 1H, COOH), 9.88 (s, 1H, NH), 9.41 (s, 1H, *H*-9), 8.50 (s, 1H, *H*-20), 8.25 (m, 1H, *H*-22), 8.20 (s, 1H, *H*-2), 8.06 (d,  $J$  = 7.8 Hz, 1H, *H*-24), 7.92 (d,  $J$  = 7.5 Hz, 2H, *H*-14), 7.78 (d,  $J$  = 7.3 Hz, 2H, *H*-17), 7.75 (s, 1H, *H*-5), 7.57 (d,  $J$  = 7.4 Hz, 1H, *H*-4 / *H*-6), 7.48-7.36 (m, 6H, *H*-4 / *H*-6, *H*-16, *H*-23, *H*-15), 4.50 (d,  $J$  = 6.8 Hz, 2H, *H*-10), 4.34 (t,  $J$  = 6.8 Hz, 1H, *H*-11).

**<sup>13</sup>C-NMR** (100 MHz, DMSO-*d*<sub>6</sub>):  $\delta$  (ppm) 162.3 (COOH), 153.5 (*C*-18), 147.4 (*C*-8), 143.8 (*C*-12), 140.8 (*C*-13), 139.7, 136.8, 130.7, 129.2 (*C*-1, *C*-3, *C*-19, *C*-21), 130.3, 129.4 (*C*-5, *C*-23), 127.7 (*C*-16), 127.1 (*C*-15), 125.2 (*C*-17), 123.8 (*C*-22), 120.4 (*C*-20), 120.2 (*C*-14), 119.9 (*C*-9), 119.8, 118.3 (*C*-4, *C*-6), 115.2 (*C*-2), 65.7 (*C*-10), 46.6 (*C*-11).

**ESI-TOF-MS** (MeOH)  $m/z$ : C<sub>30</sub>H<sub>22</sub>N<sub>4</sub>O<sub>4</sub>Li<sup>+</sup> [M+Li]<sup>+</sup>, calc.: 509.1796, found: 509.1834; C<sub>30</sub>H<sub>22</sub>N<sub>4</sub>O<sub>4</sub>Na<sup>+</sup> [M+Na]<sup>+</sup>, calc.: 525.1533, found: 525.1575; C<sub>30</sub>H<sub>22</sub>N<sub>4</sub>O<sub>4</sub>K<sup>+</sup> [M+K]<sup>+</sup>, calc.: 541.1273, found: 541.1318; C<sub>30</sub>H<sub>21</sub>N<sub>4</sub>O<sub>4</sub>NaLi<sup>+</sup> [M+Li+Na-H]<sup>+</sup>, calc.: 547.1355, found: 547.1405; C<sub>30</sub>H<sub>21</sub>N<sub>4</sub>O<sub>4</sub>LiK<sup>+</sup> [M+Li+K-H]<sup>+</sup>, calc.: 563.1092, found: 563.1147.



### 4.3 Synthesis of functional monomers

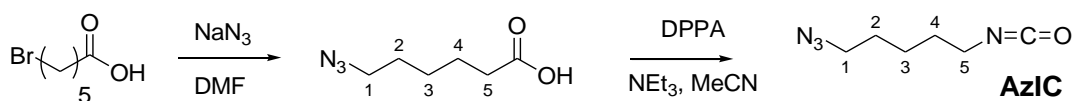


**Scheme 28.** Synthesis of 4-isocyanato-1-butyne (**AlkIC**).

The synthesis was performed according to Scheme 28, similar to a previously reported method.<sup>[286]</sup> A round-bottom flask was three times heated under vacuum and flushed with nitrogen. 4-Pentynoic acid (2.0 g, 20.4 mmol, 1.0 equiv.) and triethylamine (2.8 mL, 20.4 mmol, 1.0 equiv.) were added to the flask and were dissolved in dry acetonitrile (20 mL). Then, DPPA (4.4 mL, 20.4 mmol, 1.0 equiv.) was added under stirring. The reaction mixture was stirred for two hours at 50 °C under nitrogen. The solvent was evaporated and the product (0.7 g, 0.12 mmol, 58 %) was obtained as a colorless liquid by vacuum distillation (5 mbar, 60 °C).

<sup>1</sup>H-NMR (400 MHz, CDCl<sub>3</sub>): δ (ppm) 3.41 (t, *J* = 6.5 Hz, 2H, CH<sub>2</sub>NCO), 2.49 (td, *J* = 6.5, 2.6 Hz, 2H, CH<sub>2</sub>), 2.09 (t, *J* = 2.6 Hz, H, C≡CH).

<sup>13</sup>C-NMR (100 MHz, CDCl<sub>3</sub>): δ (ppm) 123.6 (NCO), 80.1 (C≡CH), 71.2 (C≡CH), 41.8 (CH<sub>2</sub>NCO), 21.7 (CH<sub>2</sub>).



**Scheme 29.** Synthesis of 1-azido-5-isocyanatopentane (**AzIC**).

The synthesis of **AzIC** was performed in two steps according to adapted literature procedures as shown in Scheme 29.<sup>[286-287]</sup> In the first step, 6-bromohexanoic acid (2.0 g, 10.2 mmol, 1.0 equiv.) was dissolved in DMF (20 mL) and sodium azide (2.0 g, 30.6 mmol, 3.0 equiv.) was added under stirring. The resulting mixture was heated for three hours at 50 °C. Water (45 mL) was then added and the mixture was extracted with diethyl ether (three times 45 mL). The combined organic layers were washed with brine (45 mL) and dried over MgSO<sub>4</sub>. After filtration, the solvent was removed in vacuum and the crude residue was purified with silica gel column chromatography (EA, *R<sub>f</sub>* = 0.45) to afford 6-azidohexanoic acid as slightly yellow oil (964.0 mg, 6.1 mmol, 60 %).

<sup>1</sup>H-NMR (400 MHz, CDCl<sub>3</sub>) δ (ppm) 10.86 (bs, COOH), 3.28 (t, *J* = 6.9 Hz, 2H, *H*-1), 2.38 (t, *J* = 7.4 Hz, 2H, *H*-5), 1.65 (m, 4H, *H*-2, *H*-4), 1.44 (m, 2H, *H*-3).

<sup>13</sup>C-NMR (100 MHz, CDCl<sub>3</sub>) δ (ppm) 179.6 (C=O), 51.4 (C-1), 33.9 (C-5), 28.7, 26.3, 24.3 (C-2, C-3, C-4).

IR [cm<sup>-1</sup>]: 2941 (m), 2868 (m), 2092 (s) azide, 1705 (s) carboxyl, 1458 (w), 1413 (w), 1252 (m).

In the second step, 6-azidohexanoic acid (3.7 g, 23.5 mmol, 1.0 equiv.), triethylamine (3.3 mL, 23.5 mmol, 1.0 equiv.) and acetonitrile (35 mL) were added into a dry two-necked flask equipped with magnetic stir bar, septum and gas tap. DPPA (5.1 mL, 23.5 mmol, 1.0 equiv.) was then added and the resulting mixture was stirred for two hours at 50 °C. The solvent was evaporated and 1-azido-5-isocyanatopentane (AzIC) was obtained *via* high vacuum distillation (0.09 mbar, 50 °C head temperature, 90–130 °C oil bath temperature) as a colorless viscous liquid. 3.1 g (20.1 mmol; 86 %)

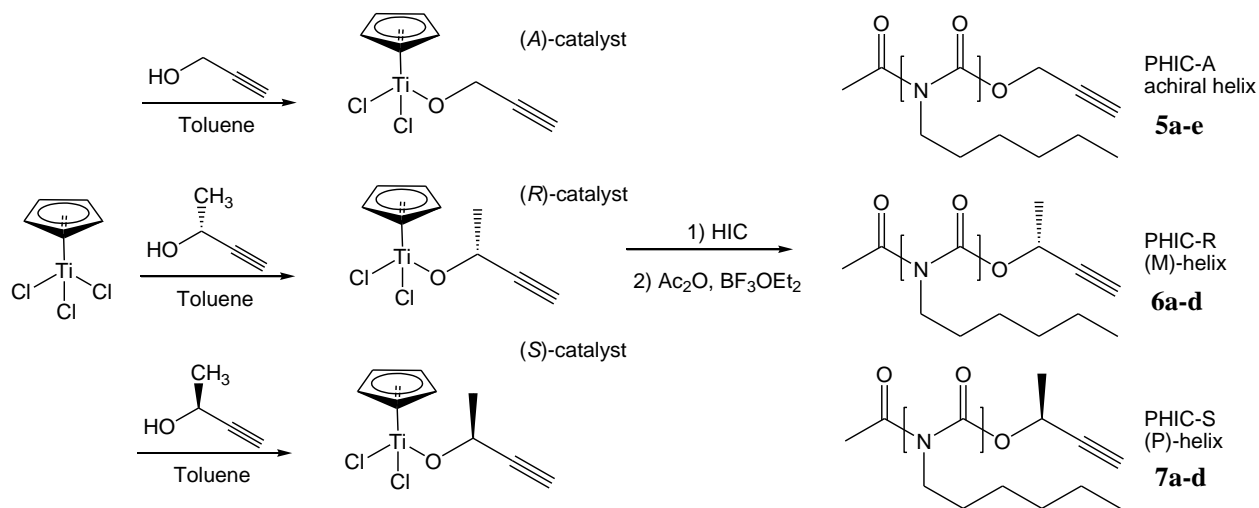
$^1\text{H-NMR}$  (400 MHz,  $\text{CDCl}_3$ )  $\delta$  (ppm) 3.31 (m, 4H, *H*-1, *H*-5), 1.64 (m, 4H, *H*-2, *H*-4), 1.47 (m, 2H, *H*-3).

$^{13}\text{C-NMR}$  (100 MHz,  $\text{CDCl}_3$ )  $\delta$  (ppm) 51.4 (*C*-1), 42.9 (*C*-5), 30.9, 28.5, 24.0 (*C*-2, *C*-3, *C*-4).

$\text{IR}$  [ $\text{cm}^{-1}$ ]: 2942 (w), 2866 (w), 2263 (s) isocyanate, 2093 (s) azide, 1460 (w), 1354 (w), 1267 (w).

## 4.4 Synthesis of polyisocyanates

### 4.4.1 Synthesis of poly(*n*-hexyl isocyanate)s



**Scheme 30.** Synthesis of achiral and chiral poly(*n*-hexyl isocyanate)s **5a-e**, **6a-d**, **7a-d**.

The synthesis of achiral and chiral poly(*n*-hexyl isocyanate) (PHIC) was performed *via* titanium-catalyzed coordination / insertion polymerization with slight modifications according to literature procedures of Novak<sup>[188-189]</sup> and Satoh<sup>[190]</sup> using titanium-alkoxide catalysts (see Scheme 30). A typical polymerization procedure was as followed. A dry Schlenk flask with a magnetic stir bar and a septum was charged with  $\text{CpTiCl}_3$  (1.0 equiv.) in a drybox, which was then dissolved in dry toluene (5 mL) and propargyl alcohol or R- / S-butyn-2-ol (1.2–2.5 equiv.) was added by Eppendorf pipette. The solution was stirred for three hours at room temperature and then the solvent was removed under vacuo. The red solid was redissolved in one or two drops of toluene and the monomer was added under stirring at 0 °C. The mixture turned orange and the magnetic stir bar seized up after about 90 minutes. The monomer was allowed to

diffuse further for 15 hours at 4 °C. The polymerization was quenched by the addition of an excess of acetic anhydride and boron trifluoride ethyl etherate (10.0–20.0 equiv.) for 24 hours. The polymer was collected by centrifugation, dissolved in chloroform and again precipitated in methanol. This process was repeated two times. The product was dried at high vacuum and analyzed with GPC, <sup>1</sup>H-NMR spectroscopy and mass spectrometry.

**Table 10.** Experimental details for the synthesis of PHICs.

Entry	CpTiCl <sub>3</sub>	Alcohol	HIC	Ac <sub>2</sub> O [mL]	BF <sub>3</sub> OEt <sub>2</sub> [mL]	Isolated Yield [%]
<b>5a</b>	315 mg 1.44 mmol	120 μL 2.16 mmol	1.0 mL 6.86 mmol	20	1.8	24
<b>5b</b> <sup>c</sup>	86 mg 0.39 mmol	40 μL 0.69 mmol	0.4 mL 2.75 mmol	/	/	19
<b>5c</b>	150 mg 0.69 mmol	60 μL 1.03 mmol	2.0 mL 13.73 mmol	16	1.7	59
<b>5d</b>	200 mg 0.92 mmol	80 μL 1.37 mmol	2.0 mL 13.73 mmol	22	2.2	75
<b>5e</b>	38 mg 0.17 mmol	20 μL 0.34 mmol	0.5 mL 3.43 mmol	16	0.9	66
<b>6a</b>	330 mg 1.51 mmol	142 μL 1.81 mmol	1.0 mL 6.86 mmol	20	1.8	27
<b>6b</b>	200 mg 0.92 mmol	108 μL 1.37 mmol	2.0 mL 13.73 mmol	22	2.2	83
<b>6c</b>	150 mg 0.69 mmol	81 μL 1.03 mmol	2.0 mL 13.73 mmol	16	1.7	81
<b>6d</b>	28 mg 0.13 mmol	40 μL 0.34 mmol	0.5 mL 3.43 mmol	20	0.4	75
<b>7a</b>	300 mg 1.37 mmol	130 μL 1.64 mmol	1.0 mL 6.86 mmol	20	1.8	40
<b>7b</b>	200 mg 0.92 mmol	109 μL 1.37 mmol	2.0 mL 13.73 mmol	22	2.2	85
<b>7c</b>	28 mg 0.13 mmol	40.0 μL 0.34 mmol	0.5 mL 3.43 mmol	20	0.4	72
<b>7d</b>	150 mg 0.69 mmol	82 μL 1.03 mmol	2.0 mL 13.73 mmol	16	1.7	77

<sup>c</sup> Synthesized during master thesis and used for HPLC measurements.

#### Achiral PHIC 5:

<sup>1</sup>H-NMR (400 MHz, CDCl<sub>3</sub>): δ (ppm) 4.78 (s, 2H, OCH<sub>2</sub>), 3.69 (bs, NCH<sub>2</sub>, r.u.), 2.53 (s, 1H, C≡CH), 2.28 (s, 3H, CH<sub>3</sub>), 1.62 (bs, CH<sub>2</sub>CH<sub>2</sub>N, r.u.), 1.29 (bs, CH<sub>2</sub>, r.u.), 0.88 (bs, CH<sub>3</sub>, r.u.).

$^{13}\text{C-NMR}$  (100 MHz,  $\text{CDCl}_3$ ):  $\delta$  (ppm) 156.9 (NCO), 48.7 (NCH<sub>2</sub>), 31.6, 28.6, 26.4, 22.7 (CH<sub>2</sub>), 14.1 (CH<sub>3</sub>).

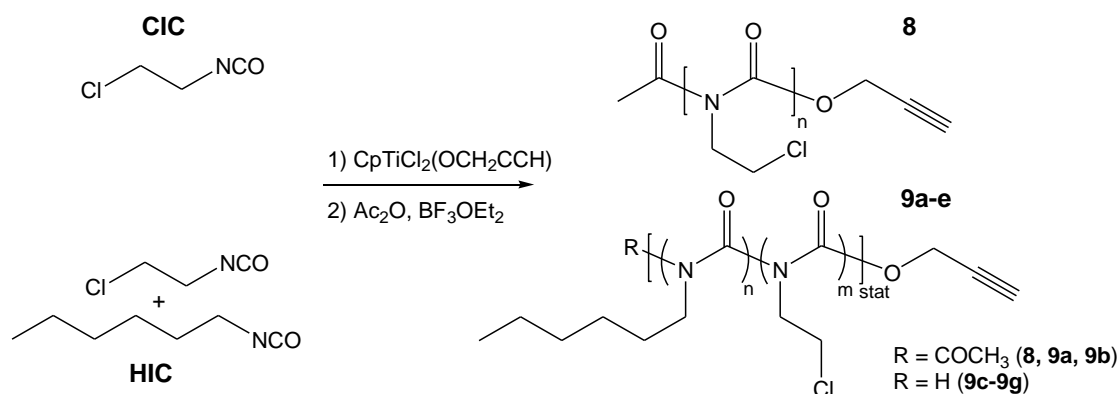
**ESI-TOF-MS** (THF / MeOH 9:1)  $m/z$ :  $\text{C}_2\text{H}_3\text{O}(\text{C}_7\text{H}_{13}\text{NO})_{23}\text{C}_3\text{H}_3\text{ONa}^+ [\text{M}_{23}+\text{Na}]^+$ , calc.: 3045.323, found: 3045.174;  $\text{C}_2\text{H}_3\text{O}(\text{C}_7\text{H}_{13}\text{NO})_{30}\text{C}_3\text{H}_3\text{ONa}_2^{2+} [\text{M}_{30}+2\text{Na}]^{2+}$ , calc.: 1979.506, found: 1979.418.

#### Chiral PHIC 6, 7:

$^1\text{H-NMR}$  (400 MHz,  $\text{CDCl}_3$ ):  $\delta$  (ppm) 5.44 (d,  $J = 5.0$  Hz, 2H, OCH<sub>2</sub>), 3.69 (bs, NCH<sub>2</sub>, r.u.), 2.53 (s, 1H, C $\equiv$ CH), 2.28 (s, 3H, CH<sub>3</sub>), 1.62 (bs, CH<sub>2</sub>CH<sub>2</sub>N, r.u.), 1.29 (bs, CH<sub>2</sub>, r.u.), 0.88 (bs, CH<sub>3</sub>, r.u.).

$^{13}\text{C-NMR}$  (100 MHz,  $\text{CDCl}_3$ ):  $\delta$  (ppm) 156.9 (NCO), 48.7 (NCH<sub>2</sub>), 31.6, 28.6, 26.4, 22.7 (CH<sub>2</sub>), 14.1 (CH<sub>3</sub>).

#### 4.4.2 Homo- and copolymerization of 2-chloroethyl isocyanate (CIC) and HIC



**Scheme 31.** Synthesis of homo- and copolymers of CIC and HIC.

The synthesis of poly(2-chloroethyl isocyanate)s (PCIC) and random copolymers with HIC was performed similar to the polymerization of HIC as shown in Scheme 31. The synthesis of **9c-9g** was performed by using a stock solution of the catalyst. Therefore, a dry Schlenk flask with a magnetic stir bar and a septum was charged with  $\text{CpTiCl}_3$  (50 mg, 0.23 mmol, 1.0 equiv.) in a drybox, which was then dissolved in dry toluene (5 mL). Propargyl alcohol (26.5  $\mu\text{L}$ , 0.46 mmol, 2.0 equiv.) was added by Eppendorf pipette. The solution was stirred for three hours at room temperature and then amounts of the solution corresponding to the desired amount of catalyst as indicated in Table 11, were transferred to separate Schlenk tubes and the solvent was removed under vacuo. The premixed monomers were added to the catalyst under stirring at 0 °C and after solidification the reaction proceeded for 15 hours at 4 °C. Quenching was achieved by addition of an excess of acetic anhydride and boron trifluoride ethyl etherate (10.0–20.0 equiv.) for 24 hours (**8**, **9a**, **9b**). All other polymerizations were stopped after one hour by the addition of methanol (**9c-9g**).

**Table 11.** Experimental details for the synthesis of PCIC and PCIC-PHIC copolymers.

Entry	CpTiCl <sub>3</sub>	Alcohol	CIC	HIC	Ac <sub>2</sub> O [mL]	BF <sub>3</sub> OEt <sub>2</sub> [mL]	Isolated Yield [mg]
<b>8</b>	53 mg 0.24 mmol	27.9 μL 0.48 mmol	0.4 mL 4.7 mmol	/	11.3	0.6	361
<b>9a</b>	46.1 mg 0.21 mmol	24.4 μL 0.42 mmol	33.3 μL 0.39 mmol	573 μL 3.9 mmol	9.9	0.5	306
<b>9b</b>	46.1 mg 0.21 mmol	24.4 μL 0.42 mmol	205.0 μL 2.4 mmol	350 μL 2.4 mmol	9.9	0.5	384
<b>9c</b>	6.7 mg 30.7 μmol <sup>a</sup>	/	42.7 μL 0.5 mmol	291.4 μL 2.0 mmol	/	/	13
<b>9d</b>	5.5 mg 25.1 μmol <sup>a</sup>	/	85.3 μL 1.0 mmol	236.6 μL 1.86 mmol	/	/	17
<b>9e</b>	10.2 mg 46.6 μmol <sup>a</sup>	/	170.6 μL 2.0 mmol	254.5 μL 2.0 mmol	/	/	14
<b>9f</b>	7.1 mg 32.4 μmol <sup>a</sup>	/	158.7 μL 1.86 mmol	127.18 μL 1.0 mmol	/	/	13
<b>9g</b>	6.0 mg 27.5 μmol <sup>a</sup>	/	170.6 μL 2.0 mmol	65.6 μL 0.5 mmol	/	/	23

<sup>a</sup> A stock solution of the catalyst (10 mg / mL) was prepared and the desired amount was transferred into separate Schlenk tubes, in which the polymerization was performed.

**8:**

<sup>1</sup>H-NMR (400 MHz, CDCl<sub>3</sub>): δ (ppm) 4.90 (s, 2H, OCH<sub>2</sub>), 4.13–3.89 (m, NCH<sub>2</sub>CH<sub>2</sub>Cl, r.u.), 2.32 (s, 3H, CH<sub>3</sub>).

**MALDI-TOF-MS** *m/z*: C<sub>2</sub>H<sub>3</sub>O(C<sub>5</sub>H<sub>5</sub>NO)<sub>15</sub>C<sub>3</sub>H<sub>3</sub>ONa<sup>+</sup> [M<sub>15</sub>+Na]<sup>+</sup>, calc.: 1703.987, found: 1704.581; H(C<sub>5</sub>H<sub>5</sub>NO)<sub>31</sub>C<sub>3</sub>H<sub>3</sub>ONa<sub>2</sub><sup>2+</sup> [M<sub>31</sub>+2Na]<sup>2+</sup>, calc.: 1686.464, found: 1687.992; H(C<sub>5</sub>H<sub>5</sub>NO)<sub>31</sub>C<sub>3</sub>H<sub>3</sub>OH<sub>2</sub><sup>2+</sup> [M<sub>31</sub>+2H]<sup>2+</sup>, calc.: 1664.482, found: 1664.146.

**9:**

<sup>1</sup>H-NMR (400 MHz, CDCl<sub>3</sub>): δ (ppm) 4.81 (s, 2H, OCH<sub>2</sub>), 4.11 (bs, CH<sub>2</sub>Cl, r.u.), 3.76 (bs, NCH<sub>2</sub>CH<sub>2</sub>Cl, r.u.), 3.69 (bs, CH<sub>2</sub>N, r.u.), 2.56 (s, 1H, C≡CH), 2.34+2.29 (s, 3H, CH<sub>3</sub>), 1.64 (bs, CH<sub>2</sub>CH<sub>2</sub>N, r.u.), 1.30 (bs, CH<sub>2</sub>, r.u.), 0.88 (bs, CH<sub>3</sub>, r.u.).

<sup>13</sup>C-NMR (100 MHz, CDCl<sub>3</sub>): δ (ppm) 156.9 (NCO), 49.1 (NCH<sub>2</sub>, HIC), 41.4 (CH<sub>2</sub>, CIC), 31.6, 28.6, 26.3, 22.7 (CH<sub>2</sub>, HIC), 20.6, 14.1 (CH<sub>3</sub>)

### Determination of copolymerization parameters:

Five copolymerizations of 2-chloroethyl isocyanate (CIC) and n-hexyl isocyanate (HIC) were performed using different feed ratios as indicated in Table 12. The polymerizations were stopped after low conversion and the copolymer composition was determined from integration of NMR spectra.

**Table 12.** Monomer composition in feed and in copolymers.

Entry	Feed composition CIC / HIC		Conversion [%]	Copolymer composition <sup>a</sup>	
	CIC ( $M_1$ )	HIC ( $M_2$ )		CIC ( $m_1$ )	HIC ( $m_2$ )
<b>9c</b>	0.20	0.80	4	0.13	0.87
<b>9d</b>	0.35	0.65	5	0.23	0.77
<b>9e</b>	0.50	0.50	3	0.34	0.66
<b>9f</b>	0.65	0.35	4	0.55	0.45
<b>9g</b>	0.80	0.20	8	0.74	0.26

<sup>a</sup> determined via <sup>1</sup>H-NMR: integration of resonances of HIC at 0.88 to 1.64 ppm and of CIC at 4.10 ppm.

The copolymerization parameters were determined according to Fineman-Ross<sup>[288]</sup> and Kelen-Tüdös<sup>[289]</sup> equations and the corresponding parameters are listed in Table 13.

**Table 13.** Finemann-Ross and Kelen-Tüdös parameters of CIC-HIC copolymer system.

Entry	$F = M_1/M_2$	$f = m_1/m_2$	$G = (F(f-1))/f$	$H = F^2/f$	$\eta = G/(\alpha+H)^1$	$\xi = H/(\alpha+H)^1$
<b>9c</b>	0.25	0.15	-1.45	0.43	-1.58	0.46
<b>9d</b>	0.54	0.30	-1.28	0.98	-0.87	0.66
<b>9e</b>	1.00	0.52	-0.93	1.93	-0.39	0.80
<b>9f</b>	1.86	1.24	0.36	2.79	0.11	0.85
<b>9g</b>	4.00	2.82	2.58	5.68	0.42	0.92

$$^1 \alpha = \sqrt{H_{min} \cdot H_{max}} = \sqrt{0.432 \cdot 5.682} = 1.56$$

Finemann-Ross:<sup>[288]</sup>

$$G = \frac{F(f-1)}{f}; H = \frac{F^2}{f}$$

$$\rightarrow \text{Plot of G against H} \rightarrow \frac{F(f-1)}{f} = r_1 \frac{F^2}{f} - r_2$$

$$y = 0.80x - 2.04$$

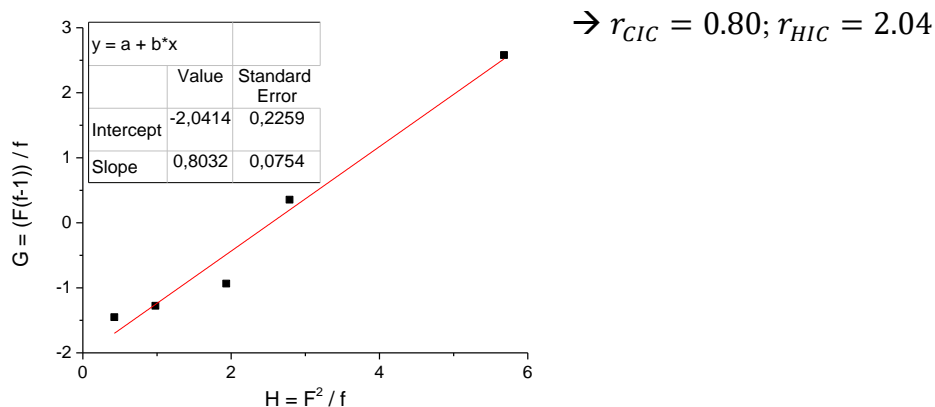


**Figure 56.** Fineman-Ross plot for the determination of copolymerization parameters for CIC-HIC copolymers 9.

Kelen-Tüdös:<sup>[289]</sup>

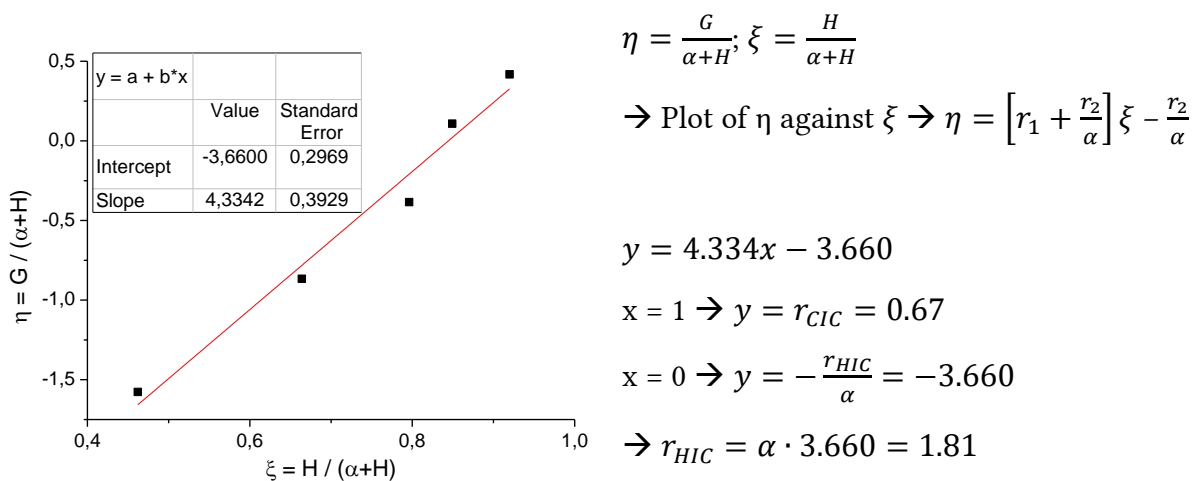
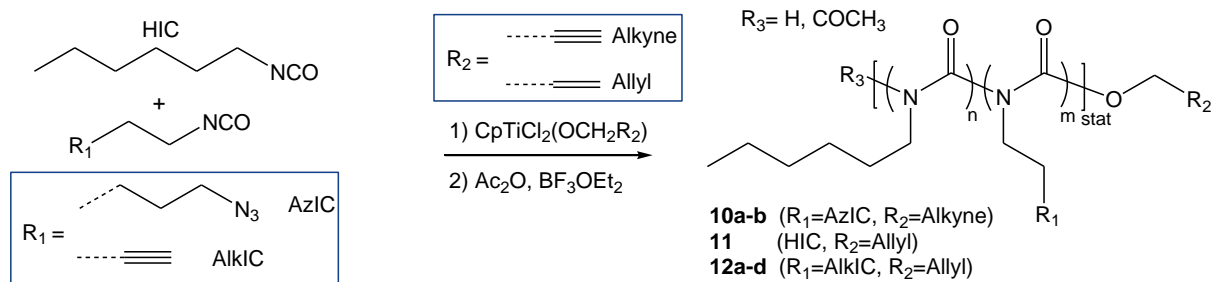


**Figure 57.** Kelen-Tüdös plot for the determination of copolymerization parameters for CIC-HIC copolymers 9.

#### 4.4.3 Copolymerization of functional isocyanates and HIC



**Scheme 32.** Synthesis of copolymers of functional isocyanates (AlkIC/AzIC) and HIC.

The synthesis of random copolymers of functional isocyanates (**AlkIC**, **AzIC**) and HIC was performed similar to the polymerization of HIC (see Scheme 32). Polymerizations **12a-12c** were quenched by the addition of methanol instead of acetic anhydride, resulting in an unprotected N-H terminal group.

**Table 14.** Experimental details for the synthesis of PHIC copolymers.

Entry	CpTiCl <sub>3</sub>	Alcohol	Copolymer	HIC	Ac <sub>2</sub> O [mL]	BF <sub>3</sub> OEt <sub>2</sub> [mL]	Isolated Yield [%]
<b>10a</b>	46.1 mg 0.21 mmol	24.4 μL 0.42 mmol	Azide 60.1 mg 0.4 mmol	572.7 μL 3.9 mol	9.9	0.5	2
<b>10b</b>	46.1 mg 0.21 mmol	24.4 μL 0.42 mmol	Azide 308.3 mg 2.0 mmol	291.0 μL 2.0 mmol	9.9	0.5	/
<b>11</b>	35.0 mg 0.16 mmol	Allyl 11.0 μL 0.16 mmol	/	460.0 μL 3.2 mmol	7.6	0.4	43
<b>12a</b>	26.8 mg 0.12 mmol	14.3 μL 0.25 mmol	Alkyne 47.6 mg 0.5 mmol	291.4 μL 2.0 mmol	/	/	13
<b>12b</b>	24.0 mg 0.11 mmol	12.8 μL 0.22 mmol	Alkyne 190.2 mg 2.0 mmol	72.8 μL 0.5 mmol	/	/	/
<b>12c</b>	29.2 mg 0.13 mmol	15.1 μL 0.26 mmol	Alkyne 142.5 mg 1.5 mmol	218.4 μL 1.5 mmol	/	/	/
<b>12d</b>	107.2 mg 0.49 mmol	57.0 μL 0.98 mmol	Alkyne 190.4 mg 2.0 mmol	1.17 mL 8.0 mmol	20.0	1.8	11

**10a:**

<sup>1</sup>H-NMR (400 MHz, CDCl<sub>3</sub>): δ (ppm) 4.79 (m, 2H, OCH<sub>2</sub>), 3.69 (bs, CH<sub>2</sub>N, r.u.), 3.25 (m, CH<sub>2</sub>N<sub>3</sub> r.u.), 2.51 (m, C≡CH + CH<sub>2</sub>CH<sub>2</sub>N r.u.), 2.28 (s, 3H, CH<sub>3</sub>), 1.91 (m, 1.64, CH<sub>2</sub>CH<sub>2</sub>N<sub>3</sub>), 1.63 (bs, CH<sub>2</sub>CH<sub>2</sub>N, r.u.), 1.30 (bs, CH<sub>2</sub>, r.u.), 0.88 (bs, CH<sub>3</sub>, r.u.).

**11:**

<sup>1</sup>H-NMR (400 MHz, CDCl<sub>3</sub>): δ (ppm) 5.93 (m, 1H, CH=CH<sub>2</sub>), 5.35 (m, 2H, CH=CH<sub>2</sub>), 4.67 (m, 2H, OCH<sub>2</sub>), 3.69 (bs, NCH<sub>2</sub>, r.u.), 2.28 (s, 3H, CH<sub>3</sub>), 1.64 (bs, CH<sub>2</sub>CH<sub>2</sub>N, r.u.), 1.30 (bs, CH<sub>2</sub>, r.u.), 0.88 (bs, CH<sub>3</sub>, r.u.).

**MALDI-TOF-MS** (*m/z*): One series is visible with a maximum corresponding to the sodium adduct of the product containing 23 repeating units: C<sub>2</sub>H<sub>3</sub>O(C<sub>7</sub>H<sub>13</sub>NO)<sub>23</sub>C<sub>3</sub>H<sub>5</sub>O [M+Na]<sup>+</sup>, calc.: 3047.338, found: 3048.079.



**12d:**

<sup>1</sup>H-NMR (400 MHz, CDCl<sub>3</sub>): δ (ppm) 5.94 (m, 1H, CH=CH<sub>2</sub>), 5.35 (m, 2H, CH=CH<sub>2</sub>), 4.68 (m, 2H, OCH<sub>2</sub>), 3.69 (bs, CH<sub>2</sub>N, r.u.), 2.58 (bs, 4H, CH<sub>2</sub>C≡CH), 2.31 + 2.28 (s, 3H, CH<sub>3</sub>), 1.93 (bs, 2H, C≡CH), 1.64 (bs, CH<sub>2</sub>CH<sub>2</sub>N, r.u.), 1.30 (bs, CH<sub>2</sub>, r.u.), 0.88 (bs, CH<sub>3</sub>, r.u.).

**ESI-TOF-MS** (*m/z*): Four single charged series appear around a maximum of *m/z* = 2920.0121 and four double charged series appear around a maximum of *m/z* = 1964.3534. The general molecular formula is: C<sub>2</sub>H<sub>3</sub>O(C<sub>5</sub>H<sub>5</sub>NO)<sub>x</sub>(C<sub>7</sub>H<sub>13</sub>NO)<sub>y</sub>C<sub>3</sub>H<sub>5</sub>O.

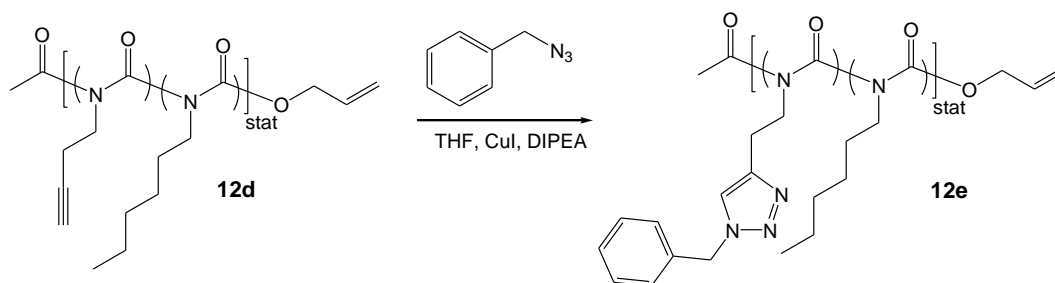
**Table 15.** Overview about different series observed in the ESI-TOF-MS spectrum of **12d**.

<i>m/z</i> measured	<i>m/z</i> simulated	x <sup>1</sup>	y <sup>1</sup>	Molecular formula
1916.829	1916.964	0	29	C <sub>2</sub> H <sub>3</sub> O (C <sub>7</sub> H <sub>13</sub> NO) <sub>30</sub> C <sub>3</sub> H <sub>5</sub> ONa <sub>2</sub>
1900.806	1900.933	1	28	C <sub>2</sub> H <sub>3</sub> O (C <sub>5</sub> H <sub>5</sub> NO) <sub>1</sub> (C <sub>7</sub> H <sub>13</sub> NO) <sub>29</sub> C <sub>3</sub> H <sub>5</sub> ONa <sub>2</sub>
1884.779	1884.902	2	27	C <sub>2</sub> H <sub>3</sub> O (C <sub>5</sub> H <sub>5</sub> NO) <sub>2</sub> (C <sub>7</sub> H <sub>13</sub> NO) <sub>29</sub> C <sub>3</sub> H <sub>5</sub> ONa <sub>2</sub>
1868.748	1868.871	3	26	C <sub>2</sub> H <sub>3</sub> O (C <sub>5</sub> H <sub>5</sub> NO) <sub>3</sub> (C <sub>7</sub> H <sub>13</sub> NO) <sub>28</sub> C <sub>3</sub> H <sub>5</sub> ONa <sub>2</sub>
3175.182	3175.441	0	24	C <sub>2</sub> H <sub>3</sub> O (C <sub>7</sub> H <sub>13</sub> NO) <sub>24</sub> C <sub>3</sub> H <sub>5</sub> ONa
3143.122	3143.378	1	23	C <sub>2</sub> H <sub>3</sub> O (C <sub>5</sub> H <sub>5</sub> NO) <sub>1</sub> (C <sub>7</sub> H <sub>13</sub> NO) <sub>23</sub> C <sub>3</sub> H <sub>5</sub> ONa
3110.062	3110.313	2	22	C <sub>2</sub> H <sub>3</sub> O (C <sub>5</sub> H <sub>5</sub> NO) <sub>2</sub> (C <sub>7</sub> H <sub>13</sub> NO) <sub>22</sub> C <sub>3</sub> H <sub>5</sub> ONa
3206.102	3206.353	3	22	C <sub>2</sub> H <sub>3</sub> O (C <sub>5</sub> H <sub>5</sub> NO) <sub>3</sub> (C <sub>7</sub> H <sub>13</sub> NO) <sub>22</sub> C <sub>3</sub> H <sub>5</sub> ONa

<sup>1</sup> x, y: Number of AlkIC and HIC units

The highest intensity peaks can be attributed to chains lacking the alkyne-functional monomer, while copolymers bearing one to three alkyne isocyanate groups can also be assigned. More than three functional groups in one chain have not been detected, confirming the results from NMR spectroscopy which indicated an average number of two functional groups per polymer chain.

#### 4.4.4 “Click”-reaction of side chain functional polyisocyanate



**Scheme 33.** “Click” reaction of PHIC-PALKIC copolymer **12d** and benzyl azide.

The “click” reaction of side chain functional polyisocyanate **12d** and benzyl azide was performed according to a general literature procedure.<sup>[195]</sup> A Schlenk-flask equipped with a magnetic stir bar was heated under vacuum and flushed with nitrogen several times. Copolymer **12d** (25 mg, 5.2  $\mu\text{mol}$ , 1.0 equiv.), benzyl azide (12.5  $\mu\text{L}$ , 0.1 mmol, 2.0 equiv.) and dry THF (2 mL) were added and the solution was degassed by purging with nitrogen for 30 minutes. CuI (0.1 mg, 0.5  $\mu\text{mol}$ , 0.1 equiv.) and DIPEA (17.5  $\mu\text{L}$ , 104.0  $\mu\text{mol}$ , 2.0 equiv.) were added and the solution was degassed by three freeze-pump-thaw cycles. The mixture was heated to 40 °C for three days, the polymer was precipitated in methanol and analyzed *via* GPC, NMR and MALDI-TOF-MS.

##### **12e:**

**<sup>1</sup>H-NMR** (400 MHz,  $\text{CDCl}_3$ ):  $\delta$  (ppm) 7.44 (m, 1H, C=CH triazole), 7.35–7.23 (m, 5H,  $H_{\text{arom}}$ ), 5.94 (m, 1H, CH=CH<sub>2</sub>), 5.47 (m, 2H, CH<sub>2</sub>-C<sub>6</sub>H<sub>5</sub>), 5.35 (m, 2H, CH=CH<sub>2</sub>), 4.69 (m, 2H, OCH<sub>2</sub>), 3.67 (bs, CH<sub>2</sub>N, r.u.), 3.09 (CH<sub>2</sub>C<sub>triazole</sub>), 2.28+2.24 (s, 3H, CH<sub>3</sub>), 1.93 (bs, 2H, C≡CH), 1.64 (bs, CH<sub>2</sub>CH<sub>2</sub>N, r.u.), 1.30 (bs, CH<sub>2</sub>, r.u.), 0.88 (bs, CH<sub>3</sub>, r.u.).

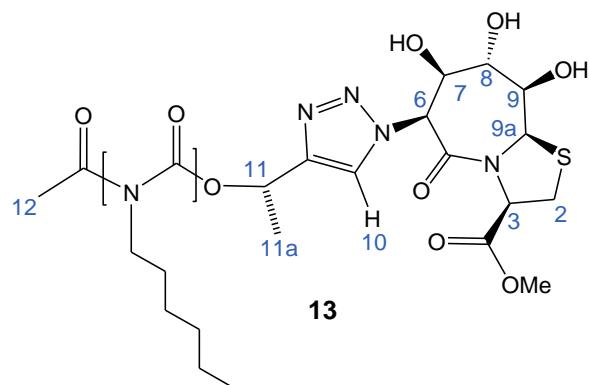
**MALDI-TOF-MS** ( $m/z$ ): Single charged series with a maximum at 2792.972 Da belongs to unfunctionalized PHIC:  $\text{C}_2\text{H}_3\text{O}(\text{C}_7\text{H}_{13}\text{NO})_{21}\text{C}_3\text{H}_5\text{ONa}$  [ $\text{HIC}_{21}+\text{Na}$ ]<sup>+</sup>, simulated 2793.139 Da. Several double charged series could be assigned, with the general molecular formula:  $\text{C}_2\text{H}_3\text{O}(\text{C}_{12}\text{H}_{12}\text{N}_4\text{O})_x(\text{C}_7\text{H}_{13}\text{NO})_y\text{C}_3\text{H}_5\text{O}$

**Table 16.** Overview about different series observed in the MALDI-TOF-MS spectrum of **12e**.

$m/z$ measured	$m/z$ simulated	$x^1$	$y^1$	Molecular formula
1916.864	1916.965	0	29	$\text{C}_2\text{H}_3\text{O}(\text{C}_{12}\text{H}_{12}\text{N}_4\text{O})_0(\text{C}_7\text{H}_{13}\text{NO})_{29}\text{C}_3\text{H}_5\text{ONa}_2$
1903.817	1903.915	1	27	$\text{C}_2\text{H}_3\text{O}(\text{C}_{12}\text{H}_{12}\text{N}_4\text{O})_1(\text{C}_7\text{H}_{13}\text{NO})_{27}\text{C}_3\text{H}_5\text{ONa}_2$
1890.302	1890.866	2	25	$\text{C}_2\text{H}_3\text{O}(\text{C}_{12}\text{H}_{12}\text{N}_4\text{O})_2(\text{C}_7\text{H}_{13}\text{NO})_{25}\text{C}_3\text{H}_5\text{ONa}_2$
1876.357	1877.818	3	23	$\text{C}_2\text{H}_3\text{O}(\text{C}_{12}\text{H}_{12}\text{N}_4\text{O})_3(\text{C}_7\text{H}_{13}\text{NO})_{24}\text{C}_3\text{H}_5\text{ONa}_2$

<sup>1</sup>  $x, y$ : Number of functionalized units and unfunctionalized HIC units .





### **13-A:**

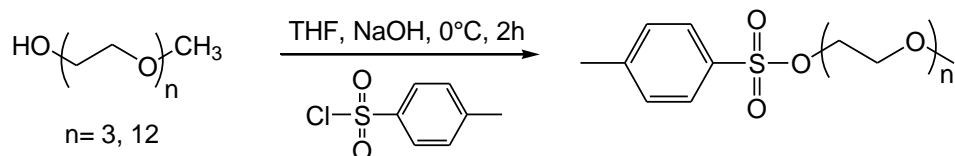
**<sup>1</sup>H-NMR** (400 MHz, CDCl<sub>3</sub>): δ (ppm) 8.14 (s, 1H, CH<sub>triazole</sub>), 6.18 (s, 1H, H-6), 5.74 (s, 1H, H-9a), 5.34 (s, 2H, H-11), 5.08 (s, 1H, H-3), 4.40-4.23 (m, 4H, H-7, H-8, H-9), 3.68 (bs, CH<sub>2</sub>N, r.u.), 3.32 (s, 2H, H-2), 2.27 (s, 3H, H-12), 1.62 (bs, CH<sub>2</sub>CH<sub>2</sub>N, r.u.), 1.29 (bs, CH<sub>2</sub>, r.u.), 0.88 (bs, CH<sub>3</sub>, r.u.).

### **13-R, -S:**

**<sup>1</sup>H-NMR** (400 MHz, CDCl<sub>3</sub>): δ (ppm) 8.07 (s, 1H, CH<sub>triazole</sub>), 6.18 (s, 1H, H-6), 6.07 (s, 1H, H-11), 5.76 (s, 1H, H-9a), 5.11 (s, 1H, H-3), 4.41-4.22 (m, 4H, H-7, H-8, H-9), 3.67 (bs, CH<sub>2</sub>N, r.u.), 3.32 (s, 2H, H-2), 2.27 (s, 3H, H-12), 1.62 (bs, CH<sub>2</sub>CH<sub>2</sub>N, r.u.), 1.29 (bs, CH<sub>2</sub>, r.u.), 0.88 (bs, CH<sub>3</sub>, r.u.).

## **4.6 Synthesis of TEG- / PEG-PHIC copolymers**

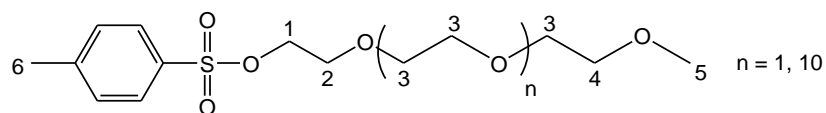
### **4.6.1 Synthesis of azide-functional TEG / PEG**



**Scheme 35.** Synthesis of tosyl-TEG / PEG.

The synthesis of azide-functional TEG was performed in two steps according to literature.<sup>[204-205]</sup> In a 100 mL Schlenk flask with septum, triethylene glycol (TEG, 10.0 g, 60.9 mmol, 1.0 equiv.) was dissolved in THF (25 mL). The solution was degassed by purging with nitrogen for 20 minutes and was cooled to 0 °C. 6 M NaOH (20.3 mL, 121.8 mmol, 2.0 equiv.) was added and a degassed solution of p-toluenesulfonyl chloride (22.1 g, 115.7 mmol, 1.9 equiv.) in THF (20 mL) was added dropwise under stirring. The reaction mixture was stirred for one hour at 0 °C and then for one hour at room temperature. The aqueous phase was extracted with diethylether (two times 50 mL), the combined organic phases were washed with 1 M NaOH and water, separated and dried over Na<sub>2</sub>SO<sub>4</sub>. After filtration and removal of the solvent, tosyl-TEG was obtained as a colorless liquid (19.0 g, 60.0 mmol, 98 %).

Poly(ethylene glycol) (PEG) monomethyl ether (550 g/mol, 10 g, 18.2 mmol), NaOH (6.1 mL, 36.4 mmol), p-TsCl (6.6 g, 34.6 mmol); Yield of tosyl-PEG: 11 g, 16 mmol, 88 %.



n = 1 (tosyl-TEG):

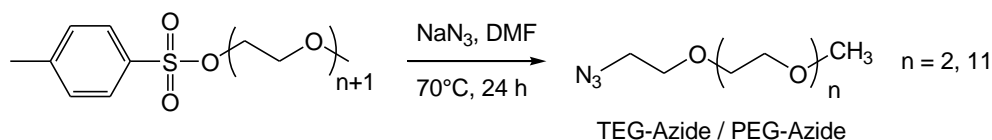
<sup>1</sup>H-NMR (400 MHz, CDCl<sub>3</sub>): δ (ppm) 7.74 (d, *J* = 8.5 Hz, 2H, *H*-arom), 7.29 (d, *J* = 7.9 Hz, 2H, *H*-arom), 4.14–4.08 (m, 2H, *H*-1), 3.65–3.62 (m, 2H, *H*-2), 3.57–3.53 (m, 6H, *H*-3), 3.49–3.46 (m, 2H, *H*-4), 3.31 (s, 3H, OCH<sub>3</sub>), 2.39 (s, 3H, CH<sub>3</sub>).

<sup>13</sup>C-NMR (100 MHz, CDCl<sub>3</sub>): δ (ppm) 144.8, 133.0, 129.8, 127.9 (*C*-arom), 72.0 (*C*-4), 70.6, 70.4 (*C*-3), 69.2, 68.6 (*C*-1, *C*-2), 58.9 (*C*-5), 21.5 (*C*-6).

n = 10 (tosyl-PEG):

<sup>1</sup>H-NMR (400 MHz, CDCl<sub>3</sub>): δ (ppm) 7.77 (d, *J* = 8.3 Hz, 2H, *H*-arom), 7.32 (d, *J* = 8.5 Hz, 2H, *H* arom), 4.15–4.12 (m, 2H, *H*-1), 3.73–3.49 (m, 45H, *H*-2, *H*-3, *H*-4), 3.35 (s, 3H, OCH<sub>3</sub>), 2.42 (s, 3H, CH<sub>3</sub>).

<sup>13</sup>C-NMR (100 MHz, CDCl<sub>3</sub>): δ (ppm) 146.8, 133.0, 130.2, 127.0 (*C*-arom), 71.9 (*C*-4), 70.8–70.4 (*C*-3), 69.3, 68.7 (*C*-1, *C*-2), 58.9 (*C*-5), 21.7 (*C*-6).

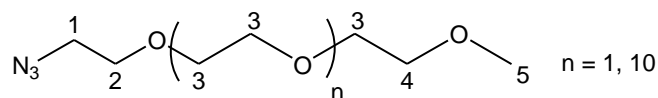


**Scheme 36.** Synthesis of azide-functional TEG / PEG.

In the second step, **Tosyl-TEG** (19.4 g, 60.8 mmol, 1.0 equiv.) was dissolved in DMF (60 mL) and degassed by purging with nitrogen for 20 minutes. Sodium azide (11.8 g, 182.4 mmol, 3.0 equiv.) was added under a counterflow of nitrogen and the reaction mixture was heated under stirring to 70 °C for 24 hours. Water (200 mL) was added and the solution was extracted with DCM (three times 100 mL). The combined organic phases were washed with brine and water (two times 50 mL), dried over Na<sub>2</sub>SO<sub>4</sub> and after filtration the solvent was removed under vacuum to yield 8.2 g (43.3 mmol, 69 %) of **TEG-Azide** as a colorless liquid.

#### PEG-Azide:

Tosyl-PEG (11.1 g, 15.8 mmol, 1.0 equiv.), DMF (60 mL), NaN<sub>3</sub> (3.1 g, 47.4 mmol, 3.0 equiv.). Yield of PEG-Azide: 7.3 g, 13.3 mmol, 84 %.



$n = 1$  (TEG-Azide):

$^1\text{H-NMR}$  (400 MHz,  $\text{CDCl}_3$ ):  $\delta$  (ppm) 3.68–3.64 (m, 8H,  $H-2$ , -3), 3.56–3.53 (m, 2H,  $H-4$ ), 3.39–3.37 (m, 5H,  $H-1$ ,  $H-5$ ).

$^{13}\text{C-NMR}$  (100 MHz,  $\text{CDCl}_3$ ):  $\delta$  (ppm) 72.1 ( $C-4$ ), 70.8–70.7 ( $C-3$ ), 70.2 ( $C-2$ ), 59.1 ( $C-5$ ), 50.8 ( $C-1$ ).

**ESI-TOF-MS** (MeOH)  $m/z$ :  $\text{C}_7\text{H}_{15}\text{N}_3\text{O}_3\text{Na}^+$  [ $\text{M}+\text{Na}$ ] $^+$ , calc.: 212.1006, found: 212.0994.

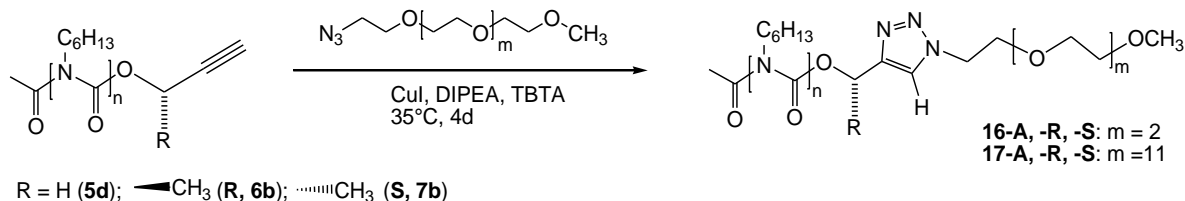
**IR** [ $\text{cm}^{-1}$ ]: 2873 (m), 2099 (s, azide), 1452 (w), 1249 (m), 1107 (s).

$n = 10$  (PEG-Azide):

$^1\text{H-NMR}$  (400 MHz,  $\text{CDCl}_3$ ):  $\delta$  (ppm) 3.67–3.61 (m, 44H,  $H-2$ ,  $H-3$ ), 3.54–3.52 (m, 2H,  $H-4$ ), 3.38–3.36 (m, 5H,  $H-1$ ,  $H-5$ ).

$^{13}\text{C-NMR}$  (100 MHz,  $\text{CDCl}_3$ ):  $\delta$  (ppm) 72.1 ( $C-4$ ), 70.8–70.6 ( $C-3$ ), 70.1 ( $C-2$ ), 59.1 ( $C-5$ ), 50.8 ( $C-1$ ).

#### 4.6.2 Synthesis of PEG-PHIC copolymers



**Scheme 37.** Synthesis of TEG- / PEG-PHIC copolymers **16-A, -R, -S** and **17-A, -R, -S**.

The procedure for the synthesis of TEG / PEG-PHIC copolymers was adapted from general literature procedures.<sup>[195]</sup> A Schlenk flask was charged with PHIC (1.0 equiv.) and TEG/PEG-azide (2.0 equiv.). THF (4 mL) was added and the solution was degassed by purging with nitrogen for 30 minutes. CuI (0.05 equiv.), DIPEA (2.0 equiv.) and TBTA (0.05 equiv.), were added under a stream of nitrogen and the solution was further degassed for 15 minutes. The reaction mixture was stirred at 35 °C for two days, then the solvent was removed under vacuo and the crude product was purified by column chromatography on silica. Unreacted PHIC was removed by using *n*-hexane / EA 10:1 or  $\text{CHCl}_3$ . Functionalized PHICs were obtained by switching the solvent mixture to *n*-hexane / EA 2:1 ( $R_f = 0.4$  (TEG-PHIC); 0.1 (PEG-PHIC)).

**Table 18.** Experimental details for the synthesis of TEG- / PEG-PHIC copolymers.

Entry	PHIC (5), (6), (7)		TEG / PEG-Azide (2.0 equiv.)	CuI (0.05 equiv.) [mg]	DIPEA (2.0 equiv.) [μL]	TBTA (0.05 equiv.) [mg]	Isolated yield [mg / %]
	$M_n$ (NMR)	m, n					
16-A	5d 5.0 kDa	300 mg 60 μmol	TEG 22 mg 120 μmol	0.57	20	1.6	80; 27
17-A		300 mg 60 μmol	PEG 66 mg 120 μmol				150; 45
16-R	6b 5.4 kDa	400 mg 74 μmol	TEG 29 mg 148 μmol	0.73	26	2.0	8; 2
17-R		400 mg 74 μmol	PEG 84 mg 148 μmol				11; 3
16-S	7b 5.3 kDa	400 mg 75 μmol	TEG 29 mg 150 μmol	0.72	26	2.0	6; 2
17-S		400 mg 75 μmol	PEG 83 mg 150 μmol				7; 2

**16-A:**

<sup>1</sup>H-NMR (400 MHz, CDCl<sub>3</sub>): δ (ppm) 7.84 (s, 1H, C=CH), 5.32 (s, 2H, OCH<sub>2</sub>), 4.55 (t, *J* = 4.7 Hz, 2H, NCH<sub>2</sub>), 3.88 (t, *J* = 5.0 Hz, 2H, NCH<sub>2</sub>CH<sub>2</sub>O), 3.80-3.54 (bs, CH<sub>2</sub>CH<sub>2</sub>O, r.u. and CH<sub>2</sub>N, r.u.), 3.37 (s, 3H, OCH<sub>3</sub>), 2.27 (s, 3H, CH<sub>3</sub>), 1.62 (bs, CH<sub>2</sub>CH<sub>2</sub>N, r.u.), 1.29 (bs, CH<sub>2</sub>, r.u.), 0.88 (bs, CH<sub>3</sub>, r.u.).

**16-R, -S:**

<sup>1</sup>H-NMR (400 MHz, CDCl<sub>3</sub>): δ (ppm) 7.74 (s, 1H, C=CH), 6.06 (s, 1H, OCH), 4.55 (m, 2H, NCH<sub>2</sub>), 3.88 (t, *J* = 5.1 Hz, 2H, NCH<sub>2</sub>CH<sub>2</sub>O), 3.80-3.50 (bs, CH<sub>2</sub>CH<sub>2</sub>O, r.u. + CH<sub>2</sub>N, r.u.), 3.38 (s, 3H, OCH<sub>3</sub>), 2.28 (s, 3H, CH<sub>3</sub>), 1.62 (bs, CH<sub>2</sub>CH<sub>2</sub>N, r.u.), 1.29 (bs, CH<sub>2</sub>, r.u.), 0.88 (bs, CH<sub>3</sub>, r.u.).

**17-A:**

<sup>1</sup>H-NMR (400 MHz, CDCl<sub>3</sub>): δ (ppm) 7.82 (s, 1H, C=CH), 5.32 (s, 2H, OCH<sub>2</sub>), 4.55 (t, *J* = 4.9 Hz, 2H, NCH<sub>2</sub>), 3.88 (t, *J* = 5.0 Hz, 2H, NCH<sub>2</sub>CH<sub>2</sub>O), 3.70-3.54 (CH<sub>2</sub>CH<sub>2</sub>O, r.u. + CH<sub>2</sub>N, r.u.), 3.37 (s, 3H, OCH<sub>3</sub>), 2.27 (s, 3H, CH<sub>3</sub>), 1.62 (bs, CH<sub>2</sub>CH<sub>2</sub>N, r.u.), 1.29 (bs, CH<sub>2</sub>, r.u.), 0.88 (bs, CH<sub>3</sub>, r.u.).

<sup>13</sup>C-NMR (100 MHz, CDCl<sub>3</sub>): δ (ppm) 156.9 (NCO), 70.7 (OCH<sub>2</sub>), 59.2 (OCH<sub>3</sub>), 48.7 (NCH<sub>2</sub>), 31.6, 28.6, 26.4, 22.7 (CH<sub>2</sub>), 14.1 (CH<sub>3</sub>)

**ESI-TOF-MS:** Several high molecular weight double charged series appear with a distance of 63.6 Da around a maximum of  $m/z = 2355.083$ . Several low molecular weight triple charged series appear with a distance of 42.4 Da around a maximum of  $m/z = 1592.412$ . The series can be assigned to products containing different numbers of EO units and HIC units. Examples of assigned series are given below:

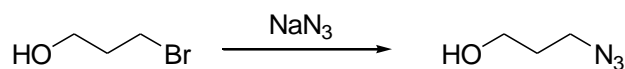
$m/z$ measured	$m/z$ simulated	Number of EO units	Number of HIC units	Molecular formula
1576.087	1576.507	7	33	$C_{206}H_{371}N_{31}O_{30}Na_2$
1578.080	1578.167	10	32	$C_{206}H_{371}N_{31}O_{30}Na_2$
1579.075	1579.492	13	31	$C_{204}H_{357}N_{33}O_{29}Na_2$

### 17-R, -S:

**$^1H$ -NMR** (400 MHz,  $CDCl_3$ ):  $\delta$  (ppm) 7.73 (s, 1H, C=CH), 6.05 (s, 1H, OCH), 4.54 (m, 2H, NCH<sub>2</sub>), 3.88 (t,  $J = 5.2$  Hz, 2H, NCH<sub>2</sub>CH<sub>2</sub>O), 3.80-3.54 (CH<sub>2</sub>CH<sub>2</sub>O, r.u. + CH<sub>2</sub>N, r.u.), 3.38 (s, 3H, OCH<sub>3</sub>), 2.28 (s, 3H, CH<sub>3</sub>), 1.62 (bs, CH<sub>2</sub>CH<sub>2</sub>N, r.u.), 1.29 (bs, CH<sub>2</sub>, r.u.), 0.88 (bs, CH<sub>3</sub>, r.u.).

## 4.7 Synthesis of rhodamine-labeled PHIC

### 4.7.1 Synthesis of azide-functionalized rhodamine



**Scheme 38.** Synthesis of 1-azido-3-propanol.

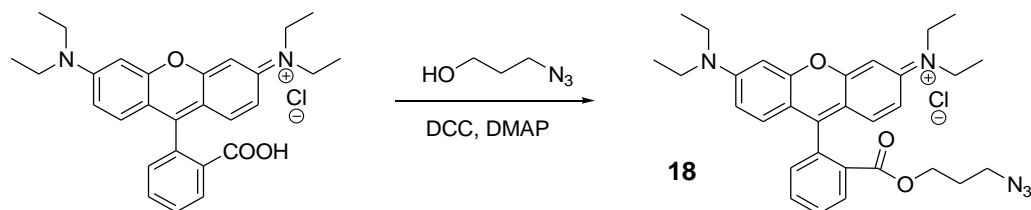
The synthesis of 1-azido-3-propanol was performed according to literature.<sup>[290]</sup> 1-Bromo-3-propanol (3.2 g, 2.1 mL, 23.0 mmol, 1.0 equiv.) was dissolved in DMF (20 mL) and sodium azide (4.5 g, 69.0 mmol, 3.0 equiv.) was added. The reaction mixture was heated under stirring to 50 °C for 24 hours. Afterwards, the mixture was filtered and the solvent was removed under vacuo. The resulting liquid was dissolved in EA (100 mL) and washed with water (100 mL) and brine (100 mL). The organic phase was dried over Na<sub>2</sub>SO<sub>4</sub>, filtered and the solvent was removed under vacuum, yielding a colorless liquid (1.6 g, 16.0 mmol, 70 %).

**$^1H$ -NMR** ( $CDCl_3$ , 400 MHz):  $\delta$  (ppm) 3.75 (bs, 2H, CH<sub>2</sub>OH), 3.45 (t,  $J = 6.6$  Hz, 2H, CH<sub>2</sub>N<sub>3</sub>), 1.83 (p,  $J = 6.5$  Hz, 2H, CH<sub>2</sub>CH<sub>2</sub>CH<sub>2</sub>), 1.63 (bs, 1H, OH).

**$^{13}C$ -NMR** ( $CDCl_3$ , 100 MHz):  $\delta$  (ppm) 60.2 (CH<sub>2</sub>OH), 48.7 (CH<sub>2</sub>), 31.6 (CH<sub>2</sub>N<sub>3</sub>).

**IR** [ $cm^{-1}$ ]: 3349 (b), 2947 (w), 2882 (w), 2092 (s, azide), 1259 (w), 1049 (w).



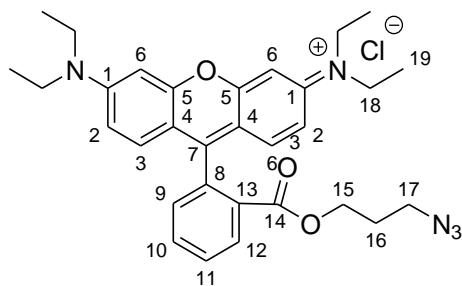


**Scheme 39.** Synthesis of 1-azido-3-propylrhodamine ester (**18**).

The reaction was performed similar to a previously reported literature.<sup>[290]</sup> In a Schlenk-flask, rhodamine B (2.0 g, 4.2 mmol, 1.0 equiv.) was dissolved in dry DCM (50 mL) under an argon atmosphere. 1-Azido-3-propanol (460 mg, 4.6 mmol, 1.1 equiv.) and DMAP (48 mg, 0.4 mmol, 0.1 equiv.) were added, and the solution was cooled to 0 °C. DCC (1.74 g, 8.4 mmol, 2.0 equiv.) was added and the solution was stirred and warmed to room temperature overnight. The white precipitate was filtered off, DCM (50 mL) was added and the organic phase was washed with NaHCO<sub>3</sub> (two times 100 mL) and water (100 mL). The organic phase was dried over Na<sub>2</sub>SO<sub>4</sub>, filtered and the solvent was removed in vacuo. The resulting dark violet solid was purified using silica gel column chromatography (DCM / MeOH = 20:1; *R<sub>f</sub>* = 0.2). After removal of the solvent, a dark violet solid was obtained (1.5 g, 2.9 mmol, 70 %).

**<sup>1</sup>H-NMR** (CDCl<sub>3</sub>, 400 MHz):  $\delta$  (ppm) 8.27 (dd, *J* = 7.9, 1.0 Hz, 1H, *H*-12), 7.82 (td, *J* = 7.5, 1.3 Hz, 1H, *H*-9), 7.74 (td, *J* = 7.7, 1.3 Hz, 1H, *H*-10), 7.33 (dd, *J* = 7.9, 1.2 Hz, 1H, *H*-11), 7.06 (d, *J* = 9.5 Hz, 2H, *H*-3), 6.89 (dd, *J* = 9.5, 2.4 Hz, 2H, *H*-2), 6.87 (d, *J* = 2.4 Hz, 2H, *H*-6), 4.11 (t, 2H, *H*-15), 3.59 (q, *J* = 7.2 Hz, 8H, *H*-18), 3.16 (t, *J* = 6.6 Hz, 2H, *H*-17), 1.70 (p, 2H, *H*-16), 1.32 (t, *J* = 7.1 Hz, 12H, *H*-19).

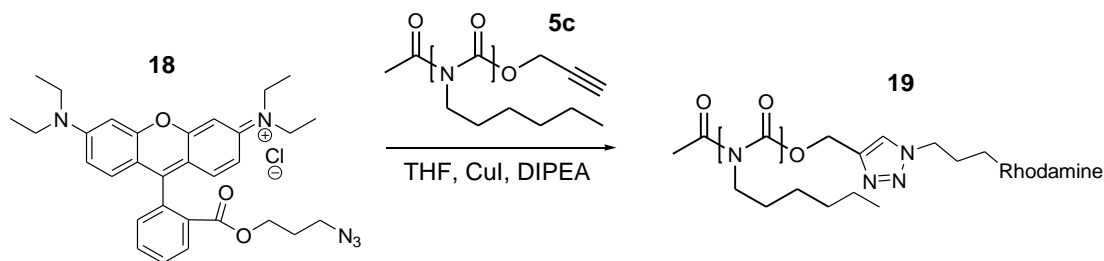
**<sup>13</sup>C-NMR** (CDCl<sub>3</sub>, 100 MHz):  $\delta$  (ppm) 165.1 (*C*-14), 158.7, 157.9, 155.7 (*C*-7, *C*-1, *C*-5), 133.6 (*C*-9), 131.5 (*C*-12), 131.3 (*C*-3), 130.6 (*C*-10), 130.5 (*C*-11), 129.9 (*C*-8), 114.4 (*C*-2), 113.6 (*C*-4), 96.7 (*C*-6), 62.7 (*C*-15), 48.1 (*C*-17), 46.2 (*C*-18), 28.1 (*C*-16), 12.8 (*C*-19).



**ESI-TOF-MS** (MeOH) *m/z*: C<sub>31</sub>H<sub>36</sub>N<sub>5</sub>O<sub>3</sub> [M-Cl]<sup>+</sup>, calc.: 526.2818, found: 526.2807; C<sub>29</sub>H<sub>34</sub>N<sub>5</sub>O<sub>3</sub> [M-Cl-C<sub>2</sub>H<sub>2</sub>]<sup>+</sup>, calc.: 498.2505, found: 498.2505 (Cleavage of one ethylene group); C<sub>27</sub>H<sub>32</sub>N<sub>5</sub>O<sub>3</sub> [M-Cl-2(C<sub>2</sub>H<sub>2</sub>)]<sup>+</sup>, calc.: 470.2192, found: 471.2591 (Cleavage of two ethylene groups).

**IR** [cm<sup>-1</sup>]: 3433 (b), 2973 (w), 2923 (w), 2097 (m, azide), 1772 (m), 1718 (m), 1590 (s), 1415 (s), 1339 (m), 1181 (m), 1132 (w), 1074 (w).

#### 4.7.2 “Click” reaction of rhodamine-azide with PHIC

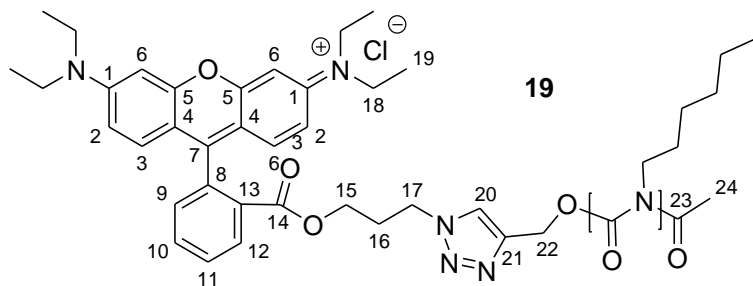


**Scheme 40.** Synthesis of rhodamine-labeled PHIC **19**.

The procedure was adapted from a general literature procedure<sup>[195]</sup> according to Scheme 40. A dry Schlenk flask was charged with PHIC **5c** (200.0 mg, 4.5 kDa, 44.0  $\mu\text{mol}$ , 1.0 equiv.) and rhodamine-azide **18** (29.7 mg, 53.0  $\mu\text{mol}$ , 1.2 equiv.). THF (4 mL) was added and the solution was degassed by bubbling with nitrogen for 30 minutes. CuI (0.9 mg, 4.4  $\mu\text{mol}$ , 0.1 equiv.) and DIPEA (16.0  $\mu\text{L}$ , 88.0  $\mu\text{mol}$ , 2.0 equiv.) were added under a stream of nitrogen and the solution was further degassed for 15 minutes. The reaction mixture was stirred at 35  $^{\circ}\text{C}$  for 24 hours, then the solvent was removed under vacuo and the crude product was purified by silica gel column chromatography (DCM / MeOH 100:1,  $R_f$  = 0.2) to obtain **19** as a violet solid product (25 mg, 11 %).

**$^1\text{H-NMR}$**  ( $\text{CDCl}_3$ , 400 MHz):  $\delta$  (ppm) 8.30 (bs, 2H, *H*-12, *H*-20), 7.78–7.76 (m, 2H, *H*-9, *H*-10), 7.29 (m, 1H, *H*-11), 7.11 (d,  $J$  = 9.5 Hz, 2H, *H*-3), 6.90 (dd,  $J$  = 9.5, 2.4 Hz, 2H, *H*-2), 6.83 (d,  $J$  = 2.4 Hz, 2H, *H*-6), 5.29 (bs, 2H, *H*-22), 4.38 (bs, 2H, *H*-15), 4.13 (t,  $J$  = 6.0 Hz, 2H, *H*-17), 3.69 (bs,  $\text{CH}_2\text{N}$ , r.u.), 3.62 (q,  $J$  = 7.5 Hz, 8H, *H*-18), 2.27 (s, 3H,  $\text{COCH}_3$ ), 2.14 (p,  $J$  = 6.5 Hz, 2H, *H*-16), 1.61 (bs,  $\text{CH}_2\text{CH}_2\text{N}$ , r.u.), 1.31 (m, *H*-19, overlapping), 1.28 (bs,  $\text{CH}_2$ , r.u.), 0.87 (bs,  $\text{CH}_3$ , r.u.).

**$^{13}\text{C-NMR}$**  ( $\text{CDCl}_3$ , 100 MHz):  $\delta$  (ppm) 165.0 (*C*-14), 159.9, 157.9, 155.8 (*C*-7, *C*-1, *C*-5), 156.9 (NCO), 131.5 (*C*-12, *C*-3), 130.7 (*C*-10, *C*-11), 114.5 (*C*-2), 113.7 (*C*-4), 96.6 (*C*-6), 48.7 (*C* r.u.), 46.2 (*C*-18), 31.6 + 28.5 + 26.4 + 22.7 + 14.1 (*C* r.u.), 12.7 (*C*-19).



**MALDI-TOF-MS** ( $m/z$ ):  $\text{C}_2\text{H}_3\text{O}(\text{C}_7\text{H}_{13}\text{NO})_{27}\text{C}_{34}\text{H}_{39}\text{N}_5\text{O}_4$   $[\text{M}-\text{Cl}]^+$ , calc.: 4058.017, found: 4057.218.

## 4.8 Synthesis of $\beta$ -turn mimetic peptide conjugates

The synthesis of  $A\beta_{40}$  and of peptide conjugates containing  $A\beta_{40}$  and  $A\beta_{16-35}$  sequences was performed with standard Fmoc solid-phase peptide synthesis (SPPS) on a CEM microwave peptide synthesizer LibertyBlue. Therefore, PHB-TentaGel resins (0.19 mmol/g) were used on a 0.05 mmolar scale. The Fmoc-protecting groups were removed using 20 % piperidine in DMF (0.1 % Oxyma, 1.5 min, 90 °C). Then, washing with DMF and subsequent coupling with the desired amino acid (3 equiv.) was performed, using  $N,N'$ -diisopropylcarbodiimide (DIC, 3 equiv.) as coupling agent and ethyl 2-cyano-2-(hydroxyimino)acetate (Oxyma, 3 equiv.) as additive. Couplings were performed at elevated temperature (90 °C) for three minutes (ten minutes for His, Gly) and Arg couplings were performed twice.

Introduction of the  $\beta$ -turn mimetics was achieved outside of the synthesizer, using DMF as solvent with a slightly modified procedure. Coupling was achieved in 12 hours at room temperature under gentle stirring, using HOBt (3 equiv.), DIC (3 equiv.) and the desired Fmoc-protected turn mimetic (3 equiv.). As coupling of Fmoc-4-ABA failed with the standard procedure, coupling was performed using DCM as solvent and DIC (3 equiv.) as coupling reagent.

After confirmation of the successful coupling by MALDI-TOF-MS, the remaining amino acids were coupled as described above. Final side chain deprotection and cleavage from the resin was achieved at room temperature in three hours using a mixture of TFA, triisopropylsilane, water and phenol (92.5 : 2.5 : 2.5 : 2.5 Vol%).

Purification of the peptides was performed using preparative reversed phase HPLC with water (A) and acetonitrile (B) as mobile phases, both containing 0.1 % TFA. The sample were dissolved in DMSO and eluted with a linear gradient from 5 % B to 90 % B in 90 minutes. The final peptide was characterized by HPLC (Dionex Ultimate 3000) using a PLRP-S column and the same gradient used for preparative HPLC with a time range of 15 minutes. Furthermore, MALDI-TOF-MS was conducted showing the single charged  $[M+H]^+$  peak and the double charged  $[M+2H]^{2+}$  peak as summarized in Table 19. Coupling with turn mimetic 4 resulted in higher yields than coupling with turn mimetic 3.

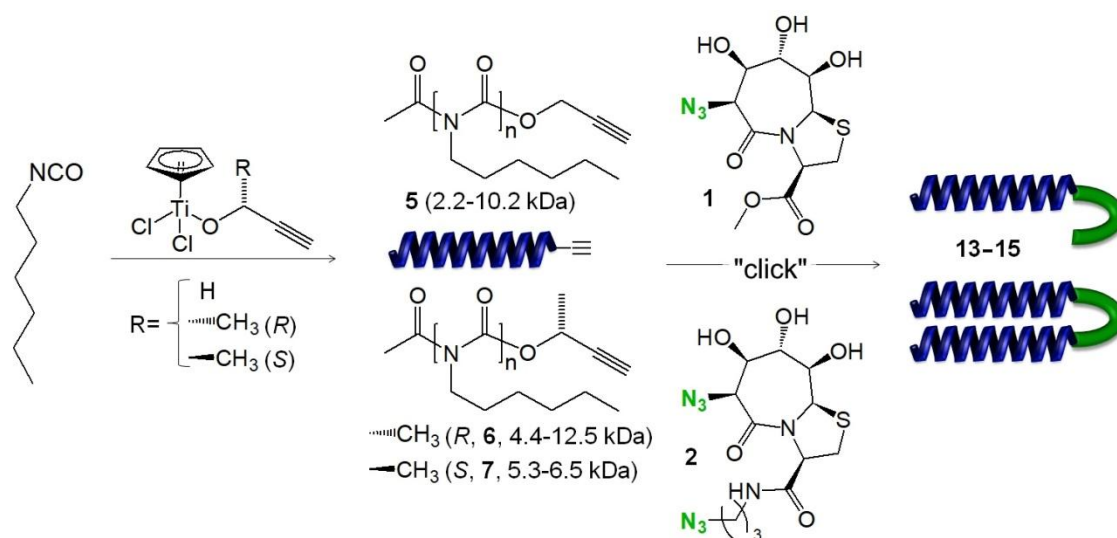
**Table 19.** Overview about synthesized peptide conjugates **20–24**.

Entry	Replaced amino acids	Peptide sequence	Turn structure	$[M+H]^+$	$[M+H]^+$	$[M+2H]^{2+}$	$[M+H]^{2+}$
				measured	simulated	measured	simulated
<b>20a</b>	G25-S26	A $\beta_{40}$	<b>3</b>	4455.410	4456.175	2228.724	2228.592
<b>20b</b>	G25-S26	A $\beta_{16-35}$	<b>3</b>	2235.848	2236.158	1118.364	1118.583
<b>20c</b>	S26-N27	A $\beta_{40}$	<b>3</b>	4398.351	4399.154	2200.243	2200.080
<b>20d</b>	N27-K28	A $\beta_{40}$	<b>3</b>	4357.400	4358.091	2179.796	2179.549
<b>21a</b>	G25-S26	A $\beta_{40}$	<b>4</b>	4447.539	4448.193	2224.807	2224.600
<b>21b</b>	G25-S26	A $\beta_{16-35}$	<b>4</b>	2227.980	2228.176	1114.421	1114.592
<b>21c</b>	S26-N27	A $\beta_{40}$	<b>4</b>	4390.484	4391.172	2196.119	2196.090
<b>21d</b>	V24-G25	A $\beta_{40}$	<b>4</b>	4435.520	4436.157	2218.311	2218.582
<b>22</b>	G25-S26	A $\beta_{40}$	5-AVA	4284.522	4285.176	2142.810	2143.092
<b>23</b>	G25-S26	A $\beta_{40}$	4-ABA	4304.237	4305.145	2152.623	2153.076
<b>24</b>	G25-S26	A $\beta_{40}$	3-ABA	4305.240	4305.145	2153.078	2153.076
A $\beta_{40}$	/	A $\beta_{40}$	/	4329.839	4330.162	2165.575	2165.584

## 5 Summary

In the scope of this thesis,  $\beta$ -turn mimetics bearing different functional groups were designed to be used for the attachment of polymers and the embedding into peptides, enabling further structural investigations concerning chirality of polymer conjugates and aggregation behavior of the peptide conjugates.

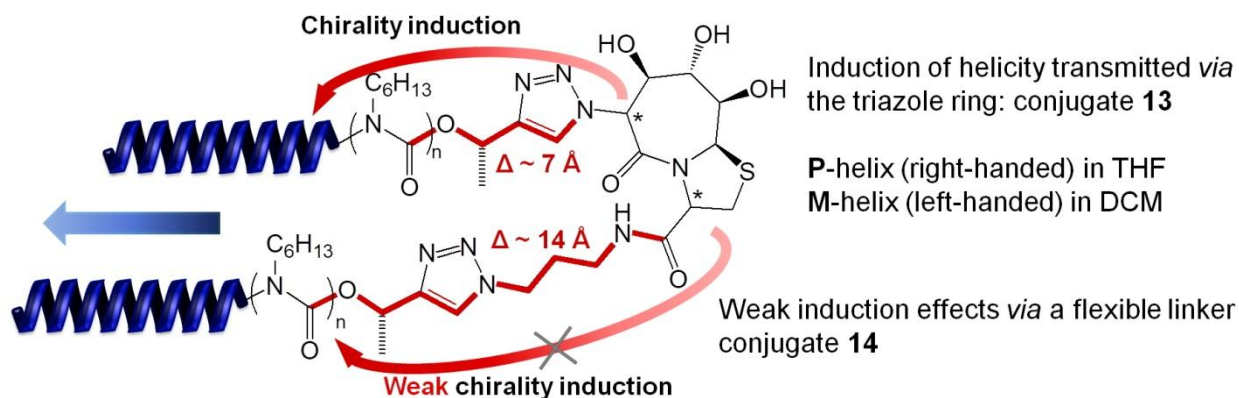
Helical polyisocyanates with different molecular weights ( $M_n = 2200$ – $12500$  g/mol; PDI = 1.08–1.23), helicity and side chain functionality were synthesized by titanium-catalyzed coordination polymerization, enabling the introduction of an alkyne moiety and a chiral center on one side, while quenching with acetic anhydride and boron trifluoride resulted in an acetyl end-capped polymer (see Scheme 41, 5–7).



**Scheme 41.** Synthetic pathway for the  $\beta$ -turn mimetic polymer conjugates (**13–15**). Alkyne-functionalized poly(*n*-hexyl isocyanate)s (PHICs) (**5–7**) with different chirality were synthesized *via* titanium-catalyzed polymerization. Subsequent "click" reaction with  $\beta$ -turn mimetics **1** or **2** yielded the final polymer conjugates **13–15**.

$\beta$ -Turn mimetics **1** and **2** containing a rigid bicyclic structure and either one or two azide functionalities for further modification were synthesized and subsequently linked to PHICs of different helicity *via* CuAAC "click" reaction to yield conjugates **13–15**. The successful coupling was shown by HPLC, GPC, NMR-spectroscopy and mass spectrometry methods. As a comparison to the  $\beta$ -turn mimetic PHICs and to investigate whether a simple hydrophilic linker provides similar structural effects as a rigid hydrophilic  $\beta$ -turn mimetic, linkage to triethylene glycol (TEG) or poly(ethylene glycol) (PEG) was performed to obtain amphiphilic block-copolymers **16** and **17**. Furthermore, side chain functional PICs were synthesized to investigate the ability for modifications in the side chain. Copolymerizations of HIC with 2-chloroethyl isocyanate (CIC) and an alkyne-functional monomer were successfully conducted and the copolymerization parameters of the former were determined. Furthermore, "click" coupling in the side chain was successful.

Helical PHICs, their  $\beta$ -turn mimetic conjugates and block-copolymers bearing ethylene oxide chains were investigated in view of their helicity and were thus subjected to circular dichroism studies. A molecular weight influence on the helicity of pure PHIC was observable in THF, revealing the dynamic nature of the helix. Thus, one chiral end group is sufficient to induce helicity in the polymer chain up to about 5 kDa. Furthermore, chirality induction of the  $\beta$ -turn mimetic on the polymer chain was investigated in different solvents. Achiral PHIC exhibited helicity upon linkage to the  $\beta$ -turn mimetic *via* a triazole moiety (**15-A**, see Scheme 42). The resulting signal in CD spectroscopy was much stronger than for the pure  $\beta$ -turn mimetic, indicating that the sergeant and soldiers principle applies and thus one chiral linker in a distance of about 7 Å is sufficient to induce chirality in the polymer chain.



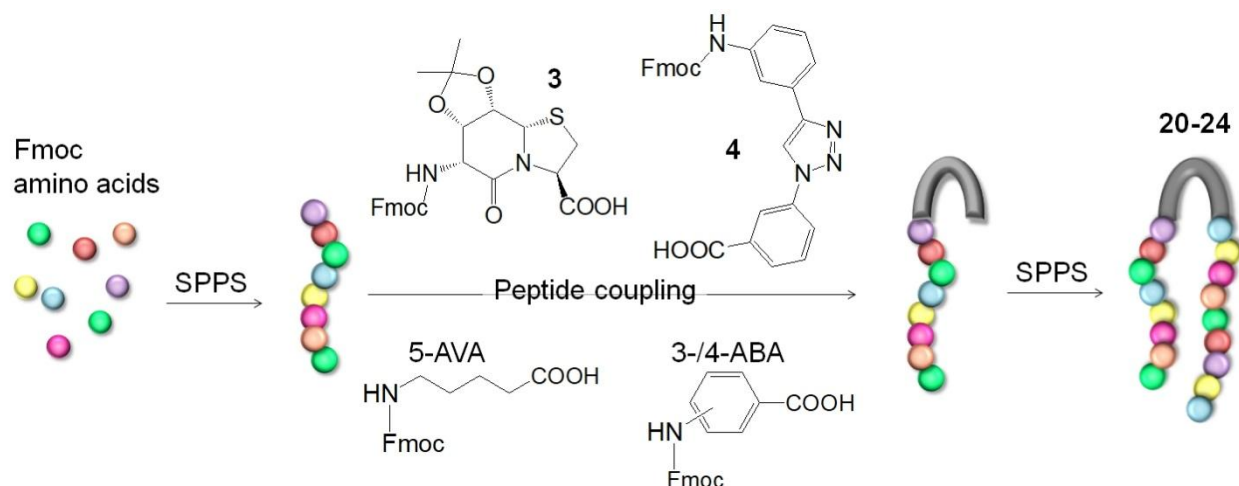
**Scheme 42.** Induction effects in  $\beta$ -turn mimetic polymer conjugates. A rigid triazole moiety linking the  $\beta$ -turn mimetic and helical PHIC transmits chirality and induces a preferred helical sense in the polymer chain depending on the solvent. In THF a right-handed helix is obtained, while in DCM a left-handed helix is obtained. Only a weak influence on chirality is observable upon attachment *via* a flexible linker and longer distance between the chiral  $\beta$ -turn mimetic and the polymer backbone.

Additionally, the attachment of a polymer chain to the  $\beta$ -turn mimetic *via* a flexible linker with a distance of 14 Å results in a preferred handedness of the helix. However this effect is only visible in DCM, whereas in THF only weak induction effects occur, which can be attributed to a donor effect in THF. Interestingly, also chiral PHICs were influenced by the  $\beta$ -turn mimetic, resulting in a right-handed helix in THF and a left-handed helix in DCM for all one-arm conjugates **13** attached to the  $\beta$ -turn mimetic *via* the short triazole linker. However, introducing a flexible linker in between the  $\beta$ -turn mimetic and the polymer chain (conjugates **14**) and thus increasing the distance to the chiral center, results in weak induction effects.

Moreover, also amphiphilic copolymers with TEG / PEO units revealed solvent-dependent behavior. In THF, weak signals were observed in CD spectra of the copolymers, thus indicating the vanishing of a preferred helical sense, while this effect was less pronounced in DCM. Interestingly, in *n*-hexane an inversion of the signal occurred, which can relate to the low solubility of the EO chains in this solvents, inducing an inversion of the helical sense in the copolymers.

Further investigations were carried out at the air / water interface recording surface pressure-area isotherms using a Langmuir-Blodgett trough. At low surface pressures, the surface area per molecule could be correlated with the helix of PHIC lying flat on the surface, while at higher surface pressures multilayers are formed. Helices standing straight on the surface could be excluded according to the obtained values for the surface area per molecule. Attachment of hydrophilic  $\beta$ -turn mimetics or ethylene glycol chains resulted in a higher stability of the monolayer, indicated by a higher surface pressure that is reached in comparison to pure PHIC due to the anchoring to the water surface by the hydrophilic molecules. Furthermore, a rhodamine-labeled PHIC dye was synthesized for epifluorescence measurements at the air / water interface. The images taken during compression of a monolayer reveal a more homogeneous distribution of the dye for the  $\beta$ -turn mimetic conjugates in comparison to the pure PHIC due to the attachment of a hydrophilic moiety.

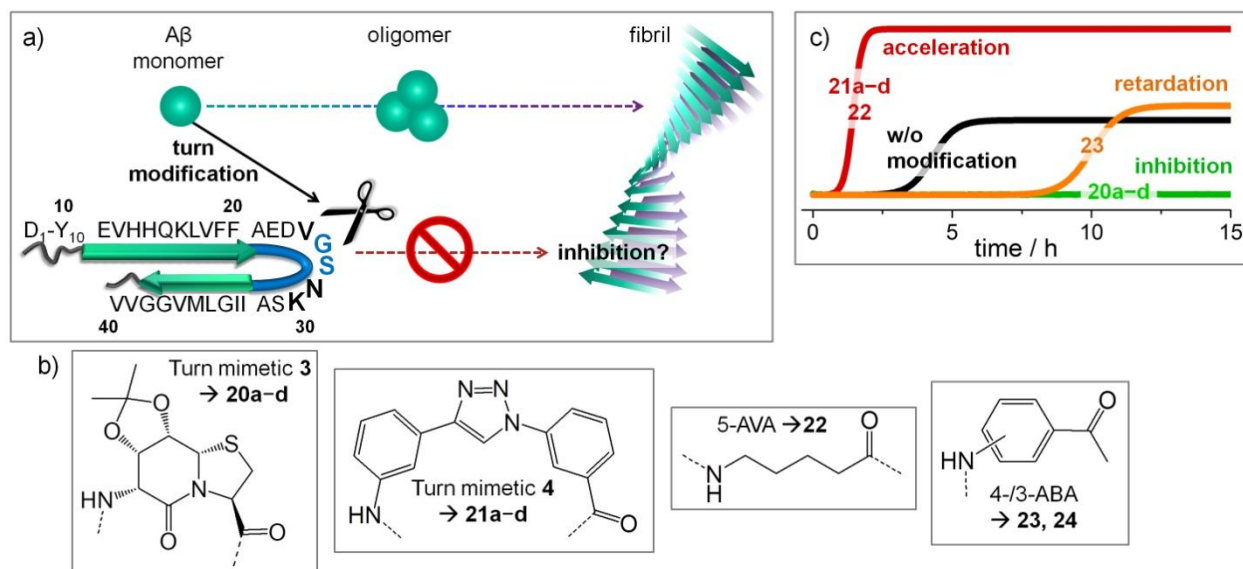
In the peptide approach (see Scheme 43), amyloid  $\beta$  (1–40) peptide sequences were synthesized *via* solid phase peptide synthesis (SPPS), followed by peptide coupling with  $\beta$ -turn mimetics and further elongation *via* SPPS to yield the final  $\beta$ -turn mimetic peptide-conjugates, which were analyzed *via* HPLC and MALDI-TOF mass spectrometry after purification.



**Scheme 43.** Synthetic pathways for the  $\beta$ -turn mimetic peptide-conjugates (20–24). Peptides were synthesized by Fmoc solid phase peptide synthesis (SPPS) followed by introduction of the  $\beta$ -turn mimetics 3, 4, 5-AVA and 3-/4-ABA and further elongation by SPPS yielding peptide conjugates 20–24.

$\beta$ -Turn mimetic peptide conjugates were investigated regarding their aggregation behavior. Therefore, ThT assays were performed, revealing the influence of turn structure on the fibrillation propensity. Thus,  $\beta$ -turn mimetic conjugates 21a–d, containing an aromatic TAA turn mimetic 4, showed fast aggregation and high fluorescence intensity, indicating that the formation of  $\beta$ -sheet structure is facilitated. In contrast,  $\beta$ -turn mimetic conjugates 20a–d, containing a bicyclic BTD turn mimetic 3 lacked the ability to fibrillate, as shown by a low fluorescence in ThT assays and random coil structure in CD spectroscopy. Furthermore, implementing a flexible linker as in conjugate 22 resulted in a fast aggregation, whereas rigid

aromatic linkers introduced in conjugates **23** and **24** increased the lag time. Hence, the rigidity, hydrophobicity and exact structure of the turn affect the fibrillation propensity of amyloid  $\beta$  peptides and should thus also influence the  $\beta$ -sheet structure of the formed fibrils. This was further investigated using circular dichroism spectroscopy, revealing slight shift in the minimum around 218 nm which can be attributed to the formation of  $\beta$ -sheet. Moreover, mixtures of  $\beta$ -turn mimetic peptides and wild type  $A\beta_{40}$  were investigated to reveal whether inhibition of aggregation can be induced using these modified peptides as additives. Interestingly, both synthesized  $\beta$ -turn mimetics **3** and **4** showed the same position effect upon investigation in mixtures, revealing the strongest inhibition upon replacement of positions Gly25-Ser26 in conjugates **20a** and **21a**. Two other artificial peptides (**21c**, **21d**) containing the triazole turn mimetic **4** possessed no inhibition effect as it was expected from their fast aggregation. Replacement of two other positions with the BTD turn mimetic **3** resulted also in inhibition of fibrillation (conjugates **20c**, **20d**), but to a smaller extent than the one at position Gly25-Ser26.



**Scheme 44.** a) Turn modification of  $A\beta_{40}$  in the region of V24–K28 was performed to investigate the influence on aggregation of  $A\beta$ . b) Structures of  $\beta$ -turn mimetics **3**, **4**, 5-AVA and 4-/3-ABA introduced into peptide conjugates **20a–d**, **21a–d** and **22–24**. c) Aggregation investigations using ThT assays and CD spectroscopy revealed accelerated aggregation for conjugates **21a–d** and **22**, retardation for conjugate **23** and complete inhibition of aggregation for conjugates **20a–d**.

With these promising results in mind, a structure reduction of the conjugates with the best inhibiting properties, namely **20a** and **21a**, was performed. Therefore, only the short segment of  $A\beta_{16-35}$  was used, containing the two major  $\beta$ -sheet sequences of the full-length peptide, as well as the turn region in which positions Gly25-Ser26 were replaced by BTD **3** or TAA **4**, yielding conjugates **20b** and **21b**. While **21b** provided no inhibiting effect, **20b** retained some of the inhibiting properties of its full-length analogue **20a** as shown by ThT assays and confirmed by CD measurements.



The present work provides insights into the possibility to inhibit amyloid aggregation by turn modification. Especially for conjugates **20a** and **20b** precise structural analysis *e.g. via* NMR spectroscopy would be of great interest to deduce the influence of such modifications on the overall fibrillar structure. This remains an open topic for future investigations.

## 6 Appendix

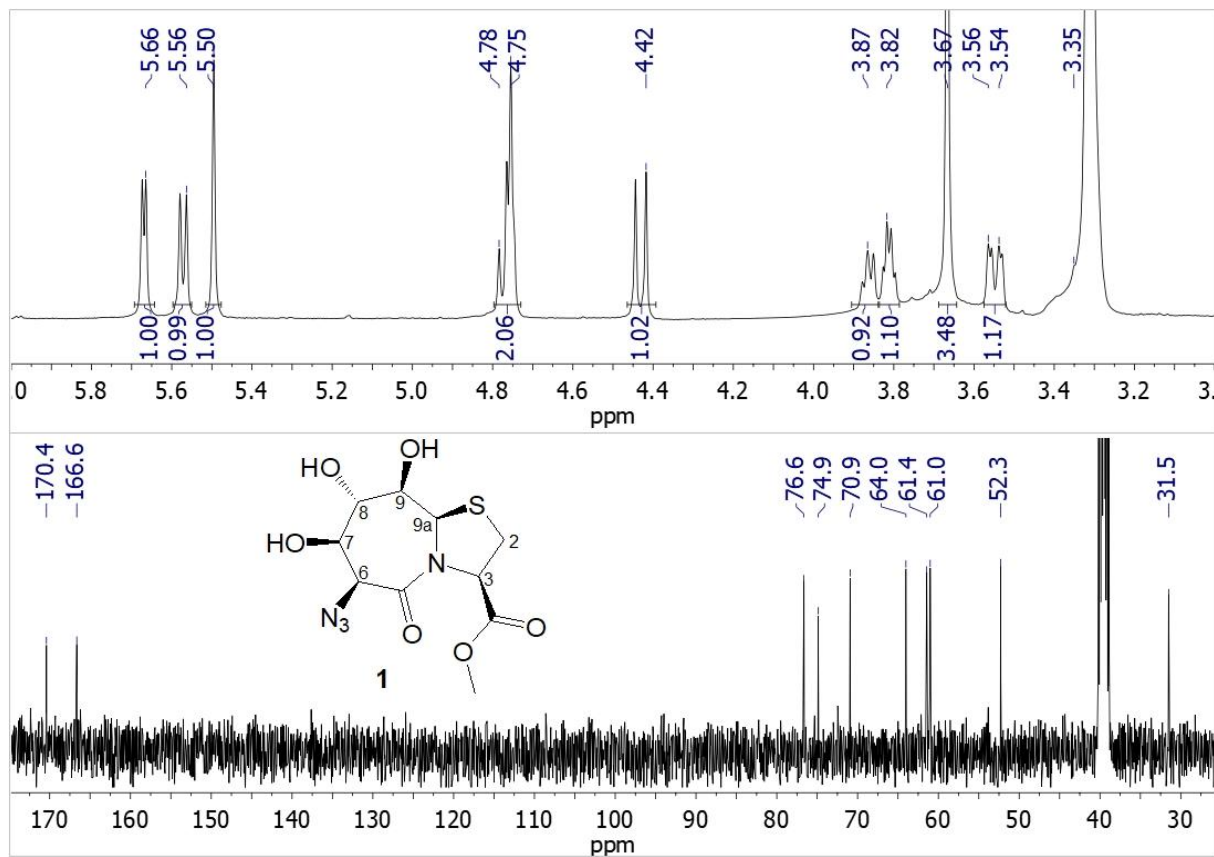


Figure A1.  $^1\text{H}$ - and  $^{13}\text{C}$ -NMR spectrum of BT D 1.

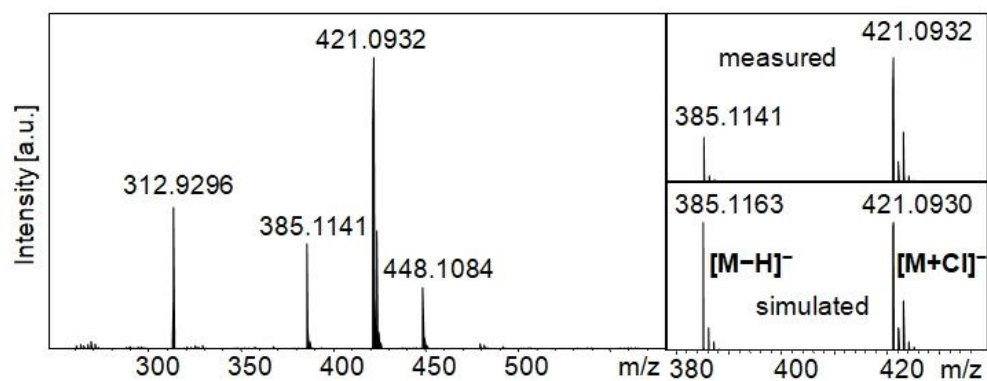


Figure A2. ESI-TOF-MS of BT D 2.

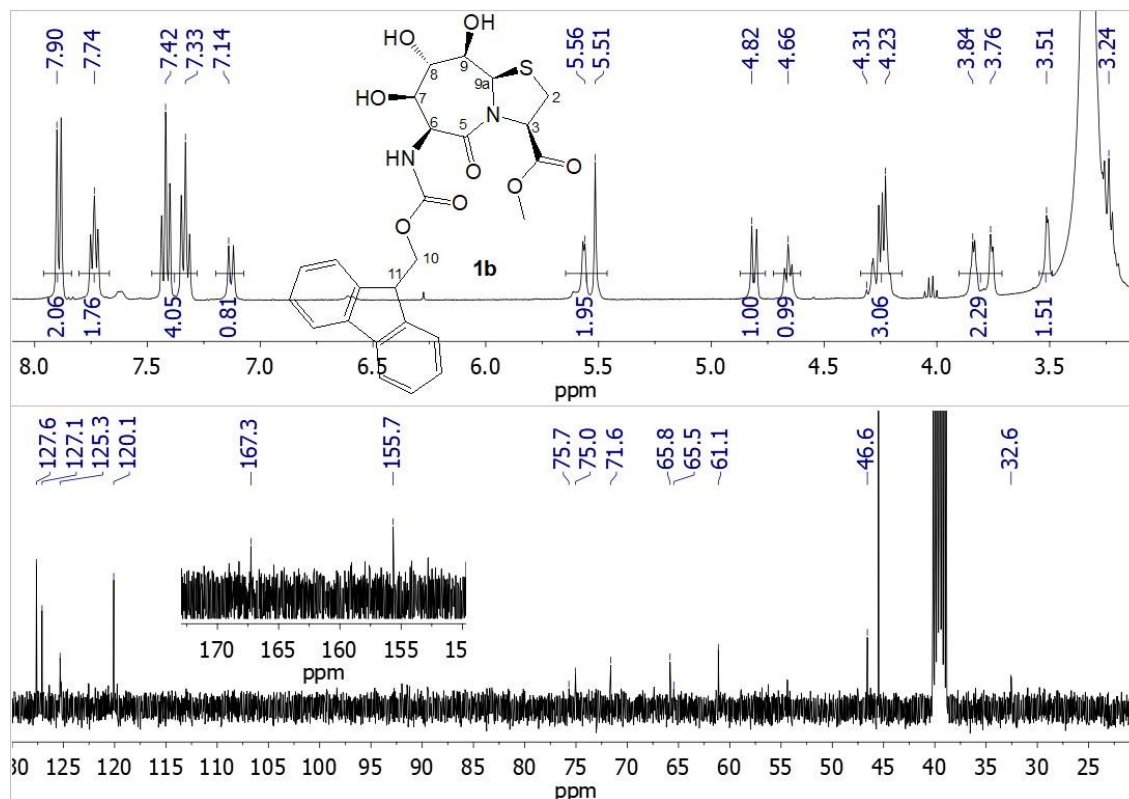


Figure A3.  $^1\text{H}$ - and  $^{13}\text{C}$ -NMR spectrum of BTD **1b**.

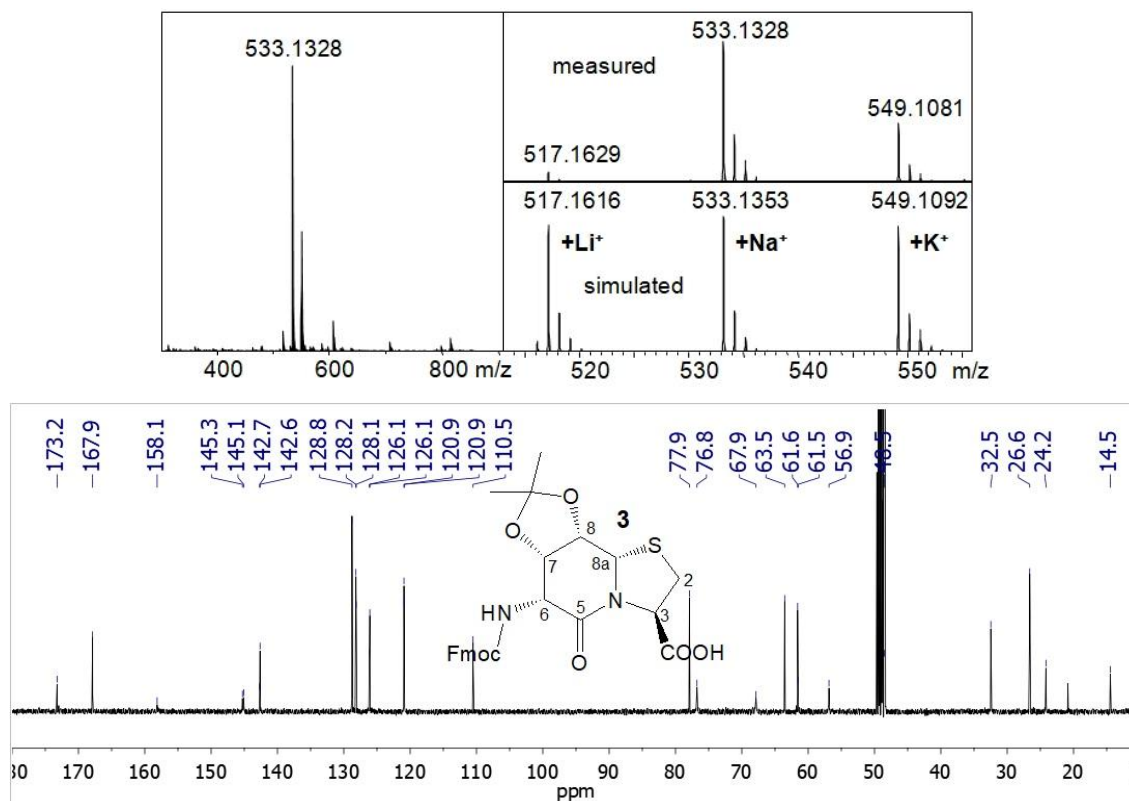


Figure A4. ESI-TOF-MS (top) and  $^{13}\text{C}$ -NMR spectrum (bottom) of BTD **3**.

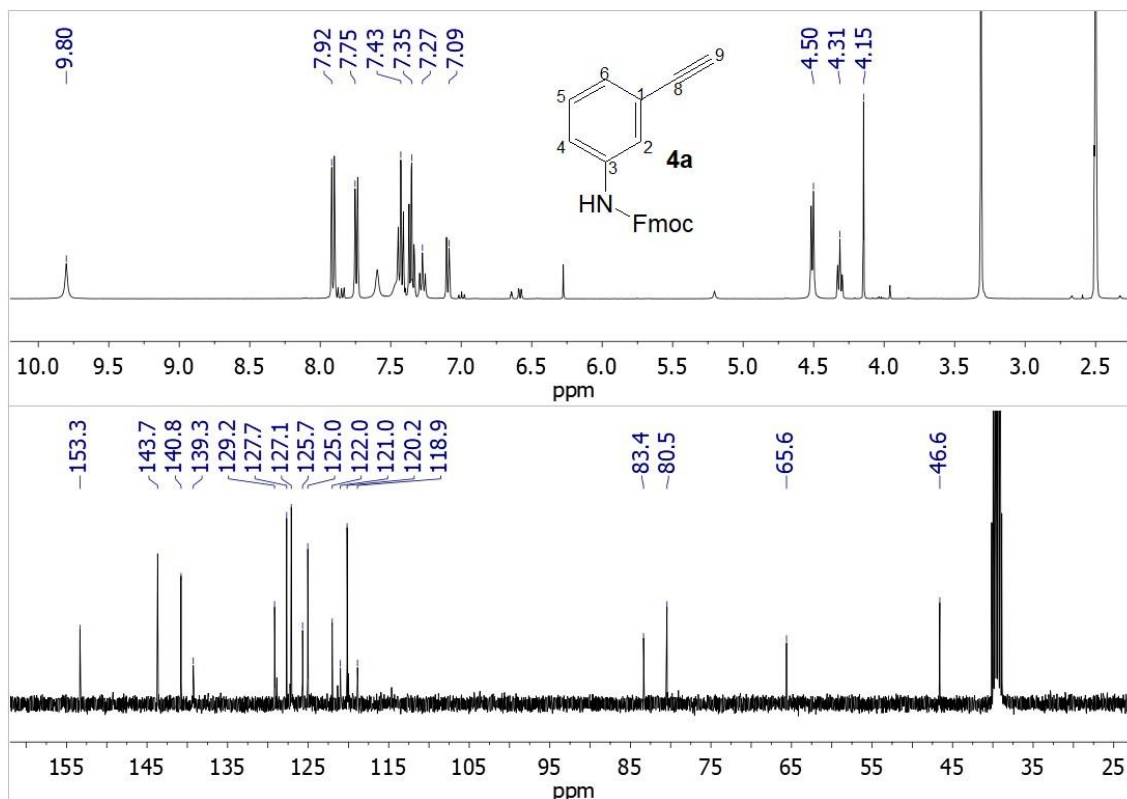


Figure A5.  $^1\text{H}$ - and  $^{13}\text{C}$ -NMR spectrum of (9H-fluoren-9-yl)methyl (3-ethynylphenyl)carbamate **4a**.

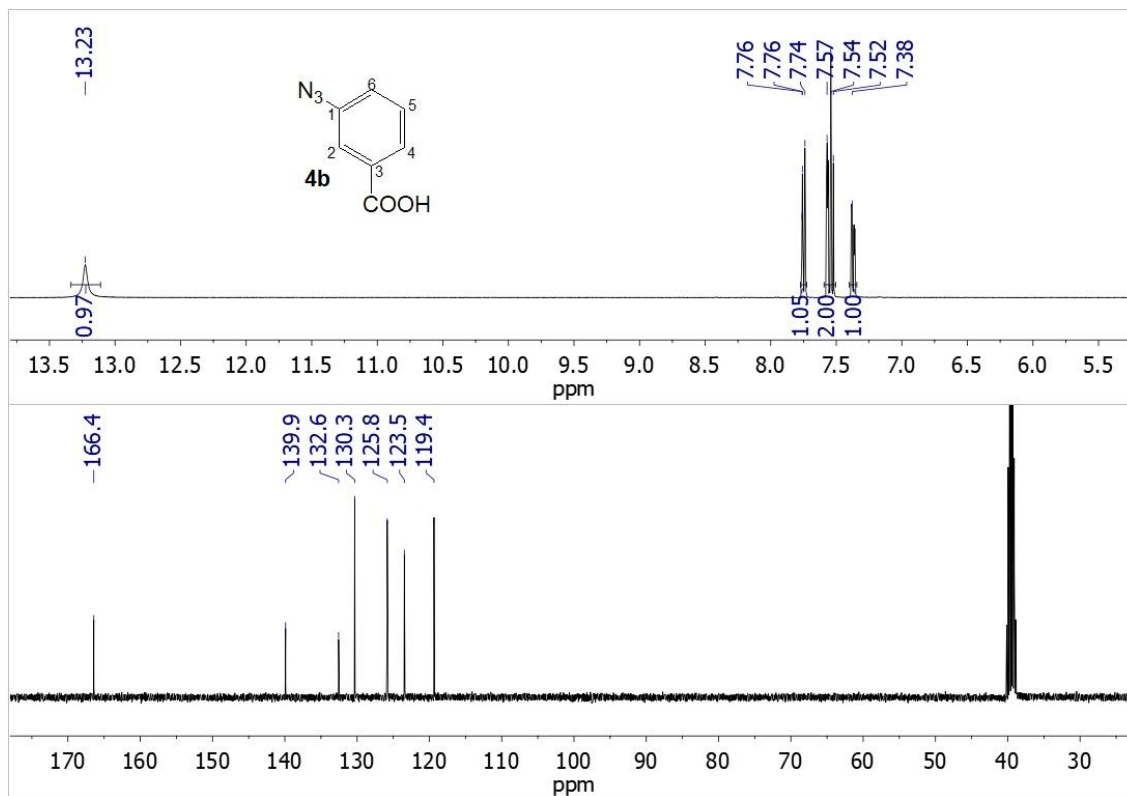


Figure A6.  $^1\text{H}$ - and  $^{13}\text{C}$ -NMR spectrum of azidobenzoic acid **4b**.

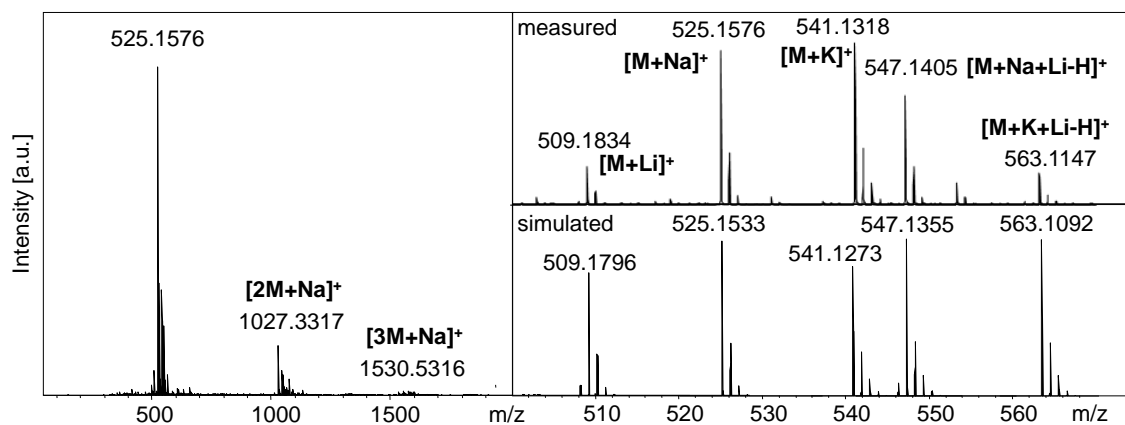


Figure A7. ESI-TOF-MS spectrum of triazole turn mimetic 4.

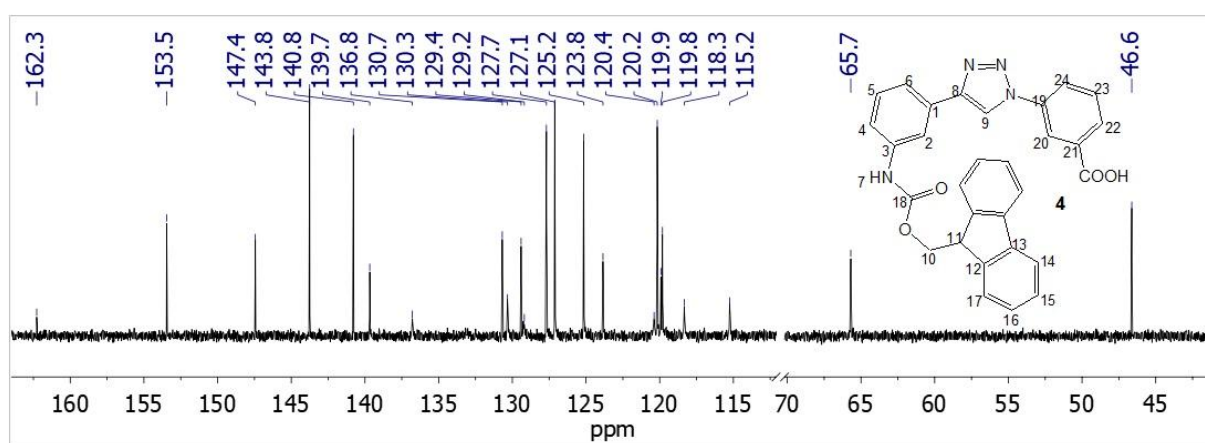


Figure A8.  $^{13}\text{C}$ -NMR spectrum of triazole turn mimetic 4.

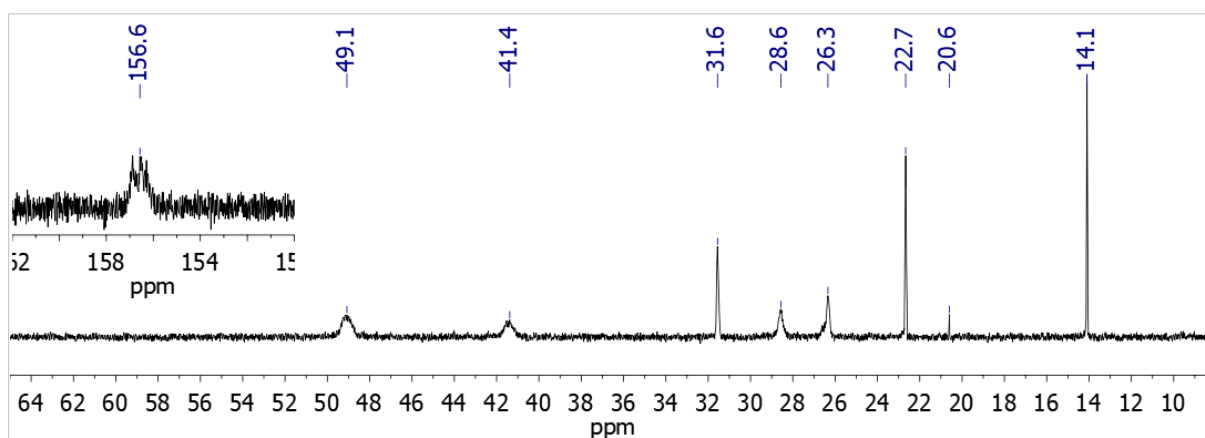


Figure A9.  $^{13}\text{C}$ -NMR spectrum of PHIC-PCIC 9b.

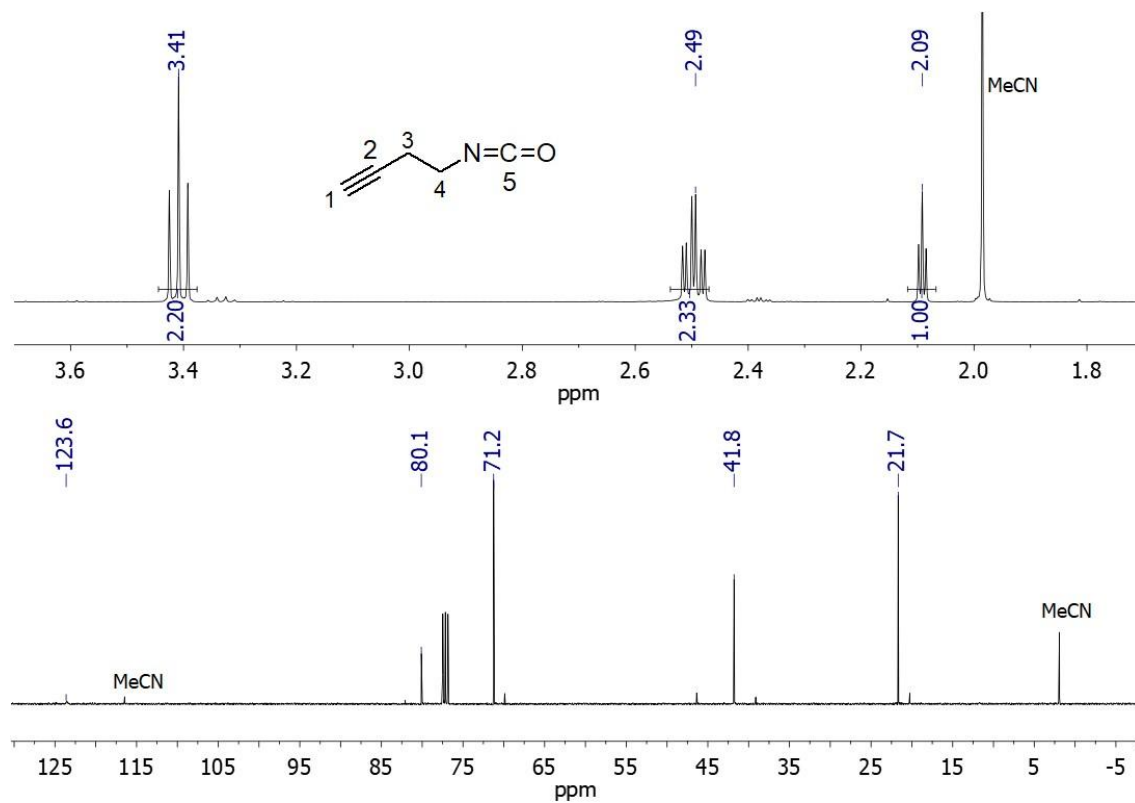


Figure A10. <sup>13</sup>C-NMR spectrum of 4-isocyanato-1-butyne (AlkIC).

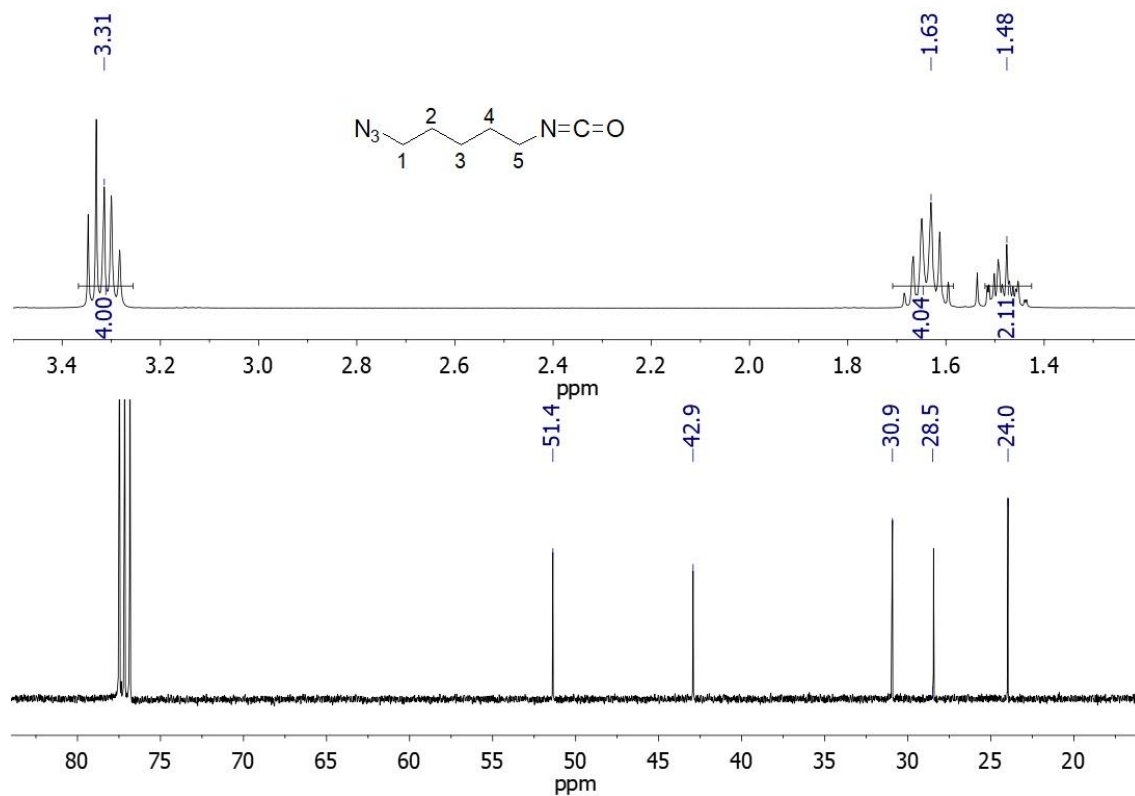


Figure A11. <sup>1</sup>H- and <sup>13</sup>C-NMR spectrum of 1-azido-5-isocyanatopentane AzIC.

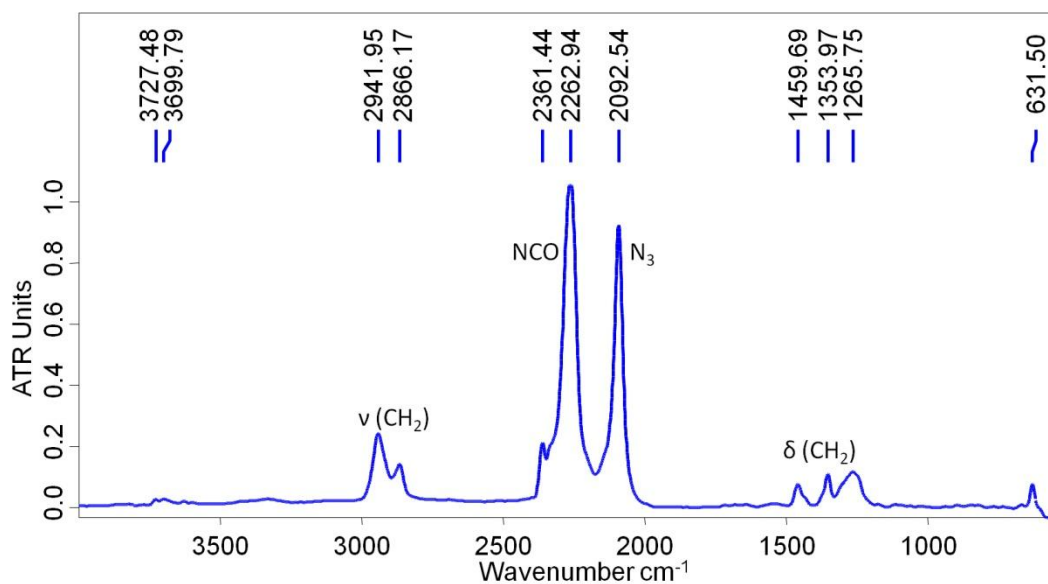


Figure A12. IR spectrum of 1-Azido-5-isocyanatopentane **AzIC**.

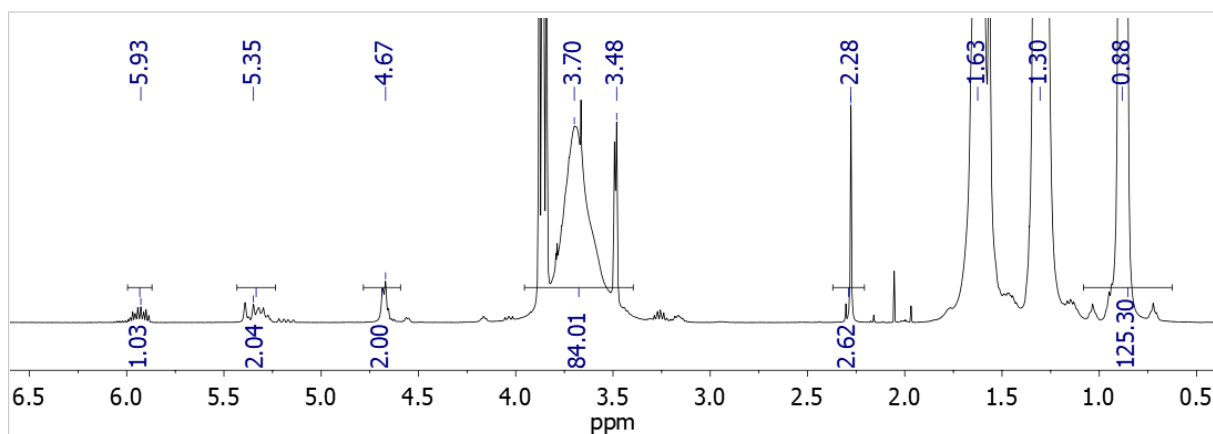


Figure A13. <sup>1</sup>H-NMR spectrum of PHIC-Allyl **11**.

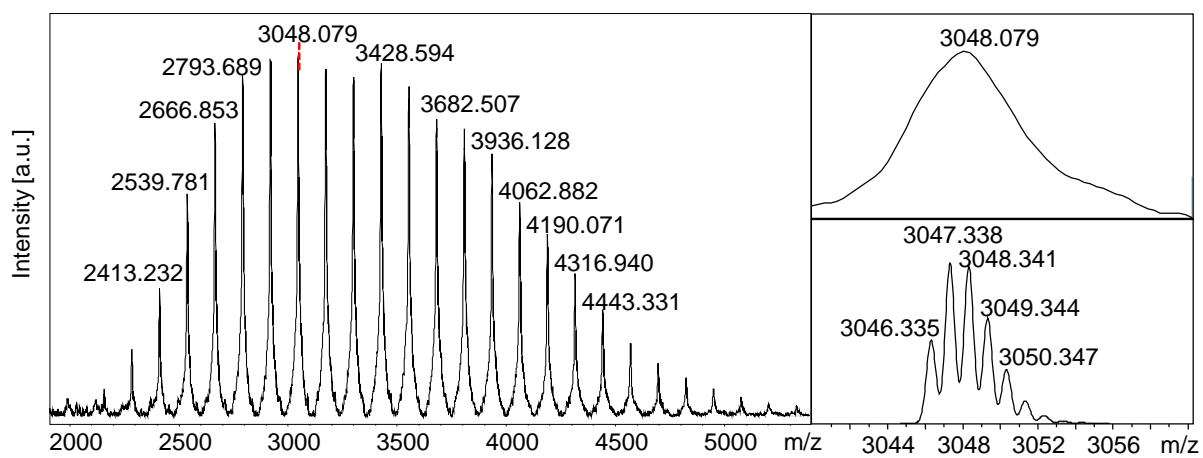


Figure A14. MALDI-TOF-MS spectrum of PHIC-Allyl **11**.

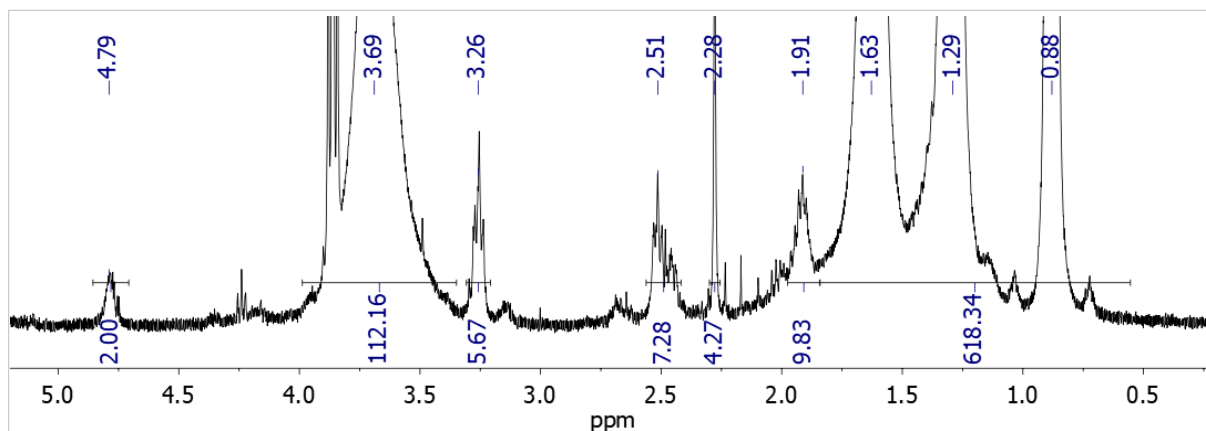


Figure A15.  $^1\text{H}$ -NMR spectrum of PHIC-PAzIC 10a.

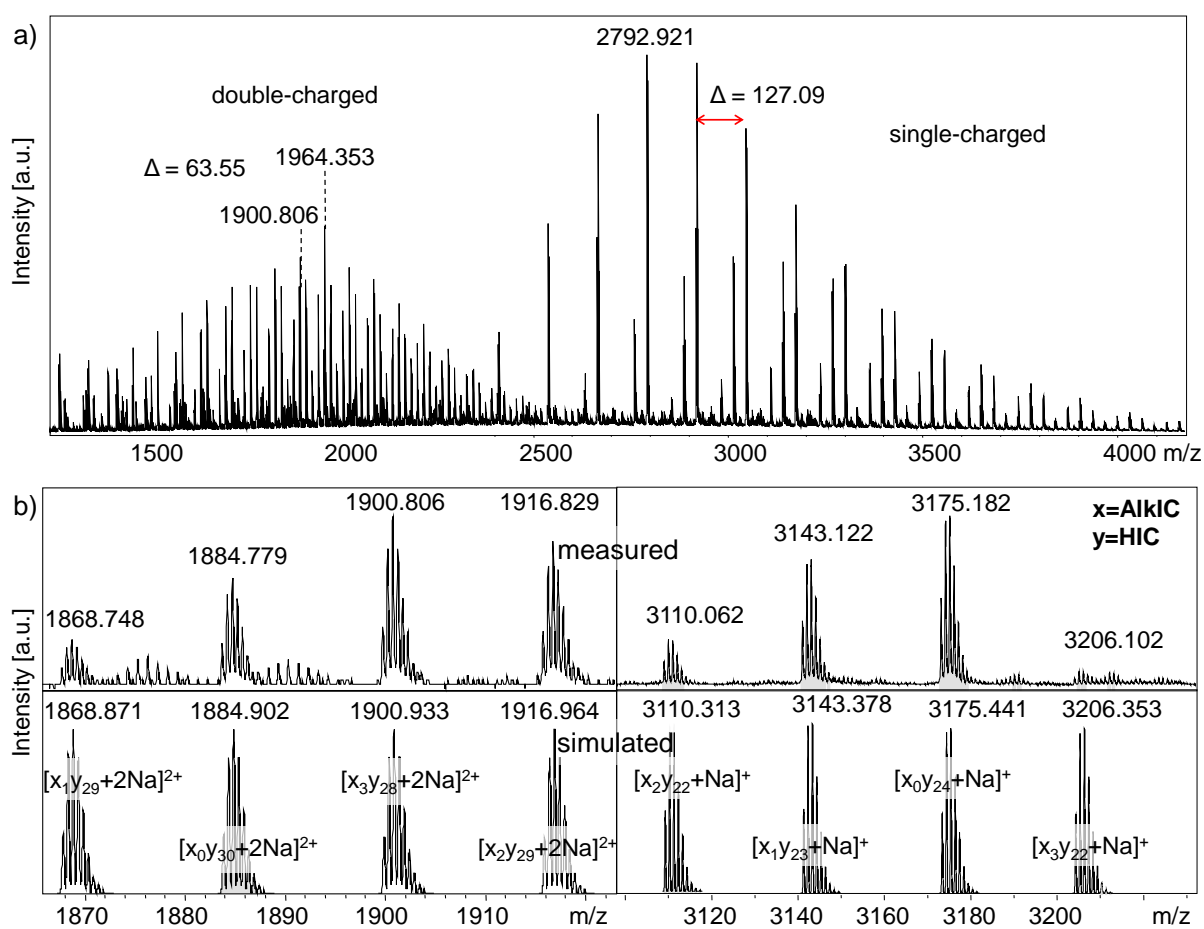
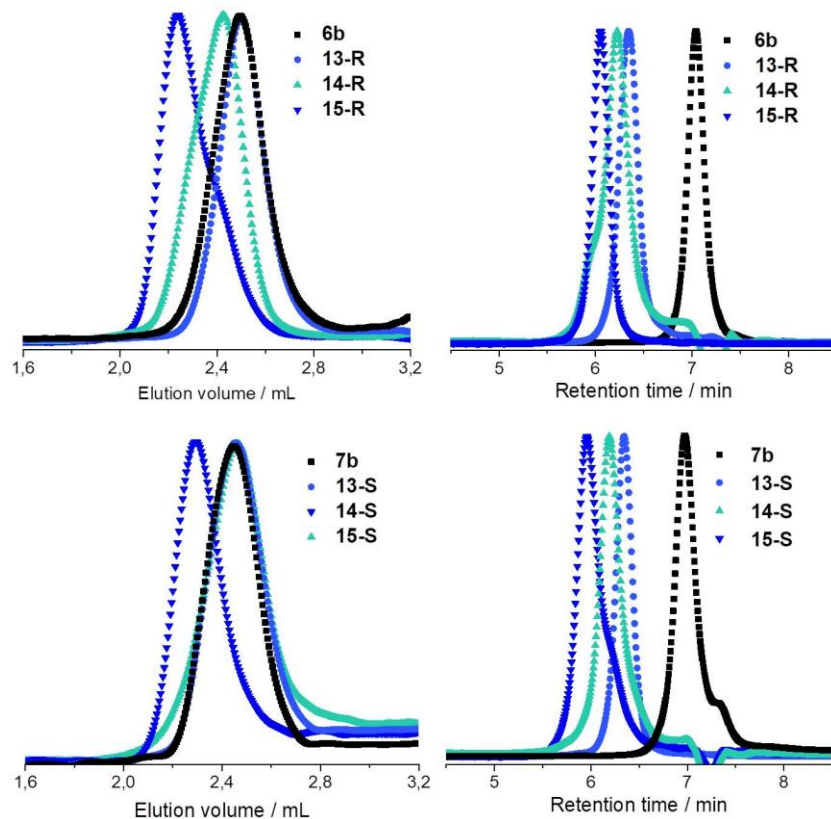
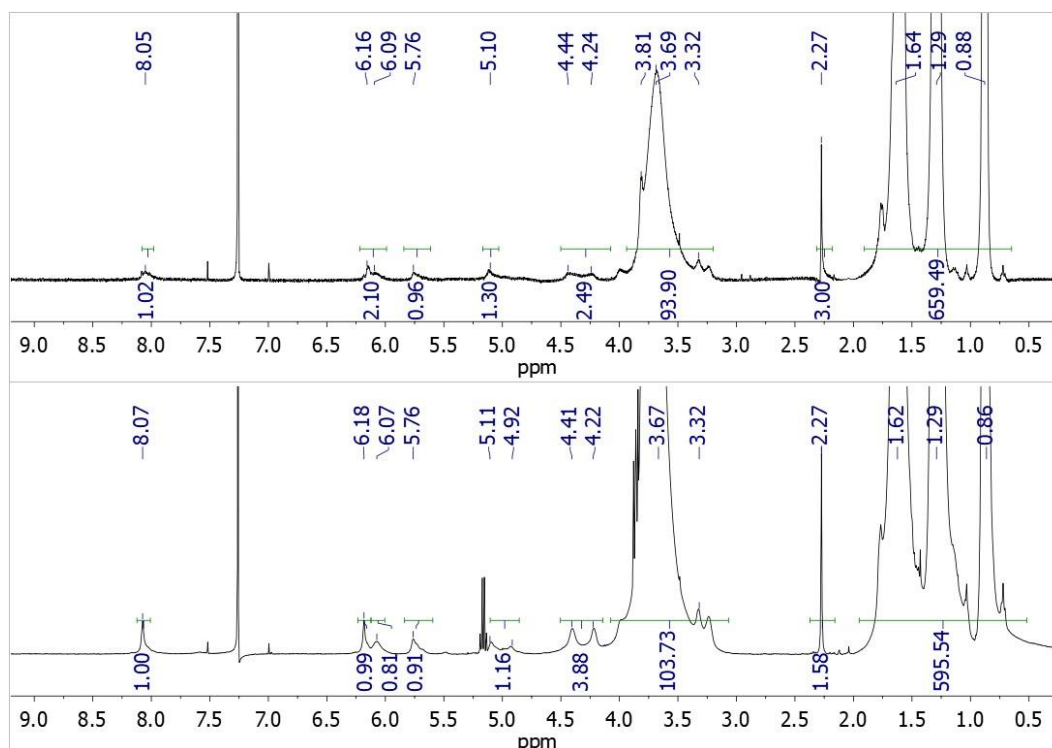


Figure A16. ESI-TOF-MS spectrum of PHIC-co-AlkIC 12d; a) full spectrum, b) measured (top) and simulated (bottom) series.





**Figure A17.** GPC- and HPLC-measurements of chiral PHICs **6b**, **7b** and of BTD-conjugates **13-14-15-R** (top) and **13-14-15-S** (bottom).



**Figure A18.** <sup>1</sup>H-NMR spectrum of BTD-conjugates **13-R** (top) and **13-S** (bottom).

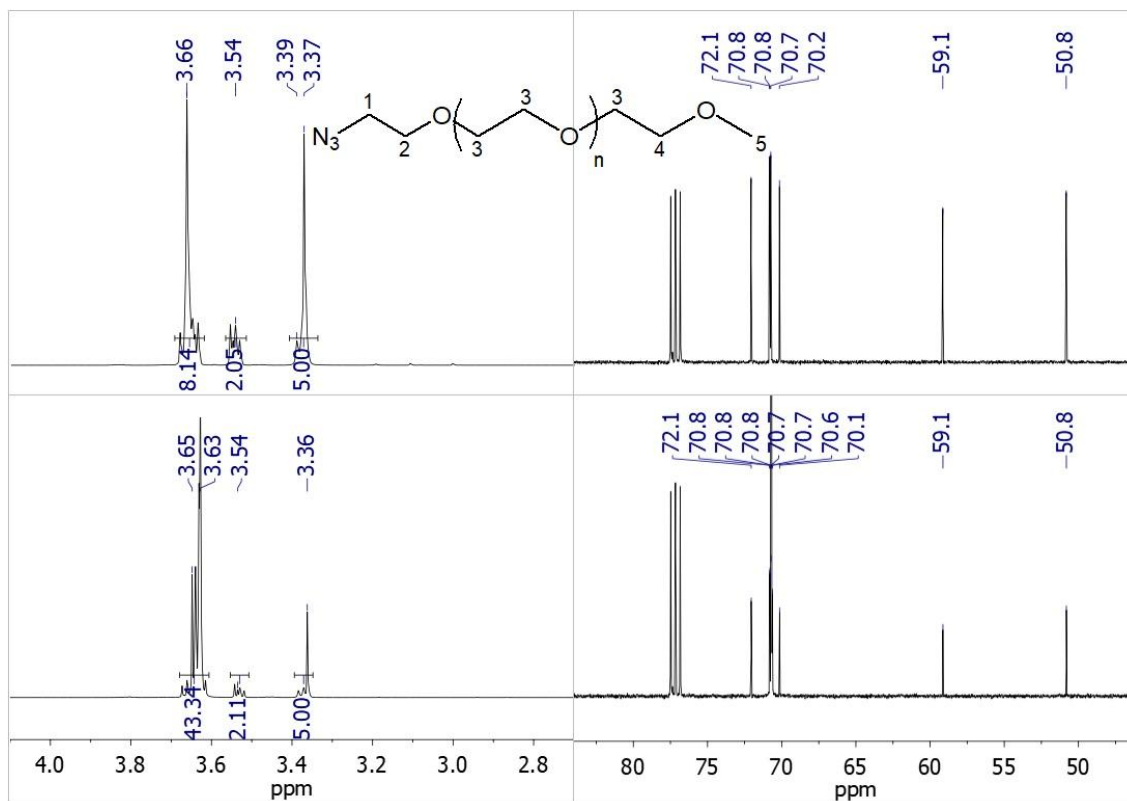


Figure A19.  $^1\text{H}$ -NMR (left) and  $^{13}\text{C}$ -NMR spectra (right) of TEG-azide (top) and PEO-azide (bottom).

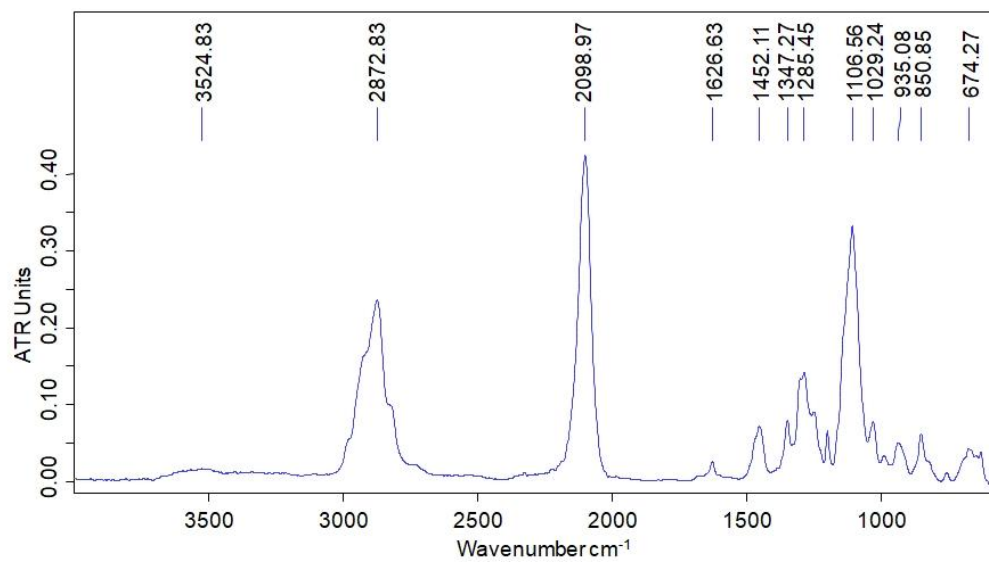


Figure A20. IR spectrum of TEG-azide.

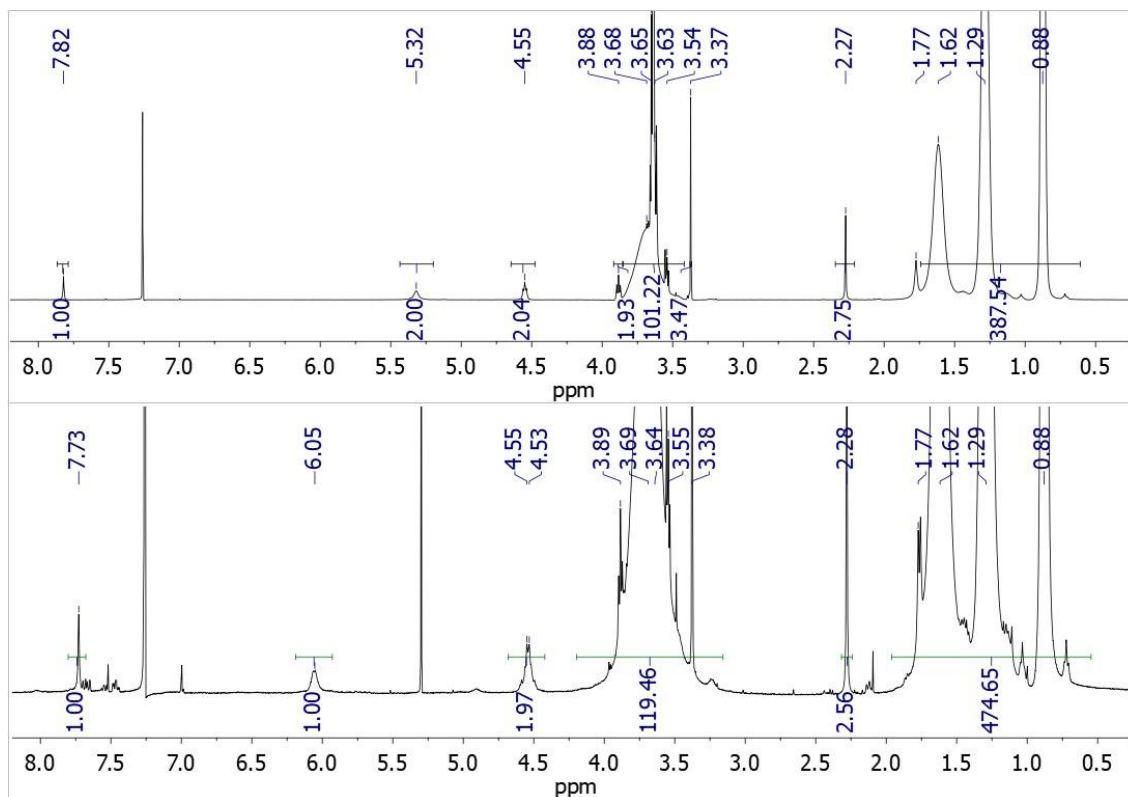


Figure A21.  $^1\text{H-NMR}$  spectrum of PHIC-PEO 17-A (top) and 17-R (bottom).

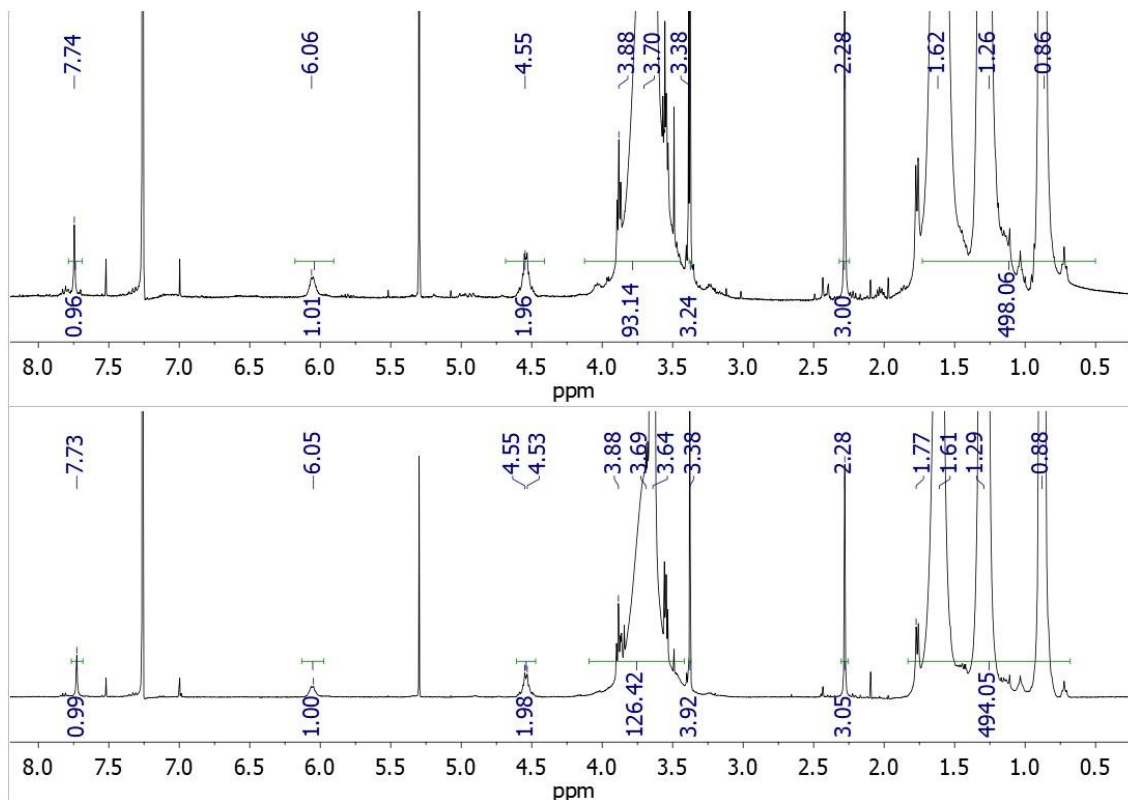
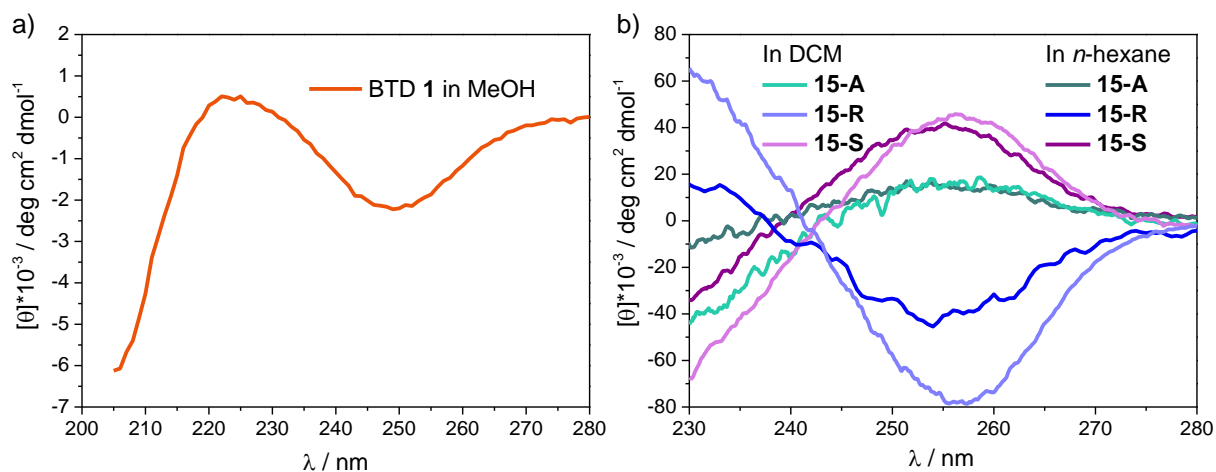
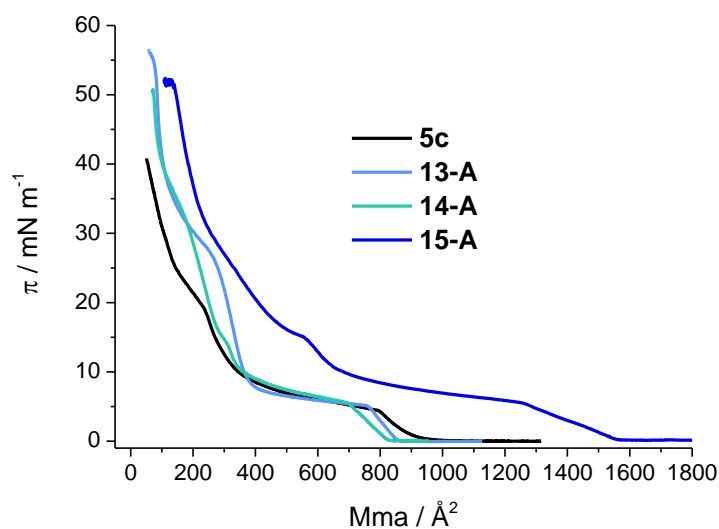


Figure A22.  $^1\text{H-NMR}$  spectrum of PHIC-TEG / -PEO 16-S (top) and 17-S (bottom).



**Figure A23.** CD spectra of a) BTD **1** in methanol; b) two-arm PHIC-BTD conjugates **15-A**, **15-R** and **15-S** in DCM and *n*-hexane



**Figure A24.** Langmuir isotherm of PHIC **5c** and BTD-conjugates **13-A**, **14-A**, **15-A**.

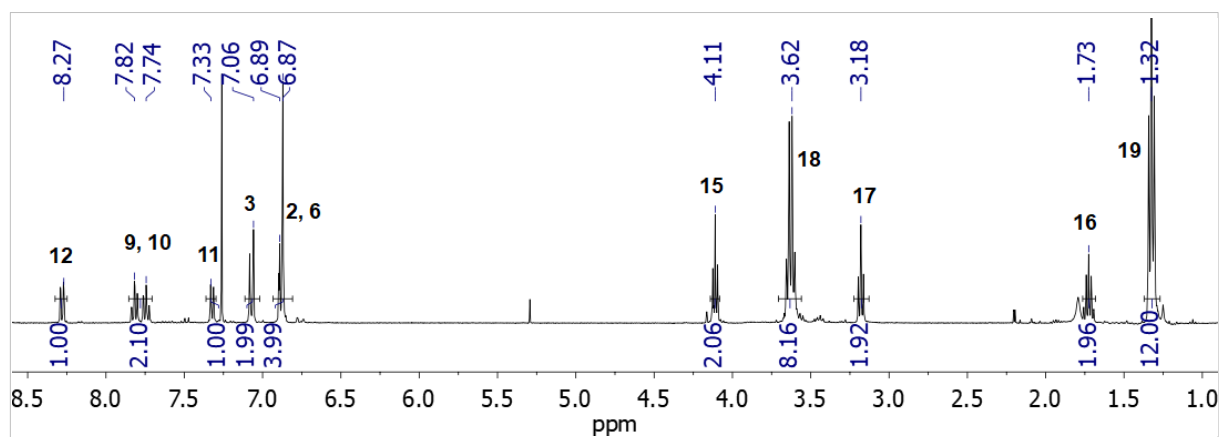


**Figure A25.**  $^1\text{H-NMR}$  spectrum of rhodamine-azide **18**.

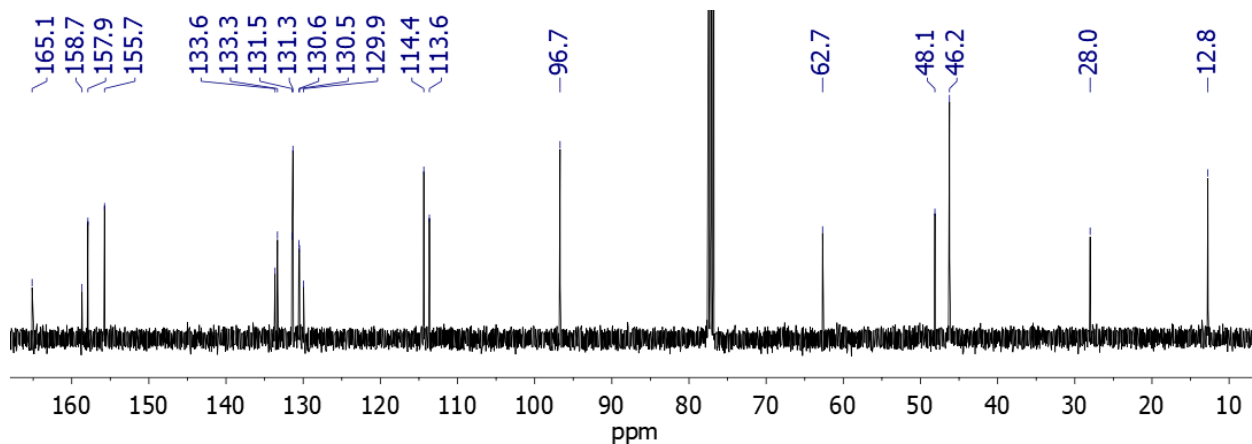


Figure A26.  $^{13}\text{C}$ -NMR spectrum of rhodamine-azide **18**.

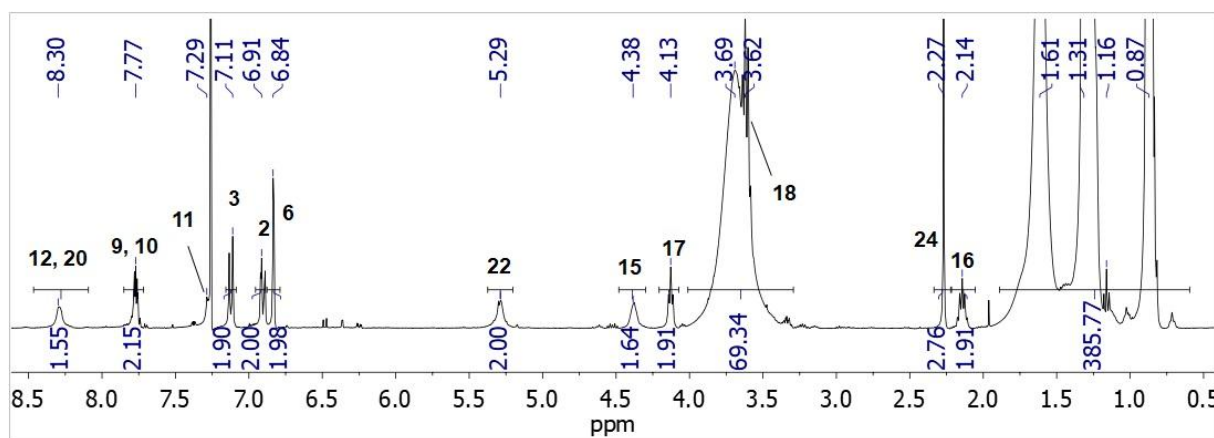


Figure A27.  $^1\text{H}$ -NMR spectrum of rhodamine-labeled PHIC **19**.

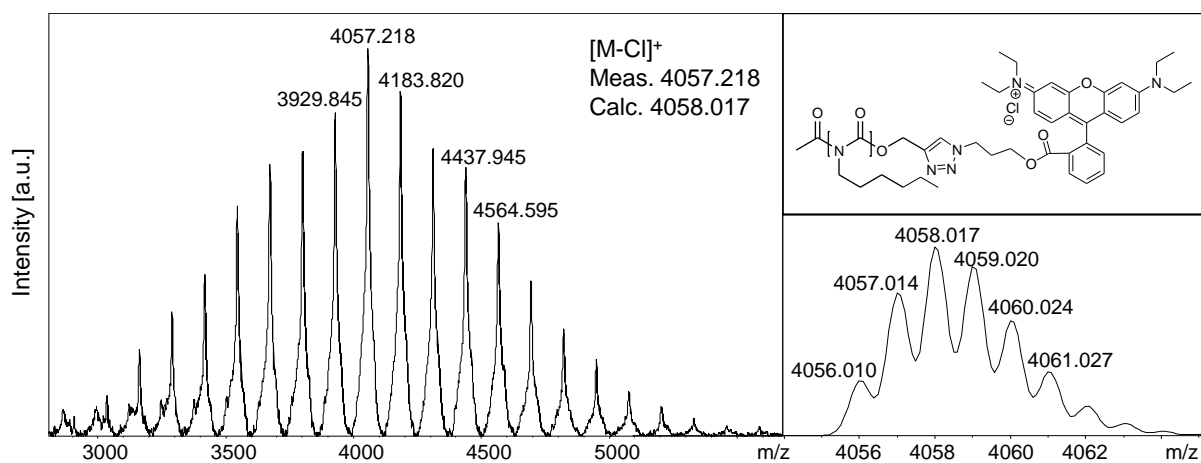


Figure A28. MALDI-TOF spectrum of rhodamine-labeled PHIC **19**.

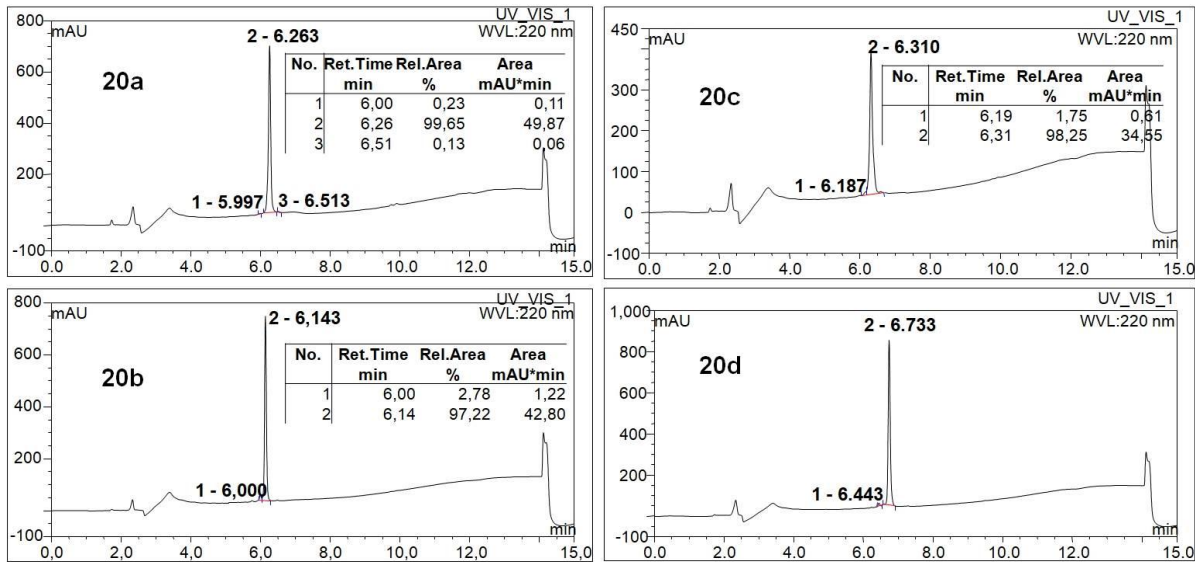


Figure A29. HPLC traces of  $\beta$ -turn mimetic peptide conjugates 20a–20d.

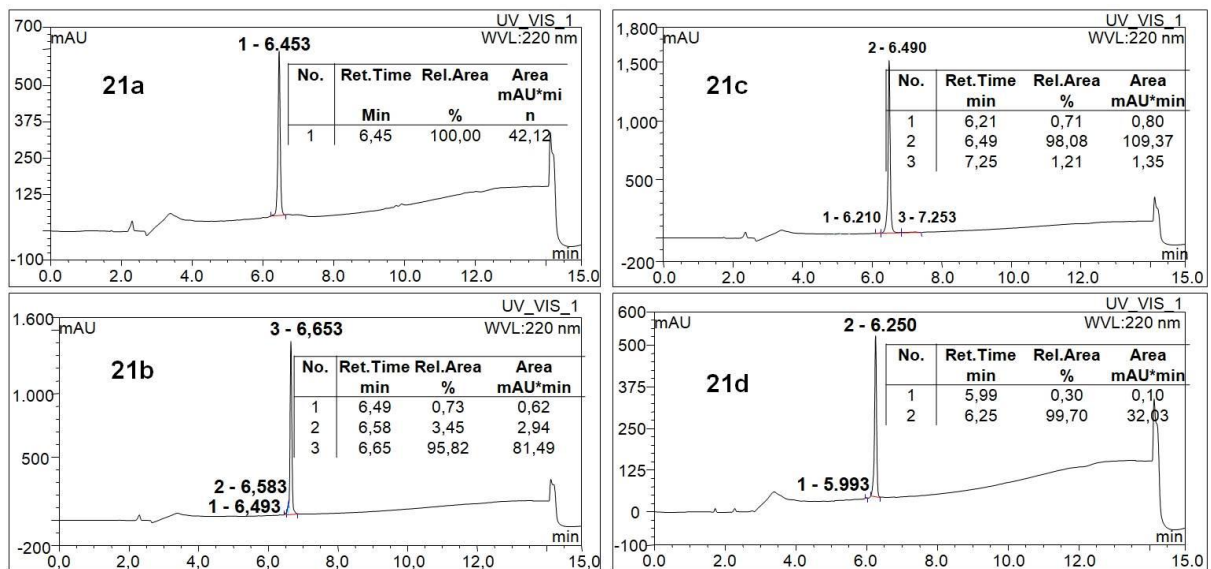


Figure A30. HPLC traces of  $\beta$ -turn mimetic peptide conjugates 21a–21d.

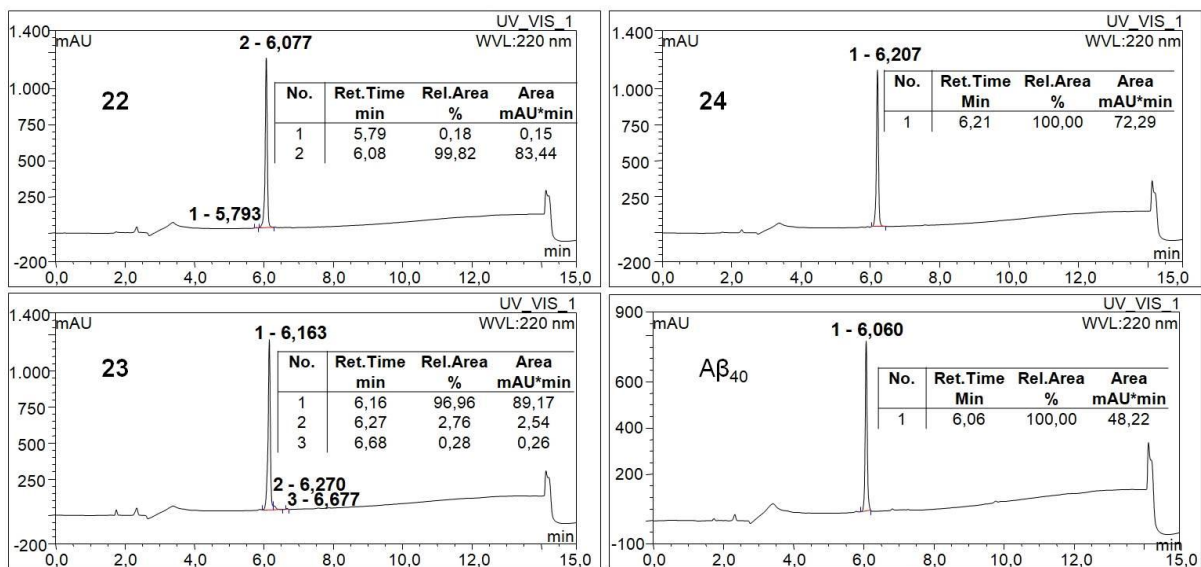


Figure A31. HPLC traces of  $\beta$ -turn mimetic peptide conjugates 22–24 and of  $A\beta_{40}$ .

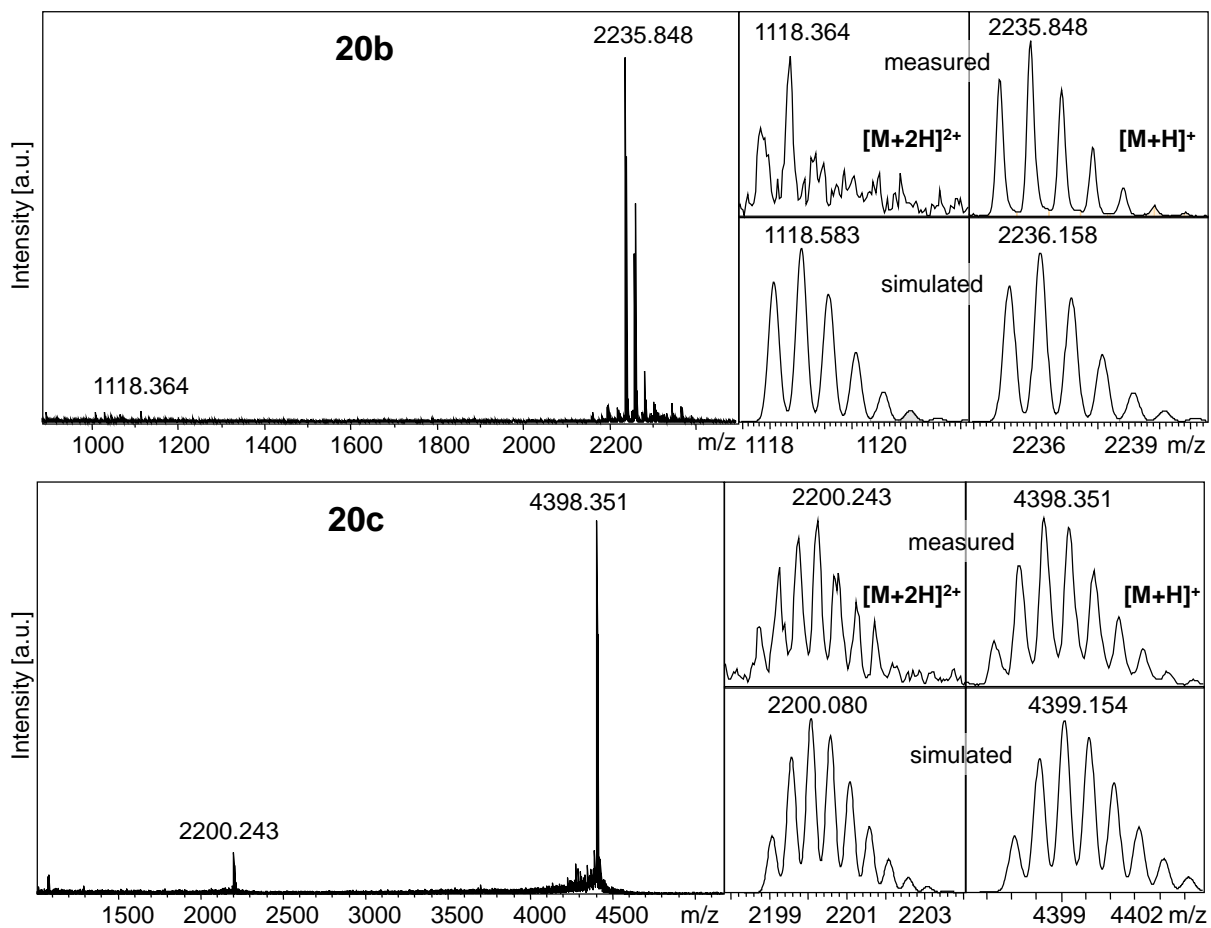


Figure A32. MALDI-TOF-MS of peptide conjugates 20b, 20c.



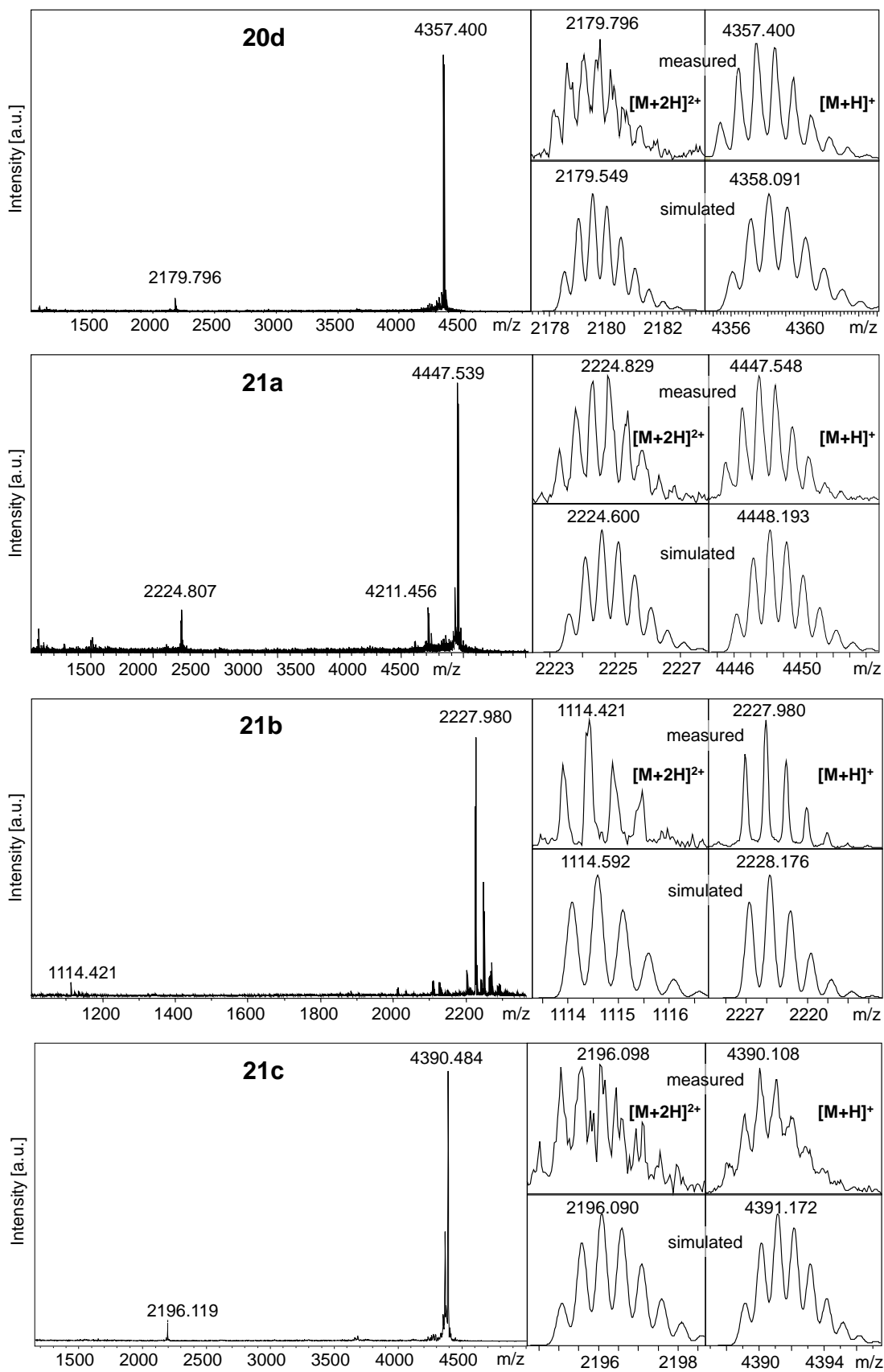


Figure A33. MALDI-TOF-MS of peptide conjugates 20d, 21a, 21b, 21c.



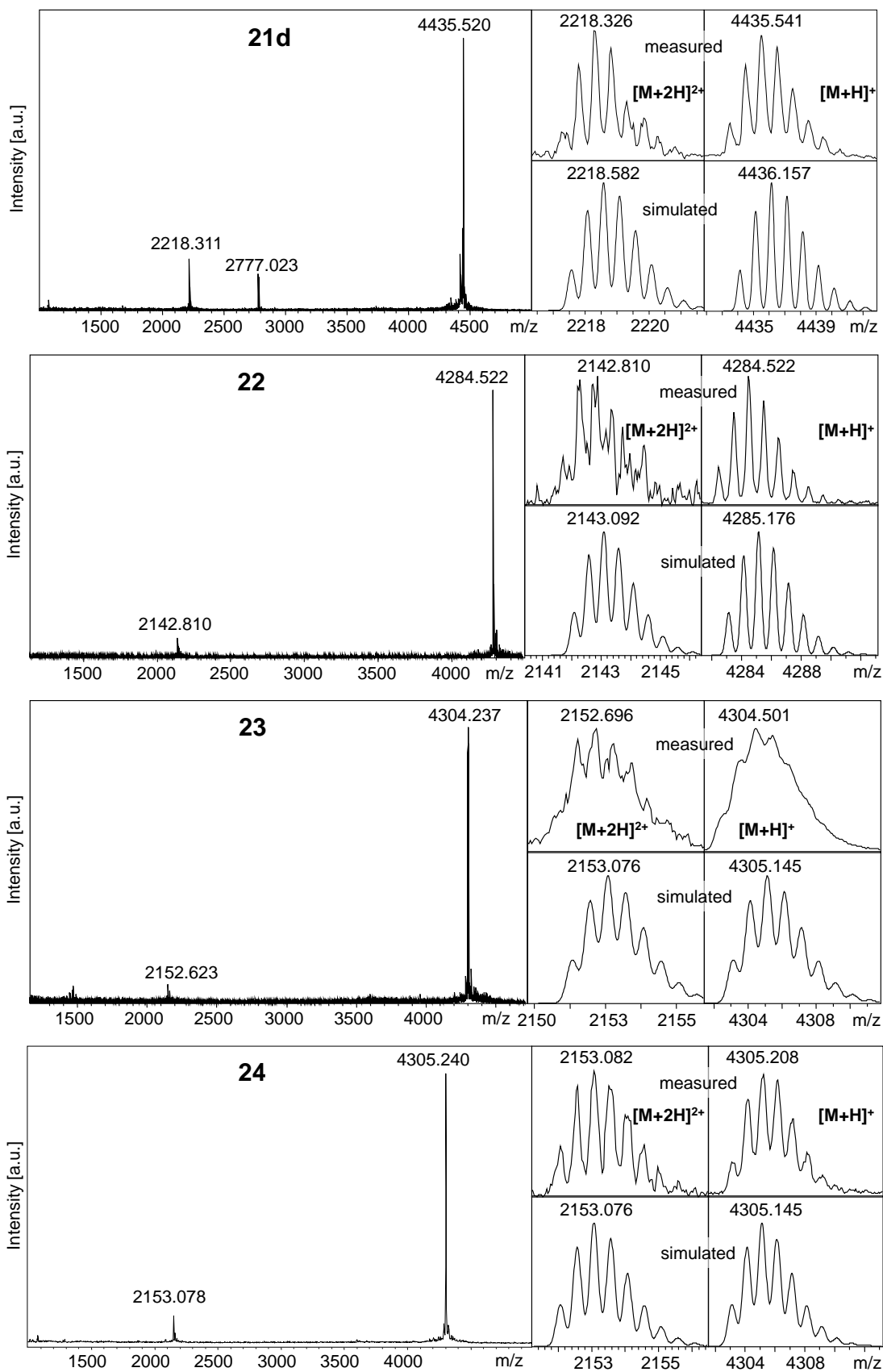


Figure A34. MALDI-TOF-MS of peptide conjugates 21d, 22, 23, 24.

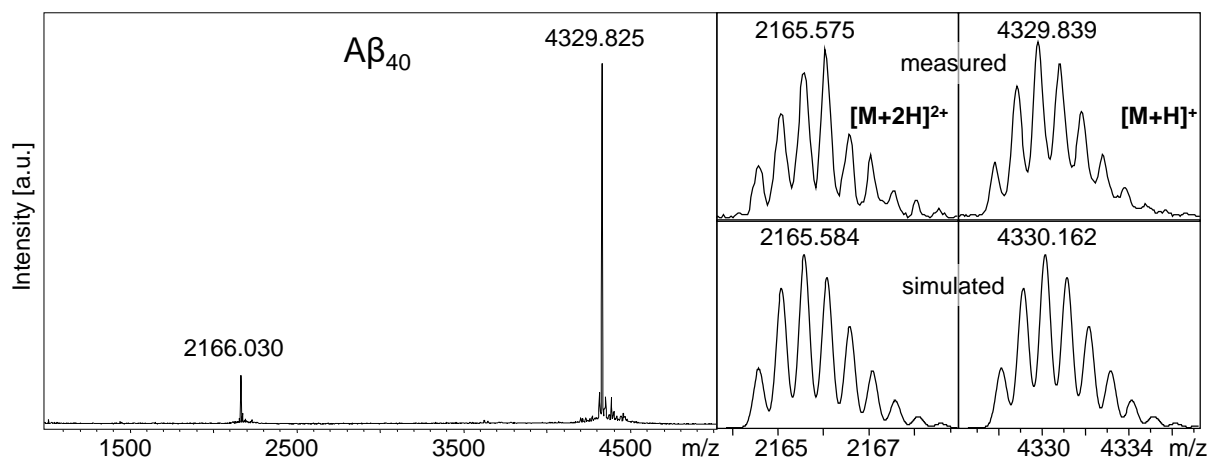


Figure A35. MALDI-TOF-MS of  $A\beta_{40}$ .

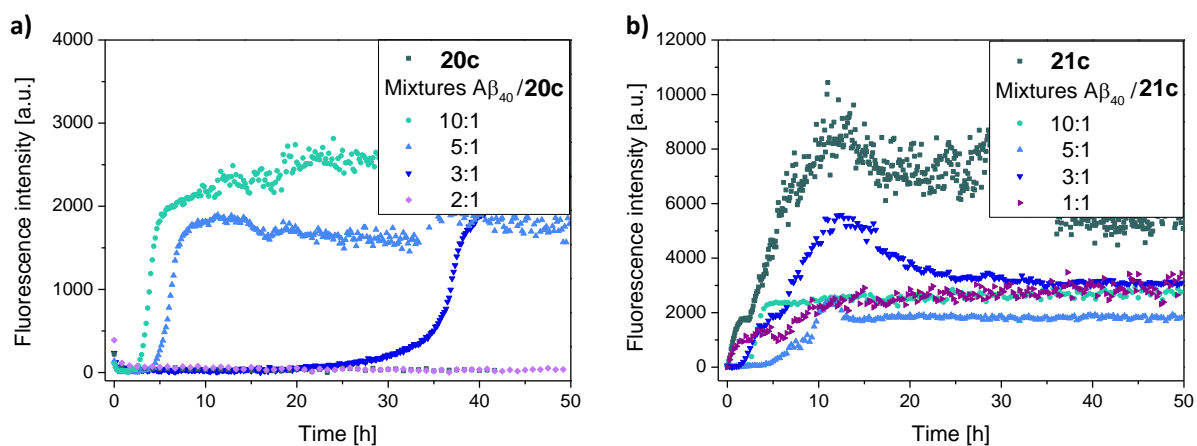


Figure A36. ThT assay of mixtures of  $A\beta_{40}$  with a) 20c and b) 21c.

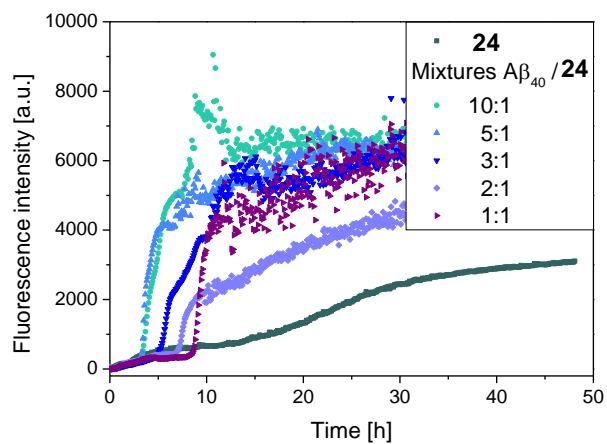
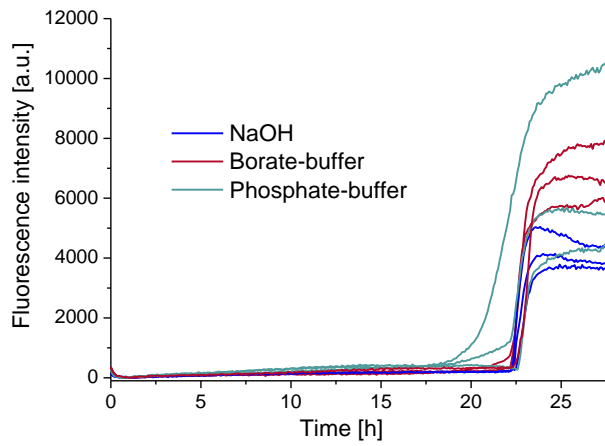
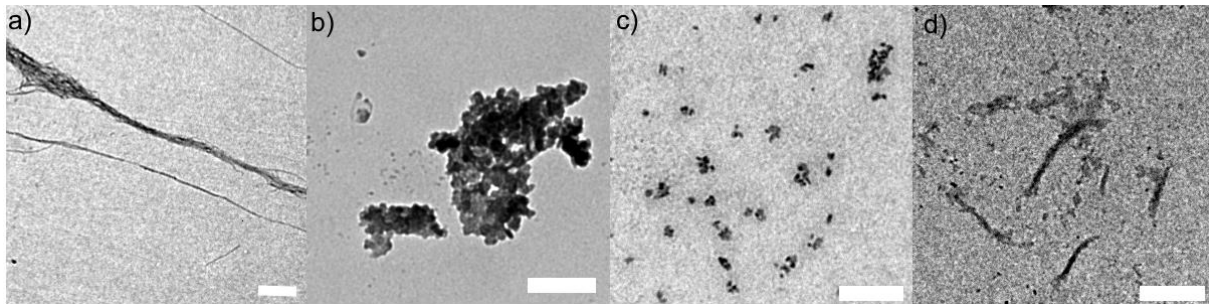


Figure A37. ThT assay of mixtures of  $A\beta_{40}$  with 24.



**Figure A38.** ThT assay of WT A $\beta$ 40 disaggregated in different buffer solutions.



**Figure A39.** TEM images of a) A $\beta$ <sub>40</sub>, b), c) 20c and d) 20d. Scale bars indicate a) 500nm, b)-d) 100nm.

## 7 References

- [1] Berg, J. M.; Tymoczko, J. L.; Gatto jr., G. J.; Stryer, L.; *Stryer Biochemie, Vol. 8*, Springer Spektrum, Berlin, Heidelberg, **2018**.
- [2] Ramachandran, G. N.; Ramakrishnan, C.; Sasisekharan, V.; *J. Mol. Biol.* **1963**, 7(1), 95-99.
- [3] Pauling, L.; Corey, R. B.; Branson, H. R.; *Proc. Natl. Acad. Sci. U. S. A.* **1951**, 37(4), 205-211.
- [4] Low, B. W.; Baybutt, R. B.; *J. Am. Chem. Soc.* **1952**, 74(22), 5806-5807.
- [5] Cooley, R. B.; Arp, D. J.; Karplus, P. A.; *J. Mol. Biol.* **2010**, 404(2), 232-246.
- [6] Bragg, W. L.; Kendrew, J. C.; Perutz, M. F.; *Proc. R. Soc. London, A* **1950**, 203(1074), 321-357.
- [7] Pauling, L.; Corey, R. B.; *Proc. Natl. Acad. Sci. U. S. A.* **1951**, 37(5), 251-256.
- [8] Pauling, L.; Corey, R. B.; *Proc. Natl. Acad. Sci. U. S. A.* **1951**, 37(11), 729-740.
- [9] Daggett, V.; *Acc. Chem. Res.* **2006**, 39(9), 594-602.
- [10] Marcelino, A. M. C.; Gierasch, L. M.; *Biopolymers* **2008**, 89(5), 380-391.
- [11] Perutz, M. F.; Rossmann, M. G.; Cullis, A. F.; Muirhead, H.; Will, G.; North, A. C. T.; *Nature* **1960**, 185(4711), 416-422.
- [12] Kendrew, J. C.; Bodo, G.; Dintzis, H. M.; Parrish, R. G.; Wyckoff, H.; Phillips, D. C.; *Nature* **1958**, 181(4610), 662-666.
- [13] Chou, K.-C.; *Anal. Biochem.* **2000**, 286(1), 1-16.
- [14] Venkatachalam, C. M.; *Biopolymers* **1968**, 6(10), 1425-1436.
- [15] Lewis, P. N.; Momany, F. A.; Scheraga, H. A.; *Biochim. Biophys. Acta* **1973**, 303(2), 211-229.
- [16] Wilmot, C. M.; Thornton, J. M.; *J. Mol. Biol.* **1988**, 203(1), 221-232.
- [17] Hutchinson, E. G.; Thornton, J. M.; *Protein Sci.* **1994**, 3(12), 2207-2216.
- [18] Whitby, L. R.; Boger, D. L.; *Acc. Chem. Res.* **2012**, 45(10), 1698-1709.
- [19] Dyson, J. H.; Cross, K. J.; Houghten, R. A.; Wilson, I. A.; Wright, P. E.; Lerner, R. A.; *Nature* **1985**, 318, 480.
- [20] Chou, P. Y.; Fasman, G. D.; *J. Mol. Biol.* **1977**, 115(2), 135-175.
- [21] Craik, D. J.; Fairlie, D. P.; Liras, S.; Price, D.; *Chem. Biol. Drug Des.* **2013**, 81(1), 136-147.
- [22] Otvos, L., Jr.; Wade, J. D.; *Front. Chem.* **2014**, 2, 62-62.
- [23] Gibbs, A. C.; Bjorndahl, T. C.; Hodges, R. S.; Wishart, D. S.; *J. Am. Chem. Soc.* **2002**, 124(7), 1203-1213.
- [24] Bomar, M. G.; Song, B.; Kibler, P.; Kodukula, K.; Galande, A. K.; *Org. Lett.* **2011**, 13(21), 5878-5881.
- [25] Haque, T. S.; Gellman, S. H.; *J. Am. Chem. Soc.* **1997**, 119(9), 2303-2304.
- [26] Karle, I. L.; Awasthi, S. K.; Balaram, P.; *Proc. Natl. Acad. Sci. U. S. A.* **1996**, 93(16), 8189-8193.
- [27] Masterson, L. R.; Etienne, M. A.; Porcelli, F.; Barany, G.; Hammer, R. P.; Veglia, G.; *Peptide Sci.* **2007**, 88(5), 746-753.
- [28] Raghavender, U. S.; Aravinda, S.; Rai, R.; Shamala, N.; Balaram, P.; *Org. Biomol. Chem.* **2010**, 8(14), 3133-3135.
- [29] Arnold, U.; Hinderaker, M. P.; Nilsson, B. L.; Huck, B. R.; Gellman, S. H.; Raines, R. T.; *J. Am. Chem. Soc.* **2002**, 124(29), 8522-8523.
- [30] Cavelier-Frontin, F.; Achmad, S.; Verducci, J.; Jacquier, R.; Pèpe, G.; *J. Mol. Struct. Theochem* **1993**, 286, 125-130.
- [31] Jolliffe, K. A.; *Aust. J. Chem.* **2018**, 71(10), 723-730.

- [32] Laufer, B.; Chatterjee, J.; Frank, A. O.; Kessler, H.; *J. Pept. Sci.* **2009**, *15* (3), 141-146.
- [33] Chalmers, D. K.; Marshall, G. R.; *J. Am. Chem. Soc.* **1995**, *117* (22), 5927-5937.
- [34] Ghosh, D.; Lahiri, P.; Verma, H.; Mukherjee, S.; Chatterjee, J.; *Chem. Sci.* **2016**, *7* (8), 5212-5218.
- [35] Memeo, M. G.; Bruschi, M.; Bergonzi, L.; Desimoni, G.; Faita, G.; Quadrelli, P.; *ACS Omega* **2018**, *3* (10), 13551-13558.
- [36] André, C.; Legrand, B.; Deng, C.; Didierjean, C.; Pickaert, G.; Martinez, J.; Averlant-Petit, M. C.; Amblard, M.; Calmes, M.; *Org. Lett.* **2012**, *14* (4), 960-963.
- [37] Kueh, J. T. B.; Choi, K. W.; Williams, G. M.; Moehle, K.; Bacsa, B.; Robinson, J. A.; Brimble, M. A.; *Chem. Eur. J.* **2013**, *19* (12), 3807-3811.
- [38] Wu, C.-F.; Zhao, X.; Lan, W.-X.; Cao, C.; Liu, J.-T.; Jiang, X.-K.; Li, Z.-T.; *J. Org. Chem.* **2012**, *77* (9), 4261-4270.
- [39] Aemissegger, A.; Kräutler, V.; van Gunsteren, W. F.; Hilvert, D.; *J. Am. Chem. Soc.* **2005**, *127* (9), 2929-2936.
- [40] Dong, S.-L.; Löweneck, M.; Schrader, T. E.; Schreier, W. J.; Zinth, W.; Moroder, L.; Renner, C.; *Chem. Eur. J.* **2006**, *12* (4), 1114-1120.
- [41] Freidinger, R. M.; Veber, D. F.; Perlow, D. S.; Brooks; Saperstein, R.; *Science* **1980**, *210* (4470), 656-658.
- [42] Nagai, U.; Sato, K.; *Tetrahedron Lett.* **1985**, *26* (5), 647-650.
- [43] Nagai, U.; Sato, K.; Nakamura, R.; Kato, R.; *Tetrahedron* **1993**, *49* (17), 3577-3592.
- [44] Bag, S. S.; Jana, S.; Yashmeen, A.; De, S.; *Chem. Commun.* **2015**, *51* (25), 5242-5245.
- [45] Celentano, V.; Diana, D.; Di Salvo, C.; De Rosa, L.; Romanelli, A.; Fattorusso, R.; D'Andrea, L. D.; *Chem. Eur. J.* **2016**, *22* (16), 5534-5537.
- [46] Anfinsen, C. B.; *Science* **1973**, *181* (4096), 223-230.
- [47] Dobson, C. M.; *Nature* **2003**, *426*, 884.
- [48] Gomes, C. M.; Faisca, P. F. N.; in *Protein Folding. SpringerBriefs in Molecular Science*, Springer, Cham, **2019**.
- [49] Kim, P. S.; Baldwin, R. L.; *Annu. Rev. Biochem.* **1982**, *51* (1), 459-489.
- [50] Udgaonkar, J. B.; Baldwin, R. L.; *Nature* **1988**, *335* (6192), 694-699.
- [51] Dyson, H. J.; Wright, P. E.; *Curr. Opin. Struct. Biol.* **1993**, *3* (1), 60-65.
- [52] Baldwin, R. L.; *Trends Biochem. Sci.* **1989**, *14* (7), 291-294.
- [53] Daggett, V.; Fersht, A. R.; *Trends Biochem. Sci.* **2003**, *28* (1), 18-25.
- [54] Dill, K. A.; *Biochemistry* **1990**, *29* (31), 7133-7155.
- [55] Nölting, B.; Golbik, R.; Neira, J. L.; Soler-Gonzalez, A. S.; Schreiber, G.; Fersht, A. R.; *Proc. Natl. Acad. Sci. U. S. A.* **1997**, *94* (3), 826-830.
- [56] Itzhaki, L. S.; Otzen, D. E.; Fersht, A. R.; *J. Mol. Biol.* **1995**, *254* (2), 260-288.
- [57] Dill, K. A.; Ozkan, S. B.; Shell, M. S.; Weikl, T. R.; *Annu. Rev. Biophys.* **2008**, *37* (1), 289-316.
- [58] S'ali, A.; Shakhnovich, E.; Karplus, M.; *Nature* **1994**, *369* (6477), 248-251.
- [59] Baldwin, R. L.; *Nature* **1994**, *369* (6477), 183-184.
- [60] Onuchic, J. N.; and, Z. L.-S.; Wolynes, P. G.; *Annu. Rev. Phys. Chem.* **1997**, *48* (1), 545-600.
- [61] Dill, K. A.; Chan, H. S.; *Nat. Struct. Biol.* **1997**, *4* (1), 10-19.
- [62] Onuchic, N. J.; Nymeyer, H.; García, A. E.; Chahine, J.; Socci, N. D.; in *Adv. Protein Chem., Vol. 53*, Academic Press, **2000**, pp. 87-152.
- [63] Jahn, T. R.; Radford, S. E.; *The FEBS Journal* **2005**, *272* (23), 5962-5970.
- [64] Adamcik, J.; Mezzenga, R.; *Angew. Chem. Int. Ed.* **2018**, *57* (28), 8370-8382.
- [65] Lewandowska, A.; Ołdziej, S.; Liwo, A.; Scheraga, H. A.; *Biophys. Chem.* **2010**, *151* (1), 1-9.

- [66] Muñoz, V.; Thompson, P. A.; Hofrichter, J.; Eaton, W. A.; *Nature* **1997**, *390*, 196.
- [67] Dinner, A. R.; Lazaridis, T.; Karplus, M.; *Proc. Natl. Acad. Sci. U. S. A.* **1999**, *96* (16), 9068-9073.
- [68] Muñoz, V.; Ghirlando, R.; Blanco, F. J.; Jas, G. S.; Hofrichter, J.; Eaton, W. A.; *Biochemistry* **2006**, *45* (23), 7023-7035.
- [69] Du, D.; Gai, F.; *Biochemistry* **2006**, *45* (44), 13131-13139.
- [70] Du, D.; Zhu, Y.; Huang, C.-Y.; Gai, F.; *Proc. Natl. Acad. Sci. U. S. A.* **2004**, *101* (45), 15915-15920.
- [71] Jäger, M.; Nguyen, H.; Crane, J. C.; Kelly, J. W.; Gruebele, M.; *J. Mol. Biol.* **2001**, *311* (2), 373-393.
- [72] Shukla, R. T.; Kumar, N.; Sasidhar, Y. U.; *J. Pept. Sci.* **2013**, *19* (8), 516-527.
- [73] Seshasayee, A. S. N.; Raghunathan, K.; Sivaraman, K.; Pennathur, G.; *J. Mol. Model.* **2006**, *12* (2), 197-204.
- [74] Collinet, B.; Garcia, P.; Minard, P.; Desmadril, M.; *Eur. J. Biochem.* **2001**, *268* (19), 5107-5118.
- [75] Sharpe, T.; Jonsson, A. L.; Rutherford, T. J.; Daggett, V.; Fersht, A. R.; *Protein Sci.* **2007**, *16* (10), 2233-2239.
- [76] Sweeney, P.; Park, H.; Baumann, M.; Dunlop, J.; Frydman, J.; Kopito, R.; McCampbell, A.; Leblanc, G.; Venkateswaran, A.; Nurmi, A.; Hodgson, R.; *Transl. Neurodegener.* **2017**, *6*, 6-6.
- [77] Khanam, H.; Ali, A.; Asif, M.; Shamsuzzaman; *Eur. J. Med. Chem.* **2016**, *124*, 1121-1141.
- [78] Iadanza, M. G.; Jackson, M. P.; Hewitt, E. W.; Ranson, N. A.; Radford, S. E.; *Nat. Rev. Mol. Cell Biol.* **2018**, *19* (12), 755-773.
- [79] Bonar, L.; Cohen, A. S.; Skinner, M. M.; *Proc. Soc. Exp. Biol. Med.* **1969**, *131* (4), 1373-1375.
- [80] Eanes, E. D.; Glenner, G. G.; *J. Histochem. Cytochem.* **1968**, *16* (11), 673-677.
- [81] Abelein, A.; Abrahams, J. P.; Danielsson, J.; Gräslund, A.; Jarvet, J.; Luo, J.; Tiiman, A.; Wärmländer, S. K. T. S.; *J. Biol. Inorg. Chem.* **2014**, *19* (4), 623-634.
- [82] Harper, J. D.; Peter T. Lansbury, J.; *Annu. Rev. Biochem.* **1997**, *66* (1), 385-407.
- [83] Morgan, C.; Colombres, M.; Nuñez, M. T.; Inestrosa, N. C.; *Prog. Neurobiol.* **2004**, *74* (6), 323-349.
- [84] Arosio, P.; Knowles, T. P. J.; Linse, S.; *Phys. Chem. Chem. Phys.* **2015**, *17* (12), 7606-7618.
- [85] Kreutzer, A. G.; Nowick, J. S.; *Acc. Chem. Res.* **2018**, *51* (3), 706-718.
- [86] Meisl, G.; Yang, X.; Hellstrand, E.; Frohm, B.; Kirkegaard, J. B.; Cohen, S. I. A.; Dobson, C. M.; Linse, S.; Knowles, T. P. J.; *Proc. Natl. Acad. Sci. U. S. A.* **2014**, *111* (26), 9384-9389.
- [87] Cukalevski, R.; Yang, X.; Meisl, G.; Weininger, U.; Bernfur, K.; Frohm, B.; Knowles, T. P. J.; Linse, S.; *Chem. Sci.* **2015**, *6* (7), 4215-4233.
- [88] Cohen, S. I. A.; Linse, S.; Luheshi, L. M.; Hellstrand, E.; White, D. A.; Rajah, L.; Otzen, D. E.; Vendruscolo, M.; Dobson, C. M.; Knowles, T. P. J.; *Proc. Natl. Acad. Sci. U. S. A.* **2013**, *110* (24), 9758-9763.
- [89] Petkova, A. T.; Ishii, Y.; Balbach, J. J.; Antzutkin, O. N.; Leapman, R. D.; Delaglio, F.; Tycko, R.; *Proc. Natl. Acad. Sci. U. S. A.* **2002**, *99* (26), 16742-16747.
- [90] Petkova, A. T.; Yau, W.-M.; Tycko, R.; *Biochemistry* **2006**, *45* (2), 498-512.
- [91] Bertini, I.; Gonnelli, L.; Luchinat, C.; Mao, J.; Nesi, A.; *J. Am. Chem. Soc.* **2011**, *133* (40), 16013-16022.
- [92] Paravastu, A. K.; Leapman, R. D.; Yau, W.-M.; Tycko, R.; *Proc. Natl. Acad. Sci. U. S. A.* **2008**, *105* (47), 18349-18354.
- [93] Lu, J.-X.; Qiang, W.; Yau, W.-M.; Schwieters, Charles D.; Meredith, Stephen C.; Tycko, R.; *Cell* **2013**, *154* (6), 1257-1268.

- [94] Petkova, A. T.; Leapman, R. D.; Guo, Z.; Yau, W.-M.; Mattson, M. P.; Tycko, R.; *Science* **2005**, *307* (5707), 262-265.
- [95] Qiang, W.; Yau, W.-M.; Lu, J.-X.; Collinge, J.; Tycko, R.; *Nature* **2017**, *541*, 217.
- [96] Ghosh, U.; Yau, W.-M.; Tycko, R.; *Chem. Commun.* **2018**, *54* (40), 5070-5073.
- [97] Lazo, N. D.; Grant, M. A.; Condrón, M. C.; Rigby, A. C.; Teplow, D. B.; *Protein Sci.* **2005**, *14* (6), 1581-1596.
- [98] Hoyer, W.; Grönwall, C.; Jonsson, A.; Ståhl, S.; Härd, T.; *Proc. Natl. Acad. Sci. U. S. A.* **2008**, *105* (13), 5099-5104.
- [99] Roychoudhuri, R.; Lomakin, A.; Bernstein, S.; Zheng, X.; Condrón, M. M.; Benedek, G. B.; Bowers, M.; Teplow, D. B.; *J. Mol. Biol.* **2014**, *426* (13), 2422-2441.
- [100] Bhowmik, D.; Mote, K. R.; MacLaughlin, C. M.; Biswas, N.; Chandra, B.; Basu, J. K.; Walker, G. C.; Madhu, P. K.; Maiti, S.; *ACS Nano* **2015**, *9* (9), 9070-9077.
- [101] Van Cauwenberghe, C.; Van Broeckhoven, C.; Sleegers, K.; *Genet. Med.* **2015**, *18*, 421.
- [102] Bekris, L. M.; Yu, C.-E.; Bird, T. D.; Tsuang, D. W.; *J. Geriatr. Psychiatry Neurol.* **2010**, *23* (4), 213-227.
- [103] Murakami, K.; Irie, K.; Morimoto, A.; Ohigashi, H.; Shindo, M.; Nagao, M.; Shimizu, T.; Shirasawa, T.; *Biochem. Biophys. Res. Commun.* **2002**, *294* (1), 5-10.
- [104] Tibben, A.; Hofman, A.; De Jonghe, C.; Van Broeckhoven, C.; Van Duijn, C. M.; Van Harskamp, F.; Roks, G.; Tanghe, H.; De Koning, I.; Van Swieten, J. C.; Cruts, M.; Niermeijer, M. F.; Kumar-Singh, S.; *Brain* **2000**, *123* (10), 2130-2140.
- [105] Betts, V.; Leissring, M. A.; Dolios, G.; Wang, R.; Selkoe, D. J.; Walsh, D. M.; *Neurobiol. Dis.* **2008**, *31* (3), 442-450.
- [106] Yang, X.; Meisl, G.; Frohm, B.; Thulin, E.; Knowles, T. P. J.; Linse, S.; *Proc. Natl. Acad. Sci. U. S. A.* **2018**, *115* (26), E5849-E5858.
- [107] Qiang, W.; Yau, W.-M.; Luo, Y.; Mattson, M. P.; Tycko, R.; *Proc. Natl. Acad. Sci. U. S. A.* **2012**, *109* (12), 4443-4448.
- [108] Hendriks, L.; van Duijn, C. M.; Cras, P.; Cruts, M.; Van Hul, W.; van Harskamp, F.; Warren, A.; McInnis, M. G.; Antonarakis, S. E.; Martin, J.-J.; Hofman, A.; Van Broeckhoven, C.; *Nat. Genet.* **1992**, *1* (3), 218-221.
- [109] Yagi-Utsumi, M.; Dobson, C. M.; *Biol. Pharm. Bull.* **2015**, *38* (10), 1668-1672.
- [110] Walsh, D. M.; Hartley, D. M.; Condrón, M. M.; Selkoe, D. J.; Teplow, D. B.; *Biochem. J.* **2001**, *355* (Pt 3), 869-877.
- [111] Tomiyama, T.; Nagata, T.; Shimada, H.; Teraoka, R.; Fukushima, A.; Kanemitsu, H.; Takuma, H.; Kuwano, R.; Imagawa, M.; Ataka, S.; Wada, Y.; Yoshioka, E.; Nishizaki, T.; Watanabe, Y.; Mori, H.; *Ann. Neurol.* **2008**, *63* (3), 377-387.
- [112] Schütz, A. K.; Vagt, T.; Huber, M.; Ovchinnikova, O. Y.; Cadalbert, R.; Wall, J.; Güntert, P.; Böckmann, A.; Glockshuber, R.; Meier, B. H.; *Angew. Chem. Int. Ed.* **2015**, *54* (1), 331-335.
- [113] Berhanu, W. M.; Alred, E. J.; Hansmann, U. H. E.; *J. Phys. Chem. B* **2015**, *119* (41), 13063-13070.
- [114] Melchor, J. P.; McVoy, L.; Van Nostrand, W. E.; *J. Neurochem.* **2000**, *74* (5), 2209-2212.
- [115] Miravalle, L.; Tokuda, T.; Chiarle, R.; Giaccone, G.; Bugiani, O.; Tagliavini, F.; Frangione, B.; Ghiso, J.; *J. Biol. Chem.* **2000**, *275* (35), 27110-27116.
- [116] Nilsberth, C.; Westlind-Danielsson, A.; Eckman, C. B.; Condrón, M. M.; Axelman, K.; Forsell, C.; Stenh, C.; Luthman, J.; Teplow, D. B.; Younkin, S. G.; Näslund, J.; Lannfelt, L.; *Nat. Neurosci.* **2001**, *4*, 887.

- [117] Cheng, I. H.; Scarce-Levie, K.; Legleiter, J.; Palop, J. J.; Gerstein, H.; Bien-Ly, N.; Puoliväli, J.; Lesné, S.; Ashe, K. H.; Muchowski, P. J.; Mucke, L.; *J. Biol. Chem.* **2007**, *282* (33), 23818-23828.
- [118] Lo, C.-J.; Wang, C.-C.; Huang, H.-B.; Chang, C.-F.; Shiao, M.-S.; Chen, Y.-C.; Lin, T.-H.; *Amyloid* **2015**, *22* (1), 8-18.
- [119] Johansson, A.-S.; Berglind-Dehlin, F.; Karlsson, G.; Edwards, K.; Gellerfors, P.; Lannfelt, L.; *FEBS J.* **2006**, *273* (12), 2618-2630.
- [120] Levy, E.; Carman, M.; Fernandez-Madrid, I.; Power, M.; Lieberburg, I.; van Duinen, S.; Bots, G.; Luyendijk, W.; Frangione, B.; *Science* **1990**, *248* (4959), 1124-1126.
- [121] Grabowski, T. J.; Cho, H. S.; Vonsattel, J. P. G.; Rebeck, G. W.; Greenberg, S. M.; *Ann. Neurol.* **2001**, *49* (6), 697-705.
- [122] Tycko, R.; Sciarretta, K. L.; Orgel, J. P. R. O.; Meredith, S. C.; *Biochemistry* **2009**, *48* (26), 6072-6084.
- [123] Xi, W.; Hansmann, U. H. E.; *J. Chem. Phys.* **2018**, *148* (4), 045103.
- [124] Van Nostrand, W. E.; Melchor, J. P.; Cho, H. S.; Greenberg, S. M.; Rebeck, G. W.; *J. Biol. Chem.* **2001**, *276* (35), 32860-32866.
- [125] Hu, Y.; Zheng, H.; Su, B.; Hernandez, M.; Kim, J. R.; *Biochim. Biophys. Acta, Proteins Proteom.* **2012**, *1824* (10), 1069-1079.
- [126] Doran, T. M.; Anderson, E. A.; Latchney, S. E.; Opanashuk, L. A.; Nilsson, B. L.; *J. Mol. Biol.* **2012**, *421* (2), 315-328.
- [127] Doran, T. M.; Anderson, E. A.; Latchney, S. E.; Opanashuk, L. A.; Nilsson, B. L.; *ACS Chem. Neurosci.* **2012**, *3* (3), 211-220.
- [128] Hamada, Y.; Miyamoto, N.; Kiso, Y.; *Bioorg. Med. Chem. Lett.* **2015**, *25* (7), 1572-1576.
- [129] Yashima, E.; Maeda, K.; Iida, H.; Furusho, Y.; Nagai, K.; *Chem. Rev.* **2009**, *109* (11), 6102-6211.
- [130] Nakano, T.; Okamoto, Y.; *Chem. Rev.* **2001**, *101* (12), 4013-4038.
- [131] Bur, A. J.; Fetters, L. J.; *Chem. Rev.* **1976**, *76* (6), 727-746.
- [132] Mayer, S.; Zentel, R.; *Prog. Polym. Sci.* **2001**, *26* (10), 1973-2013.
- [133] Okamoto, Y.; Suzuki, K.; Ohta, K.; Hatada, K.; Yuki, H.; *J. Am. Chem. Soc.* **1979**, *101* (16), 4763-4765.
- [134] Miller, R. D.; Michl, J.; *Chem. Rev.* **1989**, *89* (6), 1359-1410.
- [135] Liu, J.; Lam, J. W. Y.; Tang, B. Z.; *Chem. Rev.* **2009**, *109* (11), 5799-5867.
- [136] Nolte, R. J. M.; *Chem. Soc. Rev.* **1994**, *23* (1), 11-19.
- [137] Hill, D. J.; Mio, M. J.; Prince, R. B.; Hughes, T. S.; Moore, J. S.; *Chem. Rev.* **2001**, *101* (12), 3893-4012.
- [138] Gellman, S. H.; *Acc. Chem. Res.* **1998**, *31* (4), 173-180.
- [139] Avan, I.; Hall, C. D.; Katritzky, A. R.; *Chem. Soc. Rev.* **2014**, *43* (10), 3575-3594.
- [140] Seebach, D.; Gardiner, J.; *Acc. Chem. Res.* **2008**, *41* (10), 1366-1375.
- [141] Semetey, V.; Rognan, D.; Hemmerlin, C.; Graff, R.; Briand, J.-P.; Marraud, M.; Guichard, G.; *Angew. Chem. Int. Ed.* **2002**, *41* (11), 1893-1895.
- [142] Nelson, J. C.; Saven, J. G.; Moore, J. S.; Wolynes, P. G.; *Science* **1997**, *277* (5333), 1793-1796.
- [143] Xu, Y.-X.; Zhan, T.-G.; Zhao, X.; Li, Z.-T.; *Org. Chem. Front.* **2014**, *1* (1), 73-78.
- [144] Gong, B.; *Acc. Chem. Res.* **2012**, *45* (12), 2077-2087.
- [145] Sebaoun, L.; Maurizot, V.; Granier, T.; Kauffmann, B.; Huc, I.; *J. Am. Chem. Soc.* **2014**, *136* (5), 2168-2174.
- [146] Elacqua, E.; Geberth, G. T.; Vanden Bout, D. A.; Weck, M.; *Chem. Sci.* **2019**, *10* (7), 2144-2152.



- [147] ter Huurne, G. M.; Voets, I. K.; Palmans, A. R. A.; Meijer, E. W.; *Macromolecules* **2018**, *51* (21), 8853-8861.
- [148] Zhang, J.; Tanaka, J.; Gurnani, P.; Wilson, P.; Hartlieb, M.; Perrier, S.; *Polym. Chem.* **2017**, *8* (28), 4079-4087.
- [149] Altintas, O.; Barner-Kowollik, C.; *Macromol. Rapid Commun.* **2012**, *33* (11), 958-971.
- [150] Altintas, O.; Barner-Kowollik, C.; *Macromol. Rapid Commun.* **2016**, *37* (1), 29-46.
- [151] Matsumoto, K.; Terashima, T.; Sugita, T.; Takenaka, M.; Sawamoto, M.; *Macromolecules* **2016**, *49* (20), 7917-7927.
- [152] Altintas, O.; Artar, M.; ter Huurne, G.; Voets, I. K.; Palmans, A. R. A.; Barner-Kowollik, C.; Meijer, E. W.; *Macromolecules* **2015**, *48* (24), 8921-8932.
- [153] Hosono, N.; Gillissen, M. A. J.; Li, Y.; Sheiko, S. S.; Palmans, A. R. A.; Meijer, E. W.; *J. Am. Chem. Soc.* **2013**, *135* (1), 501-510.
- [154] Appel, E. A.; Dyson, J.; del Barrio, J.; Walsh, Z.; Scherman, O. A.; *Angew. Chem. Int. Ed.* **2012**, *51* (17), 4185-4189.
- [155] Willenbacher, J.; Schmidt, B. V. K. J.; Schulze-Suenninghausen, D.; Altintas, O.; Luy, B.; Delaittre, G.; Barner-Kowollik, C.; *Chem. Commun.* **2014**, *50* (53), 7056-7059.
- [156] Schmidt, B. V. K. J.; Hetzer, M.; Ritter, H.; Barner-Kowollik, C.; *Prog. Polym. Sci.* **2014**, *39* (1), 235-249.
- [157] Yilmaz, G.; Uzunova, V.; Napier, R.; Becer, C. R.; *Biomacromolecules* **2018**, *19* (7), 3040-3047.
- [158] Altintas, O.; Krolla-Sidenstein, P.; Gliemann, H.; Barner-Kowollik, C.; *Macromolecules* **2014**, *47* (17), 5877-5888.
- [159] Tuten, B. T.; Chao, D.; Lyon, C. K.; Berda, E. B.; *Polym. Chem.* **2012**, *3* (11), 3068-3071.
- [160] Song, C.; Li, L.; Dai, L.; Thayumanavan, S.; *Polym. Chem.* **2015**, *6* (26), 4828-4834.
- [161] Kröger, A. P. P.; Boonen, R. J. E. A.; Paulusse, J. M. J.; *Polymer* **2017**, *120*, 119-128.
- [162] Rubio-Cervilla, J.; Barroso-Bujans, F.; Pomposo, J. A.; *Macromolecules* **2016**, *49* (1), 90-97.
- [163] Perez-Baena, I.; Asenjo-Sanz, I.; Arbe, A.; Moreno, A. J.; Lo Verso, F.; Colmenero, J.; Pomposo, J. A.; *Macromolecules* **2014**, *47* (23), 8270-8280.
- [164] Zhang, J.; Gody, G.; Hartlieb, M.; Catrouillet, S.; Moffat, J.; Perrier, S.; *Macromolecules* **2016**, *49* (23), 8933-8942.
- [165] Ormategui, N.; García, I.; Padro, D.; Cabañero, G.; Grande, H. J.; Loinaz, I.; *Soft Matter* **2012**, *8* (3), 734-740.
- [166] Perez-Baena, I.; Loinaz, I.; Padro, D.; García, I.; Grande, H. J.; Odriozola, I.; *J. Mater. Chem.* **2010**, *20* (33), 6916-6922.
- [167] de Luzuriaga, A. R.; Ormategui, N.; Grande, H. J.; Odriozola, I.; Pomposo, J. A.; Loinaz, I.; *Macromol. Rapid Commun.* **2008**, *29* (12-13), 1156-1160.
- [168] Freytag, K.; Säfken, S.; Wolter, K.; Namyslo, J. C.; Hübner, E. G.; *Polym. Chem.* **2017**, *8* (48), 7546-7558.
- [169] Wang, F.; Pu, H.; Jin, M.; Wan, D.; *Macromol. Rapid Commun.* **2016**, *37* (4), 330-336.
- [170] Beijer, F. H.; Sijbesma, R. P.; Kooijman, H.; Spek, A. L.; Meijer, E. W.; *J. Am. Chem. Soc.* **1998**, *120* (27), 6761-6769.
- [171] Altintas, O.; Lejeune, E.; Gerstel, P.; Barner-Kowollik, C.; *Polym. Chem.* **2012**, *3* (3), 640-651.
- [172] Bai, Y.; Feng, X.; Xing, H.; Xu, Y.; Kim, B. K.; Baig, N.; Zhou, T.; Gewirth, A. A.; Lu, Y.; Oldfield, E.; Zimmerman, S. C.; *J. Am. Chem. Soc.* **2016**, *138* (35), 11077-11080.
- [173] Rothfuss, H.; Knöfel, N. D.; Roesky, P. W.; Barner-Kowollik, C.; *J. Am. Chem. Soc.* **2018**, *140* (18), 5875-5881.
- [174] Kröger, A. P. P.; Paulusse, J. M. J.; *J. Control. Release* **2018**, *286*, 326-347.

- [175] Tooley, C. A.; Pazicni, S.; Berda, E. B.; *Polym. Chem.* **2015**, *6* (44), 7646-7651.
- [176] Rodriguez, K. J.; Hanlon, A. M.; Lyon, C. K.; Cole, J. P.; Tuten, B. T.; Tooley, C. A.; Berda, E. B.; Pazicni, S.; *Inorg. Chem.* **2016**, *55* (19), 9493-9496.
- [177] Ogura, Y.; Artar, M.; Palmans, A. R. A.; Sawamoto, M.; Meijer, E. W.; Terashima, T.; *Macromolecules* **2017**, *50* (8), 3215-3223.
- [178] Brik, A.; Alexandratos, J.; Lin, Y.-C.; Elder, J. H.; Olson, A. J.; Wlodawer, A.; Goodsell, D. S.; Wong, C.-H.; *ChemBioChem* **2005**, *6* (7), 1167-1169.
- [179] Li, X.; *Chem. Asian J.* **2011**, *6* (10), 2606-2616.
- [180] Ahmad Fuaad, A. A. H.; Azmi, F.; Skwarczynski, M.; Toth, I.; *Molecules* **2013**, *18* (11), 13148-13174.
- [181] Tremmel, P.; Geyer, A.; *Angew. Chem. Int. Ed.* **2004**, *43* (43), 5789-5791.
- [182] Geyer, A.; Bockelmann, D.; Weissenbach, K.; Fischer, H.; *Tetrahedron Lett.* **1999**, *40* (3), 477-478.
- [183] Geyer, A.; Moser, F.; *Eur. J. Org. Chem.* **2000**, *2000* (7), 1113-1120.
- [184] Tremmel, P.; Geyer, A.; *J. Am. Chem. Soc.* **2002**, *124* (29), 8548-8549.
- [185] Eckhardt, B.; Grosse, W.; Essen, L.-O.; Geyer, A.; *Proc. Natl. Acad. Sci. U. S. A.* **2010**, *107* (43), 18336-18341.
- [186] Zeng, L.-F.; Zhang, R.-Y.; Yu, Z.-H.; Li, S.; Wu, L.; Gunawan, A. M.; Lane, B. S.; Mali, R. S.; Li, X.; Chan, R. J.; Kapur, R.; Wells, C. D.; Zhang, Z.-Y.; *J. Med. Chem.* **2014**, *57* (15), 6594-6609.
- [187] Chen, S.; Zhang, S.; Bao, C.; Wang, C.; Lin, Q.; Zhu, L.; *Chem. Commun.* **2016**, *52* (89), 13132-13135.
- [188] Patten, T. E.; Novak, B. M.; *J. Am. Chem. Soc.* **1991**, *113* (13), 5065-5066.
- [189] Patten, T. E.; Novak, B. M.; *J. Am. Chem. Soc.* **1996**, *118* (8), 1906-1916.
- [190] Satoh, T.; Ihara, R.; Kawato, D.; Nishikawa, N.; Suemasa, D.; Kondo, Y.; Fuchise, K.; Sakai, R.; Kakuchi, T.; *Macromolecules* **2012**, *45* (9), 3677-3686.
- [191] Ute, K.; Asai, T.; Fukunishi, Y.; Hatada, K.; *Polym. J.* **1995**, *27* (4), 445-448.
- [192] Lien, L. T. N.; Kikuchi, M.; Narumi, A.; Nagai, K.; Kawaguchi, S.; *Polym. J.* **2008**, *40* (11), 1105-1112.
- [193] Deike, S.; Master thesis, Martin Luther University Halle-Wittenberg **2014**.
- [194] Deike, S.; Binder, W. H.; *Macromolecules* **2017**, *50* (7), 2637-2644.
- [195] Binder, W. H.; Sachsenhofer, R.; *Macromolecular Rapid Communications* **2007**, *28* (1), 15-54.
- [196] Binder, W. H.; Sachsenhofer, R.; *Macromol. Rapid Commun.* **2008**, *29* (12-13), 952-981.
- [197] Meldal, M.; *Macromol. Rapid Commun.* **2008**, *29* (12-13), 1016-1051.
- [198] Kolb, H. C.; Finn, M. G.; Sharpless, K. B.; *Angew. Chem.* **2001**, *113* (11), 2056-2075.
- [199] Meldal, M.; Tornøe, C. W.; *Chem. Rev.* **2008**, *108* (8), 2952-3015.
- [200] Beierle, J. M.; Horne, W. S.; van Maarseveen, J. H.; Waser, B.; Reubi, J. C.; Ghadiri, M. R.; *Angew. Chem. Int. Ed.* **2009**, *48* (26), 4725-4729.
- [201] Oh, K.; Guan, Z.; *Chem. Commun.* **2006**(29), 3069-3071.
- [202] Malke, M.; Barqawi, H.; Binder, W. H.; *ACS Macro Lett.* **2014**, *3* (4), 393-397.
- [203] Shah, P. N.; Min, J.; Chae, C.-G.; Nishikawa, N.; Suemasa, D.; Kakuchi, T.; Satoh, T.; Lee, J.-S.; *Macromolecules* **2012**, *45* (22), 8961-8969.
- [204] Molla, M. R.; Prasad, P.; Thayumanavan, S.; *J. Am. Chem. Soc.* **2015**, *137* (23), 7286-7289.
- [205] Wei, T.; Jung, J. H.; Scott, T. F.; *J. Am. Chem. Soc.* **2015**, *137* (51), 16196-16202.
- [206] Testa, B.; *Helv. Chim. Acta* **2013**, *96* (3), 351-374.
- [207] Hembury, G. A.; Borovkov, V. V.; Inoue, Y.; *Chem. Rev.* **2008**, *108* (1), 1-73.
- [208] Liu, M.; Zhang, L.; Wang, T.; *Chem. Rev.* **2015**, *115* (15), 7304-7397.

- [209] Zhu, H.-J.; in *Organic Stereochemistry* (Ed.: Wiley-VCH), **2015**, pp. 1-29.
- [210] Yashima, E.; Maeda, K.; Iida, H.; Furusho, Y.; Nagai, K.; *Chem. Rev.* **2009**, *109* (11), 6102-6211.
- [211] Shmueli, U.; Traub, W.; Rosenheck, K.; *J. Polym. Sci., Polym. Phys. Ed.* **1969**, *7* (3), 515-524.
- [212] Berger, M. N.; Tidswell, B. M.; *J. Polym. Sci. Polym. Symp.* **1973**, *42* (3), 1063-1075.
- [213] Alemán, C.; Green, M. M.; *Macromol. Theory Simul.* **2001**, *10* (2), 100-107.
- [214] Murakami, H.; Norisuye, T.; Fujita, H.; *Macromolecules* **1980**, *13* (2), 345-352.
- [215] Norisuye, T.; Tsuboi, A.; Teramoto, A.; *Polym. J.* **1996**, *28* (4), 357-361.
- [216] Green, M. M.; Andreola, C.; Munoz, B.; Reidy, M. P.; Zero, K.; *J. Am. Chem. Soc.* **1988**, *110* (12), 4063-4065.
- [217] Lifson, S.; Green, M. M.; Andreola, C.; Peterson, N. C.; *J. Am. Chem. Soc.* **1989**, *111*, 8850-8858.
- [218] Choinopoulos, I.; Koinis, S.; Pitsikalis, M.; *J. Polym. Sci. Part A* **2015**, *53* (18), 2141-2151.
- [219] Pijper, D.; Feringa, B. L.; *Angew. Chem. Int. Ed.* **2007**, *46* (20), 3693-3696.
- [220] Nath, G. Y.; Samal, S.; Park, S.-Y.; Murthy, C. N.; Lee, J.-S.; *Macromolecules* **2006**, *39* (18), 5965-5966.
- [221] Sakai, R.; Satoh, T.; Kakuchi, R.; Kaga, H.; Kakuchi, T.; *Macromolecules* **2004**, *37* (11), 3996-4003.
- [222] Green, M. M.; Khatri, C.; Peterson, N. C.; *J. Am. Chem. Soc.* **1993**, *115* (11), 4941-4942.
- [223] Green, M. M.; Garetz, B. A.; Munoz, B.; Chang, H.; Hoke, S.; Cooks, R. G.; *J. Am. Chem. Soc.* **1995**, *117* (14), 4181-4182.
- [224] Green, M. M.; Reidy, M. P.; Johnson, R. D.; Darling, G.; O'Leary, D. J.; Willson, G.; *J. Am. Chem. Soc.* **1989**, *111*, 6452-6454.
- [225] Lifson, S.; Felder, C. E.; Green, M. M.; *Macromolecules* **1992**, *25*, 4142-4148.
- [226] Shah, P. N.; Min, J.; Lee, J.-S.; *Chem. Commun.* **2012**, *48* (6), 826-828.
- [227] Shah, P. N.; Min, J.; Kim, H.-J.; Park, S.-Y.; Lee, J.-S.; *Macromolecules* **2011**, *44* (20), 7917-7925.
- [228] Green, M. M.; Peterson, N. C.; Sato, T.; Teramoto, A.; Cook, R.; Lifson, S.; *Science* **1995**, *268* (5219), 1860-1866.
- [229] Green, M. M.; Park, J.-W.; Sato, T.; Teramoto, A.; Lifson, S.; Selinger, R. L. B.; Selinger, J. V.; *Angew. Chem. Int. Ed.* **1999**, *38* (21), 3138-3154.
- [230] Cook, R.; Johnson, R. D.; Wade, C. G.; O'Leary, D. J.; Munoz, B.; Green, M. M.; *Macromolecules* **1990**, *23* (14), 3454-3458.
- [231] Ramos Lermo, E.; M. W. Langeveld-Voss, B.; A. J. Janssen, R.; W. Meijer, E.; *Chemical Communications* **1999**(9), 791-792.
- [232] Itoh, T.; Shichi, T.; Yui, T.; Takagi, K.; *Langmuir* **2005**, *21* (8), 3217-3220.
- [233] Marty, R.; Nigon, R.; Leite, D.; Frauenrath, H.; *J. Am. Chem. Soc.* **2014**, *136* (10), 3919-3927.
- [234] Leiras, S.; Freire, F.; Seco, J. M.; Quinoa, E.; Riguera, R.; *Chem. Sci.* **2013**, *4* (7), 2735-2743.
- [235] Yunosuke, A.; Toshiki, A.; Hongge, J.; Shingo, H.; Takeshi, N.; Yuriko, K.; Lijia, L.; Yu, Z.; Masahiro, T.; Takashi, K.; *Chem. Lett.* **2012**, *41* (3), 244-246.
- [236] Tang, H.-Z.; Boyle, P. D.; Novak, B. M.; *J. Am. Chem. Soc.* **2005**, *127* (7), 2136-2142.
- [237] Wu, J.; Pearce, E. M.; Kwei, T. K.; Lefebvre, A. A.; Balsara, N. P.; *Macromolecules* **2002**, *35* (5), 1791-1796.
- [238] Deike, S.; Malke, M.; Lechner, B.-D.; Binder, W. H.; *Polymers* **2017**, *9* (8), 369.
- [239] Kawaguchi, M.; Yamamoto, M.; Kurauchi, N.; Kato, T.; *Langmuir* **1999**, *15* (4), 1388-1391.

- [240] Kawaguchi, M.; Ishikawa, R.; Yamamoto, M.; Kuki, T.; Kato, T.; *Langmuir* **2001**, *17* (2), 384-387.
- [241] Gargallo, L.; Becerra, N.; Sandoval, C.; Pitsikalis, M.; Hadjichristidis, N.; Leiva, A.; Radic, D.; *J. Appl. Polym. Sci.* **2011**, *122* (2), 1395-1404.
- [242] Kawaguchi, M.; Suzuki, M.; *J. Colloid Interface Sci.* **2005**, *288* (2), 548-552.
- [243] Itou, T.; Chikiri, H.; Teramoto, A.; Aharoni, S. M.; *Polym. J.* **1988**, *20* (2), 143-151.
- [244] Morioka, T.; Shibata, O.; Kawaguchi, M.; *Langmuir* **2010**, *26* (17), 14058-14063.
- [245] Morioka, T.; Shibata, O.; Kawaguchi, M.; *Langmuir* **2010**, *26* (23), 18189-18193.
- [246] Malzert, A.; Boury, F.; Saulnier, P.; Benoit, J. P.; Proust, J. E.; *Langmuir* **2000**, *16* (4), 1861-1867.
- [247] Gonçalves da Silva, A. M.; Filipe, E. J. M.; d'Oliveira, J. M. R.; Martinho, J. M. G.; *Langmuir* **1996**, *12* (26), 6547-6553.
- [248] Sauer, B. B.; Yu, H.; *Macromolecules* **1989**, *22* (2), 786-791.
- [249] Logan, J. L.; Masse, P.; Gnanou, Y.; Taton, D.; Duran, R. S.; *Langmuir* **2005**, *21* (16), 7380-7389.
- [250] McConnell, H. M.; *Annu. Rev. Phys. Chem.* **1991**, *42* (1), 171-195.
- [251] Levine, H.; *Protein Sci.* **1993**, *2* (3), 404-410.
- [252] Chandrakesan, M.; Bhowmik, D.; Sarkar, B.; Abhyankar, R.; Singh, H.; Kallianpur, M.; Dandekar, S. P.; Madhu, P. K.; Maiti, S.; Mithu, V. S.; *J. Biol. Chem.* **2015**, *290* (50), 30099-30107.
- [253] Stanger, H. E.; Gellman, S. H.; *J. Am. Chem. Soc.* **1998**, *120* (17), 4236-4237.
- [254] Liu, R.; McAllister, C.; Lyubchenko, Y.; Sierks, M. R.; *J. Neurosci. Res.* **2004**, *75* (2), 162-171.
- [255] Chandrakesan, M.; Sarkar, B.; Mithu, V. S.; Abhyankar, R.; Bhowmik, D.; Nag, S.; Sahoo, B.; Shah, R.; Gurav, S.; Banerjee, R.; Dandekar, S.; Jose, J. C.; Sengupta, N.; Madhu, P. K.; Maiti, S.; *Chem. Phys.* **2013**, *422*, 80-87.
- [256] Tjernberg, L. O.; Näslund, J.; Lindqvist, F.; Johansson, J.; Karlström, A. R.; Thyberg, J.; Terenius, L.; Nordstedt, C.; *J. Biol. Chem.* **1996**, *271* (15), 8545-8548.
- [257] Tjernberg, L. O.; Lilliehöök, C.; Callaway, D. J. E.; Näslund, J.; Hahne, S.; Thyberg, J.; Terenius, L.; Nordstedt, C.; *J. Biol. Chem.* **1997**, *272* (19), 12601-12605.
- [258] Lowe, T. L.; Strzelec, A.; Kiessling, L. L.; Murphy, R. M.; *Biochemistry* **2001**, *40* (26), 7882-7889.
- [259] Watanabe, K.-i.; Nakamura, K.; Akikusa, S.; Okada, T.; Kodaka, M.; Konakahara, T.; Okuno, H.; *Biochem. Biophys. Res. Commun.* **2002**, *290* (1), 121-124.
- [260] Arai, T.; Sasaki, D.; Araya, T.; Sato, T.; Sohma, Y.; Kanai, M.; *ChemBioChem* **2014**, *15* (17), 2577-2583.
- [261] Bortolini, C.; Klausen, L. H.; Hoffmann, S. V.; Jones, N. C.; Saadeh, D.; Wang, Z.; Knowles, T. P. J.; Dong, M.; *ACS Nano* **2018**, *12* (6), 5408-5416.
- [262] Ma, B.; Nussinov, R.; *Proc. Natl. Acad. Sci. U. S. A.* **2002**, *99* (22), 14126-14131.
- [263] Brahm, S.; Brahm, J.; *J. Mol. Biol.* **1980**, *138* (2), 149-178.
- [264] Greenfield, N. J.; *Nat. Protoc.* **2006**, *1* (6), 2876-2890.
- [265] Wägele, J.; De Sio, S.; Bruno, V.; Jochen, B.; Ott, M.; *bioRxiv* **2018**.
- [266] Adler, J.; Scheidt, H. A.; Kruger, M.; Thomas, L.; Huster, D.; *Phys. Chem. Chem. Phys.* **2014**, *16* (16), 7461-7471.
- [267] Lindberg, D. J.; Wranne, M. S.; Gilbert Gatty, M.; Westerlund, F.; Esbjörner, E. K.; *Biochem. Biophys. Res. Commun.* **2015**, *458* (2), 418-423.
- [268] Younan, N. D.; Viles, J. H.; *Biochemistry* **2015**, *54* (28), 4297-4306.

- [269] Di Carlo, M. G.; Minicozzi, V.; Foderà, V.; Militello, V.; Vetri, V.; Morante, S.; Leone, M.; *Biophys. Chem.* **2015**, *206*, 1-11.
- [270] Manzoni, C.; Colombo, L.; Bigini, P.; Diana, V.; Cagnotto, A.; Messa, M.; Lupi, M.; Bonetto, V.; Pignataro, M.; Airoidi, C.; Sironi, E.; Williams, A.; Salmona, M.; *PLoS One* **2011**, *6* (9), e24909.
- [271] Krotee, P.; Griner, S. L.; Sawaya, M. R.; Cascio, D.; Rodriguez, J. A.; Shi, D.; Philipp, S.; Murray, K.; Saelices, L.; Lee, J.; Seidler, P.; Glabe, C. G.; Jiang, L.; Gonen, T.; Eisenberg, D. S.; *J. Biol. Chem.* **2017**.
- [272] Hilt, S.; Altman, R.; Kálai, T.; Maezawa, I.; Gong, Q.; Wachsmann-Hogiu, S.; Jin, L.-W.; Voss, J. C.; *Molecules* **2018**, *23* (8), 2010.
- [273] Fezoui, Y.; Hartley, D. M.; Harper, J. D.; Khurana, R.; Walsh, D. M.; Condron, M. M.; Selkoe, D. J.; Lansbury, P. T.; Fink, A. L.; Teplow, D. B.; *Amyloid* **2000**, *7* (3), 166-178.
- [274] Sonzini, S.; Stanyon, H. F.; Scherman, O. A.; *Phys. Chem. Chem. Phys.* **2017**, *19* (2), 1458-1465.
- [275] Wu, J. W.; Breydo, L.; Isas, J. M.; Lee, J.; Kuznetsov, Y. G.; Langen, R.; Glabe, C.; *J. Biol. Chem.* **2010**, *285* (9), 6071-6079.
- [276] Breydo, L.; Kurouski, D.; Rasool, S.; Milton, S.; Wu, J. W.; Uversky, V. N.; Lednev, I. K.; Glabe, C. G.; *Biochem. Biophys. Res. Commun.* **2016**, *477* (4), 700-705.
- [277] Awasthi, A.; Matsunaga, Y.; Yamada, T.; *Exp. Neurol.* **2005**, *196* (2), 282-289.
- [278] Wei, W.; Wang, X.; Kusiak, J. W.; *J. Biol. Chem.* **2002**, *277* (20), 17649-17656.
- [279] O'Nuallain, B.; Thakur, A. K.; Williams, A. D.; Bhattacharyya, A. M.; Chen, S.; Thiagarajan, G.; Wetzel, R.; in *Methods Enzymol.*, Vol. 413, Academic Press, **2006**, pp. 34-74.
- [280] Schlenzig, D.; Manhart, S.; Cinar, Y.; Kleinschmidt, M.; Hause, G.; Willbold, D.; Funke, S. A.; Schilling, S.; Demuth, H.-U.; *Biochemistry* **2009**, *48* (29), 7072-7078.
- [281] Piechotta, A.; Parthier, C.; Kleinschmidt, M.; Gnoth, K.; Pillot, T.; Lues, I.; Demuth, H.-U.; Schilling, S.; Rahfeld, J.-U.; Stubbs, M. T.; *J. Biol. Chem.* **2017**, *292* (30), 12713-12724.
- [282] Geyer, A.; Moser, F.; *Eur. J. Org. Chem.* **2000**, *2000* (7), 1113-1120.
- [283] Tremmel, P.; Geyer, A.; *J. Am. Chem. Soc.* **2002**, *124* (29), 8548-8549.
- [284] Horger, R.; Geyer, A.; *Org. Biomol. Chem.* **2006**, *4* (24), 4491-4496.
- [285] Eckhardt, B.; Grosse, W.; Essen, L.-O.; Geyer, A.; *Proc. Natl. Acad. Sci. U. S. A.* **2010**, *107* (43), 18336-18341.
- [286] Ouairy, C. M. J.; Ferraz, M. J.; Boot, R. G.; Baggelaar, M. P.; van der Stelt, M.; Appelman, M.; van der Mare, G. A.; Florea, B. I.; Aerts, J. M. F. G.; Overkleeft, H. S.; *Chem. Commun.* **2015**, *51* (28), 6161-6163.
- [287] Yamakoshi, H.; Dodo, K.; Palonpon, A.; Ando, J.; Fujita, K.; Kawata, S.; Sodeoka, M.; *J. Am. Chem. Soc.* **2012**, *134* (51), 20681-20689.
- [288] Fineman, M.; Ross, S. D.; *J. Polym. Sci.* **1950**, *5* (2), 259-262.
- [289] Kelen, T.; Tüdös, F.; *J. Macromol. Sci. A* **1975**, *9* (1), 1-27.
- [290] Baier, G.; Siebert, J. M.; Landfester, K.; Musyanovych, A.; *Macromolecules* **2012**, *45* (8), 3419-3427.

# Curriculum Vitae

## Persönliche Angaben

Stefanie Deike

Röpziger Str. 1

06110 Halle (Saale)

\*23.07.1990, Braunschweig

Ledig

## Berufserfahrung

Seit 02/2015                      Wissenschaftliche Mitarbeiterin, Arbeitsgruppe Prof. W. H. Binder,  
Makromolekulare Chemie, Martin-Luther-Universität Halle-  
Wittenberg

Promotionsstudium

## Ausbildung

10/2012 – 12/2014              Masterstudium Chemie, Martin-Luther-Universität Halle-Wittenberg  
Vertiefung: Makromolekulare Chemie

09/2013 – 03/2014              Auslandssemester, École nationale supérieure de chimie de  
Montpellier, Frankreich

10/2009 – 09/2012              Bachelorstudium Chemie, Martin-Luther-Universität Halle-Wittenberg

09/2000 – 07/2009              Ernst-Mach-Gymnasium Haar (bei München), Abitur

## Sprachkenntnisse

Englisch                              Fließend (C1)

Französisch                          Sehr gut (B2)

## Publikationsliste

Deike, S.; Binder, W.H., Induction of Chirality in  $\beta$ -Turn Mimetic Polymer Conjugates *via* Postpolymerization “Click” Coupling. *Macromolecules* **2017**, *50*, 2637-2644.

Deike, S.; Malke, M.; Lechner, B.D.; Binder, W. H., Constraining polymers into beta-turns: miscibility and phase segregation effects in lipid monolayers. *Polymers* **2017**, *9*, 369.

Kumar, S.; Deike, S.; Binder, W. H., One-Pot Synthesis of Thermo-responsive Amyloidogenic Peptide-Polymer Conjugates *via* Thio-Bromo “Click” Reaction of RAFT Polymers. *Macromol. Rapid Commun.* **2017**, 1700507.

## Konferenzbeiträge

S. Deike, W. H. Binder; “Synthesis and assembly of  $\beta$ -turn mimetic polymer conjugates”, Bordeaux Polymer Conference, 28.–31. Mai 2018, Bordeaux, Frankreich, Vortrag.

S. Deike, W. H. Binder; “Induction of chirality in  $\beta$ -turn mimetic polymer conjugates *via* postpolymerization “click” coupling”, APME (Advanced Polymer *via* Macromolecular Engineering), 21.–25. Mai 2017, Ghent, Belgien, Poster P068.

S. Deike, M. Malke, W. H. Binder; „Helical  $\beta$ -turn mimetic polymer-conjugates“, Biennial Meeting of the GDCh-Division Macromolecular Chemistry, 11.–13. September 2016, Halle (Saale), Deutschland, Poster P06.

S. Deike, M. Malke, W. H. Binder; „Helical  $\beta$ -turn mimetic polymer-conjugates“, Warwick Polymer Conference, 11.–14. Juli 2016, Coventry, England, Poster P289.

S. Deike, M. Malke, W. H. Binder; “Beta-turn mimetic helical polymers”, European Polymer Federation Congress (EPF), 22.–26. Juni 2015, Dresden, Deutschland, Poster SYN-P-048.

Halle (Saale), 14.08.2019

---

Stefanie Deike

## **Eigenständigkeitserklärung**

Hiermit erkläre ich an Eides statt, dass ich die vorliegende Dissertation selbstständig und ohne fremde Hilfe verfasst und keine anderen, als die von mir angegebenen Quellen und Hilfsmittel verwendet habe.

Außerdem erkläre ich, dass die vorliegende Dissertation an keiner anderen wissenschaftlichen Einrichtung zur Erlangung eines akademischen Grades eingereicht wurde.

Halle (Saale), 14.08.2019

---

Stefanie Deike